UNIVERSITY OF CALIFORNIA
RIVERSIDE

Illuminating the Dark: Globular Clusters as Probes of the Dark Matter Content of Dwarf Galaxies

A Dissertation submitted in partial satisfaction
of the requirements for the degree of

Doctor of Philosophy

in

Physics

by

Jessica E. Doppel

June 2023

Dissertation Committee:

Dr. Laura V. Sales, Chairperson
Dr. Gabriela Canalizo
Dr. Anson D'Aloisio

The Dissertation of Jessica E. Doppel is approved:

Committee Chairperson

University of California, Riverside

Acknowledgments

The work completed in this dissertation would not have been possible without the support of many individuals along the way. First and foremost, I would like to thank my friends and family for cheering me on along the way, regardless of whether or not they entirely understood what I was working on. For providing me the mentorship and guidance necessary to complete this work and for helping me come into my own as a researcher, I would like to thank my advisor, Laura Sales. I would like to acknowledge the insight and feedback from my collaborators that have added new dimensions to much of the work in this dissertation. I am deeply thankful for the graduate student community—both within and outside of the the astronomy department—for being a force of support and positive change throughout my time here. Lastly, but certainly not least, I would like to thank the astronomy department faculty—especially my committee members Gaby Canalizo and Anson D'Aloisio—for their mentorship and advice for continuing along the academic career path.

I would like to acknowledge funding from UCR's Chancellor's Distinguished Fellowship, Graduate Research Mentorship Program Fellowship, Provost Fellowship, and Dissertation Year Program Fellowship in addition to a Short Term Research Grant from the DAAD.

This work utilizes the Illustris and IllustrisTNG50 (hereafter TNG50) simulations, which have been made publicly available. I would like to acknowledge the DAAD, the IllustrisTNG collaboration, and the Max Planck Institute for Astrophysics for allowing me early access to the TNG50 simulation and for hosting me during that time. Finally, I

acknowledge several open-sources python packages for allowing me to complete both my globular cluster model and the subsequent analyses: Matplotlib (Hunter 2007), NumPy (Harris et al. 2020), Scipy (Virtanen et al. 2020), PySPHviewer (Benitez-Llambay 2015), Numba (Lam et al. 2015), and illustris_python (Nelson et al. 2015).

This dissertation is composed of drafts of articles that have been accepted (Chapters 2 & 3) or that will be submitted (Chapter 4) for publication by Oxford University Press in the Monthly Notices of the Royal Astronomical Society, written by myself and my collaborators: Jessica E. Doppel, Laura Sales, Dylan Nelson, Annalisa Pillepich, Eric Peng, Elisa Toloba, Mario Abadi, Felipe Ramos-Almendares, Jose Benavides, Julio Navarro, Federico Marinacci, Jill Naiman, Paul Torrey, Mark Vogelsberger, Rainer Weinberger and Lars Hernquist.

ABSTRACT OF THE DISSERTATION

Illuminating the Dark: Globular Clusters as Probes of the Dark Matter Content of Dwarf Galaxies

by

Jessica E. Doppel

Doctor of Philosophy, Graduate Program in Physics
University of California, Riverside, June 2023
Dr. Laura V. Sales, Chairperson

We have developed a post-processing tagging technique to model globular clusters (GCs) in cosmological hydrodynamical simulations. We have applied our method to the Illustris and TNG50 simulations to study several aspects of GCs in galaxy groups and clusters, regimes where no other theoretical technique is available to link galaxies, halos and GCs. We find that GCs are good tracers of dark matter–both in terms of their radial distribution and shape to trace the host halos in groups and clusters, but also through their kinematics to constrain the dynamical mass of dwarf galaxies. We have used our catalogs to establish one-to-one comparison to observational determinations of dark matter mass in dwarfs, finding that while systems with more than 10 GC may recover the right dark matter mass content via Jeans modeling and other derived mass estimators, for dwarfs with less than 10 GCs, assumptions in the prior and different methods to estimate the velocity dispersion may heavily bias the ability to infer dark matter mass from kinematics. We find that dwarf galaxies are consistent with populating an extrapolation of a single power-law relation between GC mass and halo mass observed for more massive systems, at least all the

way down to dwarfs comparable to dwarf spheroidals in the Local Group ($M_* = 5 \times 10^6 \mathrm{M}_\odot$). Lastly, we explore the GC systems of the set of morphologically defined ultra-diffuse galaxies (UDGs) within the TNG50 simulation. Observationally, the kinematics of the GC systems of UDGs show a large diversity, with systems ranging from apparent "failed galaxies" living in overly-massive dark matter halos to the opposite extreme, where UDGs are seemingly dark-matter free. We use our GC catalog to demonstrate that much of this diversity, in particular towards low GC numbers, might arise as a combination of a low number of dynamical tracers coupled to ongoing tidal disruption—in agreement with evidence of stellar streams in some of the UDGs with low velocity dispersion—as well as contamination from GCs in the intracluster medium.

Contents

List of Figures

List of Tables

Chapter 1

Introduction

Thus far, all efforts to directly detect dark matter (DM) have proven unsuccessful. Through indirect detection, namely through various luminous tracers, we can infer that DM dominates the matter content of the Universe. For example, through measurements of galactic rotation curves (see e.g., Rubin et al. 1978), we find that galaxies reside at the dense, often cuspy, centers of extended DM halos. The DM halos themselves grow from smaller halos combining into larger ones, as can be observed in instances of galaxy mergers. Coupled with observations of the cosmic microwave background (CMB) that show the universe is expanding, these observations serve as confirmation for several predictions of the ΛCDM framework (see White and Rees 1978; White and Frenk 1991) for dark matter, that:

1. DM is composed of cold, collisionless particles that collapse into halos with a cuspy structure

2. structure grows hierarchically, meaning that smaller halos merge into larger objects.

Thus, ΛCDM is one of the most successful models to describe DM on the cosmological scale.

ΛCDM is not, however, without its uncertainties and challenges. Historically, ΛCDM has suffered discrepancies with observations, particularly of small scale structure. For example, DM only simulations of the universe predicted many more DM substructure than there were observed luminous satellites: the missing satellite problem (Klypin et al. 1999). This particular tension has since been resolved by both the inclusion of baryonic physics in simulations and with more complete and deeper surveys that can detect fainter satellites (see e.g. Sales et al. 2022, and references therein). Of additional concern at the scale of dwarf galaxies is the too big to fail problem (Boylan-Kolchin et al. 2011), wherein DM only simulations predicted too many dark subhalos that should have hosted a luminous component. While this problem is similarly alleviated by the inclusion of baryons in simulations of the local group, it is currently unclear whether this solves the problem in other environments (Sales et al. 2022). Other uncertainties at dwarf scales include the core-cusp problem (where many dwarf galaxies are observed to reside in cored rather than cuspy DM halos, see Flores and Primack 1994; Moore 1994), and the diversity of dwarf galaxy rotation curves (Santos-Santos et al. 2020). While many of these additional tensions between simulation and observation are eased by the inclusion of baryonic physics in high-resolution simulations, other proposed solutions include invoking more exotic models of DM, such as warm dark matter (WDM) (e.g., Ludlow et al. 2016) and self-interacting DM (SIDM) (see Vogelsberger et al. 2014c) models. These uncertainties thus present dwarf galaxies as key laboratories to test dark matter models or, perhaps, to provide further confirmation for ΛCDM .

The kinematics of luminous tracers is a particularly strong indicator of the presence of DM—DM interacts with baryonic matter via gravity, so the way things move can reveal the presence of mass that is otherwise unseen. For example, using the kinematics of different populations of stars to calculate dynamical mass within their half-light radii, one can construct the DM distribution for a given galaxy (Walker and Peñarrubia 2011). There are, of course, limitations to which sort of tracers can be used to infer DM content. While the velocities of individual stars can be observed for relatively nearby galaxies (Walker et al. 2007; Simon and Geha 2007; Strigari et al. 2008; Kirby et al. 2014, among others), such observations become extremely difficult for more distant objects. The kinematics of gas associated to galaxies or galaxy clusters has also been used as a tracer of DM (Alabi et al. 2016, 2017; Longobardi et al. 2018), but for galaxies that are devoid of gas, this method cannot be applied. Given their ability to be observed over large distances, globular cluster (GC) kinematics can also be used to estimate DM content (e.g., Alabi et al. 2016; Toloba et al. 2016; Alabi et al. 2017; Toloba et al. 2018; van Dokkum et al. 2018b).

Globular clusters (GCs) are particularly powerful tracers of the underlying dark matter distribution of the Universe. They are ubiquitious—observed to be associated to galaxies on scales from dwarf galaxies (e.g., Simon et al. 2021; Toloba et al. 2016; Sánchez-Janssen et al. 2019) to the environments of nearby massive galaxy clusters such as Virgo and Coma (Lee et al. 2010; Peng et al. 2011). GCs have also recently been mapped in galaxy clusters at intermediate redshifts by JWST observations in SMACS J0723.3-7327, at $z \sim 0.4$ (Lee et al. 2022). Their relative brightness, compared to diffuse stars in their host galaxies, make them ideal (and sometimes, the only) targets for photometric or spectroscopic studies

that infer properties of otherwise untraceable dark matter. For instance, studies of dozens of galaxies have shown a scaling relation between the GCs mass and their host galaxy's dark matter (DM) halos (e.g., Peng et al. 2008; Harris et al. 2015), while their velocity dispersion may be used for recovering the dynamical mass of their host galaxies (Doppel et al. 2021). Additionally, observations of the formation of extreme stellar clusters in galaxy mergers suggests a potential connection between GCs and galaxy formation (Portegies Zwart et al. 2010).

The rich environments of galaxy groups and clusters host a diverse set of galaxies—spanning from dwarfs to massive ellipticals—making them the targets of many observational surveys. It is in these dense environments where most GCs are found, not only associated to the individual galaxies within the environment as well as associated to the intracluster medium (Lee et al. 2010; Peng et al. 2011; Alamo-Martínez and Blakeslee 2017; Madrid et al. 2018; Lee et al. 2022). We find a wealth of observations of the GC systems of dwarf galaxies in these systems (e.g., Peng et al. 2006; Jordán et al. 2007; Peng et al. 2008; Toloba et al. 2016; Forbes et al. 2018; Prole et al. 2019; Lim et al. 2020; Carlsten et al. 2022, among others), which allows us to probe their DM content with their GC systems. A large amount of scatter is found in the properties of the GC systems—in their GC number, specific frequency, velocity dispersion, and, to a lesser extent, their luminosity function—of dwarf galaxies. This diversity implies a wide range of inferred DM content. For ultra-diffuse galaxies (UDGs) (van Dokkum et al. 2015a,b), a subset of dwarf-mass galaxies whose extended stellar components create their very low surface brightness appearance, this range is even more pronounced, with GC numbers and kinematics suggesting DM halos ranging

from being on par with that of the Milky Way (Beasley et al. 2016; Peng and Lim 2016, Toloba et al., in prep) to having little to no DM at all (van Dokkum et al. 2018b, 2019a; Danieli et al. 2019).

The abundant observations of GCs that reside in galaxy groups and clusters provides an opportunity to characterize the properties of GC systems across a large number of dwarf galaxies. To do this, we need to turn to theoretical and numerical models to understand the processes that shape the GC systems of galaxies across a range of environments. However, even with the plethora of observational information of GCs available, their formation and existence in dense environments has proven particularly difficult to study from this standpoint.

The difficulty in studying GCs arises primarily from the large dynamical range of scales necessary to resolve their formation in conjunction with their host galaxies and environments. While simulations of individual, isolated star clusters can resolve the formation and internal dynamics of stellar clusters and proto-GCs themselves (see e.g., Grudić et al. 2021), this method does intrinsically separate them from events in their host galaxies themselves. At the scales of simulations of individual galaxies, resolving individual stars becomes extremely computationally expensive, but it does allow us to study the potential formation sites of stellar clusters (e.g., Kim et al. 2017; Ma et al. 2020; Sameie et al. 2022; Li et al. 2022), though any stellar clump that is created quickly gets destroyed by numerical effects. At the scale of galaxy groups and clusters where most GCs are observed to reside, it is computationally cost prohibitive to resolve the scales of GC formation in conjunction to their galaxies, much less the host galaxy group or cluster itself. However, to circum-

vent this limitation, we have developed a post-processing particle tagging technique that allows us to add GCs to simulations of large cosmological volumes (see Ramos et al. 2015; Ramos-Almendares et al. 2018, 2020; Doppel et al. 2023).

In this dissertation, we explore the predictions of our post-processing GC tagging model and how those predictions connect to both galaxy formation and dark matter. In Chapter 2, we discuss the systematics of using GCs as tracers of dynamical mass for dwarf galaxies in simulated galaxy clusters on par with Virgo, in particular, how different statistical methods of obtaining their velocity dispersion can affect inferences made about the amount of DM presence, and possible processes for the formation of galaxies with unusually low GC velocity dispersions. In Chapter 3, we present an improved GC particle tagging method applied to the state of the are IllustrisTNG50 simulation. Here, we explore the GC content of galaxies across a wide range of environments, from simulated groups on par with the mass of Centaurus A to that of the Virgo cluster. We test whether the $M_{GC} - M_{halo}$ relation described in Harris et al. (2015) can be extended into the dwarf galaxy regime, and the resultant predictions for GC numbers in the intracluster medium, in dwarf galaxies, and for the GC occupation fraction. In Chapter 4, we focus on the GCs of ultradiffuse galaxies, exploring their abundance and the effects of contaminating GCs in the inference of their dark matter mass. Finally in Chapter 5, we provide a summary of the main results.

Chapter 2

Paper I: Globular clusters as tracers of the dark matter content of dwarfs in galaxy clusters[1]

2.1 Abstract

Globular clusters (GCs) are often used to estimate the dark matter content of galaxies, especially dwarfs, where other kinematic tracers are lacking. These estimates typically assume spherical symmetry and dynamical equilibrium, assumptions that may not hold for the sparse GC population of dwarfs in galaxy clusters. We use a catalog of

[1]This chapter contains a draft of an article that has been accepted for publication in April 2021 by Oxford University Press in the Monthly Notices of the Royal Astronomical Society written Jessica E. Doppel, Laura V. Sales, Julio F. Navarro, Mario G. Abadi, Eric W. Peng, Elisa Toloba and Felipe Ramos-Almendares

GCs tagged onto the Illustris simulation to study the accuracy of GC-based mass estimates. We focus on galaxies in the stellar mass range $10^8 - 10^{11.8}$ $M_\odot$ identified in 9 simulated Virgo-like clusters. Our results indicate that mass estimates are, on average, quite accurate in systems with GC numbers $N_{\rm GC} \geq 10$ and where the uncertainty of individual GC line-of-sight velocities is smaller than the inferred velocity dispersion, $\sigma_{\rm GC}$. In cases where $N_{\rm GC} \leq 10$, however, biases may result depending on how $\sigma_{\rm GC}$ is computed. We provide calibrations that may help alleviate these biases in methods widely used in the literature. As an application, we find a number of dwarfs with $M_* \sim 10^{8.5}\,M_\odot$ (comparable to the ultradiffuse galaxy DF2, notable for the low σ_{GC} of its 10 GCs) with $\sigma_{\rm GC} \sim 7$ - 15 kms^{-1}. These DF2 analogs correspond to relatively massive systems at their infall time ($M_{200} \sim 1$ - 3×10^{11} $M_\odot$) which have retained only 3-17 GCs and have been stripped of more than 95% of their dark matter. Our results suggest that extreme tidal mass loss in otherwise normal dwarf galaxies may be a possible formation channel for ultradiffuse objects like DF2.

2.2 Introduction

Pioneering models of galaxy formation established that dwarf galaxies must have been inefficient at forming stars in order to reconcile the observed abundance of faint galaxies with the number of dark matter halos predicted in hierarchical formation models like the Cold Dark Matter scenario (CDM, White and Rees 1978; White and Frenk 1991). These ideas were confirmed by studies of rotation curves in late-type dwarf irregulars (Carignan and Freeman 1988; Broeils 1992; Côté et al. 2000; Swaters et al. 2009), and of the stellar kinematics of stars in dwarf spheroidals of the Milky Way and Local Group (Walker et al.

2007; Simon and Geha 2007; Strigari et al. 2008; Kirby et al. 2014), which demonstrated that dwarf galaxies are indeed heavily dark matter dominated.

The precise distribution of the dark matter compared to the luminous mass in these systems is less well known. Although dark-matter-only simulations suggest a universal mass profile (Navarro et al. 1996b), observations reveal instead a rich diversity of mass profiles in the inner few kiloparsecs of gas rich dwarfs (Oman et al. 2015). This diversity problem has elicited a number of proposals, which can be grouped into three main categories: (i) baryonic and feedback processes that may alter the dark mass profile (Navarro et al. 1996a; Pontzen and Governato 2012; Read et al. 2016a); (ii) uncertainties in the interpretation of rotation curves due to non-circular motions and/or triaxiality (Hayashi and Navarro 2006; Pineda et al. 2017; Read et al. 2016b; Oman et al. 2019); and (iii) more radical changes to the nature of dark matter, such as light axions (Marsh and Pop 2015), or the inclusion of a non-negligible self-interaction cross section (Spergel and Steinhardt 2000; Firmani et al. 2000; Creasey et al. 2017; Santos-Santos et al. 2020). Additionally, some baryon-only dwarfs could be the result of more exotic processes, such as energetic AGN outflows generating gas shells that fragment into individual dwarf-like mass objects (e.g. Natarajan et al. (1998)).

Early-type (i.e., spheroidal) dwarfs may provide important and independent constraints on these ideas. Common in high-density environments, such as groups and clusters, or simply as satellites of MW-like hosts, early type dwarfs are gas-poor, dispersion-dominated systems whose dark matter content may shed light on our understanding of dark matter and its interplay with baryons during galaxy assembly.

The lack of gas means that studies of early-type dwarfs require a different dynamical tracer. The relative brightness and extended spatial distributions of globular clusters (GCs) make them competitive kinematic tracers of galaxy mass. Indeed, in elliptical galaxies, GC studies have enabled constraints on enclosed mass and dark matter fractions with accuracy comparable to studies of HI rotation curves in spirals (Alabi et al. 2016, 2017; Longobardi et al. 2018).

Extending these studies to dwarf galaxies is challenging because the number of bright GCs in dwarfs is substantially smaller than in massive systems. For example, several hundred GCs have been used to map the mass distribution around bright galaxies like M87 in Virgo (Zhu et al. 2014; Li et al. 2020) and several dozens for luminous ellipticals in the SLUGGS survey (Forbes et al. 2017). For comparison, in dwarfs with $M_* \leq 10^9 M_\odot$, this quickly reduces to fewer than ~ 20 GCs per galaxy.

Despite this, GC studies have already yielded important constraints on the dark matter content of dwarf ellipticals (dE) in the Virgo cluster (Toloba et al. 2016) and, more recently, on "ultra-diffuse" galaxies (UDGs, van Dokkum et al. 2016), where kinematic measurements of the unresolved stellar population are hindered by their low surface brightness (Beasley et al. 2016; Toloba et al. 2018; van Dokkum et al. 2018a)

As in late-type dwarfs, GC studies of early-type dwarfs also suggest a wide range of dark matter content, with important consequences for the formation paths of UDGs and, potentially, for the nature of dark matter. Of particular interest is the discovery of at least one UDG dwarf, NGC 1052-DF2 (hereafter "DF2", for short) , where the extremely low value of the velocity dispersion of the GC (van Dokkum et al. 2018a; Wasserman et al.

2018) and stellar (Danieli et al. 2019) populations hint at little to no dark matter content for this dwarf with estimated stellar mass $M_* \sim 3 \times 10^8 M_\odot$. Although the exact value of the velocity dispersion of GCs (as well as the distances to galaxy (Trujillo et al. 2019) is still being debated ($\sigma_{\rm GC} \sim$ 5-10 km/s) and may depend on model assumptions (van Dokkum et al. 2018a; Martin et al. 2018; Laporte et al. 2019), it is at least a factor of ~ 3 smaller than that measured for the similar UDG system DF44, which has comparable stellar mass ($\sigma_* \sim 35$ km/s, van Dokkum et al. 2019b), which is broadly consistent with GC velocity dispersions of other dEs of similar stellar mass in the Virgo cluster Toloba et al. (2016).

Another puzzling dwarf also associated to NGC 1052 is DF4, a UDG where the measured GC velocity dispersion $\sigma_* \sim 4.2$ km/s leaves little room for dark matter (van Dokkum et al. 2019a), though the distance to this system, as with that of DF2, is still under discussion (Monelli and Trujillo 2019). The existence of dwarfs with similar stellar mass but such a wide range of morphology and dark matter content presents a clear challenge to current galaxy formation models.

Several scenarios have been proposed to form UDGs, including (i) feedback effects combined with environmental gas removal (Chan et al. 2018; Di Cintio et al. 2017; Jiang et al. 2019; Tremmel et al. 2020); (ii) unusually large dark matter halos or failed MW-like galaxies (van Dokkum et al. 2015a); (iii) dwarf halos with large spin (Amorisco and Loeb 2016; Mancera Piña et al. 2020); (iv) puffed up stellar systems due to the removal of gas to ram-pressure stripping (Safarzadeh and Scannapieco 2017); (v) tidal stripping of cored dark matter halos (Carleton et al. 2019); or (vi) a mixed population made of both: born

low-surface brightness dwarfs and tidal remnants of cuspy halos from more massive tidally stripped galaxies (Sales et al. 2020).

Encouragingly, the observational evidence seems to support a variety of formation paths for UDGs. For instance, the number of associated GCs varies widely, from ~ 30 in DF17 (Peng and Lim 2016) to some UDGs in Coma with no associated GCs at all (Beasley and Trujillo 2016; Lim et al. 2018). A systematic study of UDGs and their GCs in the Virgo cluster also confirms the trends found in Coma (Lim et al. 2020). More detailed, kinematical studies of 3 UDGs in Virgo have also revealed wide variations in enclosed dark matter mass, including one object, VLSB-D, with clear signatures of ongoing tidal disruption (Toloba et al. 2018). Intriguingly, of the 3 UDGs studied, VLSB-D has the largest stellar mass ($M_* \sim 7.9 \times 10^8 \mathrm{M}_\odot$) but also the lowest GC velocity dispersion, $\sigma = 16^{+6}_{-4}$ km/s.

It is tempting then to consider the following hypothesis: could the low velocity dispersion measured for some UDGs (DF2, DF4, VLSB-D) be explained as a result of tidal effects in cluster or group environments? Or, in other words, can simulations reproduce a GC velocity dispersion as low as $\sigma_{\rm GC} \sim 10$ km/s (or lower) in a galaxy with stellar mass as high as $M_* \sim 3 \times 10^8\, M_\odot$? Analytical arguments, combined with the cosmological hydrodynamical simulations presented in Sales et al. (2020), seem to suggest that this is indeed possible, but more detailed work is needed to fully validate this possibility.

We study these issues here using a catalog of GCs tagged onto the Illustris simulation (Ramos-Almendares et al. 2020). The simulation follows the dynamical evolution of dwarfs in clusters, providing an ideal tool to quantify the effects of tidal disruption, departures from equilibrium, and scarcity of tracers. We further use the simulations to look

into the tidal disruption formation scenario for objects like DF2. Our paper is organized as follows. The GC model and galaxy selection criteria are described in Sec. 2.3 and 2.4. We evaluate the accuracy of mass estimators in Sec. 2.5, with special emphasis on different methods to measure velocity dispersion, the number of targets, and the effects of tidal disruption. In Sec. 2.6 we use our simulated galaxies and GCs to look for DF2 analogs. We conclude and summarize our main results in Sec. 2.7.

2.3 Methods

We use the highest resolution run of the Illustris cosmological, hydrodynamical simulation (Illustris-1) (Vogelsberger et al. 2014a,b; Genel et al. 2014; Sijacki et al. 2015). The simulation has a box size of 106.5 Mpc on a side and assumes cosmological parameters consistent with the WMAP9 (Hinshaw et al. 2013) results. At the resolution used here, the mass per particle is 1.3×10^6 $M_\odot$ and 6.26×10^6 $M_\odot$ for the baryonic and dark matter components respectively, with a maximum gravitational softening length of 710 pc.

The galaxy formation model used by Illustris includes stellar evolution and supernova feedback, black hole growth and mergers, AGN feedback, as well primordial and metal line cooling, among others. The simulation matches a number of observables well, including the Tully-Fisher relation (Torrey et al. 2014; Vogelsberger et al. 2014b), the cosmic star formation density (Genel et al. 2014), the galaxy mass and luminosity functions (Vogelsberger et al. 2014b), and the wide range of colors and morphologies of the present-day galaxy population (Sales et al. 2015; Snyder et al. 2015; Rodriguez-Gomez et al. 2017).

2.3.1 Galaxy sample

Our galaxy sample consists of members of the 9 most massive clusters, with masses comparable to the Virgo cluster ($M_{200} > 8 \times 10^{13} \mathrm{M}_{\odot}$), in Illustris-1. Throughout this paper, we shall define virial quantities as measured at the radius containing 200 times the critical density of the universe. Halos and subhalos are identified using a combination of a friends-of-friends algorithm (FoF, Davis et al. 1985) and SUBFIND (Springel et al. 2001; Dolag et al. 2009). We use the SUBLINK merger trees (Rodriguez-Gomez et al. 2015) to trace the assembly of these clusters back in time. We follow the infall and posterior evolution of satellite galaxies identified in these 9 host clusters at $z = 0$, focusing on those in the stellar mass range $10^8 < M_* < 6 \times 10^{11} \mathrm{M}_{\odot}$. The minimum stellar mass cut implies a minimum of ~ 60 stellar particles in our objects, which we consider to be sufficiently resolved for the purpose of this analysis. Additionally, we require a minimum stellar mass at infall $M_* \geq 5 \times 10^8 \mathrm{M}_{\odot}$which guarantees on average more than 16,000 particles including dark matter, gas, and stars at infall. Our simulated galaxy catalog contains a total of 3777 satellite galaxies, and it records the *infall time* of each galaxy as the last time, before accretion, that it was the central galaxy of its own FoF halo.

2.3.2 Adding GCs to Illustris

Illustris follows the global star formation properties of galaxies but does not have the resolution to form or follow GCs. In our study, GCs are added to the simulation in post processing by tagging selected dark matter particles in galaxy halos to match, on average, the known properties of the GC population and its dependence on halo mass. The method

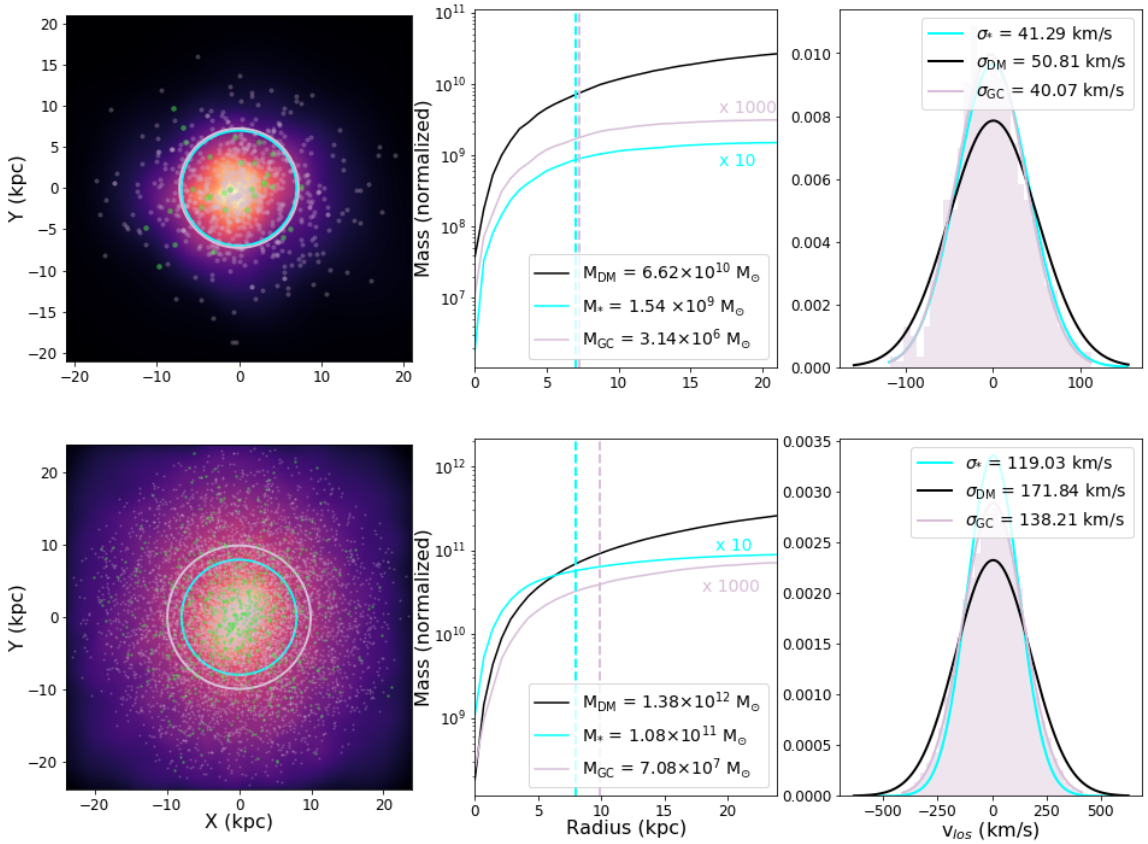

Figure 2.1: *Left:* XY projections of the stellar component (color scale in the background), GC candidates (pinkish points), and realistic GCs (green points), for a dwarf galaxy (top) and a Milky Way mass galaxy (bottom) belonging to the largest simulated galaxy cluster in Illustris. Pink and cyan circles indicate the 3D half mass radius of GC candidates and stars, respectively. *Middle:* normalized cumulative mass profiles for the dark matter (black curve), stars (blue curve) and GC candidates (pink curve) associated to these galaxies. The mass profile of the GC candidates has been multiplied by a factor of $\times 1000$, and the stellar profile has been normalized by a factor of $\times 10$. Masses as quoted in the legend. Half mass radius of stars and GCs are highlighted with vertical dashed lines. *Right:* line-of-sight velocity distributions for the GC candidates of these two galaxies (pink shade) along with the best fitting Gaussian in the same color. For comparison, we overplot the best-fitting Gaussians for the velocity distribution of the stars (cyan) and the dark matter in black. Note the similarities of their shapes and dispersion, values quoted for the latter for each galaxy.

was introduced in Ramos-Almendares et al. (2020), where details may be found. We include a brief description here for completeness.

The tagging process takes place, for each galaxy, at its cluster infall time. At that time, the procedure first identifies dark matter particles satisfying a prescribed density distribution; in particular, a Hernquist (1990) profile with scale radius, $a_{\rm HQ} = \alpha\, r_{\rm NFW}$, where $r_{\rm NFW}$ is the scale radius of the halo's best-fitting NFW profile (Navarro et al. 1996b), and α is a parameter that controls the spatial extent of the GC population. We use here two values of $\alpha = 0.5$ and 3 in order to select candidate tracers of the red and blue GC populations respectively. (Our analysis below, however, does not distinguish between these two populations.) Note that this method by construction selects all particles that are consistent with the energy distribution of GCs, which, in general, is a larger set of particles than the typical number of GCs associated to a galaxy. We therefore must subsample the set of *candidate* GCs to obtain a *realistic* population of GCs. This subsampling is done randomly and assumes that the mass of each GC is $10^5 {\rm M}_\odot$.

For these GC candidates, we assume that the total stellar mass of the GC population, $M_{\rm GC}$, scales with halo virial mass in a manner consistent with the results of Harris et al. (2015). Note that this relation holds at $z = 0$ while our procedure is applied at infall; thus, some adjustments are necessary, as some GCs may be lost to the cluster due to tidal effects. As shown by Ramos-Almendares et al. (2020), a simple relation at infall of the form

$$M_{\rm GC} = a M_{200}^b, \tag{2.1}$$

with $a = 2.0 \times 10^{-7}$, 3.5×10^{-4} and $b = 1.15$, 0.9 for red and blue GCs respectively, matches the Harris et al. (2015) relation well at $z = 0$. These tagged particles are then used to trace

the GC population of cluster galaxies after infall, as well as intracluster GC populations, which is made of all GCs stripped from galaxies after infall. At $z = 0$, the remaining candidates are subsampled assuming a fixed mass of $m_{\rm GC} = 10^5 {\rm M}_\odot$ per GC to determine a realistic number of GCs.

A specific caveat of this procedure is that we tag and follow only the population of *surviving* GCs and we do not account –by design– for the internal evolution of stellar clusters. Instead, our catalog can be used to study the dynamical process that GCs are subjected to within galaxy clusters after each galaxy, with their corresponding GC system, has been accreted into the cluster host.

The GC catalog created following this procedure has been shown to reproduce, without further adjustment, some key observational properties, including the large scatter in the specific frequency S_N for dwarf galaxies and the formation of an extended and diffuse population of "intracluster" GCs (Ramos-Almendares et al. 2020). In this paper we focus on the GC population around each surviving galaxy in the cluster at $z = 0$ in order to check to the accuracy of GC-based estimates of the total dynamical masses of cluster galaxies.

2.4 GCs of simulated cluster galaxies

We show in Fig. 2.1 two examples of our simulated galaxies and their GC system. The top and bottom rows correspond to, respectively, a dwarf ($M_* = 1.5 \times 10^9 {\rm M}_\odot$) and a luminous galaxy ($M_* \sim 10^{11} {\rm M}_\odot$). The left column shows a stellar map projection on which, to illustrate the tagging procedure, we superimpose the full population of tagged

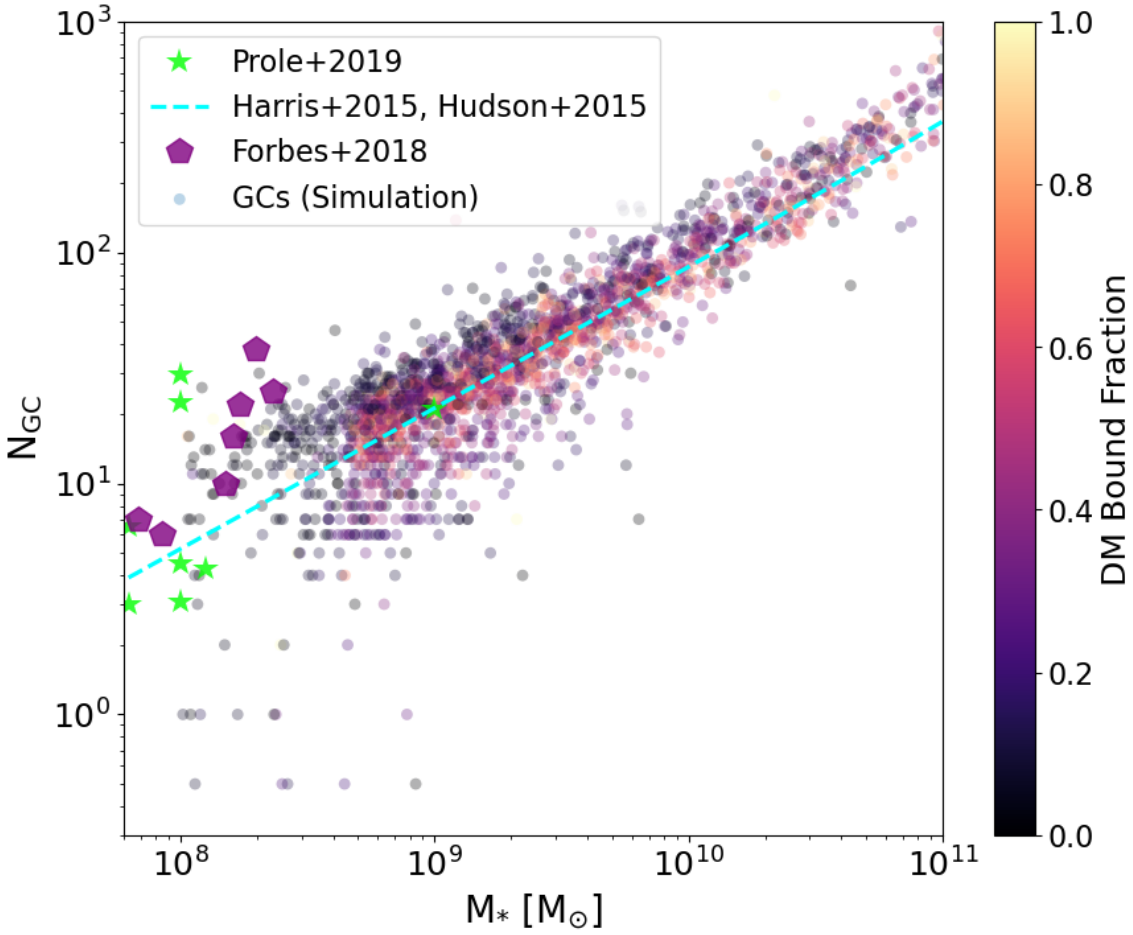

Figure 2.2: Realistic number of GCs, N_{GC}, versus the stellar mass of the host galaxy, M_*, colored by the bound dark matter fraction (see section 2.4). Our GC model is calibrated to reproduce on average the M_{GC} - M_{halo} relation from Harris et al. (2015) (cyan dashed line). Note that tidal stripping partially introduces a significant scatter from galaxy to galaxy, specially on the low mass end. The number of GCs for the lowest mass dwarfs in roughly consistent with observations in Prole et al. (2019) and Forbes et al. (2018) that were not part of the model calibration.

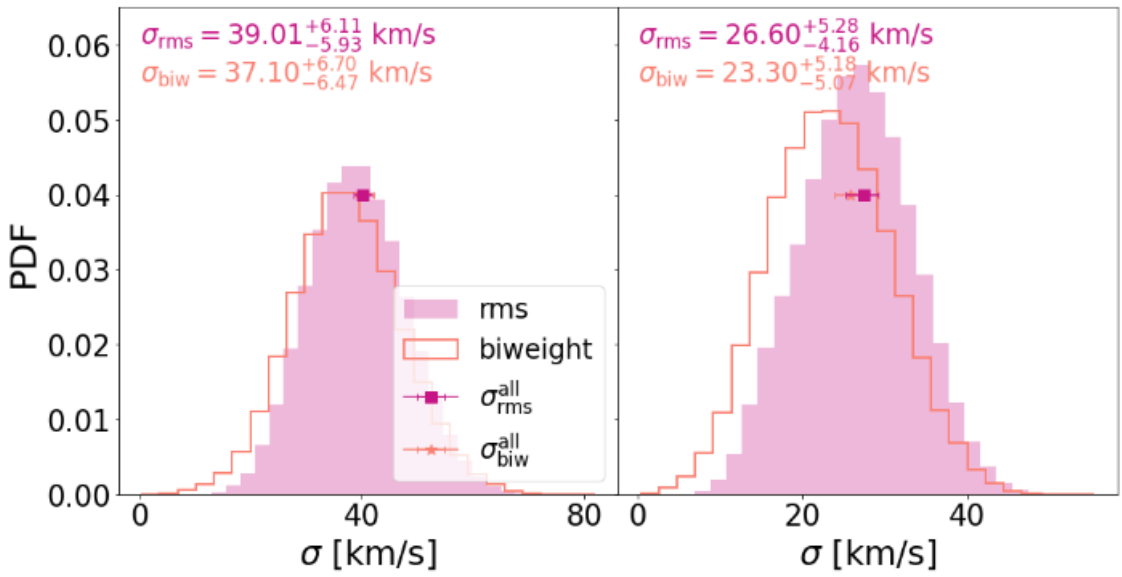

Figure 2.3: An illustration of the impact of using different definitions for the line-of-sight velocity dispersion σ_{los} of GCs in two simulated dwarfs (the left panel corresponds to the dwarf in the top panel of Fig. 2.1). Each panel shows the probability distribution function (PDF) of 10^5 random realizations of σ_{los} estimates using subsamplings of 10 GCs out of ~ 400 (left) and ~ 270 (right) GC candidate particles for the example dwarfs. We adopt two commonly used definitions, simple r.m.s (filled magenta) and biweight (open orange). These methods can predict slightly differently shaped PDFs, as well as different median values of line-of-sight velocity dispersion as quoted (uncertainties correspond to 25%-75% quartiles of the σ distributions). The r.m.s and biweight velocity dispersion of the underlying parent sample of ~ 400 and ~ 270 candidate GCs are shown with squared symbols (90% confidence interval is also shown as error bars). Although most of the σ estimates for each 10 GC draws would reasonably agree between r.m.s and biweight, for some realizations biweight estimates may underestimate the velocity dispersion compared to its r.m.s definition.

"candidate GCs" (pink points) as well as, in green, the actual particles selected as GCs in this case. The middle column shows the cumulative mass distribution with radius of the stellar component (cyan), dark matter (black) and GC candidates (pink). The GC spatial distribution is similar to that of the stars in the dwarf galaxy, but is significantly more extended than the stellar component of the more massive galaxy, in good agreement with well-established observational trends (e.g., Georgiev et al. 2010; Forbes 2017; Hudson and Robison 2018; Prole et al. 2019). The line-of-sight velocity distributions of these 3

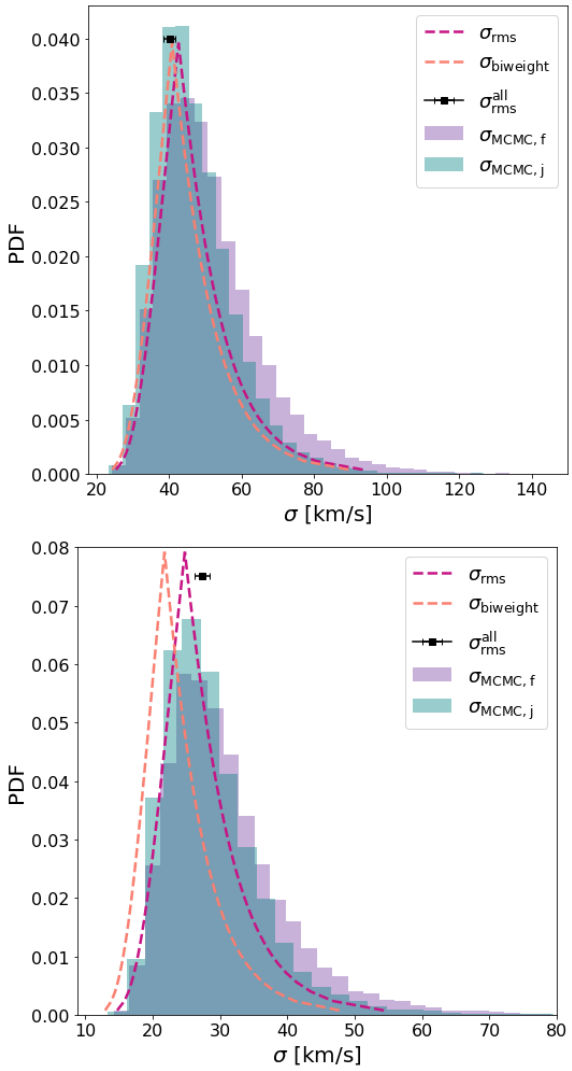

Figure 2.4: Velocity dispersion and confidence intervals calculated using different methods: r.m.s (magenta), biweight (orange), MCMC with flat prior (purple) and MCMC with Jeffreys prior (teal). We show in each panel one particular realizations of 10 GCs for the dwarfs in Fig. 2.3. For most possible drawings, the estimates of σ with different methods agree well and identify the true underlying (r.m.s) velocity dispersion of the whole ~ 400 (left) and ~ 270 (right) GC candidate sample ($\sigma^{\rm all}_{\rm RMS}$ square symbol). In some cases as highlighted on the right, biweight may result on a slightly underestimated velocity dispersion compared to the other methods.

components are shown in the right column and show that the GC velocity dispersion is comparable to that measured for the stars and the dark matter within three times the half-mass radius of the stars ($r \sim 3r_{h,*}$). Best-fit Gaussian distributions to each component are also included for comparison.

In order to minimize the number of potential interlopers (i.e., intracluster GCs, or GCs belonging to nearby galaxies) we associate GCs with each individual galaxy using a (3D) distance cut, i.e., $r \leq 3r_{h,*}$, and a velocity cut, which applies a 3-σ clipping criterion for membership in the line-of-sight velocities (projected in a random direction). This last step is effective at removing most (although not all) contamination from intracluster GCs and other chance alignments. We have explicitly checked that none of the results presented in this paper change qualitatively if the radial cutoff is varied in the range 2-5$r_{h,*}$. GCs satisfying the criteria of distance and velocity are then considered associated to each galaxy and used for dynamical mass estimation.

Fig. 2.2 shows that our tagging procedure yields realistic numbers of GCs as a function of their stellar mass. Although by construction the model reproduces the main trend with M_* reported by Harris et al. (2015, dashed cyan line) after assuming the M_*-M_{200} relation in Hudson et al. (2015), it is interesting to see the substantial scatter at fixed M_*, which results despite the fact that the relation adopted between GC mass and halo mass (Eq. 2.1) is assumed to be scatter-free. Moreover, the scatter in number of GCs, $N_{\rm GC}$, increases towards low-mass galaxies, in good agreement with observations (Peng et al. 2008; Prole et al. 2019; Forbes et al. 2018). For instance, a $M_* \sim 10^9 {\rm M}_\odot$ cluster dwarf may show 5-20 GCs, or even none (symbols artificially shifted to $N_{\rm GC} = 0.5$). Within

the simulation, this scatter results almost exclusively by the effects of tidal stripping in the cluster environment. Indeed, symbols in Fig. 2.2 are color coded by the DM bound fraction, the ratio of dark matter mass that the SUBFIND catalogs records for a galaxy at $z = 0$ to that at its infall time. As discussed in Ramos-Almendares et al. (2020), tidal stripping effects seem to be critical to explain the origin of the scatter in this relation and of its dependence on mass.

Note that we only tag at infall galaxies with $M_*(t = t_{\rm inf}) \geq 5 \times 10^8 {\rm M}_\odot$, meaning that all simulated systems in our sample with a present day stellar mass $M_* \leq 5 \times 10^8 {\rm M}_\odot$result from tidal stripping that has affected its stellar component. This can be seen in the low remaining dark matter bound fraction of most galaxies in that mass range in Fig. 2.2. In other words, for $M_* = 1\text{-}5 \times 10^8 {\rm M}_\odot$ range at present day, our sample only includes the tidally stripped objects–those that satisfied at infall the tagging criteria with $M_* > 5 \times 10^8 {\rm M}_\odot$. Simulated dwarfs in this mass range at z = 0 that have never been above the mass threshold for GC tagging are not included in our sample, a topic we return to in Sec. 2.6.

2.5 Dynamical mass estimators

Under the hypothesis of spherical symmetry and dynamical equilibrium, the mass enclosed by a collisionless population of tracers within their half-mass radius may be written as:

$$ {\rm M}(< {\rm r}_{1/2}) \approx 3 {\rm G}^{-1} \sigma^2_{\rm los} {\rm r}_{1/2} \tag{2.2} $$

where $\sigma_{\rm los}$ is the line of sight velocity dispersion of the tracers; $r_{1/2}$ is the 3D (de-projected) half-mass radius of the tracers; and $M(< {\rm r}_{1/2})$ is the total enclosed mass within $r_{1/2}$ (G is Newton's gravitational constant). This mass estimator has been shown to be relatively insensitive to the anisotropy parameter of the orbits (commonly referred to as β) and to projection effects (see; e.g., Wolf et al. 2010). Similar formulae have been presented by other groups, but the main variation is in the value of the proportionality constant or in the definition of the radius that the derived enclosed mass applies to. For simplicity, we focus on the reminder of this paper in the Wolf et al. (2010) estimator, but we have explicitly checked that similar conclusions apply when using different models, such as those presented by Walker and Peñarrubia (2011) or Errani et al. (2018). It should be noted that mass estimated derived from the Jeans Equation are sensitive to the assumed underlying mass distribution (Hayashi and Inoue 2018).

We may use our tagged catalog of GCs to assess how well Eq. 2.2 recovers the dynamical mass of simulated cluster galaxies in Illustris. One challenge in this case is estimating $\sigma_{\rm los}$, which is well defined when several dozen GCs are present, but is less robust for the small number of tracers available in the regime of dwarf galaxies (see Fig. 2.2). In what follows, we will drop the "line of sight" from the subscript, but we will still refer to the 1D velocity dispersion projected along a random direction, as measured in observations.

2.5.1 Velocity dispersion estimates

Several methods are widely used to compute σ. Here, we consider the following three: (i) the r.m.s of tracer velocities, $\sigma_{\rm rms}$ (see; e.g., Prada et al. 2003); (ii) the biweight

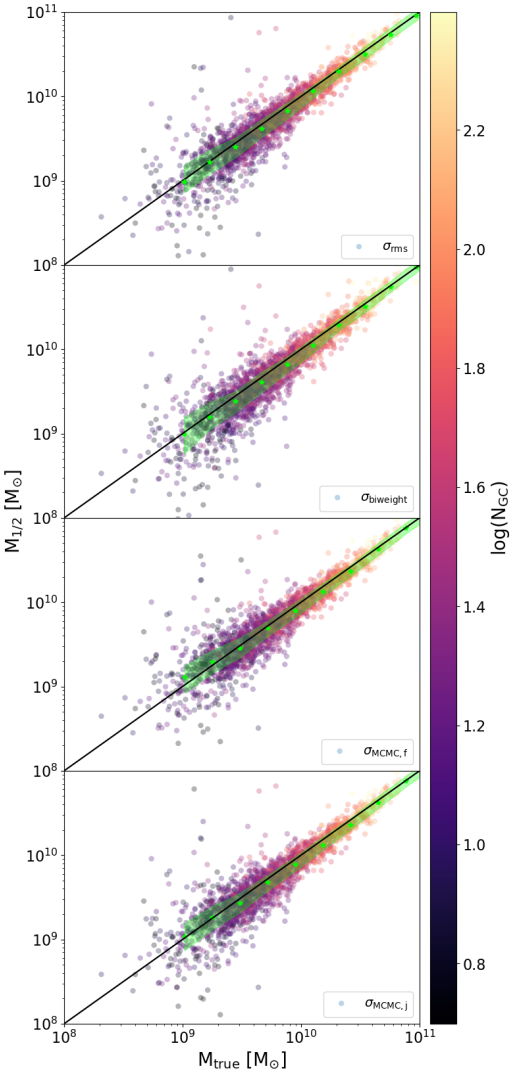

Figure 2.5: Comparison between the true (x-axis) and estimated (y-axis) dynamical mass measured for simulated galaxies at half-number radius of GCs using Wolf et al. (2010). Symbols are colored by the log of the number of globular clusters, N_{GC} associated to the host galaxy (color bar). The one-to-one line is shown in black, and the running median of the estimated dynamical mass $M_{1/2}$ at fixed $M_{\rm true}$ is shown in green symbols with 25%-75% quartiles indicated by the green shading. From top to bottom panels correspond to our three $\sigma_{\rm los}$ definitions: rms, biweight and MCMC (flat and Jeffreys priors). On average, all methods to quantify velocity dispersion perform very well to estimate mass on a sufficiently large sample of galaxies. However, the scatter increases for galaxies with a low number of GCs (darker symbols) which might result on significant deviation for individual objects. These deviations from the one-to-one line are systematic depending on the definition of $\sigma_{\rm los}$, as explored in Fig. 2.6.

velocity dispersion ($\sigma_{\rm biweight}$) (Beers et al. 1990; van Dokkum et al. 2018a; Girardi et al. 2008; Veljanoski et al. 2014); and (iii) a velocity dispersion, $\sigma_{\rm MCMC}$, estimated using a Markov-Chain-Monte-Carlo (MCMC) method applied to the individual velocities (Hogg et al. 2010; Widrow et al. 2008; Martin et al. 2018; van Dokkum et al. 2018c). Details on each method, as implemented here, are given in Appendix A.

Each of these methods has their own advantages and disadvantages. The r.m.s velocity dispersion has the advantage of simplicity but it may give biased results in case of non-Gaussian velocity distributions. The biweight method, on the other hand, is ideal when high levels of contamination are expected since it places more weight towards velocities closer to the median of the distribution, however, it cannot be used for systems with less than 5 tracers (Beers et al. 1990).

The MCMC approach enables a proper treatment of observational uncertainties, but it suffers from sensitivity to the shape of the priors assumed. In this study, we shall compare results using a flat prior distribution or Jeffreys prior, where the latter is usually considered more robust for low number of tracers (e.g., see Martin et al. 2018). We shall indicate the choice of prior with subscripts "f" and "j", respectively, when needed. See Appendix A for more details on the prior calculation.

For a given set of tracers, the σ probability distribution functions (PDFs) obtained with each of these methods may have slightly different shapes. We show this for the r.m.s and biweight distributions in Fig. 2.3 using two dwarfs as examples, the galaxy introduced in the top row of Fig. 2.1 which is characterized by an intrinsically nearly Gaussian line-of-sight velocity distribution (left panel) and a different dwarf selected to have a non-Gaussian line-

of-sight distribution of GC candidates with kurtosis and skewness 0.39 and 1.04, respectively (right panel). The PDFs shown in Fig. 2.3 correspond to velocity dispersion estimates obtained from 10^5 independent random selections of 10 GCs from among the ~ 400 (left) and ~ 270 (right) candidate GC particles that remain associated with these galaxies at $z = 0$.

While the r.m.s (filled magenta) and the biweight (open orange) methods show similar distributions, the biweight shows a systematic (albeit small) trend towards lower σ values, especially for non-Gaussian parent samples as illustrated for the dwarf on the right panel. This can be understood in light of the weight assignment for the biweight method, which tends to down-weight values further away from the median of the sample.

Reassuringly, the PDF distribution for these 10-GC re-sampling shows, in both methods, a well defined peak that agrees well with the velocity dispersion of the underlying parent distribution of ~ 400 and ~ 270 candidate GC particles (square symbols). However, this exercise highlights one of the main problems with the discreteness of the dynamical tracers: depending on the particular 10-GC realization, one might obtain estimates far from the true underlying velocity dispersion.

It is interesting to further explore the ability of different methods to estimate the true σ under the condition of a limited number of tracers. We do this by selecting one particular realization of 10 GCs from each of our examples in Fig. 2.3. For each of these two realizations, we estimate the confidence intervals assuming a Gaussian parent distribution in Fig. 2.4 for the r.m.s (magenta) and biweight (orange) methods.

We see that in both cases, estimates show a large degree of overlap between r.m.s and biweight, which would be the case for most of the possible 10-GC re-samplings. However, due to the low-velocity bias seen in biweight in Fig. 2.3, the estimated velocity dispersion with this method may substantially underestimate the true value for some specific samplings (right panel), a possibility that should be kept in mind when working with biweight estimates.

Fig. 2.4 also shows the corresponding PDF for the MCMC method using both, a flat (purple) and Jeffreys (teal) priors. For each 10-GC subsampling, the PDF is calculated by a random walk through (σ, $\langle v \rangle$) parameter space over 10^5 iterations using a Gaussian jumping distribution with a dispersion of 5 km s^{-1}. For both realizations in Fig. 2.4 the MCMC method is able to recover the true σ, with uncertainties that agree well with the simpler r.m.s method.

Faint dwarf galaxies can have even less than 10 GCs and the systematic effects explored here for each method may therefore become stronger. In what follows, we use our GC catalog to extend this study to a statistical sample of galaxies in Illustris to explore how the dynamical mass estimates are impacted by the finite number of GCs tracers and underlying assumptions of Gaussianity in the distribution.

2.5.2 Mass estimates

For each of the 3777 simulated cluster galaxies we may use the "realistic" number of GCs drawn from the list of candidates to compute the GC half number radius, $r_{1/2}$, and velocity dispersion using different estimators, $\sigma_{\rm rms}$, $\sigma_{\rm biweight}$ and $\sigma_{\rm MCMC}$. We then apply Eq. 2.2 to estimate their dynamical mass $M_{1/2}$ and compare the results obtained with each

estimator with the true mass enclosed within $r_{1/2}$, as measured directly from the particle information in the simulation, $M_{\rm true}$. Fig. 2.5 shows the results, with the solid black line indicating a one-to-one relation and points color-coded by the logarithm of the number of associated GCs used in the calculation. Green symbols show the median in bins of $M_{\rm true}$ and the shading indicates the 25%-75% quartiles.

We find, on average, a remarkably good agreement between the estimated dynamical mass $M_{1/2}$ and the true mass, supporting the use of simple estimators as that presented in Wolf et al. (2010) to determine the dynamical mass of galaxies using GCs as tracers (similar conclusions hold for estimators proposed in Walker and Peñarrubia (2011) or Errani et al. (2018)).

This result is not trivial, as many of the assumptions, such as sphericity and/or dynamical equilibrium, on which the estimator is based do not apply to our systems. Our results agree with Laporte et al. (2013a), who reported a similar conclusion although applied to *stellar* (not GC) tracers in dwarf spheroidal galaxies of the MW. The authors generalized the Bullock and Johnston (2005) method to cosmological triaxial systems (Laporte et al. 2013b) and find that the deviations from sphericity are compensated by a trade-off between the changes on the line of sight velocity dispersion and those in the half mass radius that are measured in different projections, canceling out in combination any systematic effect in spherical mass estimators such as Eq. 2.2.

A closer inspection of Fig. 2.5 reveals that systems with a low number of GCs (dark symbols) tend to have larger scatter around the one-to-one line. This coincides with the low mass regime, where dwarf galaxies often have only a few, or up to a dozen GCs.

Mass estimators tend to perform poorly with a low number of tracers, specially due to the errors in estimating velocity dispersion and half mass/number radius using only a handful of tracers.

We explore this in more detail in Fig. 2.6, where we show for our simulated galaxies the ratio of the estimated and the true mass as a function of the number of tracers used to calculate $M_{1/2}$ from Eq. 2.2. Every galaxy in our catalog is used at each point along the x-axis, using in each case a new random realization of $N_{GC} = 2, 3, ...N$ GCs, with N being the maximum number of of *candidate* GCs that were tagged for a given galaxy. Note that this is different from the procedure in Fig 2.5, where each galaxy is included only once using their *realistic* number of GCs. This is done to explicitly check how the number of available tracers affects/imporves the mass estimates keeping everything else fixed in the sample.

The upper panel in Fig. 2.6 corresponds to velocity dispersion estimates using r.m.s (magenta) and biweight (orange), where for each galaxy we calculate σ as the median of the PDF corresponding to 10^5 sub-samplings of GCs with a given number of N tracers (similar to Fig. 2.3). The bottom panel of Fig. 2.6 shows a similar exercise but using MCMC with flat (purple) and Jefferson (teal) priors. Due to computational demands, MCMC estimation corresponds, for each galaxy, to a single realization of N-tracers using 10^5 iterations across parameter (σ, $\langle v \rangle$) parameter space as done in Fig. 2.4, where $\langle v \rangle$ is the assumed average 1D velocity.

We find some interesting trends. First, the accuracy of the mass estimator depends strongly on the number of tracers but not on the galaxy mass. Different shaped symbols in Fig. 2.6 indicate 5 stellar mass ranges of our galaxies, as quoted in the legend, but symbols

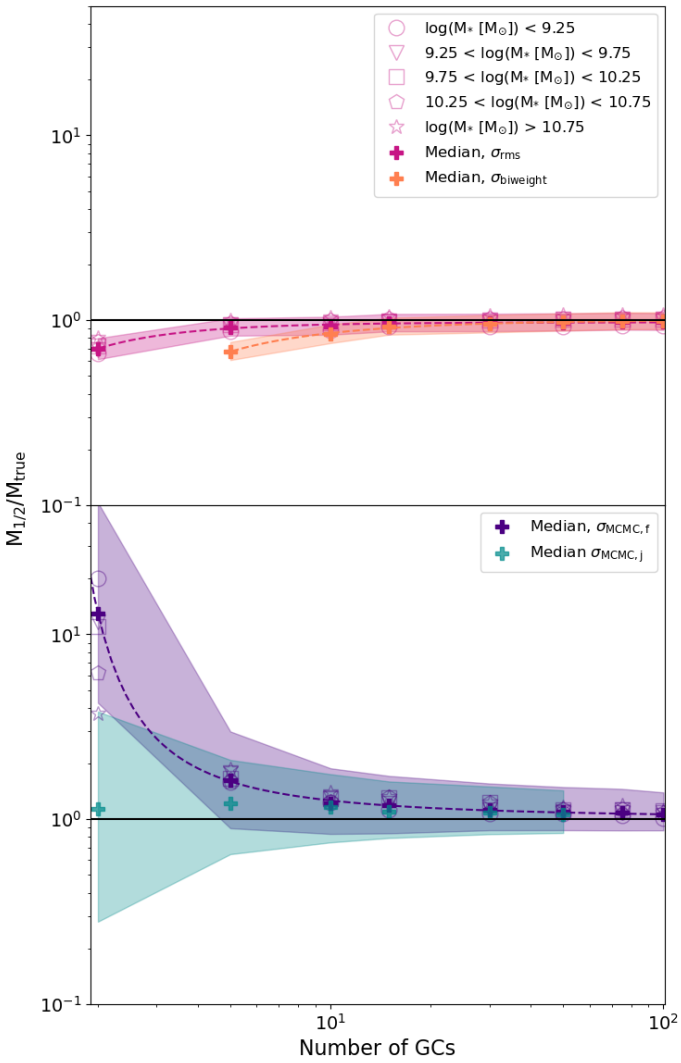

Figure 2.6: Median of the ratio of the estimated mass to the true mass, $M_{1/2}/M_{\rm true}$ as a function of number of GCs used in the estimate of $\sigma_{\rm los}$ following: the rms (magenta) and biweight (orange) in the top panel and MCMC methods with flat (purple) and Jeffreys (teal) priors in the bottom. Filled symbols show the median, shaded area the quartiles. We find no significant trend with stellar mass of the galaxies once $\rm N_{GC}$ is fixed (see open symbols). However, we find a strong trend with the number of tracers: $\sigma_{\rm rms}$ and $\sigma_{\rm biweight}$ tend to underpredict the dynamical mass while $\sigma_{\rm MCMC}$ overpredict the mass for a low number of GCs. These systematic trends can be corrected using a simple calibration (see dashed lines) shown in Eq. 2.3 and 2.4 with coefficients listed in Table 2.1. Note that mass estimates are accurate for galaxies with a sufficiently large number of tracers, for example $M_{1/2}$ is within 10-15% from the true mass for galaxies with $\rm N_{GC} \geq 30$.

tend to overlap suggesting little to no dependence on mass. Second, the r.m.s estimates recover the mass within 10% for $\sim$ 5-10 GCs while biweight requires 15-20 GCs to recover the mass with the same accuracy. MCMC with a flat prior converges more slowly, needing 30-40 GCs to recover the mass within 10% while Jeffreys prior brings the requirements down to 10-15 GCs for a 10% accuracy.

Another interesting point to highlight from Fig. 2.6 is the systematic deviations on the mass estimates for the different σ measurements. Whereas $\sigma_{\rm MCMC,f}$ will tend to overestimate the mass when using fewer than $\sim$ 30 GCs (see purple symbols), $\sigma_{\rm rms}$ and $\sigma_{\rm biweight}$ will underestimate the mass in the case of a low number of tracers (magenta and orange symbols). Noteworthy, using Jeffreys priors for the MCMC method can help mitigate the overestimation bias when the number of tracers is small $N_{\rm GC} \leq 5$ (green symbols), with significantly improved accuracy compared to assuming a flat prior. For larger number of tracers the assumptions on the prior do not have a significant impact.

Our results in Fig. 2.6 may be used as calibrations to improve the accuracy of mass estimation in observations of galaxies with a low number of GCs. We model the ratio $\rm M_{1/2}/M_{true}$ in for $\sigma_{\rm MCMC}$ and $\sigma_{\rm biweight}$ as:

$$\log\left(\frac{\rm M_{1/2}}{\rm M_{true}}\right) = \frac{\rm a}{(\log(N_{GC}) + c)^{b}} \tag{2.3}$$

where a, b and c are the best fit to the medians for each method in Fig. 2.6, and the results are shown with dashed purple and orange lines for MCMC (flat prior) and biweight, respectively. Following a similar procedure, we use the following function to describe the accuracy of mass estimation when using r.m.s velocity dispersions:

Estimate	a	b	c	Equation
$\sigma_{\rm rms}$	-1.535	1.057	0.963	2.4
$\sigma_{\rm biweight}$	-1.956	1.110	1.004	2.4
$\sigma_{\rm MCMC,f}$	0.097	1.908	-0.024	2.3

Table 2.1: Values for the parameters in equations 2.3 and 2.4 for each of the $\sigma_{\rm los}$ estimates.

$$\frac{\rm M_{1/2}}{\rm M_{true}} = \frac{\rm a}{\rm N_{GC}^{b}} + c \tag{2.4}$$

Our best fit values a, b and c for the three velocity dispersion estimates are summarized in Table 2.1. We hasten to add that the corrections for the MCMC case will depend on the shape of the prior. For example, in the case of the Jeffreys prior the correction to the median is roughly well described by a constant upwards shift factor of ~ 1.5, albeit with a significant object to object scatter.

2.5.3 Impact of tidal stripping

As an important application of our GC catalog, we can use the cosmological simulations of galaxies within realistic cluster environments to quantify how much tidal stripping might affect the accuracy of mass recovery techniques similar to Eq. 2.2 using GCs as tracers. Since Jeans modeling assumes the system to be in equilibrium, tidal stripping could potentially bias the results or cause the mass estimators to perform less accurately for significantly stripped and disturbed systems, as suggested by Smith et al. (2013) in the context of galaxy harassment.

We find that, contrary to these expectations, Eq. 2.2 performs *on average* extremely well even in cases with significant mass loss. Fig. 2.7 shows the ratio of recovered

mass using GCs, $M_{1/2}$, to the real mass from the simulation, $M_{\rm true}$, compared to the fraction of dark matter mass that is still bound (DM bound fraction), which we define to be the ratio of the present day dark matter mass of a galaxy to that at its time of infall. Different colors correspond to different stellar mass ranges for our galaxies and we find no significant trend with mass. This test uses $\sigma_{\rm MCMC}$ (with flat priors) to estimate the velocity dispersion of each galaxy using their realistic number of GCs in our catalog, but we have explicitly checked that the conclusions do not change if we use either $\sigma_{\rm MCMC,j}$, $\sigma_{\rm rms}$ or $\sigma_{\rm biweight}$.

A more detailed look at tidally stripped systems might reveal, however, important trends affecting the shape of the velocity distribution of tagged GC candidates. Fig. 2.8 quantifies the kurtosis (top) and skewness (bottom) of the line-of-sight velocity distribution of GCs for each of our galaxies as a function of their retained dark matter mass fraction. A perfectly Gaussian function corresponds to kurtosis and skewness being both consistent with zero. The cyan line and shaded regions correspond to the median and 1 σ scatter of the sample at fixed bound mass fraction.

Although GCs might *reasonably* be well described by Gaussians, our sample of candidate GCs systems show a systematic trend to negative kurtosis (median ~ -0.3 for objects with no significant stripping) and overall significant scatter in both kurtosis and skewness. Histograms on the right panels of Fig. 2.8 show examples of the shape of the velocity distribution of GCs for galaxies with either high or low skewness or kurtosis.

These deviations from Gaussianity might be more common for galaxies under severe tidal stripping (dark matter bound fraction lower than a few percent), which exhibit a bias towards higher values of kurtosis and skewness and increased scatter, especially

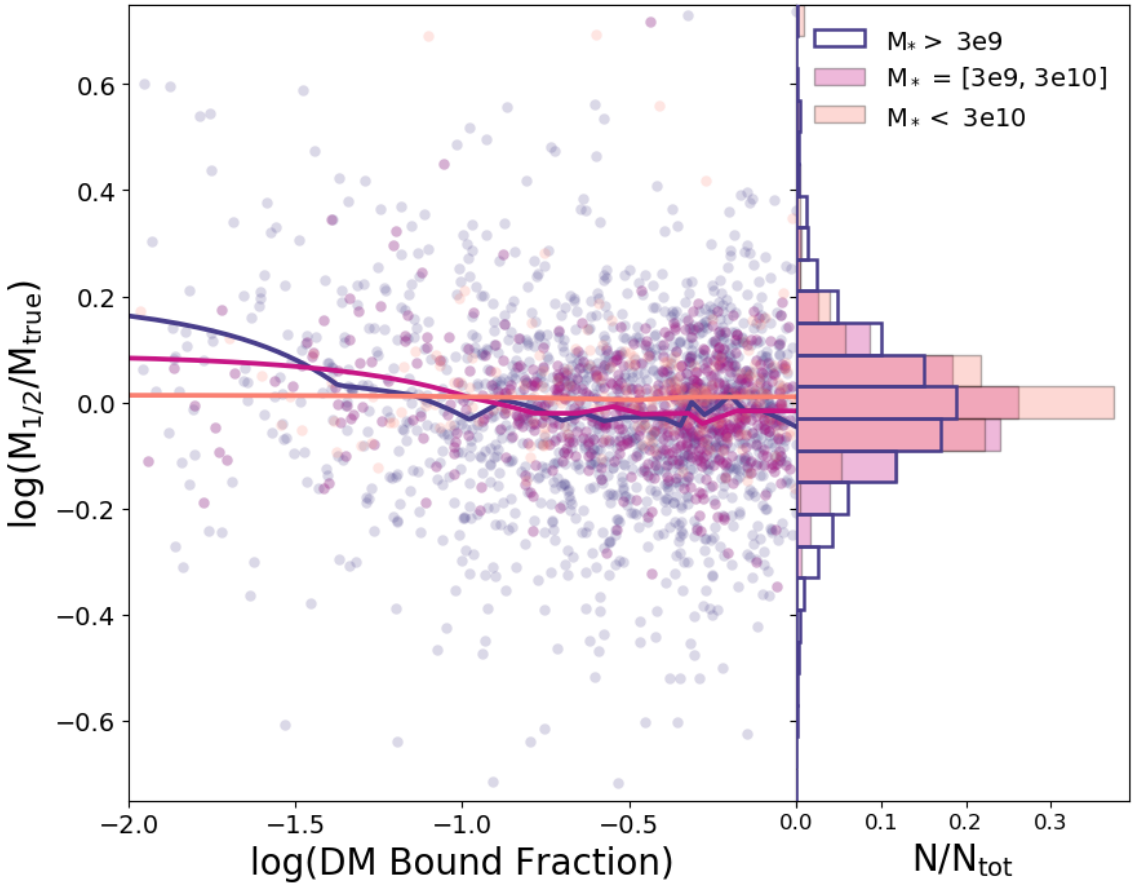

Figure 2.7: Ratio between the estimated mass using GCs to the true mass in simulated galaxies as a function of the amount of tidal stripping experienced. We show results for $\sigma_{\rm MCMC}$ but similar results applies to the other definitions. The fraction of bound DM mass (x-axis) is calculated as the $z = 0$ dark matter mass compared to the infall value. In general, the median of $M_{1/2}/M_{\rm true}$ of the sample (solid lines) shows little dependence on the remaining dark matter bound mass fraction, providing confidence on mass estimation methods even within the tidal environment of clusters. We find no significant trend with the galaxies stellar mass (see different colors).

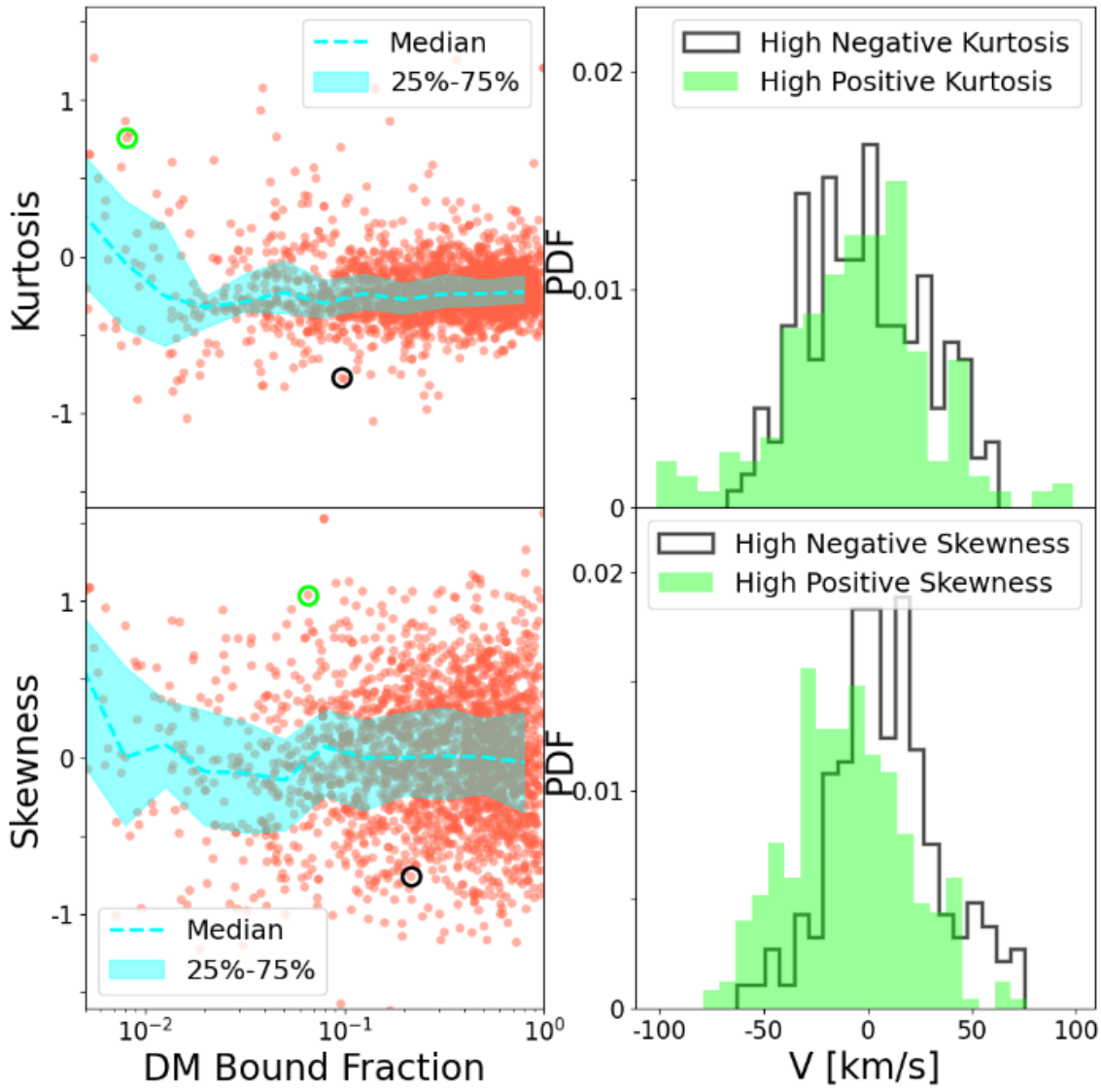

Figure 2.8: *Left*: Kurtosis (upper panel) and skewness (lower panel) as a function of the fraction of dark matter mass retained at z = 0 compared to that at infall. The median and 25-75 percentile range are shown by the cyan dotted lines and shading respectively. While the scatter of the skewness with respect to the DM bound fraction remains relatively constant, the scatter of the kurtosis increases as the DM bound fraction decreases. We also see an increase in the median of both the kurtosis and skewness with a decrease in DM bound fraction, suggesting that tidal stripping might induce a bias towards higher values. *Right*: Examples of non-Gaussian velocity distributions for extreme values of Kurtosis (upper panel) and extreme values of skewness (lower panel). The color of the histograms corresponds to the same colored circled points on the right panels.

in kurtosis. These results are important in light of the common-practice assumption of Gaussianity to estimate the uncertainties in the velocity dispersion of GCs in observational studies. How can skewness and kurtosis affect the calculated confidence intervals?

Confidence intervals are formally defined as the probability that the true variance of a given sample (in this case, all GCs candidates) lays within the confidence interval of the variance of a random subsample (for example, the realistic GC number) drawn from such parent distribution. If the underlying population is non-Gaussian, that probability would be expected to change and therefore confidence intervals can be over- or under-estimated. We show this in Fig. 2.9 using the r.m.s method (circles). For each galaxy we generate 1000 resampling of 10 GCs and compare the re-calculated confidence intervals to that of a Gaussian distribution. See Appendix C for more details.

We find that variations in kurtosis result in well-defined trends for the non-Gaussian confidence intervals (top left panel Fig. 2.9). In GC systems with intrinsic negative kurtosis, the confidence intervals are overestimated, meaning that the probability of finding the true variance within the computed confidence interval is actually larger than the case of a Gaussian distribution. For such systems, the observed value is actually *more* accurate than expected in a Gaussian case. The opposite is true for systems with positive kurtosis, where confidence intervals are underestimated. The scale of the effect varies with the confidence level being considered, varying from 10-20% for the 68% percentile (magenta) to $\sim 5\%$ for 95% confidence level (salmon).

Given the overall bias of our GC population in Fig. 2.8 towards negative kurtosis, current uncertainties calculated in observations might actually be on the conservative side

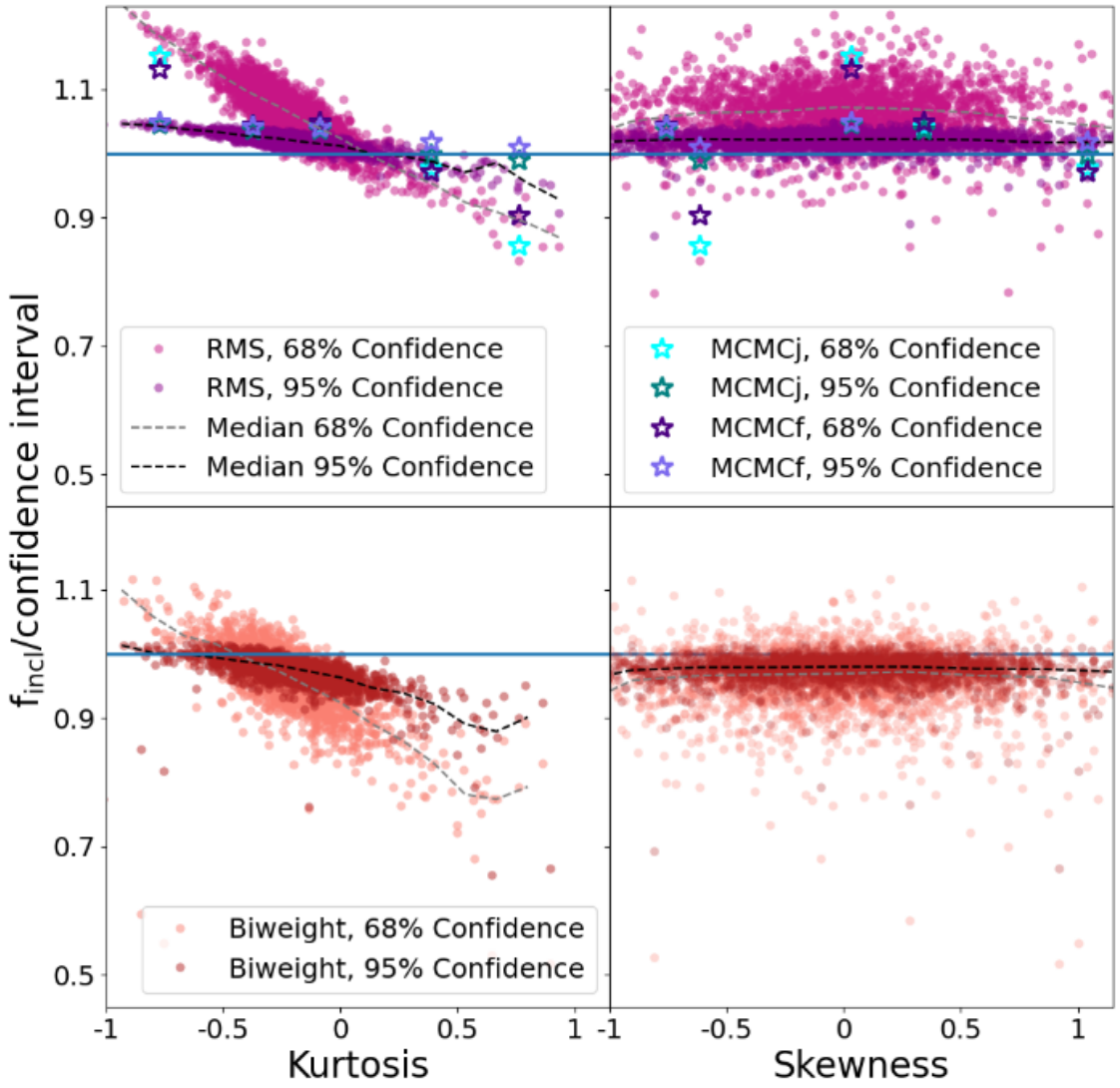

Figure 2.9: Correction to the Gaussian confidence intervals as a function of kurtosis (left) and skewness (right) of the distribution of candidate GCs associated to our galaxy sample. Estimates are based on 1000 resampling of 10 GCs (see text for details). The top and bottom row correspond to r.m.s and biweight estimates, respectively. Overlaid on the top row, we show with starred symbols the same calculation but using both MCMC methods for the four systems highlighted in Fig. 2.7 plus our fiducial dwarf in the top panel of Fig. 2.1. Different colors correspond to 68% and 95% confidence intervals, as labeled. Thin dashed lines highlight the median correction at fixed kurtosis or skewness. Non-Gaussianities may have a significant (and systematic) impact on accuracy estimates, in particular for high/low kurtosis values.

and constrains actually tighter than currently estimated. This, however, changes for systems under severe tidal disruption, expected to show more often positive kurtosis values that could result on confidence intervals being currently underestimated in the literature.

A similar exercise sorting our galaxies by their skewness (top right panel of Fig. 2.9) shows no significant dependence of the correction to confidence intervals with this parameter. Note that although these results were derived for r.m.s estimates, examples calculated from MCMC are consistent with these results (starred symbols). For completeness, we also show the correction levels for biweight velocity dispersion (see bottom panels of Fig. 2.9) which agree well with those calculated for r.m.s.

We conclude that although the overall velocity dispersion and dynamical mass estimates perform remarkably well *on average*, even under severe tidal disruption, in individual objects, kurtosis might be an important factor to consider when reporting confidence intervals in observations. This seems roughly independent of the particular method used to calculate the velocity dispersion, at least among the three explored here: r.m.s, biweight and MCMC. Unfortunately, estimating kurtosis or skewness in a sample with only a handful of GCs is challenging. Our theoretical results should be interpreted mostly as a warning that large deviations from Gaussianity may occur and would have a sizable impact on the estimated confidence intervals. This may have important consequences when dealing with systems where tidal disruption may be suspected to be important, as is the case of some ultradiffuse dwarf galaxies.

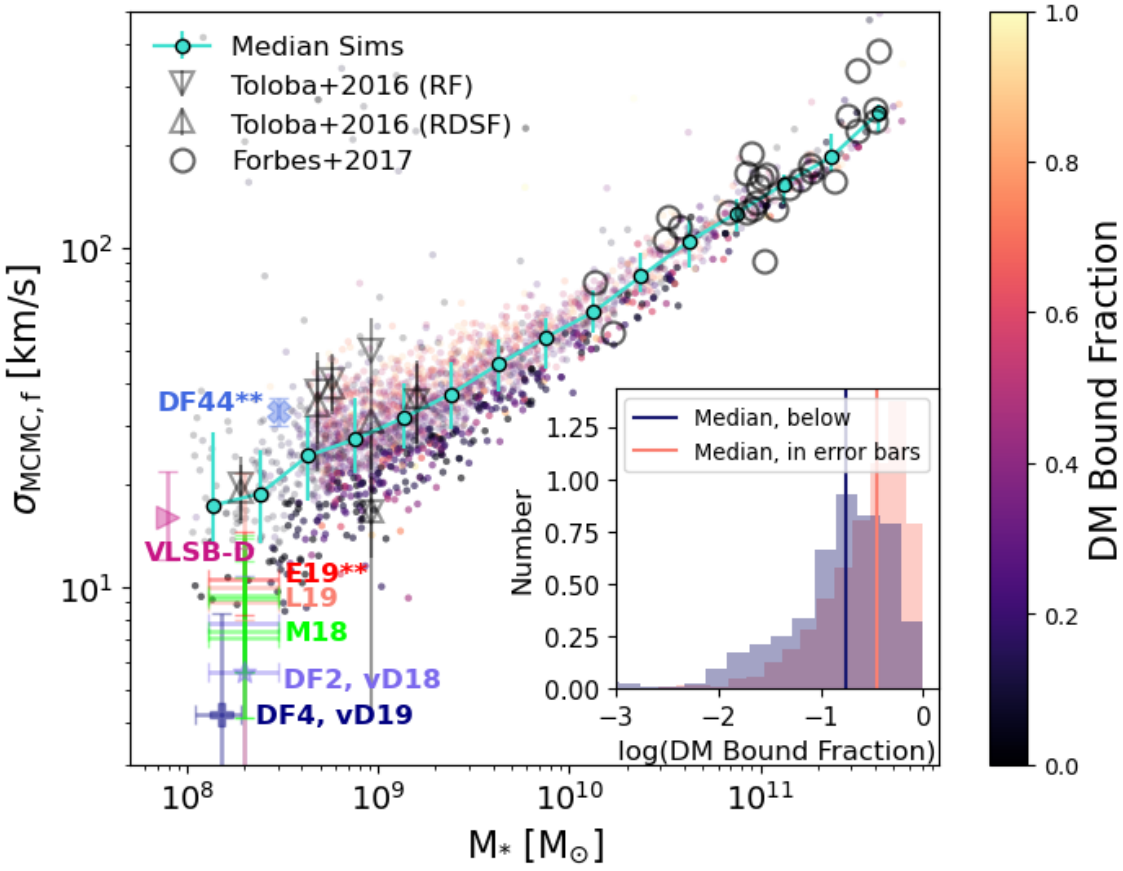
Median Sims
Toloba+2016 (RF)
Toloba+2016 (RDSF)
Forbes+2017
DF44**
VLSB-D
E19**
L19
M18
DF2, vD18
DF4, vD19
Median, below
Median, in error bars
Number
log(DM Bound Fraction)
$\sigma_{MCMC,f}$ [km/s]
M_* [$M_\odot$]
DM Bound Fraction

Figure 2.10 *(previous page)*: Predicted line-of-sight velocity dispersion of simulated GCs, $\sigma_{\rm MCMC,f}$, as a function of host galaxy stellar mass in our simulations, color-coded by the DM bound fraction, $M_{\rm DM,z=0}$ / $M_{\rm DM,inf}$ of each galaxy. The median trend (cyan) is in good agreement with observational constraints from SLUGGS on the high mass end (open circles) and also dE galaxies in Virgo Toloba et al. (2016) using both their RF (rotation fit) and RDSF (rotation and dispersion simultaneous fit) methods. The color gradient in the simulated points shows that at fixed M_* galaxies that have experienced more tidal disruption have the lowest GC velocity dispersion (darker symbols). We highlight this by selecting all simulated galaxies below and within 1σ scatter of the mean relation (see points with higher opacity and those within the cyan error bars) and plotting their distribution of retained dark matter mass in the small inset. These low $\sigma_{\rm MCMC,f}$ galaxies have retained only 17% (median) of their initial dark matter mass compared to about 36% of that for galaxies within 1 σ of the median. Interestingly, ultradiffuse galaxies with similar stellar masses show a wide range of velocity dispersion. Data for only 4 UDGs are available in this mass range, VLSB-D (Toloba et al. 2018), DF44** (van Dokkum et al. 2019b), DF4 (van Dokkum et al. 2019a) and several estimates for DF2: vD19 (lavander, van Dokkum et al. 2019b), M18 (green, Martin et al. 2018), L19 (orange, Laporte et al. 2019), E19** (red, Emsellem et al. 2019). (Double asterisks indicate velocity dispersion of the stellar component and not from GCs.) Examples like DF2 and DF4 sit at the lowest bounds of velocity dispersion with $\sigma \leq 10$ km/s. These results hint at tidal disruption as a possible formation path for objects like DF2 and DF4. In particular, some of our simulated galaxies overlap with the constraints for DF2.

2.6 Dark matter content in dwarfs estimated from the kinematics of GCs

Dwarf galaxies place constraints and challenges to the cosmological ΛCDM scenario and, with it, an opportunity to test theoretical predictions and validate (or falsify) the cosmological model. One of the basic predictions of galaxy formation models in the ΛCDM framework is that dwarf galaxies inhabit relatively massive halos. A number of observational efforts have therefore focused on measuring the dark matter content in dwarfs. In the case of cluster dwarfs, which are in their majority gas poor and of low surface brightness, GCs are often the best dynamical tracers given their luminosity and extended spatial distribution.

Studies of the kinematics of GCs in several dE galaxies in Virgo have revealed a wide range of velocity dispersion for GCs in $M_* \sim 10^9 M_\odot$ dwarfs (Toloba et al. 2016). However, other studies targeting ultra-diffuse dwarfs have revealed a much wider GC velocity dispersion range, including the detection of some UDGs where σ_{GC} is so low that, at face value, it suggests systems that are "dark matter free" (van Dokkum et al. 2018a,b, 2019b; Toloba et al. 2018). This result offers vital clues to our understanding of the formation paths of UDGs in clusters.

We use our tagged GC catalog in Illustris to study the population and kinematics of GCs predicted for dwarfs in clusters like Virgo. Fig. 2.10 shows the $\sigma_{MCMC,f}$ of GCs as a function of the stellar mass in our simulated cluster galaxies. We choose $\sigma_{MCMC,f}$ to facilitate the comparison with observational data. The median of the simulated relation is indicated in cyan, with vertical error bars corresponding to the r.m.s scatter.

In the dwarf regime (i.e., $M_* < 10^9\,M_\odot$) our estimates of $\sigma_{\rm GC}$ agree well with those of dEs in Virgo (data from Toloba et al. 2016, shown in grey triangles in Fig. 2.10). This is encouraging, since the GC tagging method relies on observations and calibrations done at higher masses, and the power-law relation between halo mass and GC mass is an extrapolation over this mass range. Moreover, the tagging is done at the moment of infall into the cluster and not at present day, making this comparison mostly a prediction of the model. Furthermore, it is reassuring that the velocity dispersion predicted for more massive ellipticals agree well with constraints from the SLUGGs survey (see open gray circles, Forbes et al. 2017).

Our calculations have so far not included the effect of individual errors in the measured velocity of each GC. In the dwarf galaxy regime, observations typically have individual errors of order 3-10 km s^{-1} per GC (Toloba et al. 2016, 2018; van Dokkum et al. 2018a). We have checked that adding random Gaussian errors with 10 km s^{-1} to our GC velocities only increases $\sigma_{\rm MCMC,f}$ on average by $\sim$ 20% on our lowest velocity dispersion objects, with increasingly smaller effect towards more massive systems. For instance, in galaxies with $\sigma_{\rm MCMC,f} \sim 25$ km s^{-1}, the MCMC velocity dispersion calculated assuming 10 km s^{-1} errors exceeds that without errors by $\sim$ 5% (median, see Fig. B.1). The overestimation is even smaller if we assume random errors with amplitude 5 km s^{-1} instead (see Appendix B for more details).

Simulated galaxies in Fig. 2.10 are colored by their retained (bound) dark matter fraction, calculated, defined as before as the ratio present-day dark matter mass given by SUBFIND compared to that at the moment of infall. We find a clear gradient of $\sigma_{\rm MCMC}$ at

fixed M_*, where galaxies with high GC velocity dispersion tend to retain most of their dark matter mass while low $\sigma_{\rm MCMC}$ values are dominated by galaxies that have lost more than 80% of their dark matter mass. To highlight this we show in the inset panel the distribution of bound dark matter mass fraction for all galaxies that deviate by more than one-sigma below the median relation (included points are highlighted with a higher symbol opacity). Galaxies this far down in velocity dispersion have retained typically only 17% of their initial dark matter halo.

Can tidal stripping explain the low GC velocity dispersion found in some UDGs like DF2? We show in Fig. 2.10 several measurements for the velocity dispersion of this dwarf as determined by different teams using slightly different assumptions (Martin et al. 2018; Laporte et al. 2019; van Dokkum et al. 2018a). Interestingly, we find a few simulated dwarfs with $\sigma_{\rm MCMC}$ consistent with the upper end of the range measured in the literature for DF2. These objects in our simulations seem significantly tidally stripped (dark color points), in agreement with the arguments discussed in the previous paragraph.

These results are intriguing, since tidal disruption has been proposed as one of the mechanisms that may transform normal galaxies into UDGs in clusters (Carleton et al. 2019; Sales et al. 2020; Leigh and Fragione 2020; Macciò et al. 2020), and some observational evidence for the case of stripping has recently been presented (Montes et al. 2020). Although the simulations do not have the resolution to follow the morphological changes of these galaxies, our results suggest that the same tidal transformation might lead to velocity dispersions as low ($\sigma_{\rm GC} \sim 10$ km/s) as that observed for GCs around DF2.

We note that the stellar mass for DF2 is estimated to be about $M_* \sim 2 \times 10^8 \mathrm{M}_\odot$ (van Dokkum et al. 2018a), which is below our cutoff $M_* \geq 5 \times 10^8 \mathrm{M}_\odot$ to tag GCs onto infalling halos. This means that our sample at these small masses includes only dwarfs that were more massive in the past (and therefore fulfilled our cut of $5 \times 10^8 \mathrm{M}_\odot$ for the initial tagging). From this perspective, it is not surprising the tidal origin of our identified DF2-analogs. However, it is interesting to find objects with GC velocity dispersions as low as DF2 in our simulated clusters.

To better assess the dark matter halos inhabited by DF2 candidates, we select all our simulated dwarfs in the stellar mass range $M_* = [1\text{-}3] \times 10^8 \mathrm{M}_\odot$ and show their present-day $\sigma_{\mathrm{MCMC,f}}$ of GCs as a function of their infall virial mass in Fig. 2.11. Here each simulated dwarf is color-coded by the number of GCs retained. We find that these "DF2-analogs" have between 3-30 GCs, in good agreement with the 9-11 observed GCs around DF2. We also show that the assumption of flat (full symbols) or Jeffreys (green open circles) priors do not qualitatively change our results (in agreement with the conclusions of Martin et al. 2018). For comparison, the shaded horizontal regions in Fig. 2.11 indicate the observational estimates of the velocity dispersion of DF2 GCs according to various authors.

Although the majority of our simulated dwarfs have higher $\sigma_{\mathrm{MCMC,f}}$, there are a handful of objects that overlap with the uncertainty range from Martin et al. (2018) and Laporte et al. (2019). These objects had infall virial masses consistent with dwarf halos in the range $M_{200}^{\mathrm{inf}} \sim [0.3\text{-}3] \times 10^{11} \mathrm{M}_\odot$, comparable to that estimated for, for example, the Large Magellanic Cloud (LMC) in the Milky Way. For these objects, the number of GCs

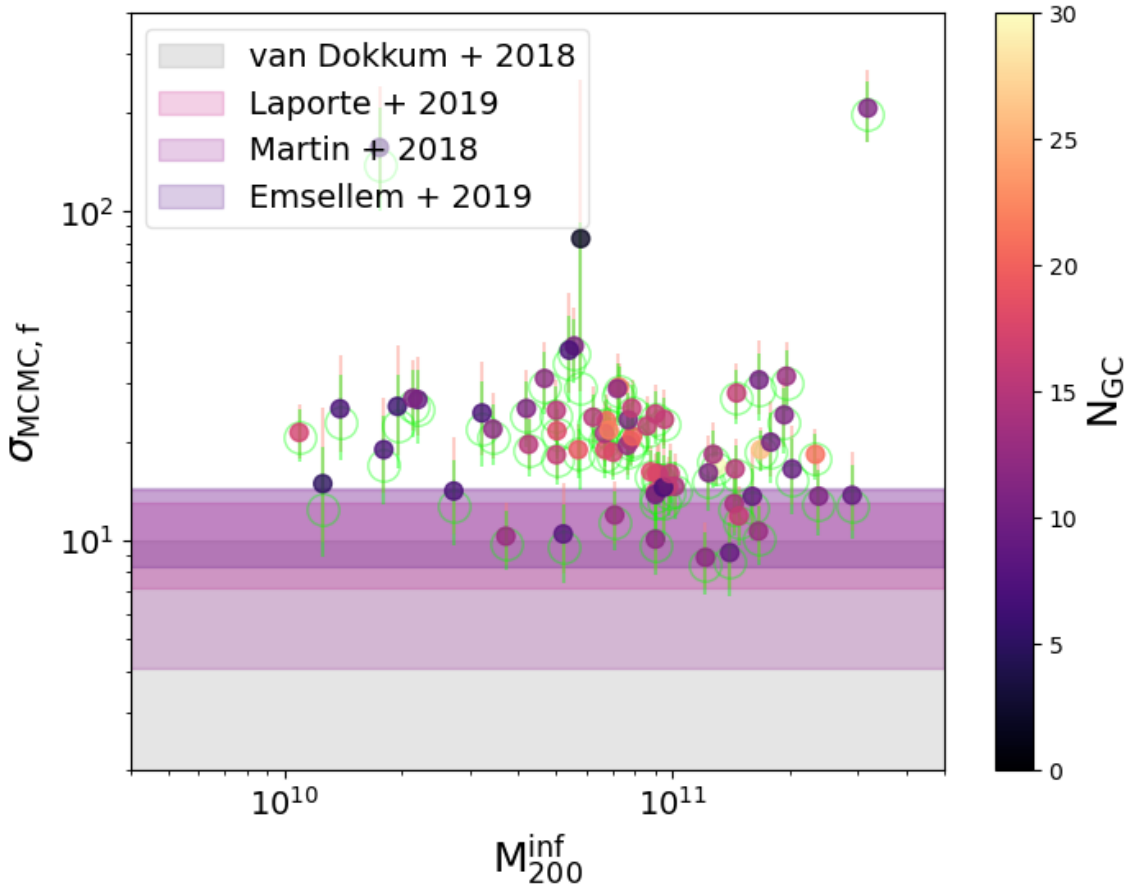

Figure 2.11: GCs velocity dispersion $\sigma_{\mathrm{MCMC,f}}$ for simulated dwarfs in the stellar mass range comparable to DF2, $M_* = 1\text{-}3 \times 10^8 \mathrm{M}_\odot$ as a function of their infall virial mass M_{200}^{inf}. The vertical error bars correspond to the 68 percent confidence interval for the MCMC velocity dispersion estimate (flat priors are shown in full symbols, open green circles show Jeffreys priors). Several of our simulated objects show GCs velocity dispersion that are compatible with the upper end of observational estimates for DF2 (see shaded areas). These kinematic analogs of DF2 have 3-17 GCs still bound at $z = 0$ (color bar) in good agreement with the ~ 10 GCs currently known for DF2. Our simulations suggest that DF2-like objects may have infell as dwarf halos with $M_{200}^{\mathrm{inf}} = 0.3\text{-}3 \times 10^{11} \mathrm{M}_\odot$ losing more than 90% of their dark matter mass at present day.

predicted by our tagging method (3-17) agrees well with the ~ 10 GCs found associated to DF2.

We note that there are still significant uncertainties in the measurement of the GC velocity dispersion in DF2. If lower values are proven more accurate, this would place DF2 close to the even more "dark-matter-free" UDG DF4 (as least as suspected from its stellar velocity dispersion). Additional formation mechanisms might be needed to explain the very low dark matter density in these extreme class of objects, such as a "tidal-dwarf" origin (see; e.g., Zwicky 1956; Schweizer 1978; Mirabel et al. 1992). The presence of dark matter cores driven by dark matter self-interactions or by baryonic feedback could represent a possible solution to this problem. Furthermore, higher resolution simulations would be needed to resolve such low dark matter contents.

Considering non-Gaussianities and the corrections to confidence intervals explored in Sec. 2.5.3, if the GC population of DF2 had positive kurtosis, then the uncertainty ranges estimated should be revised upwards, which would help alleviate the tension. In particular, the estimate from van Dokkum et al. (2018a) is based in $\sigma_{\rm biweight}$, for which we find a systematic underestimation of the confidence intervals compared to a Gaussian in the case of positive kurtosis (see Fig. 2.9). Assuming a correction level of 15% (corresponding to an intrinsic kurtosis ~ 0.75) DF2 could increase the upper limit of the 90% confidence interval from 10.5 km/s to 12.1 km/s, bringing it closer to other estimates[2].

We conclude that it is indeed possible that DF2 may have formed as the result of a normal dwarf halo that has been stripped of more than 90% of its mass. Low surface

[2]We note that the procedure in van Dokkum et al. (2018c) (and reproduced by Martin et al. (2018)) is slightly different than derived in Sec. 2.5.3, since they jointly estimate confidence intervals and intrinsic velocity dispersion in a single step.

brightness stellar tails, elongated morphology or evidence of rotation for its GC system (such as that found by Lewis et al. (2020)) could help confirm its tidal nature but their absence will not conclusively rule out this formation path. This highlights the urgent need for more observational campaigns targeting the kinematics of GCs around UDGs to more robustly constrain their global dark matter content.

2.7 Summary

We use a catalog of GCs tagged onto the cosmological hydrodynamical simulation Illustris to study the accuracy of dynamical mass estimates based on the radial extension and line-of-sight velocities of GCs systems. In particular, we analyze the GC system of satellite galaxies in 9 simulated galaxy clusters with virial mass $M_{200} \sim 10^{14}\mathrm{M}_{\odot}$. Our sample consist of 3777 galaxies in the mass range $M_* = 10^8$-$6 \times 10^{11}\mathrm{M}_{\odot}$.

We find that mass estimators of the form $\mathrm{M} \propto \sigma^2 \mathrm{r}$ do a remarkably good job at estimating mass when using GCs as tracers, specially when having 10 or more GCs. For galaxies that have a smaller number of GCs with measured kinematics, the particular definition of velocity dispersion used may systematically bias the results. Using the r.m.s and biweight velocity dispersion (Girardi et al. 2008; Veljanoski et al. 2014; van Dokkum et al. 2018a) tends to underestimate the dynamical mass, while other methods used in the literature such as σ_{MCMC} (Widrow et al. 2008; Hogg et al. 2010; Toloba et al. 2016; Martin et al. 2018) tend, on the contrary, to overestimate masses for low N_{GC}. In the case of MCMC the shape of the prior may play an important role, with Jeffreys prior resulting on

a lower bias compared to a flat prior. We provide fitting formulas in Eq. 2.4 and 2.3 that might help correct for these effects in observational samples with less than 10 GC tracers.

Surprisingly, the accuracy of the recovered mass estimation depends little on the level of tidal disruption suffered by the galaxy, indicating that satellite galaxies in clusters are, in their majority, in state of quasi-equilibrium as soon as they move away from their pericenters (see; e.g., Peñarrubia et al. 2009). Our results provide strong support for the use of GC kinematics to estimate dynamical masses even in high density environments such as clusters. A word of caution is necessary in the case of systems with significant tidal stripping, where significant deviations in kurtosis may arise as a consequence of the tidal disruption effects and may impact the estimated confidence intervals.

We use our results to compare the dark matter content of cluster dwarfs predicted in our simulations with available observational constraints in nearby clusters and groups. We find good agreement with the median and scatter measured for dwarf ellipticals in Virgo. Moreover, we find that tidal disruption creates scatter in the measured M_*-$\sigma_{\rm GC}$ such that at a fixed M_*, smaller velocity dispersions correlate with larger mass losses to tidal disruption. On average, galaxies that lay below the median relation by 1σ have lost $\sim 83\%$ of their infall dark matter mass.

In observations, there is large scatter in the velocity dispersion of GCs for dwarfs with $M_* \leq 10^9 {\rm M}_\odot$, with the most extreme outliers being ultra-diffuse galaxies DF2 and DF4. These UDGs have estimated GC velocity dispersions in the range $7-10$ km/s (DF2) and $\sigma \sim 4.2$ km/s (DF4) suggesting that they are extremely dark matter deficient. Interestingly, we identify a set of dark matter poor DF2-analogs in our simulation that have similar

stellar masses, 3-17 bound GCs, and a velocity dispersion of those GCs $\sigma_{\rm MCMC} \sim 10$ km/s, consistent with the upper envelope of measured values for DF2. The progenitors of these DF2 analogs fell into the cluster as dwarf halos with $M_{200}^{\rm inf} = [0.3\text{-}3] \times 10^{11} {\rm M}_{\odot}$but have lost more than 90% of their mass to tidal disruption. Interestingly, tidal disruption has also been proposed as possible mechanism to form UDGs in clusters (Carleton et al. 2019; Sales et al. 2020; Leigh and Fragione 2020; Macciò et al. 2020; Montes et al. 2020). Our results suggest that the same mechanism may be able to explain simultaneously the ultra-diffuse nature *and* low GC velocity dispersion in objects alike DF2 within ΛCDM.

Although we do not find systems with velocity dispersions as low as that inferred for DF4, we are limited by numerical resolution in our Illustris sample. The small number of UDGs with available kinematical data does not allow for a proper evaluation of how common or rare dark-matter poor dwarfs like DF2 and DF4 might be, or their dependence on the environment or host mass. While systematic photometric studies of UDGs and their GCs in nearby groups and clusters are starting to become available (e.g., in the Virgo cluster Lim et al. 2020), adding spectroscopic data to constrain their stellar and GC kinematics would represent the most promising avenue towards a better understanding of how UDGs form.

Explaining the large scatter in the dark matter content of dwarf galaxies is one of the outstanding challenges in the ΛCDM model. While the rotation curves of gas-rich dwarfs have revealed a wide variety of dark matter distribution in field dwarfs, GCs are starting to reveal a similarly rich complexity for gas-poor dwarfs in groups and clusters. As we look forward to larger datasets with available GC kinematical constraints for early-type

dwarfs, our results validate the use of GCs as efficient dynamical mass estimators even in the case of a modest number of GCs with measured kinematics.

Chapter 3

Paper II: Modeling globular clusters in the TNG50 simulation: predictions from dwarfs to giant galaxies[1]

[1]This chapter contains a draft of an article that has been accepted for publication in January 2023 by Oxford University Press in Monthly Notices of the Royal Astronomical Society written by Jessica E. Doppel, Laura V. Sales, Dylan Nelson, Annalisa Pillepich, Mario G. Abadi, Eric W. Peng, Federico Marinacci, Jill Naiman, Paul Torrey, Mark Vogelsberger, Rainer Weinberger and Lars Hernquist

3.1 Abstract

We present a post-processing catalog of globular clusters (GCs) for the 39 most massive groups and clusters in the TNG50 simulation of the IlllustrisTNG project (virial masses $M_{200} = [5 \times 10^{12} - 2 \times 10^{14}]$ $M_\odot$). We tag GC particles to all galaxies with stellar mass $M_* \geq 5 \times 10^6$ $M_\odot$, and we calibrate their masses to reproduce the observed power-law relation between GC mass and halo mass for galaxies with $M_{200} \geq 10^{11}$ $M_\odot$ (corresponding to $M_* \sim 10^9$ $M_\odot$). Here we explore whether an extrapolation of this M_{GC}-M_{200} relation to lower-mass dwarfs is consistent with current observations. We find a good agreement between our predicted number and specific frequency of GCs in dwarfs with $M_* = [5 \times 10^6 - 10^9]$ $M_\odot$ and observations. Moreover, we predict a steep decline in the GC occupation fraction for dwarfs with $M_* < 10^9$ $M_\odot$ which agrees well with current observational constraints. This declining occupation fraction is due to a combination of tidal stripping in all dwarfs plus a stochastic sampling of the GC mass function for dwarfs with $M_* < 10^{7.5}$ $M_\odot$. Our simulations also reproduce available constraints on the abundance of intra-cluster GCs in Virgo and Centaurus A. These successes provide support to the hypothesis that the M_{GC}-M_{200} relation holds, albeit with more scatter, all the way down to the regime of classical dwarf spheroidals in these environments. Our GC catalogs are publicly available as part of the IllustrisTNG data release.

3.2 Introduction

The formation of globular clusters (GCs) in connection to galaxies and their dark matter halos is still unclear. Currently, the most successful models link the formation of

GCs (or their early progenitors) to baryonic processes in the interstellar medium (ISM) of galaxies. These processes are connected to star formation in high density/high pressure environments (Kruijssen and Cooper 2012; Kruijssen 2015; Elmegreen 2017) and best sampled in mergers and early stages of galaxy formation (Kravtsov and Gnedin 2005; Prieto and Gnedin 2008; Li and Gnedin 2014; Renaud et al. 2015). However, GCs have also been hypothesized to form at the centers of their own low-mass dark matter halos before reionization (Peebles 1984; Boylan-Kolchin 2017), later infalling onto larger galaxies and groups and cluster halos to form the clustered GC distributions typically found in these systems (Diemand et al. 2005; Creasey et al. 2019). Although this scenario predicts older ages and lower metallicities for GCs than current measurements (Lotz et al. 2004; Bastian et al. 2020), the discovery of a few very metal poor GCs in M31, the Milky Way, and JWST observations may provide some support to such pristine formation scenarios playing at least some role in building the population of GCs observed in galaxies today (Larsen et al. 2020; Martin et al. 2022; Errani et al. 2022; Mowla et al. 2022).

Observationally, the mass in GCs is found to be a power-law function of inferred halo mass for galaxies with stellar mass $M_* \geq 10^{10}$ $M_\odot$ (Blakeslee et al. 1997; Peng et al. 2008; Spitler and Forbes 2009; Georgiev et al. 2010; Harris et al. 2013; Hudson et al. 2014; Harris et al. 2015). At face value, this relation may encode important information on the formation scenario of GCs. Theoretical models suggest that a quasi-linear power-law relation between GC mass and halo mass may arise naturally in hierarchical formation scenarios as the result of consecutive mergers, serving more as a confirmation of the hierarchical assembly of galaxies rather than shedding light on the formation mechanism of GCs themselves

(El-Badry et al. 2019). However, in the regime of dwarf galaxies ($M_* \leq 10^9$ $M_\odot$), there are fewer mergers with GC-bearing companions, offering a clearer window for the study of GC formation mechanisms than in more massive galaxies. It is therefore important to extend the study of the GC mass - halo mass relation to lower-mass galaxies.

Theoretical models linking the formation of GCs to the ISM of galaxies seem to suggest a downturn in the efficiency of GC formation in dwarfs, departing from the extrapolation of the GC mass - halo mass relation measured on more massive galaxies (El-Badry et al. 2019; Choksi and Gnedin 2019; Bastian et al. 2020). The lower efficiency of GC formation per halo mass in dwarf galaxies is naturally expected due to the lower baryonic content in low-mass halos, which limits the available gas to form stellar clusters in merger and accretion events. On the other hand, a scenario where GCs are linked to dark matter mini-halos would imply a single power-law relation between GC mass and halo mass in the regime of dwarfs, due to the self-similarity of subhalo mass in ΛCDM (e.g., Creasey et al. 2019). Although current observational constraints on the radial distribution combined with the abundance of GCs in MW-mass galaxies limits the fraction of GCs formed in mini-halos to $\sim 30\%$ (Creasey et al. 2019) for such hosts, the importance of the mini-halo formation scenario for GCs in the regime of dwarfs remains largely unconstrained.

Measuring the relation between GC mass and halo mass on the scale of dwarfs is, however, very challenging. First, while there are several methods to estimate halo mass from observables in more massive galaxies (lensing, rotation curves, abundance matching), halo mass estimates in the scale of dwarf galaxies are more scarce and uncertain. Second, GC numbers are lower in low-mass galaxies, meaning that completeness and contamination

in GC surveys impact more heavily low-mass dwarfs than estimates for high-mass galaxies. There are, however, several observational efforts to constrain the GC content in dwarf galaxies. Most notably, Forbes et al. (2018) finds that dwarfs in the Local Volume are consistent with an extrapolation of the power law relation between GC mass and halo mass observed in more massive galaxies, where halo masses for the dwarf galaxies are estimated using gas kinematics. However, other work cautions that this might be biased to include only dwarfs that have at least one GC, while including all dwarfs of a given mass in the average could lead to a departure downwards from the power-law extrapolation (Bastian et al. 2020).

In light of this discussion, another important diagnostic emerges as a potential constraint: the ability of galaxies of a given mass to host at least one GC, or the GC occupation fraction. Observations in the Virgo cluster suggest that all dwarfs with $M_* > 10^9$ $M_\odot$ have GCs, but that fraction declines quite steeply for lower-mass objects, finding 50% occupation in dwarfs with $M_* \sim 10^{7.5}$ $M_\odot$ (Sánchez-Janssen et al. 2019), which is similar to the conclusion presented in Eadie et al. (2022) using a compilation of available data for dwarfs. Recently a comparable occupation fraction was reported for dwarf galaxy satellites of MW-like primaries in the local volume (Carlsten et al. 2022). However, the available constraints involve mostly satellite dwarfs, or dwarf galaxies embedded in the gravitational potential of larger hosts, meaning that tidal stripping and other environmental effects might have influenced their original GC content, preventing a simple interpretation. Unfortunately, surveys of GCs in field dwarfs are scarce and still insufficient to constrain GC occupation fractions (e.g, Georgiev et al. 2010).

An interesting path forward is to use cosmological simulations of dwarf galaxies in high density environments to understand the connection between GCs, dwarf galaxies and their dark matter halos. This is particularly appealing since hydrodynamical cosmological simulations of representative volumes of the Universe have been powerful tools to understand and model the evolution of satellite dwarfs and their properties – such as color, mass content, morphology – in the environments of groups and clusters (Sales et al. 2015; Yun et al. 2019; Joshi et al. 2020; Vogelsberger et al. 2020; Donnari et al. 2021a; Engler et al. 2021a; Joshi et al. 2021) creating a realistic population of satellite dwarfs in good agreement with observations (Donnari et al. 2021b; Engler et al. 2021b; Riggs et al. 2022). However, the spatial and mass resolution of such simulations is too coarse to directly resolve the process of GC formation.

While employing idealized galaxy and galaxy merger set-ups (Bekki and Chiba 2002; Kruijssen et al. 2012; Renaud et al. 2015; Lahén et al. 2019; Lahén et al. 2020; Li et al. 2021) or cosmological zoom-in of galaxies at high redshifts (Kim et al. 2017; Ma et al. 2020; Sameie et al. 2022) have shown important successes on simulating the formation and evolution of GCs and their connection to the ISM of the host galaxy, these techniques are currently unable to sample the evolutionary history of galaxies until the present day and within high density environments, where most of the GC observational data is available today.

To circumvent this limitation, in this paper we develop a GC catalog added in post-processing via a particle tagging technique to make predictions on the abundance, distribution and kinematics of surviving GCs in the environments of groups and clusters at

$z = 0$. This technique is inspired by the successes of particle-tagging for studying stellar halo science (Bullock and Johnston 2005; Peñarrubia et al. 2008; Cooper et al. 2010; Laporte et al. 2013a) and it has been shown to have success in modeling the *surviving* population of GCs in cosmological simulations of galaxy clusters (Ramos et al. 2015; Mistani et al. 2016; Ramos-Almendares et al. 2018, 2020; Doppel et al. 2021)

Tagging techniques of this kind mentioned above are complementary to more detailed methods where GCs formation sites are identified in hydrodynamical simulations and followed in time by a set of sub-grid prescriptions to model their evolution until the present day (e.g., Kruijssen et al. 2011; Mistani et al. 2016; Li et al. 2017; Pfeffer et al. 2018; Keller et al. 2020; Trujillo-Gomez et al. 2021; Chen and Gnedin 2022; Reina-Campos et al. 2022). Note that most of these works also require fairly high-resolution simulations and have been mostly focused on the scale of MW-like galaxies so far. Instead, the less computationally-intensive modeling associated with particle tagging methods offer the opportunity to compile theoretical predictions for the GC content, their positions and velocities for a large number of galaxies and dwarfs with realistic properties within high density environments such as simulated groups and galaxy clusters.

Here we extend the particle-tagging method applied in Ramos-Almendares et al. (2020) for Fornax and Virgo mass galaxy clusters ($M_{200} \geq 8 \times 10^{13}$ $M_{\odot}$) that was implemented in the Illustris simulations (Vogelsberger et al. 2013, 2014a,b; Genel et al. 2014) to lower-mass dwarf galaxies using the highest-resolution hydrodynamical run of the TNG50 simulation (Pillepich et al. 2019; Nelson et al. 2019a). Thus, the tagged GCs allow us to study the GC content of a variety of galaxy groups and clusters consistent with mass esti-

mates of Centaurus A, Fornax, Hydra and Virgo, where observations of GCs are abundant. This work presents one of the largest studies of its kind, containing 39 groups and clusters including their associated 5000+ galaxies with $M_* \geq 5 \times 10^6$ $M_\odot$, and 196,611 GCs. The GC catalogs generated for this work are made publicly available[2] (see Data Availability section for accessibility information).

The paper is organized as follows. In Sec. 4.3, we present the simulation and GC tagging technique. In Sec. 3.4 we show our results on the intra-cluster GC component and benchmark our catalog using current observations. Our main results on the content of GCs in dwarf galaxies are shown in Sec. 3.5 and Sec. 3.6. We summarize our main findings in Sec. 3.7.

3.3 Methods

3.3.1 The TNG50 Simulation

We use the highest-resolution hydrodynamical run of the TNG50 simulation (Pillepich et al. 2019; Nelson et al. 2019a), which allows us to relate the properties of the tagged GCs directly to the properties of galaxies, galaxy groups or galaxy clusters that they belong to. TNG50 is an unprecedentedly high resolution cosmological hydrodynamical simulation for its volume, with a box size of 51.7 Mpc per side with 2160^3 gas and dark matter particles, allowing for a mass resolution of, on average, 8.4×10^4 $M_\odot$ for baryons and a fixed mass resolution of 4.5×10^5 $M_\odot$ for dark matter. The simulation has a gravitational softening length of 288 pc for stars and dark matter at $z = 0$. TNG50 assumes a flat, ΛCDM

[2] www.tng-project.org/doppel22

cosmology and uses cosmological parameters from Planck Collaboration et al. (2016). Its galaxy formation model follows star formation in moderately dense ISM conditions, stellar evolution and chemical enrichment via supernovae, primordial and metal line cooling of gas, as well as heating from the background radiation field, the seeding and subsequent growth of supermassive black holes as well as AGN feedback at both low and high accretion rates, and galactic winds (Weinberger et al. 2017; Pillepich et al. 2018b). The TNG50 simulation is part of the larger IllustrisTNG project (Naiman et al. 2018; Pillepich et al. 2018a; Nelson et al. 2018; Springel et al. 2018; Marinacci et al. 2018; Nelson et al. 2019b).

3.3.2 Galaxy Selection

We tag GCs in all TNG50 host halos with a virial mass $M_{200} \geq 5 \times 10^{12}$ $M_{\odot}$, (where M_{200}, refers to the mass within the virial radius r_{200} defined as the radius enclosing an average density equal to 200 times the critical density of the Universe). This selection results in 39 groups and clusters with a virial mass distribution shown in Fig. 3.1. The high-mass end is roughly on par with lower estimated virial masses of the Virgo cluster $M_{200} \sim 10^{14}$ $M_{\odot}$ (lime green circle and errorbar Karachentsev and Nasonova 2010; Weinmann et al. 2011) and Hydra 1 (brown circle and errorbar Tamura et al. 2000), Fornax cluster $M_{200} \sim 10^{14}$ $M_{\odot}$ (cyan circle and errorbar Drinkwater et al. 2001), down to Centaurus A with estimated $M_{200} \leq 10^{13}$ $M_{\odot}$ (dark purple circle and errorbar van den Bergh 2000; Karachentsev et al. 2007) and less massive elliptical systems closer to the lower-mass cut.

We identify all galaxies that interacted with each of these groups (defined here as being part of their merger tree) and achieved a maximum stellar mass $M_{*,\mathrm{max}} \geq 5 \times 10^{6}$ $M_{\odot}$ during their lifetime as candidates to host the tagged GCs. For each of our selected galaxies,

we calculate their infall time $t_{\rm inf}$, defined here by following their main branch progenitors in the Sublink merger tree (Rodriguez-Gomez et al. 2015) to the last time that the progenitor was its own central. This corresponds to the snapshot before they begin interacting with their current host galaxy group or cluster, or any lower-mass halo which eventually merges with the group or cluster (i.e., in pre-processing Benavides et al. 2020; Joshi et al. 2021). Here, we also impose a minimum of 100 dark matter particles, to remove spurious objects in the subhalo catalog. In the case of the central galaxy in each of our 39 groups, following Ramos-Almendares et al. (2020), we define the infall time as the snapshot when the main progenitor branch reaches 5% its $z = 0$ value.

The target selection process gives us 8746 progenitor galaxies to be tagged with GCs at their infall time of which 6415 survive to $z = 0$. For our study of GCs associated with satellites galaxies, our final sample includes 5453 satellite galaxies in groups and clusters with $M_* \geq 5 \times 10^6$ $M_\odot$ at $z = 0$, which guarantee well resolved galaxies with at least ~ 60 stellar particles at $z = 0$.

3.3.3 Globular Cluster Tagging

The method to tag GCs in our cosmological simulation follows mostly from the one already introduced in the Illustris simulations by Ramos-Almendares et al. (2020), with some modifications and improvements to extend the model to lower-mass galaxies. The method "tags" GCs to a set of dark matter particles, selected to have a given energy distribution (enforced through a specific distribution function) that matches observational properties of GCs systems at $z = 0$. In principle, one could choose to tag on any collisionless-type particle,

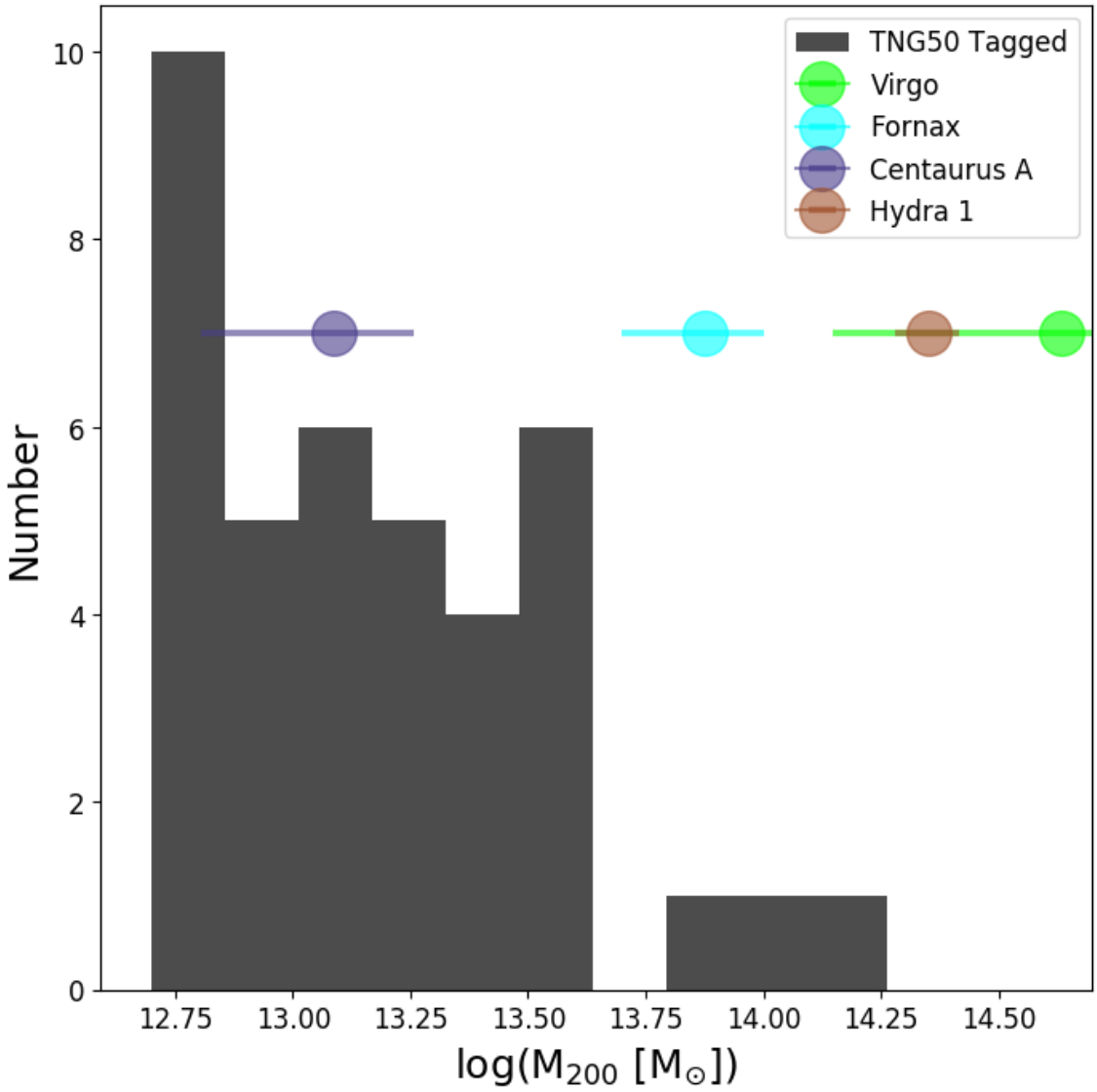

Figure 3.1: The distribution of TNG50 $z = 0$ virial masses (M_{200}) of the 39 most massive galaxy groups and clusters within the simulation to which we tag GCs (black histogram). We cover a wide range of masses, from Centaurus A on the low-mass end (dark purple circle and errorbar van den Bergh 2000; Karachentsev et al. 2007), to Fornax (cyan circle and errorbar Drinkwater et al. 2001), and to Hydra 1 (brown circle and errorbar Tamura et al. 2000) and low end mass estimates of Virgo (lime green circle and errorbar Karachentsev and Nasonova 2010; Weinmann et al. 2011) on the high-mass end. The $\sim$ 1.5 dex range of virial masses allows us to study potential effects environment might play in their $z = 0$ GCs.

for example stars. We instead favor the tagging of dark matter particles to ensure that all galaxies have enough available particles with the desired distribution function to select from when assigning GCs. In particular, GCs systems observed in galaxies are dispersion dominated and typically more extended than the stellar component. Using the dark matter component to search for suitable tracers in energy-space ensures that we maximize the number of candidate particles to host GCs since dark matter is always dispersion dominated (unlike stars in disks) and more extended than the stars. This is particularly important in the regime of dwarfs, where the stellar content is low resulting on a low number of stellar particles overall and even lower beyond the inner central regions (see for instance declining stellar halo fractions predicted in dwarf galaxies, Fig. 5 Elias et al. 2018). Following Ramos-Almendares et al. (2020), the tagging is done only once (at infall time) for each galaxy, after which the particle ID is used to identify those tagged GCs in the $z = 0$ snapshot.

The first step is to identify, for each object, the maximum subset of dark matter particles that are candidates to be GCs, defined as those that are consistent with a specified distribution in energy adopted for the GCs. We assume that the dark matter follows a NFW profile (Navarro et al. 1996b):

$$\rho_{\rm NFW}(r) = \frac{\rho^0_{\rm NFW}}{(r/r_{\rm NFW})(1 + r/r_{\rm NFW})^2} \tag{3.1}$$

which we find by best-fit to the density distribution of dark matter particles following Łokas and Mamon (2001) at infall time. We assume $r_{\rm NFW} = r_{\rm max}/\alpha$, where $r_{\rm max}$ is the radius of maximum circular velocity and $\alpha = 2.1623$ (Bullock et al. 2001). We calculate $r_{\rm max}$ for each galaxy at their time of infall.

GCs are assumed to follow a Hernquist profile (Hernquist 1990):

$$\rho_{\rm HQ}(r) = \frac{\rho^0_{\rm HQ}}{(r/r_{\rm HQ})(1+r/r_{\rm HQ})^3} \tag{3.2}$$

Two sets of GCs are tagged, one corresponding to a more extended metal poor or "blue" component, and one more concentrated and metal rich, or "red" component, with relative fraction of red to blue component following observations in Harris et al. (2015). We assume that $r_{\rm HQ} = \beta r_{\rm NFW}$, where $\beta_{\rm blue\ GCs} = 3.0$ and $\beta_{\rm red\ GCs} = 0.5$. The remaining parameter $\rho^0_{\rm HQ}$ is fit such that the number of resultant candidate particles is maximized. The procedure as well as the assumed parameters is the same as introduced in Ramos-Almendares et al. (2020) using the Illustris simulations.

For reference, the resulting radial distributions of red and blue GCs are typically within the tidal radius of surviving satellites, which are estimated to be $r_{\rm tidal} \sim 5$ - 100 kpc in our sample using analytical calculations for our highest and lowest host and satellite masses (Binney and Tremaine 2008b; Springel et al. 2008). This is confirmed by a very high fraction of tagged GCs remaining bound at $z = 0$, which show medians 96% and 85% for red and blue GCs, respectively. Note that although the sample as a whole shows large bound fractions, a minority of individual objects may lose most or in some cases *all* of their GCs for specific orbits or accretion histories, introducing scatter in some of the relations explored in Sec. 3.5.

We numerically compute the distribution function of each of these three components (dark matter NFW, blue GCs and red GCs) as Binney and Tremaine (2008a):

$$f_i(\epsilon) = \frac{1}{8\pi}\left[\int_0^\epsilon \frac{{\rm d}^2\rho_{\rm i}}{{\rm d}\psi^2}\frac{{\rm d}\psi}{\sqrt{\epsilon-\psi}} + \frac{1}{\sqrt{\epsilon}}\left(\frac{{\rm d}\rho_{\rm i}}{{\rm d}\psi}\right)\Big|_{\psi=0}\right], \tag{3.3}$$

where ρ_i is the density profile of i = DM, GCs, blue GCs, Ψ is the relative gravitational potential, and ϵ is the relative energy. Since the potential is not recorded in every snapshot, it should be noted that the potential of the dark matter particles is calculated for each progenitor subhalo via a tree gravity for computational efficiency. Then, in equally spaced bins of relative energy, we select a fraction of the particles $f_{\mathrm{HQ},i}/f_{\mathrm{NFW}}$ for i = red and blue GCs to be the GC candidate particles. We impose and additional radius cut of $r_h/3$, as suggested by Yahagi and Bekki (2005) and implemented in Ramos-Almendares et al. (2020), where r_h is the half-mass radius of the entire halo at its infall time. This is the final set of GC *candidate* particles.

The next step is to populate galaxies with a total mass in GCs, or M_{GC}. This is the key assumption of the method: galaxies follow a power-law relation between the mass of their total GC systems and their virial mass M_{200} at infall. We thus calibrate the model such that after evolving in the cluster of host potential (tidal stripping, stellar evolution), they reproduce the observed power-law $M_{\mathrm{GC}} - M_{200}$ relation at $z = 0$. More specifically, from Harris et al. (2015):

$$M_{\mathrm{GC},z=0} = aM^b_{\mathrm{halo,z=0}}, \tag{3.4}$$

where a = 2.6×10^{-8} and 4.9×10^{-5} for red and blue GCs, respectively, and the slopes $b = 1.2$ and 0.96 for red and blue GCs. As done in Harris et al. (2015), $M_{\mathrm{halo,z=0}}$ is calculated using abundance matching parameters from Hudson et al. (2015) to assign halo masses to satellites. To calibrate this relation, we select from our satellite sample described in Sec. 4.3.3, only those that survived to $z = 0$, and calculate the fraction of the candidates GC particles that are still bound to the galaxy at $z = 0$: $f_{\mathrm{bound}} = N_{\mathrm{candidates(z=0)}}/N_{\mathrm{candidates(z_{inf})}}$.

We consider a GC candidate still bound to a subhalo at present day if its corresponding dark matter particle is considered bound to the subhalo via Subfind. We then make the assumption that the relationship between $M_{\rm GC} - M_{\rm halo}$ also followed a power law at infall such that:

$$M_{\rm GC,inf} = \frac{1}{f_{\rm bound}} M_{\rm GC,z=0} = a_{\rm inf} M_{\rm halo,inf}^{b_{\rm inf}}. \tag{3.5}$$

We find the best fitting $a_{\rm inf} = 2.6 \times 10^{-7}$ and 7.3×10^{-5} and $b_{\rm inf} = 1.14$ and 0.98 for red and blue GCs respectively. The infall GC mass of each galaxy is then calculated using their virial mass from this best-fit infall relation at $t_{\rm inf}$. The result of this calibration is shown in Fig 3.2. Blue and red points represent the resulting present-day blue and red GC mass respectively for each galaxy with a given M_{200}. For reference, the magenta and cyan lines show the results from Harris et al. (2015) for red and blue GCs, respectively. Note that, despite all galaxies starting from a scatter-free infall $M_{\rm GC}$-M_{200} relation, the variations in infall time, tidal stripping and stellar evolution of the galaxies (which might influence the calculation of M_{200} from abundance matching) results in a present-day $M_{\rm GC}$-M_{200} relation with scatter, in agreement with observations (see Ramos-Almendares et al. 2018, 2020, for more detailed discussions).

Most importantly, the calibration to determine $M_{\rm GC}$ is done using only more massive galaxies, where observational constraints on the GC-halo mass relation are available. In particular, only satellites with estimated $M_{200} \geq 10^{11}$ $M_\odot$, which roughly corresponds to $M_* \geq 10^9$ $M_\odot$ using Hudson et al. (2015) are used to calibrate the model. For dwarf

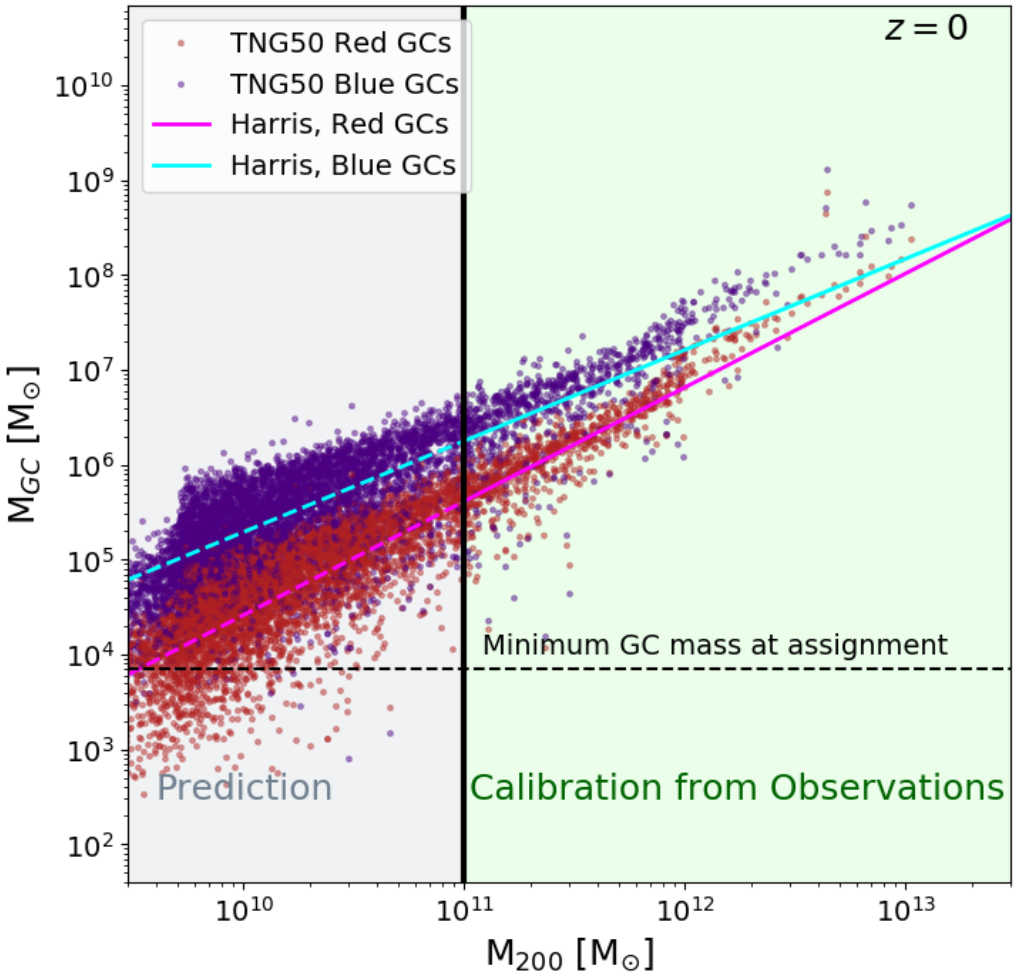

Figure 3.2: M_{GC} as a function of halo mass M_{200} at present-day from the TNG50 simulation + GC tagging model which shows the result of the mass calibration process. Individual dots show simulated galaxies for the blue (indigo) and red (red) components. The observed GC mass - halo mass relation from Harris et al. (2015) is shown in cyan and magenta solid lines for blue and red GCs, respectively. The extrapolation of those results to dwarf galaxies is indicated with the same colors but using short dashed lines. For galaxies with $M_{200} > 10^{12}$ $M_\odot$, we plot the virial mass corresponding to the simulation value rather than calculated from Hudson et al. (2015) due to large discrepancies between simulations and the abundance matching model in that regime. The calibrated red and blue GCs follow a power-law with a slope in good agreement with observations and predict a variable scatter that increases towards the low-mass end. Most importantly, results for $M_{200} < 10^{11}$ $M_\odot$ are a prediction of the model since the calibration is done only using systems more massive than this cutoff. The horizontal dashed line shows $M_{GC} = 7 \times 10^3$ $M_\odot$, our minimum individual GC mass considered to assign mass to the tagged GC particles. Galaxies below this mass are not populated with GCs in our model.

galaxies with $M_{200} < 10^{11}$ $M_\odot$, the calculated M_{GC} is a prediction of the model assuming they follow the same relation as their more massive counterparts.

3.3.4 Assigning individual GC Masses

As explained above, the tagging method first selects as many GC candidate particles as possible, by identifying all dark matter particles with matching energies to the intended GC distribution (see Sec. 3.3.3). After the mass calibration is carried out and M_{GC} is defined at infall (see Eqs. 3.4 and 4.4), the mass weight of each candidate GC particle is simply calculated by dividing M_{GC} into the identified number of candidate GC particles. This means that the weight of a given tagged GC particle could be smaller than the mass of a full GC. While working with the full set of candidate GC particles provides the most complete representation of the possible phase space for GC systems, it is convenient to define a "realistic GC catalog", where a subset of the tagged GC candidate particles are selected to match the *number* of GCs expected. We take this approach in what follows as it allows a consistent comparison to observational data.

In previous iterations of this GC tagging model, we have taken the approach of assigning all realistic GCs the same, average mass ($m_{GC} = 1 \times 10^5$ $M_\odot$) (see Ramos-Almendares et al. 2020; Doppel et al. 2021). While this approach was correct for the more massive galaxy sample presented in these previous works, the GC luminosity function in observed early-type galaxies changes with the stellar mass of the host (Jordán et al. 2007), an effect that becomes particularly important when evaluating the GC content of lower-mass dwarf galaxies (Forbes et al. 2018). Because of our increased resolution and the selection

of dwarf galaxies below $M_* \sim 10^8$ $M_\odot$, we enter the regime in which a more detailed mass modeling for the GCs is required.

We model the GC population of each galaxy at infall assuming a Gaussian distribution in luminosity (we assume a mass to light ratio (M/L) ($M_\odot$ / $L_\odot$) = 1 in the z-band), with a dispersion of z-band GC luminosities (σ_z) that reproduces the relationship with the M_B of their host galaxies at $z = 0$ as measured in Jordán et al. (2007) (see Appendix D for a more detailed discussion of this calibration). We note that we still assume a constant mean luminosity $\sim 2 \times 10^5 L_\odot$ for all GC luminosity functions, independent of the mass of the host galaxy, but we limit the maximum mass that a GC can sample to 1/100 the stellar mass of the host following observations of the most massive GCs in dwarfs (Kruijssen and Cooper 2012). We also employ a uniform low-mass (or luminosity) cutoff for individual GCs $= 7 \times 10^3$ $M_\odot$ and an upper mass/luminosity cut off equal to 5×10^6 $M_\odot$ to ensure that we are excluding massive objects that could be nuclear GCs (Kruijssen and Cooper 2012).

For each galaxy, we proceed to randomly draw individual GC masses from the resulting Gaussian distribution until the sum of all realistic GC candidates adds up to the estimated mass in GCs at infall. This steps concludes with a corresponding number of realistic GCs for each galaxy, $N_{\rm GC,inf}$. This number is always smaller than the number of particles identified as candidate GC particles in the step described in Sec. 3.3.3. We then sub-sample $N_{\rm GC,inf}$ from the list of all the GC candidate particles identified for each galaxy (enforcing that they follow the same relative energy distribution function) and we assign them one of the drawn GC masses, building one possible realization of the realistic GC

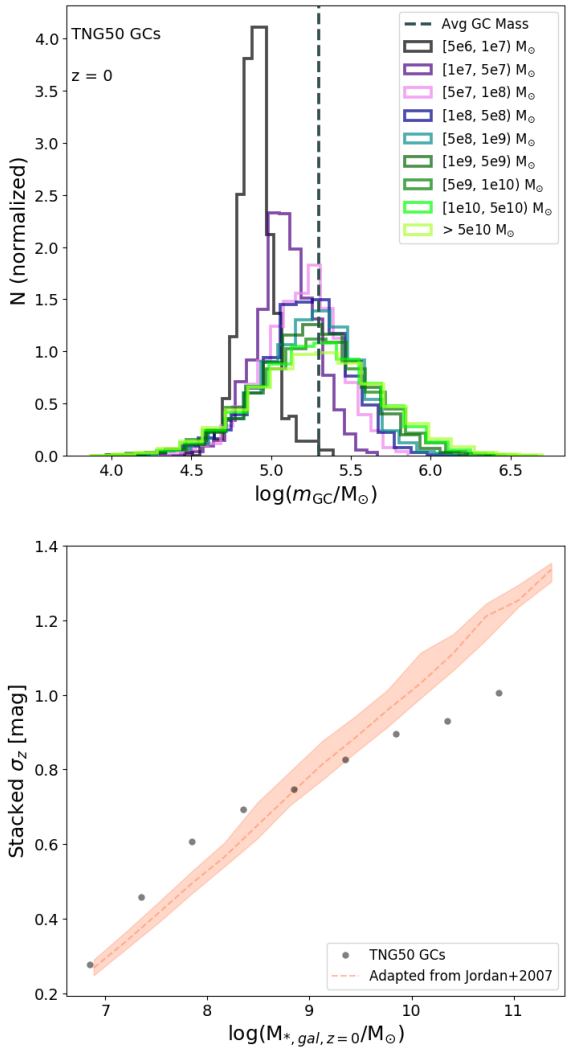

Figure 3.3: *Top:* Stacked mass functions of individual GCs in narrow bins of host galaxy stellar mass at $z = 0$, as labelled. We can quantitatively see the expected decrease in dispersion for decreasing stellar mass. We note that the downward shift of the median GC mass is due to the upper limit of $\min(5 \times 10^6\ \mathrm{M}_\odot, M_{*,\ \mathrm{infall}}/100)$, which plays a large role for lower-mass galaxies. *Bottom:* Relation between the dispersion in the z-band GC luminosity function, σ_z, and host galaxy stellar mass. Gray points show the measured dispersion of the stacked luminosity functions of our model in TNG50 shown in the top panel, and the orange shaded region shows observational expectations based on results reported in Jordán et al. (2007) adapted using the simulations to convert their B- magnitudes to M_* (median shown in dashed line, and shading corresponds to 25% - 75% scatter in each stellar mass bin). Additionally, due to the high end mass cut of 5×10^6 $\mathrm{M}_\odot$ for a single GC mass, the best-fitting luminosity function dispersions of high-mass systems are somewhat underestimated, but we do find reasonable agreement for low-mass systems.

catalog for each given galaxy. Note that further versions of the realistic catalog might be constructed by repeating the sampling of the GC luminosity function and the selection of the GC candidate particles, if so desired. In this work we employ only one realization per galaxy, but see Doppel et al. (2021) for an example of how multiple realizations per object might be used to assess the impact of low number statistics in the determination of galaxy velocity dispersion from GC tracers.

As highlighted before, the individual mass assignment to GCs is performed at infall, and particle IDs are tracked onwards to $z = 0$. Since the tagging technique is meant to model the *surviving* GCs at $z = 0$, we do not make assumptions about the shape of the *initial mass function* of GCs, nor do we take into account mass loss for individual GCs or the total destruction of GCs (see also Ramos-Almendares et al. 2020, for a detailed discussion). We instead use observational results on the evolved GC luminosity function presented in Jordán et al. (2007) to assign final masses to the tagged surviving GCs. We present in Appendix E estimates of the dynamical friction expected for the tagged GCs and demonstrate that the results presented here are not strongly affected by dynamical friction.

3.3.5 The GC population of TNG50 group and cluster members

The top panel of Fig. 3.3 shows the average GC mass functions at $z = 0$ binned in ranges of stellar mass of the host galaxy in TNG50. Notice that while the GC mass sampling and assignment is performed at infall for all galaxies, this plot shows present-day results for surviving satellite galaxies, which means individual distributions of GCs could have been affected by tidal stripping. The top panel shows a significant drop in the average GC mass for dwarf galaxies with $M_* < 10^8$ $M_\odot$, which in our model is attributed to the

upper mass cut-off to sample GC mass (set to $1/100 M_{*,\mathrm{inf}}$ for each galaxy), and confirms the importance of taking this into account when dealing with GC content in low-mass dwarf galaxies (Forbes et al. 2018).

The bottom panel of Fig. 3.3 shows in cyan symbols the dispersion in the z-band magnitudes of simulated GCs associated to each galaxy, σ_z, and how it compares to the one measured in observations (orange shaded region Jordán et al. 2007). Note that this relation is an extrapolation below $M_* < 10^8$ $\mathrm{M}_\odot$. While the overall agreement is good, there is a flattening in σ_z for our tagged GCs in high-mass galaxies, which we attribute to our absolute upper limit in the z-band luminosity/mass of individual GCs corresponding to 5×10^6 $\mathrm{M}_\odot$.

We showcase some examples of our GC catalog with the final tagging results in Fig 4.3. Pink and light blue dots indicate our tagged realistic GCs overplotted onto the stellar density predicted by TNG50, shown in the background grayscale. To create some intuition on the range of simulated objects included in our sample, we show several systems on different mass scales, from a Virgo-like galaxy cluster in the top left of the figure, a Fornax mass galaxy cluster in the top right, and a Centaurus A mass group in the bottom left. Interestingly, it is not uncommon to find substructures of GCs in our catalog: the bottom right panel shows a set of simulated GCs that appear to be following a tidal stream in the stellar component of a disrupting host galaxy. We also see correct behavior of the GCs as a whole – the red GCs are more spatially concentrated around their host galaxies than the blue GCs. While this is partially imposed by design in the model, the more centrally-concentrated tagging for the red component is done at infall, while Fig. 4.3 shows that

it is mostly preserved until $z = 0$ despite tidal stripping events and interactions with the host environment. In agreement with previous version of this tagging technique (Ramos-Almendares et al. 2018, 2020), the model predicts the formation of an intra-cluster GC component, or GCs that exist in the space between the galaxies, which is built mostly from the disruption and merging of early accreted satellite galaxies, a topic that we return to in Section 3.4.

3.4 Build up of the intracluster GC component

Observationally, the presence of GCs in the intracluster regions (or ICGCs) has been detected and surveyed in several nearby galaxy groups and clusters such as Fornax (Bassino et al. 2003; Schuberth et al. 2008), Coma (Madrid et al. 2018; Peng et al. 2011), Abell 1689 (Alamo-Martínez and Blakeslee 2017), Virgo (Lee et al. 2010; Durrell et al. 2014; Ko et al. 2017; Longobardi et al. 2018) and Centaurus A (Taylor et al. 2017). Similarly to GCs in the halo of the MW (see e.g., Keller et al. 2020), ICGC studies hold the promise to help unravel the accretion history of their host halos and important properties of the progenitor galaxies building the intracluster light of the groups and clusters (e.g., Villaume et al. 2020; Ko et al. 2022).

One of the predictions of our GC model is the formation of such an accreted ICGC component, built from a combination of GCs previously associated with galaxies that have merged to the group or cluster host and also from the stripping of surviving satellite galaxies. Such a component is not directly "tagged" or calibrated for in our simulations, but instead

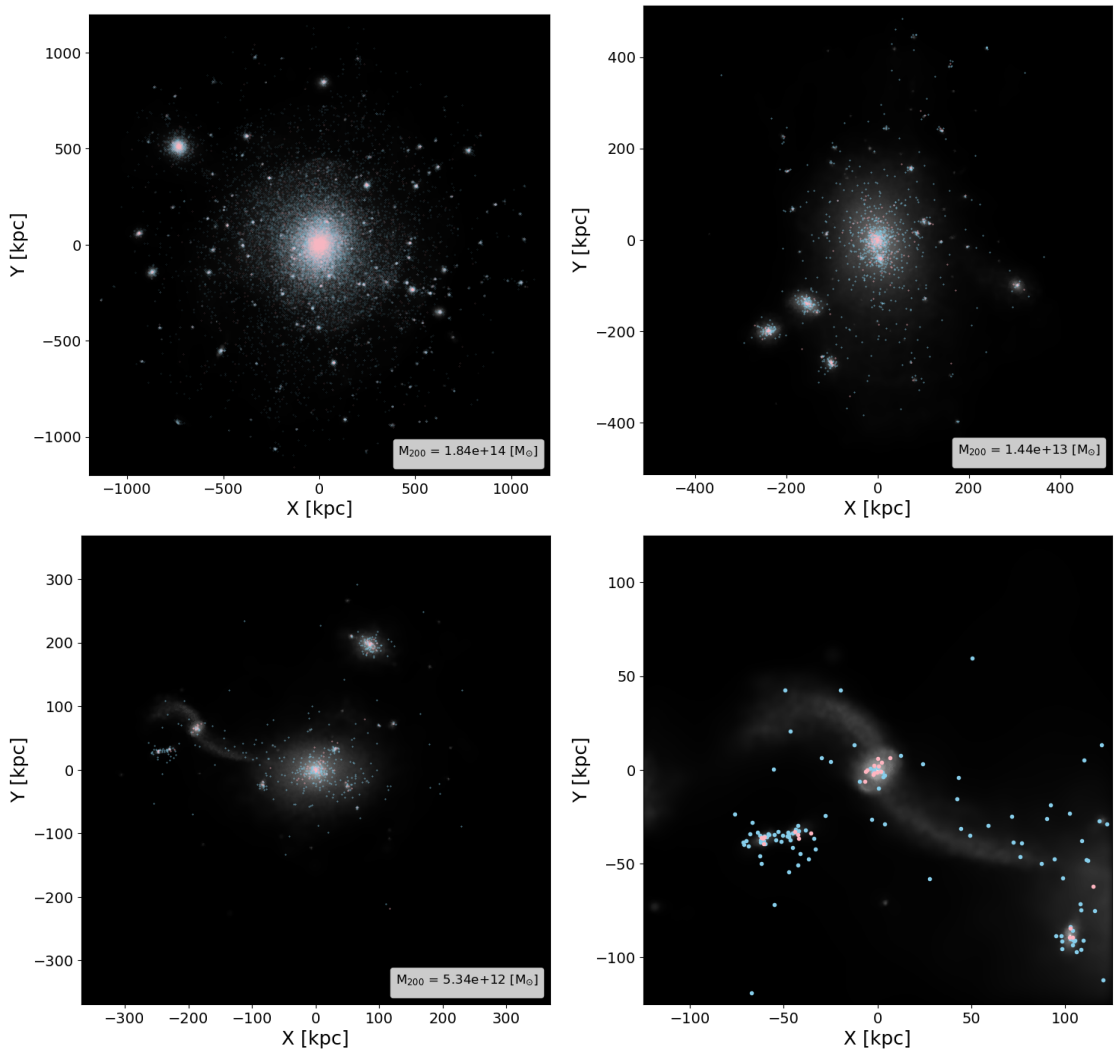

Figure 3.4: Spatial maps of one realization of our GC catalog (pink and light blue points) overplotted on a visualization of the stellar density (background grayscale) for the most massive galaxy group (a Virgo or Hydra 1 analog) (top left), a galaxy group with a viral mass around 1.5×10^{13} $M_\odot$ (top right), and one low-mass galaxy group with a virial mass $\sim 5 \times 10^{12}$ $M_\odot$ (bottom left). The bottom right shows a zoom-in of the GC particles associated with the stellar stream in the bottom left image. We find that the GCs distribute as expected, with the red population more spatially concentrated about their hosts and the blue component more spatially extended. We also find the presence of intracluster GCs, see Section 3.4 for a more detailed discussion.

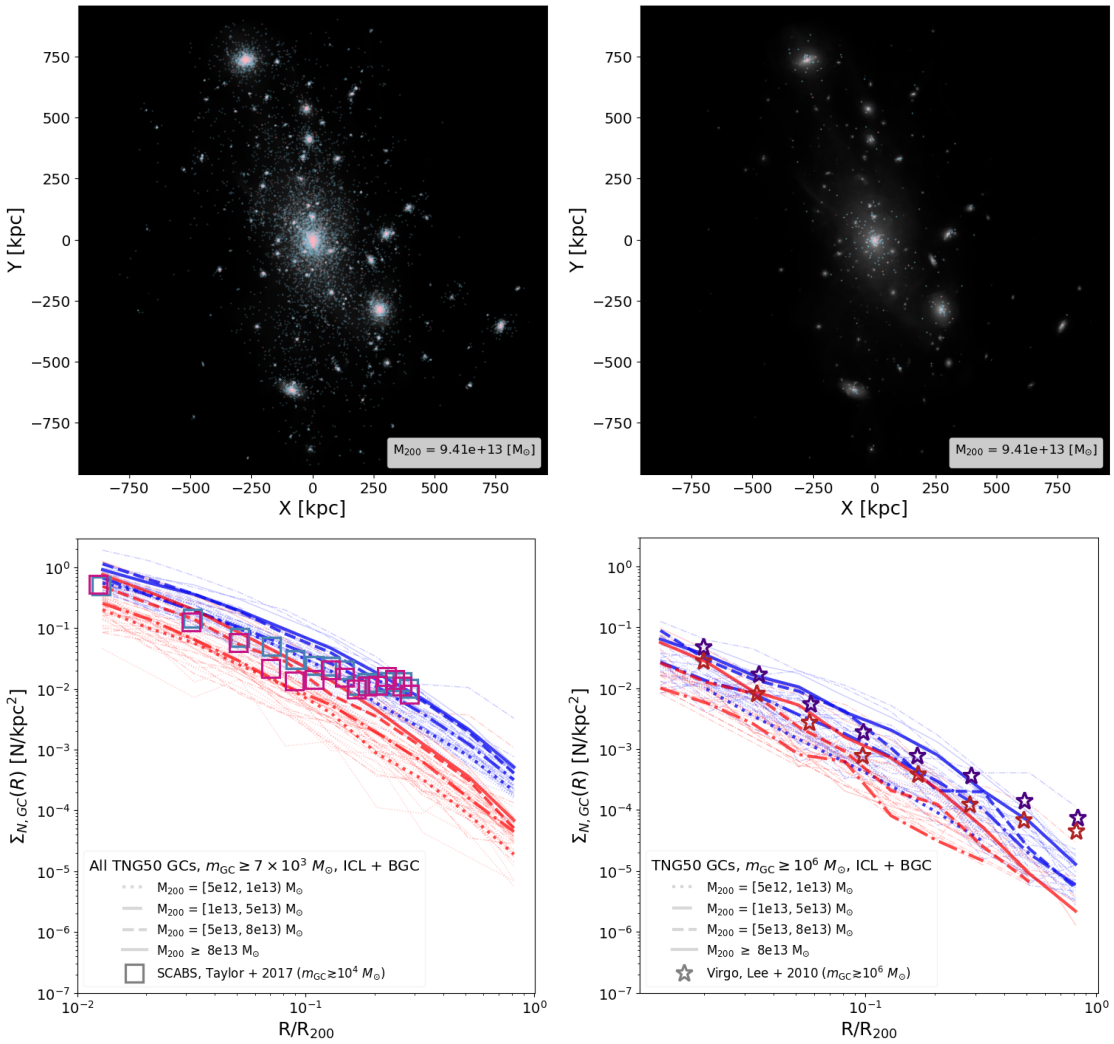

Figure 3.5: Top: Projections of the stars (background grayscale) and GCs (pink and skyblue points) for FoF group 1 all the realistic GC particles associated to the group (left) and the most massive (and thus the brightest) GC particles, defined to be those with individual GC mass $m_{\rm GC} \geq 1 \times 10^6$ M$_\odot$ (right panel). Bottom: Radial surface number density profiles for the GCs for all groups (low transparency curves) and medians for various mass bins (high alpha curves) compared to observations for the Virgo ICGCs from Lee et al. (2010, red and blue stars,) and SCABS (pink and cobalt squares, Taylor et al. 2017). The bottom left shows the profiles using all realistic GC particles and the bottom right shows the profiles using only massive GC particles, as defined for the top row. We see that this mass cut puts the predictions of the model much more in-line with what is shown in the observations from Lee et al. (2010). This visually illustrates the effects of brightness cuts in observations of the ICGCs.

is the result of the hierarchical assembly of structures in ΛCDM. More specifically, while some GCs are tagged to the central galaxies in each group, this occurs when they reach a very small fraction of their final virial mass (5%, see Sec. 4.3 for details), resulting in those GCs assigned to the central galaxy being largely subdominant (about a ∼dex less in GC numbers) compared to the accreted ICGCs acquired from tidal stripping and merging of the satellite galaxies. The study of the ICGC component is therefore an important benchmark of our GC model.

In this work, we define ICGCs to be GCs within the virial radius of a group or cluster host that are not currently gravitationally associated to any satellite as measured using Subfind. We note that while this differs from observational methods of determining GC membership to the ICL, which includes fitting profiles to distinguish the ICGCs from the GCs associated with the BCG (e.g., Taylor et al. 2017), employing radial cuts to remove the contribution of GCs of satellite galaxies (e.g., Lee et al. 2010), or using kinematic data of GCs when available (Longobardi et al. 2018), this is a definition that is best physically motivated for our purposes. We have explicitly checked that using different radius cuts for satellite galaxies to distinguish between the ICGCs from the GCs of satellites, as done in some observational studies, does not substantially change the properties of the ICGCs reported here.

The top row of Fig. 3.5 shows projections of GCs (associated to galaxies and part of the ICGCs) tagged in the second most massive group in our sample (FoF group 1), with $M_{200} \sim 9 \times 10^{13}$ $M_\odot$, comparable to the Virgo or Fornax clusters. As before, pink and light blue dots correspond to tagged red or blue GCs and the gray scale indicates the

stellar component. Because GCs are now assigned individual masses (see Sec. 3.3.4), we can create different maps mimicking different luminosity (or mass) cuts: the left panel shows all tagged GCs in FoF 1 (or equivalent all GCs above a mass cut 7×10^3 $M_\odot$) while the right panel illustrates what would be observed in a shallower survey only able to map GCs more massive than $\geq 10^6$ $M_\odot$.

As expected, the number of GCs decreases in the right panel due to the lower availability of more rare massive GCs. Interestingly, the substructure mapping should be different between these two images, as more massive GCs are preferentially formed in more massive galaxies (see top panel of Fig. 3.3), leaving dwarf galaxies underrepresented in the right panel compared to the left. The extension of our model to include the masses of individual GCs makes the current GC catalog especially useful for exploring how completeness and magnitude limits might impact observational results.

We quantify the ICGCs via their projected number density profile as a function of projected radius (normalized to the virial radius of the host) in the bottom panels of Fig. 3.5. The left and right panels correspond again to all GCs and GCs more massive than 10^6 $M_\odot$, respectively. Individual thin lines (red or blue to refer to the red or blue GCs) indicate the projected radial profiles in each of our 39 groups, while thick curves show the resulting medians when splitting our sample in four virial mass bins roughly consistent with: Virgo mass objects ($M_{\rm vir} \geq 8 \times 10^{13}$ $M_\odot$), Fornax mass objects (5×10^{13} $M_\odot \leq M_{200} < 8 \times 10^{13}$ $M_\odot$), higher-end mass estimates of Centaurus A (1×10^{13} $M_\odot \leq M_{200} < 5 \times 10^{13}$ $M_\odot$), and lower-end halo mass estimates of Centaurus A as well as massive elliptical systems ($5 \times 10^{12} \leq M_{\rm vir} < 1 \times 10^{13}$ $M_\odot$).

There is a weak dependence of the ICGC number density on host mass, with smaller mass systems having lower number densities, but the object to object scatter is large. The red ICGCs have a slightly steeper radial distribution than the blue one, as expected from the differential stripping due to their initially more biased distribution towards the centers of their host galaxies at infall, but the effect is rather small.

Global GC surveys are very challenging observationally for external and distant systems. As a result the available data is scarce. We compare our predictions with two available constraints: GCs in Cen A from the SCABS survey that correspond to a minimum GC mass of $\sim 10^4$ $M_\odot$(Taylor et al. 2017, red and blue squares) and GCs in the Virgo cluster from Lee et al. (2010). In the bottom left panel, we see that our model shows an overall good agreement with measurements in Cen A, although we predict a steeper red ICGC component than the SCABS results. Here we are assuming a virial mass $M_{200} = 10^{13}$ $M_\odot$, which corresponds to $R_{200} \sim 450$ kpc. The flattening observed in Cen A beyond $R \sim 0.2R_{200}$ might be associated with the ring-like structure detected in this system (Taylor et al. 2017) and might not necessarily be present in our sample, although we do find some interesting cases where simulations also predict a flattening. We defer this study to future work.

The observational data in Virgo corresponds to a brightness cut of 21.3 mag in the i-band, which means that only the brightest $\sim$ 13% of the GCs in the Virgo cluster are detected (Lee et al. 2010). We therefore show in the bottom right panel of Fig. 3.5 the number density profiles of GCs more massive than 10^6 $M_\odot$, which is a better match to the shallower GC survey in Virgo using SDSS data. Here we assume a 1700 kpc virial radius, which corresponds to a virial mass $\sim 5 \times 10^{14}$ $M_\odot$ following Kashibadze et al. (2020).

We find a good agreement in normalization and slope of our simulated GC catalog and these observations in Virgo, with the differentiation between blue and red GCs improved with respect to Ramos-Almendares et al. (2020), mostly driven by the improved numerical resolution in our simulations.

While the overall objective is not to reproduce in detail the observations of individual systems, it is reassuring to see that the predictions of our GC tagging method for ICGCs number densities are well in the ballpark of the observations available to date. This is particularly important given that this component is not directly tagged in the simulations, but instead is naturally built by the assembly process of groups and clusters. A more detailed study of the ICGC component and its relation with the build up of the intracluster light will be presented in future work (Ahvazi et al., *in prep*).

3.5 GC content in dwarfs to giant galaxies

The GC tagging model calibrates the total mass of globular cluster systems in galaxies at $z = 0$ using the $M_{\rm GC} - M_{200}$ power-law relation from Harris et al. (2015). As explained in detail in Sec. 3.3.3, only simulated halos with calculated $M_{200} > 10^{11}$ $\rm M_\odot$ participate in the calibration, while lower-mass objects are assumed to follow an extrapolation of that power-law. The GC content of dwarf galaxies in halos less massive than $M_{200} = 10^{11}$ $\rm M_\odot$, corresponding to $M_* \sim 10^9$ $\rm M_\odot$ in the stellar-halo mass relation of TNG50, is therefore a prediction of the model under this assumption. We explore in this section how the results obtained in the regime of dwarf galaxies compare to current observational constraints.

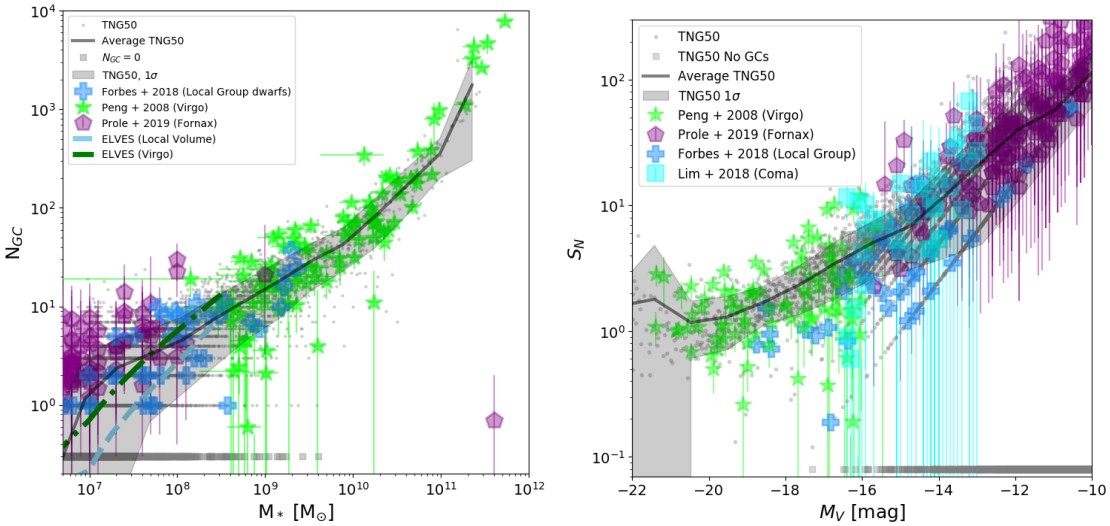

Figure 3.6: *Left:* Number of GCs, N_{GC}, as a function of host galaxy stellar mass. Simulation points are plotted as gray dots, with the average shown as the solid black line and 1σ variation shown as the gray shaded region. Simulated galaxies with no GCs after the mass function selection are shown as gray squares at $N_{GC} = 0.2$. Observational data for observed galaxies are plotted as solid lime green stars (Virgo, Peng et al. 2008), purple pentagons (Fornax, Prole et al. 2019), and blue crosses (Local Group, Forbes et al. 2018). Average results from ELVES-II in Virgo- and Local Volume-like environments are shown in dark green dot dashed and light blue dashed lines respectively. The simulation points tend to follow the trend and scatter of the observational data. *Right:* The specific frequency, S_N, as a function of host galaxy V-band magnitude, M_V. M_V and S_N have been corrected to correspond to the mass to light ratio observed for Virgo (see Appendix D). Colored shapes correspond to the same observations as before, with the addition of cyan squares (Coma Lim et al. 2018). Galaxies with $S_N = 0$ are shown as gray squares at $S_N = 0.07$. The agreement of both measures of GC abundance with observations in terms of shape and scatter suggests that the assumption that GC mass scales with halo mass holds to a reasonable extent, even into the dwarf regime.

3.5.1 Number and Specific Frequency of GCs

Fig. 3.6 shows in the left panel the relation between the number of globular clusters, $N_{\rm GC}$, and the host galaxy stellar mass, M_*, in our simulated systems (gray symbols). Individual galaxies are shown in gray points, with the median relation (including galaxies with $N_{\rm GC} = 0$) shown as the solid black line, with the $25\% - 75\%$ dispersion shown as the gray shaded region. Our results agree well in both overall shape and dispersion with available constraints from observations shown here in colored symbols: green stars from galaxies in the Virgo cluster (Peng et al. 2008), magenta pentagons for dwarfs in the Fornax cluster (Prole et al. 2019), and additional low-mass galaxies from the Local Volume in sky-blue crosses (Forbes et al. 2018). We also indicate the average results from ELVES-II reported in Carlsten et al. (2022), showing a low-mass selection of Virgo cluster dwarfs (green dot-dashed curve) and dwarfs in the Local Volume (dashed light blue). While our sample does not include low density environments such as the Local Volume, our average values for the lowest mass objects resolved in our sample track well the slope of the average number of GCs per system observed in ELVES-II.

For completeness, we also show the related quantity, specific frequency of GCs or S_N, as a function of V-band magnitude in the right panel of Fig. 3.6. We calculate the specific frequency following Harris and van den Bergh (1981):

$$S_N = N_{\rm GC} 10^{0.4(M_V+15)}, \tag{3.6}$$

where $N_{\rm GC}$ is number of GCs and M_V is the V-band absolute magnitude of the host galaxy. For most galaxies we take M_V directly from the simulation, except for the high-mass galaxies

($M_* > 10^9 M_\odot$), where we adopt a fixed mass-to-light ratio equal to 3.6 to convert from mass to luminosity following observations in the Virgo cluster (Peng et al. 2008).

The color coding on the right panel of Fig. 3.6 is the same as introduced for the left panel, with our simulated galaxies shown in gray and a set of available observational constraints using color symbols with error bars. We show galaxies with $S_N = 0$ as gray squares with $S_N = 0.07$ so that they are visible on the log scale. The median and 25-75 percentiles are calculating not including galaxies with $S_N = 0$.

Simulated S_N values overlap well with observational constraints, in particular in the regime of dwarf galaxies, where typical S_N values of several dozens to a few hundreds become common for dwarfs fainter than $M_V \sim -13$. The inclined lines seen for simulated galaxies with $M_V > -16$ correspond to discrete numbers of GCs (galaxies with 1, 2, 3 GCs) and seem to represent well several of the dwarf galaxies in the Forbes et al. (2018) sample.

While, to a certain degree, the agreement in the high-mass end of Fig. 3.6 might be expected because of the calibration of our model to follow the $M_{\rm GC}$-M_{200} relation, it is not fully guaranteed due to the following factors: (*i*) our method tags the satellite population at infall and not at $z = 0$, (*ii*) we tag based on halo mass and not M_* as shown here where galaxies continue to evolve their M_* and M_V after infall and (*iii*) we tag on total GC mass, $M_{\rm GC}$, not specifically in GC number. Most importantly, our simulations compare well with measurement of GC numbers in dwarf systems below those used to calibrate the $M_{\rm GC}$-M_{200} relation, offering support to the hypothesis that this power-law relation between GC mass and halo mass extends at least to objects with $M_* \sim 5 \times 10^6$ M$_\odot$.

Interestingly, the left panel of Fig. 3.6 shows that the average number of GCs continues to decrease with smaller M_* in the full range explored here (when including zeros). This is relevant because it helps rule out more extreme, "purely stochastic" models where the number of GCs is simply a random number in the low-mass end (e.g., El-Badry et al. 2019). We note that this purely stochastic model is not proposed as physically-motivated, but instead used in El-Badry et al. (2019) as an interesting extreme behaviour to explore the slope of the relation between halo and GC mass. Such purely stochastic models, while being able to reproduce the high-mass end of the power-law relation $M_{\rm GC}$-M_{200} due to mergers and hierarchical assembly, would provide a much shallower or constant average number of GCs with M_* in the low-mass regime where stochasticity starts to dominate. Instead, our results agree well with the conclusions presented in Forbes et al. (2018), where the slope and scatter of the GC content is consistent with a model where dwarf halos lay on an extrapolation of the GC - halo mass relation measured for more massive systems.

3.5.2 Radial extent of GCs

We show in Figure 3.7 our predictions for the (3D) radial extent of the tagged GC systems as a function of stellar mass. We use the half-number radius $r_{h,\rm GC}$ to characterize the radial extent of the GC systems, which we calculate by rank-ordering the GCs associated to each galaxy in increasing distance to their host and finding the radius of the GC that divides the sample in two. It is expected that the accuracy of this estimate scales with the number of GCs, with dwarf galaxies having the largest uncertainties given their low number of GCs. In this figure, we include only simulated galaxies with $N_{\rm GC} \geq 3$ (gray

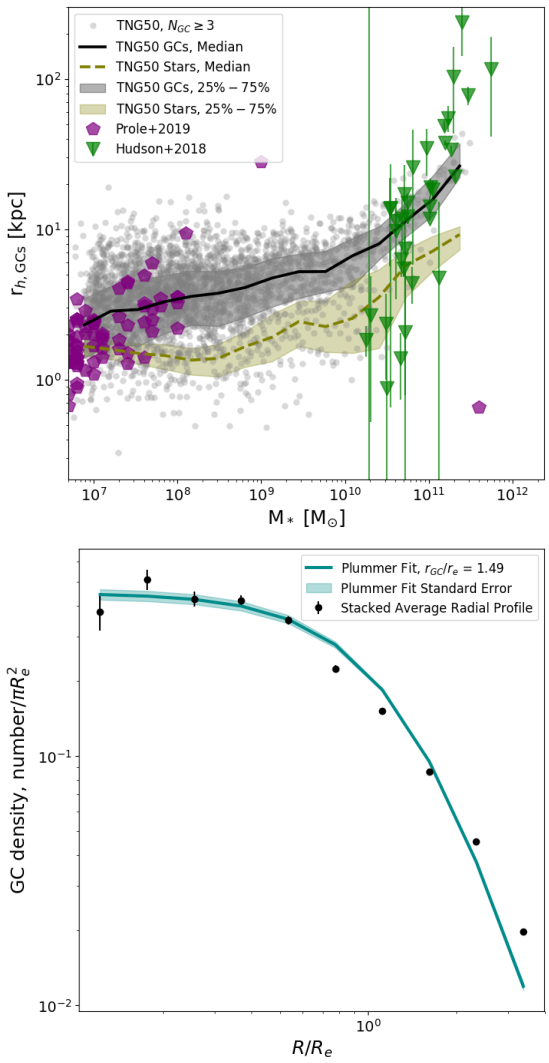

Figure 3.7: *Top:* The half number radius of GCs around TNG50 galaxies (gray points), low surface brightness galaxies from Prole et al. (2019) (purple pentagons), and higher-mass galaxies from Hudson and Robison (2018) (green triangles). We show simulated galaxies with $N_{\rm GC} \geq 3$. We find good agreement with observations for higher-mass galaxies, but find a flatter slope than the observations for dwarf mass galaxies. We do note however that the scatter in the simulated points covers the range seen in observations. *Bottom:* Low number of GCs in dwarfs may favour using alternative methods to measure a half-number radii than individual counts. Inspired by observational methods of calculating $R_{h,\rm GCS}$ in dwarfs, we show the average *stacked* radial profiles for the GCs of dwarf galaxies with stellar masses between 5×10^6 $M_\odot$ and $10^{8.5}$ $M_\odot$. The solid dark cyan line shows the best fitting Plummer profile for the stacked GCs. The error bars and the shaded region are obtained via bootstrapping. Our best-fit profile recovers the expected factor of ~ 1.5 that relates the stellar half light radius, R_e, with the GC half number radius, $R_{\rm GC}$, which is consistent with observational estimates.

circles), which allows for the determination of $r_{h,\rm GC}$ (this cut in $N_{\rm GC}$ might not necessarily apply in observations (purple pentagons and green triangles), where the half number radius is determined via profile-fitting, see below). Projected sizes in observations have been converted to 3D by multiplying the reported values by a (4/3) factor, which assumes a spherical distribution (Somerville et al. 2018).

Given the relatively high spatial resolution of TNG50 ($\sim$ 290 pc at $z = 0$), the radial extents of the GC systems considered here are numerically well resolved. Their typical sizes increase from a few kpc for dwarfs with $M_* \sim 10^7$ M$_\odot$ to $r_{h,\rm GC} \sim 40$ kpc for our largest satellite galaxy with $M_* \sim 10^{11}$ M$_\odot$, with a significant object-to-object scatter, in particular at the low-mass end. The median trend is highlighted by the black solid line, with shaded regions indicating the 25-75 percentiles in our sample. In agreement with observations, simulated GCs are typically more extended than the stellar component in galaxies, which is indicated by the gray-green shaded curve and shaded area showing the median and 25-75 percentiles of the half-mass radius of the stars in the same galaxies. On average, GCs are a factor $\sim$ 2-3 times more extended than the stars in galaxies, with a hint at a smaller ratio for low-mass galaxies.

We reproduce well typical sizes for GC systems in MW-mass galaxies, predicting $r_{h,\rm GC} \sim 10$ kpc for galaxies with $M_* = 5 \times 10^{10}$ M$_\odot$, and an increasing size with mass, in good agreement with data from Hudson and Robison (2018). This is not completely surprising since the scale parameters in the Hernquist profiles used to tag the red and blue GC components at infall were partially chosen in the original model (see Ramos-Almendares et al. 2020) to reproduce typical GC distributions in these scales.

It is interesting, however, to explore what predictions arise from extrapolating the same scaling towards low-mass galaxies. We show with purple pentagons data from dwarfs in the Fornax cluster, taken from Prole et al. (2019). While our systems overlap with the observed dwarfs, simulated galaxies seem to have systematically larger half-number radii than observations. However, we caution that the exact size measured is very sensitive to the definition chosen in systems dominated by low-number statistics, like GCs in dwarfs.

The bottom panel of Fig. 3.7 shows a different approach, often used in observations of dwarf galaxies: determining the size of GCs based on profile-fitting of the resulting stacked GC profile (instead of individual GC counting in each galaxy as in the upper panel). We show the stacked projected number density profile of GCs for dwarf galaxies with $5 \times 10^6 < M/M_\odot < 10^{8.5}$ as a function of (projected) radius normalized to the effective radius for each dwarf (see for instance Carlsten et al. 2022). Errorbars and the shaded region are calculated via bootstrapping and correspond to the r.m.s values from those realizations. The dark cyan line shows the best fitting Plummer profile for our simulated dwarfs, which suggests that the half number radius of GCs in these systems is ~ 1.5 times the half-mass radius[3], which is in good agreement with observational estimates (Georgiev et al. 2010; Carlsten et al. 2022).

Since in our model, the scaling of the GC tagging depends only on the dark matter half-mass radius (through the calculation of the best-fitting NFW profile at infall), the good agreement with the scaling of GCs and the *stellar* component of galaxies is, again,

[3]We have explicitly checked that on the high mass end, provided that the chosen profile provides a good fit to the individual GC distributions, the half mass radius computed via GC counting or via profile fitting are within statistical uncertainty of each other, being therefore less of an issue for massive galaxies with a numerous GC population than in low mass dwarfs with only a few GCs.

not guaranteed and an interesting feature of our catalog. It also points to another puzzling link between GCs and dark matter halos, in this case through radial extent instead of total mass, that may shed light on the origin and formation of GCs.

3.5.3 Dependence on environment

Recently, Carlsten et al. (2022) reported a higher GC content for dwarf galaxies in the environment of Virgo compared to dwarf satellites of the same mass in lower density environments of the Local Volume. This finding has been interpreted as an extension of a radial trend in the Virgo and Coma cluster where dwarf galaxies near the center (and therefore on higher density regions) have on average a larger specific frequency compared to those located further out (Peng et al. 2008; Lim et al. 2018). Such a trend has been explained as a natural consequence of dwarfs with inner orbits and higher environmental densities having formed their stars earlier on, with more intense star formation histories leading to the formation of GCs with a higher specific frequency (Peng et al. 2008; Mistani et al. 2016) than objects in the field.

Additionally, since dwarfs stopped forming stars in high density environments earlier than those in the field, comparing them at fixed M_* today means that the dark matter halos of those in high density environments are biased high. This follows since quiescent dwarfs today should have continued forming stars reaching higher luminosities at the present day had they stayed in the field (Mistani et al. 2016). Such an effect would also lead to a higher GC-content for early type dwarfs in groups and clusters.

Our GC catalogs sample a relatively narrow range of environments, including groups and low-mass clusters with $M_{200} = [5 \times 10^{12} - 2 \times 10^{14}]$ $M_\odot$ and no dwarfs around

MW-type galaxies (such as those in the low density regions of ELVES) or directly in the field. However, we have explicitly checked that, within the range of environments of our sample, we find no significant difference in the predicted GC number or specific frequency for simulated dwarfs in low-mass vs. high-mass host halos, nor do we find a trend with cluster-centric radii.

Our method is unable to link the GCs to the star formation histories (only infall virial mass is used to tag the GCs onto our galaxies). However, the second effect (related to the higher halo mass for dwarf galaxies in higher density environments) is naturally taken into account in our catalog. We find no significant difference in the infall mass or infall times of the surviving dwarf population between our simulated groups, which partially explains the lack of correlation between $N_{\rm GC}$ or S_N with environment seen in our sample (see Appendix F).

Noteworthy, in agreement with our predictions, dwarfs in the Fornax cluster also show no enhancement in GC number of specific frequency (Prole et al. 2019) when compared to dwarfs in the Georgiev et al. (2010) field sample. This might suggest that while the mode of star formation and differences in halo masses may imprint an excess of GCs for dwarfs in higher density environments, those effects set in at higher density environments (closer to those of Virgo and Coma clusters, $M_{200} > 5 \times 10^{14}$ M$_\odot$) than those simulated here. Surveys of dwarfs in intermediate-mass groups and low-mass clusters are needed to confirm this hypothesis and determine whether or not our GC tagging model might benefit in the future from including additional GC formation channels. For instance, an increased number of GCs forming in starburst events associated with pericenter passages have been shown

successful at explaining a cluster-centric radial gradient in GC content for cluster dwarf galaxies (e.g., Mistani et al. 2016) and the higher GC content in ultra-diffuse galaxies (e.g. Carleton et al. 2021).

3.6 GC Occupation Fraction

While all massive galaxies appear to have associated GCs, the same is not true for low-mass galaxies, some of which are observed to host no GCs. The GC occupation fraction, defined here as the fraction of galaxies at fixed stellar mass that host at least 1 GC, is an important constrain on GC formation scenarios and is fundamental to determine the minimum galaxy mass able to form GCs that survive until the present day.

As discussed in Sec. 3.2, observationally, the GC occupation fraction is found to be close to one for galaxies with stellar masses $M_* \geq 10^9$ $M_\odot$, and to sharply decrease for lower-mass galaxies (Sánchez-Janssen et al. 2019; Eadie et al. 2022; Carlsten et al. 2022). An important caveat of these studies is that the low-mass galaxies included are mostly satellite objects, although the host mass varies from the Virgo cluster to satellites of $\sim L*$ hosts in the Local Volume. We can use our GC catalog to compare with these observations and to determine the role of tidal stripping in satellite galaxies in establishing such a trend.

Black starred symbols in Fig 3.8 show the median z = 0 GC occupation fraction in our simulated galaxies as a function of host galaxy stellar mass for GCs with individual masses $m_{\rm GC} > 10^5$ $M_\odot$ to mimic the brightness cutoff from Sánchez-Janssen et al. (2019) in the Virgo cluster. In agreement with observations, our catalog predicts a decreasing occupation fraction for dwarfs with $M_* \leq 10^9$ $M_\odot$, while all galaxies more massive than

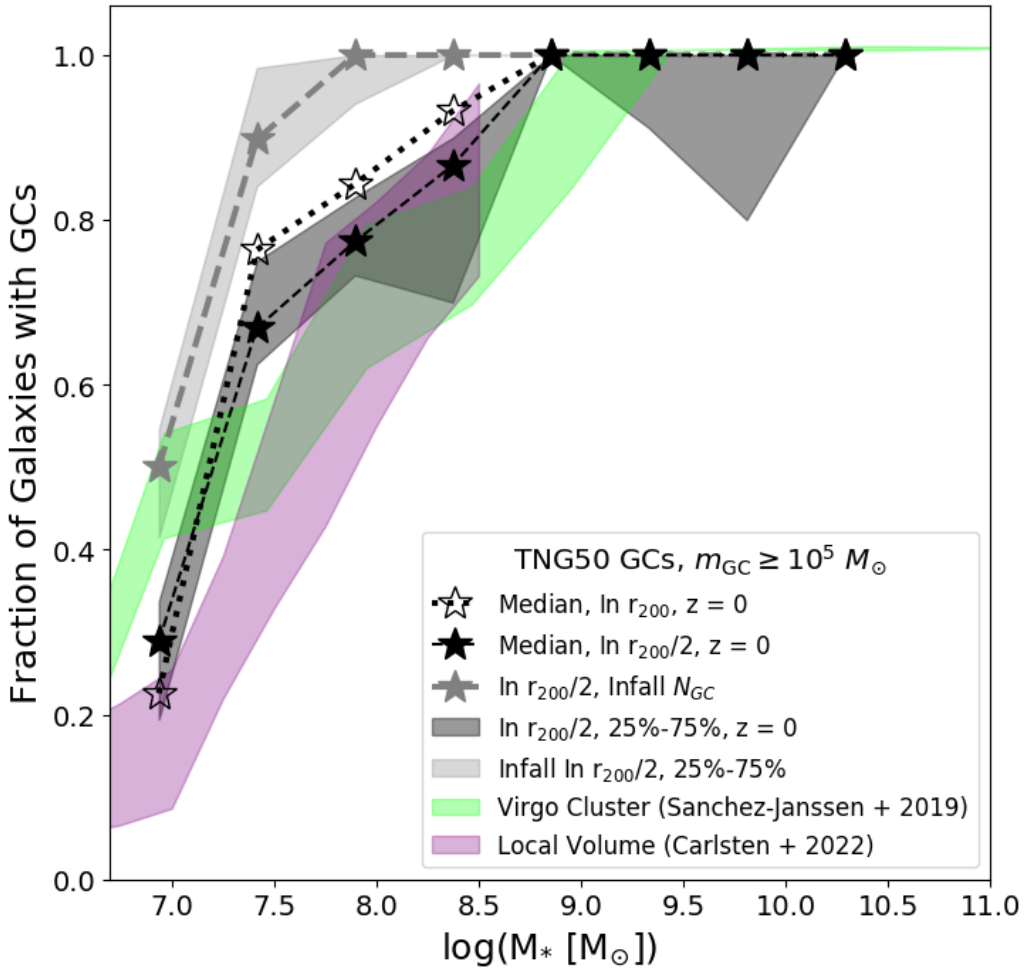

Figure 3.8: A look at GC occupation fraction (defined as the fraction of galaxies that have at least one GC associated to them) as a function of stellar mass for galaxies within $r_{200}/2$ of our selected groups. The figure shows the occupation fraction from TNG50 by infall number of GCs as the gray dotted line with stars (with the gray shaded region showing the $25\% - 75\%$ spread between environments); z $= 0$ values are shown within r_{200} by the unfilled black stars and dotted line and within $r_{200}/2$ as the filled black stars and dashed line (with the $25\% - 75\%$ spread between environments shown as the black shaded region). Observed occupation fractions from Virgo (Sánchez-Janssen et al. 2019) and the Local Volume (Carlsten et al. 2022) are shown as lime green and magenta shaded regions respectively. The difference between the dim gray and the black filled stars shows that tidal stripping has a sizable effect on setting the occupation fraction in dwarfs with $M_* < 10^9$ $M_\odot$. Lower-mass dwarfs with $M_* < 10^{7.5}$ $M_\odot$ have additionally a 50% occupation fraction already at infall, which we explain through their low total GC mass together with the stochastic sample of the GC mass function.

that are expected to host GCs. We find a weak dependence of the occupation fraction with cluster-centric radius, with occupation fraction being only slightly lower when considering satellites in the inner regions of simulated groups and clusters ($r < r_{200}/2$, solid black stars, short dashed curve) compared to including all satellites within the virial radius (open black stars, dotted curve). Shaded regions indicate 25-75 percentiles of our sample.

Encouragingly, our present-day occupation fraction agrees well with available measurements. For instance, green shaded area corresponds to galaxies within $\sim R_{200}/3-R_{200}/2$ of the Virgo cluster (Sánchez-Janssen et al. 2019) while the occupation fraction in satellite dwarfs within the Local Volume is shown in magenta (Carlsten et al. 2022). We find little variation in occupation fraction with environment across the 39 simulated groups in TNG50, which agrees well with findings reported in the two environments explored by the ELVES survey (Carlsten et al. 2022).

For comparison, we show in gray the "initial" occupation fraction, e.g., the occupation fraction measured at the infall time for our simulated dwarfs within the $r_{200}/2$ sample (gray starred symbols and dashed curve for the median, shading indicating 25-75 percentiles). Differences between the gray curve at infall and the black curve today is a direct measure of the impact of tidal stripping of GCs by the host groups and clusters, which seems to be substantial for dwarfs with $10^{7.5} < M_*/M_\odot < 10^9$.

In particular, our model predicts that all dwarfs with $M_* \sim 10^8$ $M_\odot$ should host at least one GC with mass $\sim 10^5$ $M_\odot$in the field, while such dwarfs have only 75% occupation fraction on average when observed in groups and clusters. This is a testable prediction that

might be confirmed or refuted when large observational samples of field dwarfs with their GCs become available.

On the other hand, for stellar masses lower than $M_* \sim 10^8$ M$_\odot$, the prediction for the infall GC occupation fraction is already lower than 1. For instance, our model predicts that only half of the dwarfs with $M_* \sim 10^7$ M$_\odot$ hosted at least one GC with $M_* \geq 10^5$ M$_\odot$ at infall.

Dwarfs with $M_* \sim 10^7$ M$_\odot$ have a "halo mass" $M_{200} \sim 7 \times 10^9$ M$_\odot$ (calculated following abundance matching from Hudson et al. (2015) as described in Sec. 3.3.3) and Fig. 3.2 shows that for such objects the median mass in GCs is $M_{\rm GC} \sim 2.6 \times 10^5$ M$_\odot$. This seems above our GC mass = 10^5 M$_\odot$considered for this occupation fraction calculation, raising the question of why the occupation fraction is lower than 1 at infall.

We find that the scatter around the $M_{\rm GC}$-M_{200} relation coupled to the stochastic sampling of the GC mass function (see Sec. 3.3.4) makes the chances for dwarfs of this mass to host a GC with $M = 10^5$ M$_\odot$ about half. Indeed, the maximum GC mass in our model is set to be one hundredth of the mass of the dwarf (limited inspired by observations of dwarfs in the Local Group), placing a GC with mass 10^5 M$_\odot$ close to the upper limit of the mass distribution and therefore relatively unlikely from a random normal draw (see purple histogram on the upper panel of Fig. 3.3 for the typical mass function of GCs in this mass range).

We have explicitly checked that removing the $0.01M_*$ cut for the sampling of GCs increases the occupation fraction slightly on the low mass end while leaving it unchanged for $M_* > 10^8$M$_\odot$. For instance, in our lowest mass bin the occupation fraction increases

by a factor ~ 2 as a result of a less restrictive mass distribution from which to draw the individual cluster masses. Given the observational uncertainties and variations between the Virgo and Local Volume measurements, our predictions for $M_* \sim 10^7 \mathrm{M}_\odot$ remain consistent with observations.

While stochasticity explains the initial low occupation fraction, we note that at present day, the occupation fraction has additionally dropped to 25% for dwarfs with $M_* \sim 10^7$ $\mathrm{M}_\odot$, which is due, similarly to more massive satellites, to tidal stripping from the host. This value is in good agreement with results from the Local Volume, but it is slightly lower than that measured for the Virgo cluster. Observations of dwarfs in the field for this mass range might also help constrain if our model is initially underpredicting the occupation fraction.

Another possibility is that projection effects in high-density environments such as the Virgo cluster could artificially be increasing the occupation fraction of low-mass dwarfs by assigning GCs from the intracluster component or from neighboring galaxies to these dwarfs. Occupation fraction being a requirement of only 1 GC is certainly subject to significant Poisson noise, which worsens in environments with a high background component such as clusters. We will use our catalog to explore projection effects in future work.

We highlight that the numbers presented in this section should be taken as upper limits assuming no additional GC destruction mechanism is at play after the tagging time at infall. This might not always apply, in particular in cases where dynamical friction timescales might be short, for instance, for low-mass galaxies. We show in Appendix E that considering the effects of dynamical friction does not significantly change our results. We

conclude that the occupation fraction predicted by our model is in reasonable agreement with current observational constraints and that additional data from other environments, and more specifically, from the field, would help verify (or reject) the predictions of our model.

3.7 Summary

In this work, we present a catalog of GCs tagged to the 39 most massive groups in the TNG50 simulation. Our systems have virial masses in the range $M_{200} = [5 \times 10^{12}$ - $2 \times 10^{14}]$ $M_\odot$ providing simulated analogs of massive ellipticals in the field to low-mass galaxy clusters. Known systems in this range may include Cen A, Fornax, Hydra-I or the Virgo cluster, where GC data is abundant. Our GC tagging technique follows from the one already applied to galaxy clusters with $M_{200} \geq 10^{14}$ $M_\odot$ in the Illustris simulation (Ramos-Almendares et al. 2020), with improvements to take full advantage of the increase in resolution and the inclusion of lower-mass dwarfs in our sample.

Briefly, our GCs are tagged to any satellite galaxy identified in the merger tree to have a maximum stellar mass $M_{*,\mathrm{max}} \geq 5 \times 10^6$ $M_\odot$ and that has ever interacted with our host groups. For each satellite, we identify dark matter particles in its subhalo at infall with a given energy distribution that is consistent with the phase-space that we choose for the GC systems. All galaxies are tagged at infall, after which the dynamics of their assigned GCs is followed by the simulation until the present day. This enables the prediction of GC content in galaxies from dwarfs to giant ellipticals with stellar masses in the range:

$M_* = [5 \times 10^6 - 6 \times 10^{11}]$ $M_\odot$. GCs are tagged to more than 8000 simulated galaxies across time, of which more than 5000 survive in our sample at $z = 0$.

We include a new modeling of the GC mass function that allows us to assign individual GC mass to each tagged particle. This is a necessary improvement over the previous model in Ramos-Almendares et al. (2020) which assigns all tagged particles equal GC mass. As discussed in Sec. 3.3.4 and 3.5.1, this addition is fundamental to reproducing the GC content in dwarf galaxies.

The GC tagging method relies on only one strong assumption: galaxies at infall follow a power-law relation between mass in GCs and halo mass, with a normalization and slope that is calibrated to reproduce the present-day $M_{\rm GC}$-M_{200} relation from Harris et al. (2015). Most importantly, this relation is known to hold only for galaxies with stellar mass $M_* \sim 10^9$ $M_\odot$ and above. We therefore consider only galaxies with halo mass $M_{200} > 10^{11}$ $M_\odot$ (or equivalently, $M_* \sim 10^9$ $M_\odot$) to participate in the calibration, while applying the calibrated relation to lower-mass galaxies as well. This approach allows us to make predictions on the GC systems of dwarfs with $M_* < 10^9$ $M_\odot$ under the assumption that they follow an extrapolation of the same power-law of more massive systems. In this paper we compare these predictions with available observational data on GCs of dwarf galaxies. Our main results can be summarized as follows.

- The GC tagging method naturally gives rise to the formation of an intracluster GC (ICGC) component which is in good agreement with the currently available data. Our individual GC-mass modeling allows the construction of mock observations of GCs at different brightness/mass cutoffs, which might prove a very useful tool for

theory/observation comparison once more ICGC systems are mapped in groups and clusters.

- The predicted number ($N_{\rm GC}$) and specific frequency (S_N) of GCs in dwarf galaxies with $M_* = [5 \times 10^7 - 10^9]$ M$_\odot$ are consistent with observations of dwarfs in the Local Volume as well as in clusters such as Virgo and Fornax. This provides support to the idea that low-mass dwarfs lay in an extrapolation of the GC mass - halo mass relation of more massive counterparts, in agreement with conclusions from Forbes et al. (2018). In particular, the average number of GCs as a function of galaxy mass seems in agreement with that reported for the ELVES survey in low-mass objects (Carlsten et al. 2022) and it is different from one where the number of GCs is simply a random draw in the low-mass end.

- The radial distribution of GCs around satellites in a wide range of masses is also well reproduced in our catalog, with median values ranging from $r_{h,\rm GC} \sim 2$ kpc for low-mass dwarfs with $M_* \sim 10^7$ M$_\odot$ to ~ 25 kpc for $M_* = 2 \times 10^{11}$ M$_\odot$. A closer inspection to the GCs in dwarf galaxies indicates that the low number of GCs expected might bias high the estimates of the half-number radius obtained by simply rank-ordering the identified GCs in distance. When stacking GCs of similar-mass dwarfs and finding a best-fit profile, as often performed in observations, we find that the half number radius of GCs in dwarfs is closely related to that of the stars, $r_{h,\rm GC} \sim 1.5 r_{h,*}$, which is a common assumption in the literature. This is substantially smaller than the factor ~ 3 - 5 between GCs and the size of the stellar component in more massive galaxies like the MW and giant ellipticals.

- We predict a steeply declining GC occupation fraction for dwarfs with $M_* < 10^9$ $M_\odot$, which is in reasonable agreement with current constraints from Virgo (Sánchez-Janssen et al. 2019) and the Local Volume (Carlsten et al. 2022). In our model, tidal stripping plays a significant role at lowering the occupation fraction for all dwarf galaxies, and this effect cannot be neglected when interpreting occupation fraction data in observations. For instance, we predict almost 100% occupation for dwarfs in the field with $M_* = 10^8$ $M_\odot$ e.g., hosting at least 1 GC with stellar mass 10^5 $M_\odot$, while in group and cluster environments the fraction is $\sim$ 75%, in agreement with observations. For lower-mass dwarfs, stochasticity in the sampling of the GC mass function coupled to their low GC mass content (set by their low halo mass) results in the expectation of only one in two dwarfs with $M_* \sim 10^7$ $M_\odot$ hosting a $\sim 10^5$ $M_\odot$ GC at infall. For comparison, tidal stripping effects lower this to one in four for the group and cluster environments.

Our GC tagging method is linked to an empirical calibration of the GC mass - halo mass relation and does not specifically model the formation of GCs. However, some of the results might be used to shed light on GC formation mechanisms. For example, our model naturally predicts the scaling of the size of GC systems across all masses to the dark matter halo distribution (through the half-mass radius in dark matter). The fact that we find a good agreement with observations on the typical GC system sizes from dwarfs to large galaxies suggests another puzzling link between dark matter halos and GCs, besides the scaling on mass. An interesting link between the GC sizes and the estimated virial radius has been observationally found in galaxies with mass comparable to the MW and

above (Hudson and Robison 2018). Our results suggest that a tight link between these two radii extends all the way into the dwarfs regime.

In particular, the GC radial extent in the regime of dwarf galaxies seems in agreement with the predictions from the model where GCs form at the centers of their own dark matter halos, or mini halos, as first suggested by Peebles (1984). While this is not true for more massive galaxies, where such a "cosmological" origin of GCs would predict radial distributions that are too extended compared to MW-like galaxies (Creasey et al. 2019), in the regime of dwarfs, the hierarchical clustering of these primordial mini-halos is of order few kpc, which is in good agreement with observations and predictions of our model (see Fig. 4 in Creasey et al. 2019).

This suggests that, if GCs can form in their own mini-halos and hierarchically assemble in the halos of galaxies today, the best sites to look for such objects might be dwarf galaxies, where a larger fraction of GCs would be consistent with a cosmological origin. Ultimately, only measurements of individual GC ages and metallicities would be able to fully differentiate between a primordial GC formed in its own dark matter halo, from a GC formed via baryonic processes in the ISM of galaxies (Bastian et al. 2020). Targetting GCs around dwarf galaxies with $M_* \sim 10^7$-10^8 $M_\odot$ might give us the best opportunity to narrow down GC origins.

More broadly, the GC catalog presented in this work is a useful resource to study the 6D properties of GCs in groups and clusters, environments where the ab initio formation of GCs in cosmological simulations is not yet feasible. Targeting ~ 40 systems allows the study of halo-to-halo variations and the understanding of the link between GC properties

and particular assembly history of each group; a goal that we will pursue in future work. The GC catalog created herein is made publicly available as part of the IllustrisTNG data release.

Chapter 4

Paper III: The puzzling nature of ultradiffuse galaxies and their globular clusters: normal, extreme, or somewhere in between?[1]

4.1 Abstract

Using the highest resolution run of the IllustrisTNG50 simulation in conjunction with its catalog of globular clusters (GCs), we investigate the GC systems of ultradiffuse

[1]This chapter contains a draft of an article that will be submitted for publication by Oxford Universtiy Press in Monthly Notices of the Royal Astronomical Society written by Jessica E. Doppel, Laura V. Sales, Jose Benavides, Elisa Toloba, Eric Peng, Dylan Nelson and Julio Navarro

galaxies (UDGs) that are members of the simulation's 39 most massive galaxy groups and clusters. We find that GC abundances fit well within the bounds of many observed UDGs and normal dwarf galaxies, although we do not find abundances as extreme as those observed in the Coma cluster for example. Across the range of environments that we are able to probe, with $M_{200} = [5 \times 10^{12}, 2 \times 10^{14}]$ $M_{\odot}$, we do not find the dependence of GC abundance of UDGs with their host environment as suggested by observations in Coma, Virgo, Fornax, and other low mass environments. Halo masses the selected UDGs additionally suggest that, while higher GC abundance systems tend to have higher halo masses at infall, overall, they are not substantially different than the halo masses of normal dwarf galaxies. Furthermore, the GC kinematics suggest the same–there is no kinematic distinction between the GC systems of simulated UDGs and dwarf galaxies. We find good agreement with a wide range of observations of GC velocity dispersion for UDGs, particularly those that appear to be normal dwarfs. One set of UDGs, those that appear to be "failed galaxies" we are only able to reproduce when observational techniques select interloping intracluster GCs as bound to the target UDGs.

4.2 Introduction

Ultradiffuse galaxies (UDGs), extremely low surface brightness galaxies that are observed to be quite radially extended for their stellar mass, have occupied an enigmatic place in scientific discourse in recent years due to advancements in instruments capable of observing these objects (see Abraham and van Dokkum 2014). Originally detected in the Coma cluster (see e.g., van Dokkum et al. 2015a,b; Koda et al. 2015), UDGs were thought

to reside primarily in the environments of galaxy clusters (see van Dokkum et al. 2015a,b; Koda et al. 2015; Mihos et al. 2015; Peng and Lim 2016; Yagi et al. 2016; Gannon et al. 2022), but UDGs have since been observed in a much wider range of environments (van der Burg et al. 2017; Lee et al. 2017, 2020; Marleau et al. 2021; La Marca et al. 2022; Venhola et al. 2022), including as isolated galaxies in the field (Martínez-Delgado et al. 2016; Román and Trujillo 2017; Leisman et al. 2017; Martín-Navarro et al. 2019; Rong et al. 2020). While many are observed to be devoid of gas (Martínez-Delgado et al. 2016; Papastergis et al. 2017; Román et al. 2019; Junais et al. 2021), more recent observations find gas-rich UDGs (e.g., Leisman et al. 2017; Mancera Piña et al. 2020; Jones et al. 2023) In addition to the range of gas fraction and environments, UDGs are also found to be diverse in nucleation fraction (Lim et al. 2020)

Given the apparent diversity of UDGs, it has proven particularly difficult to pinpoint their—potentially shared—formation paths. Several theoretical and numerical studies have pointed to differences between the dark matter (DM) halos that host UDGs and normal dwarfs, suggesting the possibility that UDGs reside in DM halos with higher than average spin (Amorisco and Loeb 2016; Rong et al. 2017; Mancera Piña et al. 2020; Kong et al. 2022; Benavides et al. 2023). Other studies present more baryon-focused formation scenarios. Star formation and feedback processes associated with "breathing-mode" outflows have the potential to leave the stellar component of galaxies rather extended (e.g., Di Cintio et al. 2017; Chan et al. 2018), although even the process of passively forming stars has been shown to form extremely low surface brightness galaxies consistent with UDGs (Tremmel et al. 2020). To add an additional complication in the search for UDG formation, environ-

mental effects, such as tidal heating (Carleton et al. 2019) and tidal stripping (Macciò et al. 2021; Doppel et al. 2021; Moreno et al. 2022), can give rise to UDG-like galaxies. However, combinations of the aforementioned scenarios have been found to form UDGs in simulations (Jiang et al. 2019; Sales et al. 2020), thus leaving the potential formation paths of UDGs quite entangled with one another.

Characterizing the DM content of UDGs provides an additional dimension to understanding the origin of UDGs. For example, UDGs that possess little to no dark matter could suggest a primary formation mechanism of tidal stripping, or perhaps more exotic scenarios of removing their DM content (see e.g., van Dokkum et al. 2018a, 2019a, 2022; Trujillo-Gomez et al. 2022). On the other extreme, UDGs that reside in extremely overmassive halos for their stellar mass could indicate that UDGs experienced some event that caused their star formation to suddenly cease, with their extreme radial extent a remnant of the much more massive galaxy they were otherwise destined to become (see e.g., Forbes et al. 2020; van Dokkum et al. 2017, 2015b; Toloba et al. 2023). Between these two extremes, UDGs that reside in DM halos on par with other galaxies of similar stellar mass could indicate that they are on the tail end of radial extent for dwarf galaxies, and indicate a mode of formation consistent with normal dwarf galaxies (e.g. Toloba et al. 2018; Lee et al. 2017, 2020; Saifollahi et al. 2021; Toloba et al. 2023). Illuminating the DM content of UDGs is, therefore, a necessary component for pinpointing the—potential spectrum of—formation scenarios through which UDGs may arise and help to solidify their place in our understanding of dwarf galaxies.

The DM content of UDGs, however, is as varied as their potential formation scenarios. Observations of luminous, kinematical tracers such as stars (cite DF44 and DF4 among others), GCs (see e.g. van Dokkum et al. 2018a; Toloba et al. 2018; van Dokkum et al. 2019a), and gas (Mancera Piña et al. 2020) suggest that the DM halos of UDGs span the entire range between lacking DM (such as DF2 and DF4) to residing in overamassive halos, with some more on par with that of the Milky Way than that of typical dwarf galaxies (Beasley et al. 2016; Janssens et al. 2022; Gannon et al. 2023; Toloba et al. 2023), with others occupying the space between these extremes (see e.g. Lee et al. 2017; Toloba et al. 2018; Lee et al. 2020; Saifollahi et al. 2021; Toloba et al. 2023).

For UDGs for which kinematical tracers are unavailable, we find a similar picture painted through their GC systems. The often rather numerous GCs associated to UDGs could further suggest that they reside in quite overmassive DM halos (van Dokkum et al. 2015a; Peng and Lim 2016; van Dokkum et al. 2017; Lim et al. 2018, 2020; Danieli et al. 2022; Janssens et al. 2022) if the power-law relation between GC mass and halo mass (see e.g. Peng et al. 2008; Harris et al. 2015) holds for UDGs. However, recent observations of UDGs in Coma suggest that, by GC counts, there are two types of UDGs: those that reside in apparently overmassive halos, and those that appear to reside in halos of more typical in mass for dwarf galaxies (Lim et al. 2018; Müller et al. 2021; Forbes et al. 2020; Jones et al. 2023). Even more complicating is the occasionally quite anomalous GC systems of UDGs that, in addition to being perhaps too numerous, are also too luminous (van Dokkum et al. 2018b, 2019a), suggesting that GC counts alone may not be sufficient to determine the DM mass of UDGs, but could rather be indicative of some extreme process in their formation

or evolution (van Dokkum et al. 2022).A further characterization, as well as the theoretical context, of the observations of the GC systems of UDGs will further help to disentangle the DM component of UDGs.

With the high resolution of the IllustrisTNG50 simulation (TNG50 hereafter), it is possible to morphologically define a set of simulated UDGs on par with observed UDGs (Benavides et al. 2023). Coupled with the recent addition of a catalog of GCs added to the simulation (Doppel et al. 2023), we can investigate UDGs in conjunction with their GC systems across a variety of environments, ranging from those comparable with massive elliptical systems to those comparable with the mass of the Fornax and Virgo Clusters. We can thus make a realistic comparison with the observations of the GC systems of UDGs in these types of environments to provide possible interpretations for these observations and their implications for the DM content of UDGs.

In section 4.3, we briefly discuss the details of TNG50 as well as the tagging model used to produce its GC catalog. In section 4.4, we discuss how the modeled GC abundances and kinematics compare to observations as well as what, if any, effect environment has on UDGs and their GC systems. In section 4.5, we compare mock observations of the GCs and UDGs in TNG50 to observed UDGs, and we use those mock observations to understand the inferred DM content of UDGs, both in the presence of contamination in their assigned GC systems as well as other complicating factors. Finally, in section 4.6, we provide a short summary of our results.

4.3 Methods

4.3.1 Simulation

We employ the highest resolution run of the cosmological hydrodynamical IllustrisTNG50 (Pillepich et al. 2019; Nelson et al. 2019a) simulation—which is part of the larget TNG50 project (Naiman et al. 2018; Pillepich et al. 2018a; Nelson et al. 2018; Springel et al. 2018; Marinacci et al. 2018; Nelson et al. 2019b)—for this work. TNG50 features a box size of 51.7 Mpc on each side with 2160^3 gas cells and dark matter particles evolved assuming a flat, ΛCDM cosmology consistent with parameters from Planck Collaboration et al. (2016). This configuration results in a mass resolution of, on average, $8.4 \times 10^4\ M_\odot$ for its baryonic component and $5.4 \times 10^5\ M_\odot$ for dark matter particles. The gravitational softening length is 288 pc at $z = 0$ for collisionless components.

The baryonic treatment in TNG50 is introduced in detail in (Weinberger et al. 2017; Pillepich et al. 2018b). Briefly, it includes star formation in the dense interstellar medium (ISM), stellar evolution, including chemical enrichment from supernovae; primordial cooling, metal line cooling, and heating, via background radiation, of gas; additionally, the seeding and growth of supermassive black holes, low and high accretion AGN feedback, galactic winds, and magnetic fields (Weinberger et al. 2017; Pillepich et al. 2018b).

Halos and subhalos within the TNG50 simulation are identified using the Friends-of-Friends (FOF, Davis et al. 1985) and SubFind (Springel et al. 2001; Dolag et al. 2009) respectively. In particular, we select 39 halos with virial masses between $M_{200} = [5 \times 10^{12}, 2 \times 10^{14} \mathrm{M}_\odot$(where "virial" in this study refers to quantities associated to a sphere enclosing 200 times the critical density of the universe). The mass resolution of TNG50

allows us to resolve galaxies with a stellar component of $M_* \sim 5 \times 10^6 M_\odot$, or those galaxies that contain at least 60 stellar particles. A stricter mass resolution is considered for this study: we consider UDGs in the stellar mass range $M_* = [10^{7.5}, 10^9] M_\odot$, which are resolved with a minimum of ~ 375 stellar particles. The evolution of these objects are followed using the SubLink merger trees (Rodriguez-Gomez et al. 2015).

4.3.2 GC Catalog

GCs are tagged to all galaxies that have interacted with our target groups and clusters provided they satisfy a maximum stellar mass throughout their history with 5×10^6 $M_\odot$and had a minimum of at least 100 dark matter particles (this later condition is required to avoid spurious baryonic clumps). All galaxies are tagged at their infall time, which is defined as the last time the galaxy is its own central. On average, this corresponds to the time at which a galaxy crosses the virial radius of its present day host galaxy cluster, but it might be an earlier time if the galaxy joins a smaller halo or group before infalling into the final host system (pre-processing).

GC candidate particles are selected from the DM particles associated to the host galaxy at infall time. Following Łokas and Mamon (2001), we fit an NFW profile (Navarro et al. 1996b):

$$\rho_{\rm NFW}(r) = \frac{\rho^0_{\rm NFW}}{(r/r_{\rm NFW})(1 + r/r_{\rm NFW})^2} \tag{4.1}$$

to the DM component of the galaxy. The scale radius $r_{NFW} = r_{max}/\alpha$, where r_{max} is the radius of maximum circular velocity and $\alpha = 2.1623$ (Bullock et al. 2001).

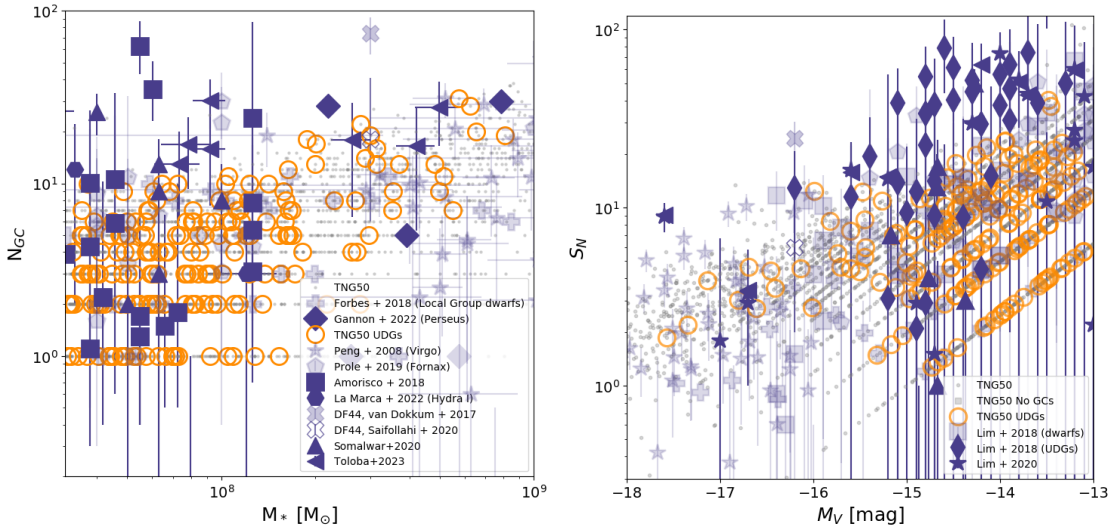

Figure 4.1: *Left*: Number of GCs (N_{GC}) as a function of host galaxy stellar mass. All simulated TNG50 satellite dwarf galaxies are shown in translucent gray points, with UDGs highlighted by unfilled orange circles. Observations of GC numbers for normal dwarf galaxies are shown in purple filled, translucent shapes, and those for UDGs in purple filled opaque shapes. We can see that while there is a large amount of scatter in the predicted GC numbers for the UDGs of TNG50, the scatter is not as large as what is seen in observed UDGs, particularly those of the Coma Cluster (opaque squares). We can see that despite the wide scatter, simulated and observational data follows (on average) similar trends. *Right:* the specific frequency of GCs (S_N) as a function of host galaxy V-band absolute magnitude. Following Doppel et al. (2023), we have applied a correction to the V-band magnitude to account for discrepancies between TNG50 and observations for high-mass galaxies. As in the left panel, all TNG50 dwarfs are shown as gray points, UDGs are highlighted by orange circles, observations of S_N for normal dwarf galaxies are shown as translucent filled purple shapes, and observations of S_N for UDGs are shown as filled, opaque purple shapes. Again, while TNG50 + GC tagging does produce quite a bit of scatter—on par with that observed for normal dwarf galaxies—the scatter is not as extreme as what is observed for the UDGs of the Coma cluster in particular (opaque purple diamonds). For both measures of GC abundance, while there is significant overlap between what is predicted by TNG50 and the GC systems observed for many UDGs, we do not predict the most extreme objects.

The GCs are assumed to follow a Hernquist (1990) profile:

$$\rho_{\rm HQ}(r) = \frac{\rho^0_{\rm HQ}}{(r/r_{\rm HQ})(1+r/r_{\rm HQ})^3} \tag{4.2}$$

which allows us to control the normalization and radial extension of the tagged GCs. We assign two populations of GCs: a red, metal rich component of GCs that formed in-situ, and blue GCs, representative of older, more metal poor GCs that were accreted to the galaxies. The red GCs are chosen to be more spatially concentrated than the blue GCs, with scale radii $r_{HQ} = 0.5 r_{NFW}$ and $3.0 r_{NFW}$ for red and blue GCs respectively. ρ_{HQ} is chosen to maximize the number of GC candidates.

The GC candidates are then selected in relative energy using the distribution function (Binney and Tremaine 2008a):

$$f_i(\epsilon) = \frac{1}{8\pi}\left[\int_0^\epsilon \frac{{\rm d}^2\rho_{\rm i}}{{\rm d}\psi^2}\frac{{\rm d}\psi}{\sqrt{\epsilon-\psi}} + \frac{1}{\sqrt{\epsilon}}\left(\frac{{\rm d}\rho_{\rm i}}{{\rm d}\psi}\right)\Big|_{\psi=0}\right], \tag{4.3}$$

where rho_i is the density profile of i = (DM, red GCs and blue GCs), Ψ is the relative gravitational potential, and ϵ is the relative energy. In equally spaced bins of relative energy, a fraction $f_{HQ,i}/f_{NFW}$, where i = red or blue GCs, of DM particles is selected. Inspired by constraints for the Milky Way (Yahagi and Bekki 2005), a cutoff radius of $r_h/3$, where r_h is the total halfmass radius of the halo in question, for the GC candidate particles.

The selected GC candidate particles are assigned masses such that by $z = 0$ those that still remain gravitationally associated to their host follow the $M_{GC} - M_{halo}$ relation from Harris et al. (2015). To make this calibration, we assume that a power-law relation similar to the $M_{GC} - M_{halo}$ relation exists at infall such that:

$$M_{\rm GC,inf} = \frac{1}{f_{\rm bound}} M_{{\rm GC},z=0} = a_{\rm inf} M_{\rm halo,inf}^{b_{\rm inf}}. \tag{4.4}$$

where f_{bound} is the fraction of GCs that are still gravitationally bound to their host galaxy at $z = 0$. We find for red and blue GCs respectively, $a_{inf} = 2.6 \times 10^{-7}$ and 7.3×10^{-5} and $b_{inf} = 1.14$ and 0.98.

Since the GC candidates are a much larger set of particles than the observed number of GCs, we subsample a realistic number of GCs from the candidates. This realistic population of GCs follows a Gaussian luminosity function using constraints from Jordán et al. (2007). Individual particle masses are obtained assuming a mass-to-light ratio of 1. GCs are randomly selected from the luminosity function until the total mass of GCs is within 7×10^3 $M_\odot$of the total calibrated infall mass. The realistic subsample of GCs is followed to $z = 0$ and constitutes the GCs we consider in this work.

The GCs in this catalog reproduce well available observational constraints in number, specific frequency and GC occupation fraction, as discussed in Doppel et al. (2023). In what follows, we investigate the specific predictions of this GC catalog for the particular case of UDGs in groups and clusters.

4.3.3 Sample of UDGs in groups and clusters

The UDGs considered for this work are satellites of these groups and clusters and were first introduced in Benavides et al. (2023). Simulated UDGs are selected to be in the stellar mass range $M_* = [10^{7.5}, 10^9]$ $M_\odot$—to ensure that there are sufficient stellar particles to resolve the structure of the galaxy. UDGs are identified as the 5% most extended outliers in the M_*-size relation, where size refers to the stellar half mass radius. These criteria results on a selection consistent with commonly assumed cut-offs to identify UDGs in observations ($R_e \geq 1.5$ and $\mu \gtrsim 24.5$).

As discussed in detail in Benavides et al. (2023), the formation mechanism of UDGs in TNG50 suggest that they inhabit mostly high-spin dark matter halos, although a sub-dominant fraction ($\sim 10\%$) of satellite UDGs was formed due to tidal effects within their groups or clusters. All simulated UDGs in TNG50 inhabit low-mass dark matter halos in the range $M_{200} \sim [10^{9.3} - 10^{11.2}]$ $M_{\odot}$that are in agreement with expectations from their stellar content. In addition, satellite UDGs are predicted to be red and quiescent while field UDGs are gas-rich and star forming, in good agreement with observational results.

Satellite UDGs have typically undergone substantial tidal stripping of their dark matter halo (median mass loss 80%) but only moderate tidal stripping of their stellar component (10% mass loss from their peak stellar mass). A total of 195 UDGs are found associated to our simulated groups in TNG50 and are the core sample of the analysis in this paper. In addition, these groups and clusters have 2195 non-UDG dwarfs in the same mass range as our UDGs that might be included when necessary for helpful comparisons.

4.4 GC abundance and kinematics: UDGs as Normal Dwarfs

We show in Fig. 4.1 the predicted GC number (N_{GC}, left panel) and GC specific frequency (S_N, right panel) for satellite dwarf galaxies in TNG50 compared to observational constraints. Overall, we find a good agreement between *all* simulated dwarfs in groups and clusters in TNG50 (gray dots) and a compilation of observational data (purple symbols) including normal dwarfs (translucent purple shapes Forbes et al. 2018; Peng et al. 2008; Prole et al. 2019; Lim et al. 2018) and UDGs (opaque purple shapes Gannon et al. 2022; Amorisco et al. 2018; van Dokkum et al. 2017; Saifollahi et al. 2021; Somerville et al. 2018;

Lim et al. 2018, 2020). We highlight simulated UDGs in TNG50 with orange empty circles, which we compare to observational constraints shown in solid purple.

Fig. 4.1 indicates that simulated UDGs display GC numbers that overlap well with the majority of observational constraints available (left panel), including systems in low mass groups (Somalwar et al. 2020) but also high density environments like Coma (Amorisco and Loeb 2016; Gannon et al. 2022). We note, however, that extreme UDGs with $N_{\rm GC} > 30$ are not present in our catalog but seem to be present in observations.

This result is not entirely unexpected: all UDGs in TNG50 are predicted to populate low-mass dwarf halos and their GC content is a reflection of such prediction. The specific frequency of GCs for these galaxies is shown on the right panel of Fig. 4.1 and confirms a similar trend: while there is good overlap for many of the simulated UDGs, very extreme values with $S_N > 30$ are not produced in our simulated sample but appear present in systems like the Virgo or Coma cluster (Lim et al. 2018, 2020).

Identifying GCs that are associated to a given galaxy in observations is not without challenge, a subject we return to in Sec.4.5. For the specific case of GC numbers or specific frequency, substantial uncertainty may exists when assigning GC membership. The iconic UDG DF44 is a good example (van Dokkum et al. 2016). Originally found to host nearly 100 GCs (van Dokkum et al. 2016), it has been now estimated to have only $\sim$ 20 GCs (Saifollahi et al. 2021). If we take the latest measurements as correct, our simulated UDGs are a good representation of galaxies like DF44. On the other hand, if earlier estimates are found to hold, then we do not find DF44 analogs in our sample. The example set by DF44 perhaps warrants a closer look into galaxies with very extreme GC content in observations.

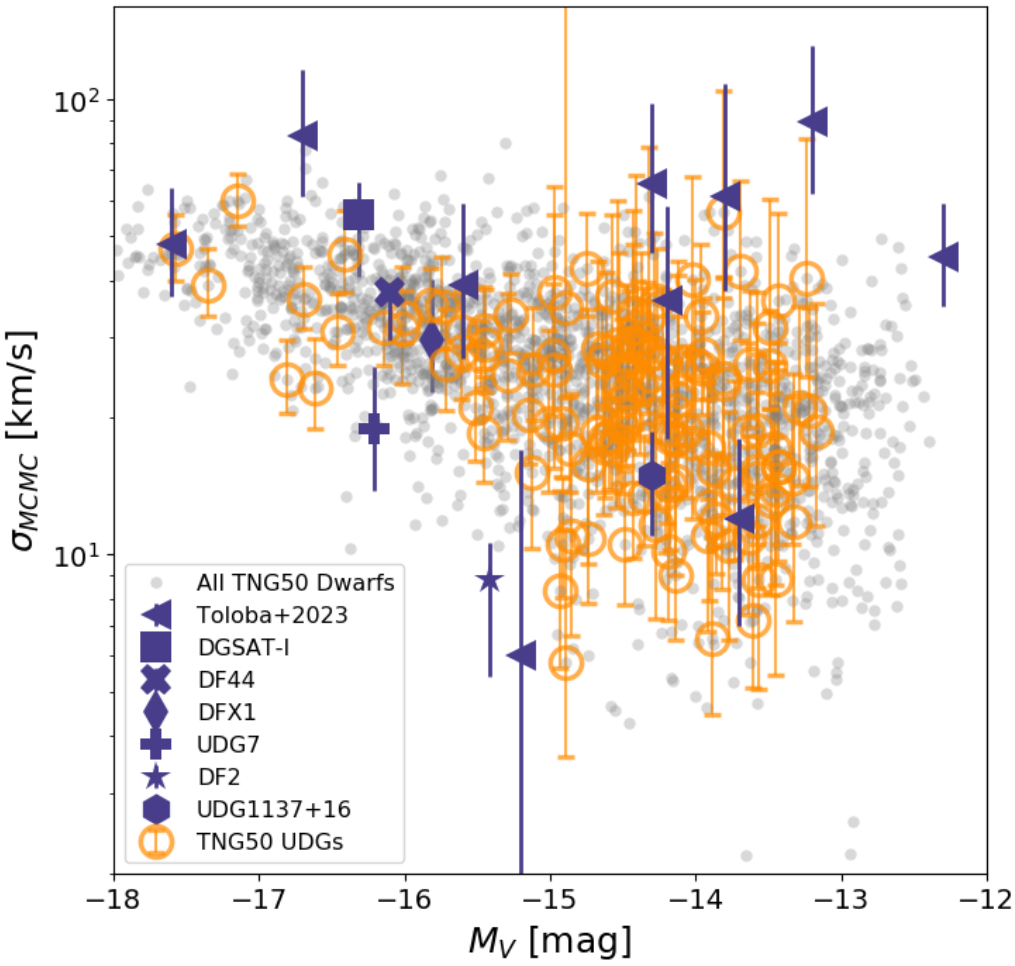

Figure 4.2: Kinematics of the GC systems of dwarf galaxies in TNG50 calculated via a Markov-Chain Monte Carlo (MCMC) method with as Jeffrey's prior plotted against host galaxy V-band magnitude, M_V. UDGs in TNG50 are highlighted with orange circles with errorbars representing the 25-75 percentiles from the PDF generated stochastically by the MCMC method. All dwarf galaxy satellites from TNG50 are shown as gray points. We show observations of GC kinematics from UDGs coming from various studies as large, solid, purple shapes. We find a wide range of UDGs represented in the literature, with some having dispersions that put them in range of "normal" dwarf galaxies, some with dispersions that put them in the dark matter deficient category. Other observed UDGs sit above what is predicted by TNG50, suggesting that they reside in rather overmassive halos. We note that much of the scatter σ_{MCMC} for the UDGs in TNG50 is due to the presence of few GC tracers, making many of the lower scattering points the product of small number statistics. UDGs and their GC systems in TNG50 thus appear to be kinematically indistinguishable from normal dwarf galaxies, but they are inconsistent with the very σ_{GC} galaxies from the Virgo Cluster (Toloba et al. 2023)

Despite the lack of direct analogs to the most extreme observed UDGs in terms of GC number, it is encouraging that our simulation reproduces a relatively wide range of GC contents, in good agreement with observational claims (e.g., Lim et al. 2020, 2018). Of particular interest are those with the largest numbers of GCs (or specific frequency) at any given mass (or luminosity). A closer look to the set of TNG50 UDGs in the top 15% of GC number and specific frequency at fixed stellar mass (and M_V) reveal that these UDGs tend to reside in higher mass—albeit still dwarf-mass—halos.

We find that this bias towards higher mass halos for more extreme UDGs is linked to earlier infall times than their less extreme counterparts, similar to our previous findings exploring normal dwarfs in the Illustris simulations (Ramos-Almendares et al. 2020). For example, we find a median infall time $t_{\rm inf} \sim 6.1$ Gyr for our large GC content UDGs compared to $t_{\rm inf} \sim 8.1$ Gyr for the rest of the UDG sample. See Fig. G.1 in the Appendix for more details.

Similar to the GC content, the velocity dispersion of observed UDGs has been shown to span a wide range. From the popular DF2 and DF4 cases having so low velocity dispersion ($\sigma < 10$ km/s) that are consistent with no dark matter at all (e.g., van Dokkum et al. 2018a; Danieli et al. 2019) to UDGs nearing $\sigma \sim 100$ km/s, compatible with halos so massive that can host MW-like galaxies. Of particular interest is the recent study by Toloba et al. (2023) which represents the first *systematic* study of GC kinematics in UDGs in the Virgo cluster, resulting in 5 UDGs consistent with $\sigma > 50$ km/s (half their sample) and MW-sized inferred dark matter halos. At least one of their UDGs is also consistent with

no dark matter, which seems to be tied to an ongoing tidal disruption for that particular UDG.

We show the measurements presented in Toloba et al. (2023) along with a compilation of other available velocity dispersion for observed UDGs in Fig. 4.2 (purple shapes). The GC velocity dispersion of simulated UDGs in TNG50 are shown with unfilled orange circles. Informed by Doppel et al. (2021), we have estimated GC velocity dispersion for these systems following an Markov-Chain Monte Carlo (MCMC) method with a Jeffreys prior on the dispersion itself, as this method was found the most adequate to estimate σ with a small number of tracers. The error bars on the orange circles show the 25%-75% spread in the velocity dispersion from the PDF stochastically generated via the MCMC method. This is analogous to the way that velocity dispersions were calculated for the GC systems of UDGs of the Virgo cluster (Toloba et al. 2023, , among others), with MCMC techniques being used as well to derive the GC (or stellar when GC kinematics are unavailable) velocity dispersions of DGSAT-1 (Martínez-Delgado et al. 2016; Martín-Navarro et al. 2019), DF44 (van Dokkum et al. 2019b), DFX1 (van Dokkum et al. 2017), UDG7 (Chilingarian et al. 2019), DF2 (van Dokkum et al. 2018a), and UDG1137+16 (Gannon et al. 2021; Forbes et al. 2021).

Encouragingly, the range of GC velocity dispersions predicted by the tagged GCs in TNG50 agrees well with several of the observational constraints for UDGs, in particular for objects with normal-dwarf velocity dispersions such as DFX1, UDG7, UDG1137+16, several Virgo UDGs, and DF44. At least half of the UDGs with available velocity measurements are consistent with a dark matter content of a dwarf-mass halo—in agreement with predictions

from our UDG sample in TNG50. Moreover, the GC velocity dispersion of simulated UDGs overlap well also with non-UDG dwarf satellites in TNG50 (gray dots). This is indeed expected from the formation scenario of UDGs in this simulation, which place them in dwarf dark matter halos consistent with the non-UDG sample (although with a small bias towards higher mass, e.g., Benavides et al. 2023).

Interestingly, we also see in Fig.4.2 several UDGs and dwarfs from TNG50 that show $\sigma_{\rm MCMC} < 10$ km/s, consistent with expectations of dark-matter free UDGs such as DF2. A closer inspection of this simulated analogs to DF2 show that several have undergone a rather significant amount of dark matter stripping (as was found in Doppel et al. 2021). However, much of the scatter in the lower σ UDGs comes from having only 3-5 GCs to recover the potential of their host halo. As Doppel et al. (2021) showed, using a Jeffrey's prior for a low number of tracers performed well in recovering dynamical mass in the *median* of the sample, but with a large galaxy-to-galaxy scatter. This is a large contributor to the source of kinematic analogs to DF2 in TNG50 and highlights the importance of having a sufficient number of tracers to make accurate *individual* dark matter mass estimates.

An important conclusion from Fig. 4.2 is that UDGs with high GC velocity dispersions, $\sigma_{\rm MCMC} > 50$ km/s, are extremely rare in our simulated sample but are rather numerous in the available observational constraints. Objects like DGSAT-1 (Martínez-Delgado et al. 2016) and NGVSUDG-09, 05, 19, 20 and A04 from the Toloba et al. (2023) study of UDGs in Virgo show GC (or stellar) velocity dispersions consistent with a large amount of dark matter in these galaxies, often interpreted as "failed" massive halos that were destined to form a galaxy more comparable to the Milky Way, but stopped forming

stars with only $\sim$ a tenth of such stellar content, resulting on an overly-massive halo given its stellar mass (van Dokkum et al. 2015a; Peng and Lim 2016; van Dokkum et al. 2017; Lim et al. 2018; Lahén et al. 2020; Danieli et al. 2022; Janssens et al. 2022). Calculations presented in Toloba et al. (2023) show that halos more massive than $M_{200} \sim 10^{12}\mathrm{M}_{\odot}$ are necessary to explain the kinematics of the large-σ_{MCMC} UDGs. Such "massive failures" are not present in the simulated UDG sample in TNG50.

This finding may have two different explanations. On one hand, this may be a legitimate disagreement between theory and observation, implying that the physical mechanisms to form such massive failed galaxies is missing from cosmological simulations (as no other simulation has reported successfully forming such dark matter dominated objects to date) and from our understanding of galaxy formation. Or, on the other hand, the origin of the large velocity dispersion in observed UDGs may be attributed to contamination and observational effects which are not currently included when comparing with theoretical predictions. We use our simulated GC catalog to more closely address whether contamination alone may explain the observed UDGs with large inferred dark matter halo masses.

4.5 Effects of Contamination on the GC velocity dispersion of UDGs

The analysis of the simulated UDGs and their GCs in Sec. 4.4 assumes that only the gravitationally associated GCs are taken into account when estimating GC numbers and kinematics in observations. For the case of the TNG50 simulations, we use information from Subfind to determine whether or not a GC remains gravitationally bound to a given

UDG. However, this is not possible in observations, where assigning membership to the GCs observed around target galaxies becomes an additional challenge.

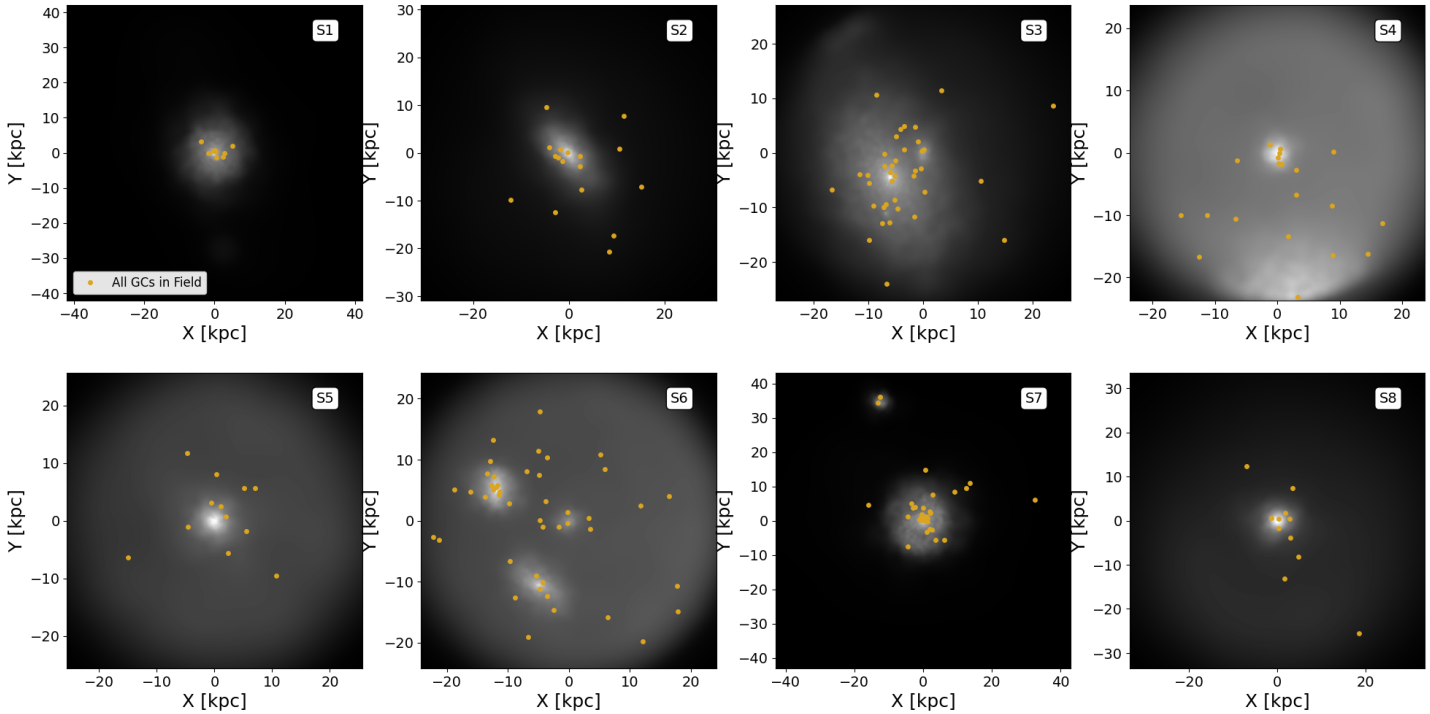
S1
S2
S3
S4
S5
S6
S7
S8
All GCs in Field
X [kpc]
Y [kpc]

Figure 4.3 *(previous page)*: X-Y projections of stars (background grayscale) and GCs (light orange points) withing $16R_e$ of 8 UDGs within TNG50. The SubFind ID of each UDG is notated in the upper right corner of each panel, with the stellar projections being generated by py-SPHviewer (Benitez-Llambay 2015). The UDGs shown are selected to have at least 8 GCs in the within $16R_e$ of the host UDG and, as is described in section 4.5 and Fig 4.2, to display a range of scenarios from quite easy to surprisingly difficult for selecting bound GCs. Several UDGs, namely S1, S2, S5, ans S8 are quite isolated, with the rest having one or more other galaxy in the field of view. From spatial information alone, determining GC boundness is not straightforward, and other properties, such as GC kinematics, should be considered as additional constraints.

In the specific sample from the Virgo cluster, where most of the available kinematical constraints on UDGs exist (Toloba et al. 2018, 2023), GC membership is based on a combined criteria in projected distance to the host galaxy: $R < 7R_e$, with R_e the effective radius of the host UDG, and an additional restriction on the relative line-of-sight velocity between the candidate GC and the UDG, set to be less than 200 km/s. We can use our simulated catalogs to evaluate the degree to which the selection effects and specific choices applied in observed samples may lead to the possible inclusion of interloper GCs, biasing the velocity or mass estimate for some UDGs.

We construct mock observations of our simulated samples by projecting all groups and clusters in a given direction and applying a similar selection criteria as described in Toloba et al. (2023). By doing so, we are considering the top two possible contamination sources: *i*) GCs associated to other galaxies that are nearby the UDG in projection and *ii*) GCs in the diffuse intra-cluster GC component (ICGCs). We define the projected effective radius $R_e = 3/4 r_{h,*}$, where $r_{h,*}$ is the 3D half-mass radius of each simulated UDG.

For illustration, Fig. 4.3 show 8 representative examples of simulated UDGs and their GC in our sample. The stellar component of the UDGs and their surroundings is represented by the background grayscale (generated using ph-SPHvierwer, Benitez-Llambay 2015), and the GCs in the frames are represented by light orange dots. We label them satellite-1 through -8, or S1-S8 for short, with a label on the upper right hand corner of each panel. We can find UDGs in relatively isolated surroundings (such as S1, S2, S5 and S8) as well as to those in crowded or obviously contaminated fields with several companion galaxies in projection (S3, S6 and S7). These examples are chosen to showcase different

levels of contamination by interlopers and are not representative of the chances to find a given case in our sample.

Next, we apply the selection criteria in GC radial velocity, $v_{proj,GC}$. Fig. 4.4 shows this for the 8 examples discussed above. For convenience, we center the GC velocities on that of the host UDG. Following Toloba et al. (2023), we consider GCs within $7R_e$ of their host galaxy and within $\pm$200 km/s of the velocity of their host galaxy as bound to the host galaxy (burgundy box). GCs that would be selected as members by this method are highlighted by purple dots, while those outside of the selection box are shown in yellow.

We use our simulation to denote additional information for each GC. Those known to be gravitationally bound to the UDGs (based on SubFind information) are outlined by gray squares. GCs that belonged to the UDG but have now been tidally stripped are outlined by teal stars, and those outlined by dark orange hexagons are GCs associated to other subhalos. Dots without any outlining shape belong to the intra-cluster GC component. In all panels we quote, on the upper right corner, the actual 1D velocity dispersion calculated with all bound GCs ($\sigma_{\rm true}$) along with the corresponding velocity dispersion computed using the objects within the selection box ($\sigma_{\rm obs}$). We emphasize that, similar to observational samples, the velocity dispersion determination is computed using an MCMC method assuming a Jeffreys prior.

In general, we find that this simple selection criteria works surprisingly well in most cases considered, with a few exceptions. We can see that for all eight featured UDGs, most of the GCs gravitationally bound to the galaxy are recovered by this selection method, with the exception of S2 and S7, which are missing respectively 5 and 1 associated GC with

the selection criteria applied. Note that in neither case does this matters for the velocity dispersion measured, which remains very close to the true value even when missing a few GCs (upper right corner of each panel). In the case of S2, the missing GCs would, however, significantly impact the (projected) half-number radius, which changes from 8 kpc in the case of all bound GCs to 3.7 kpc if considering only those within the selection box.

The inclusion of velocity information tends to alleviate projection effects on GC membership. For example, S3 and S6 in Fig. 4.3 have obvious contamination ongoing due to the overlap in projection with other satellites in the group. We can see in Fig. 4.4 that the addition of velocity cuts completely disentangles the GC population associated to S3 from the GCs associated to the secondary galaxy along the line of sight. However, this is not the case for S6, where GCs bound to the companion galaxy fulfill the criteria of membership due to chance alignment in the velocities. This results, for the specific case of S6, in a factor 2 overestimation of the velocity dispersion inferred: using the GCs within the selection box results on $\sigma_{\rm obs} \sim 50$ km/s whereas the truly associated GCs are moving with $\sigma_{\rm act} \sim 24$ km/s.

While the case of S6 demonstrates that care must be exercised when dealing with projected data, it is a type of contamination that observational studies will avoid unless absolutely necessary. In fact, none of the UDGs considered in the sample of Toloba et al. (2018) or Toloba et al. (2023) contains other galaxies in projection on the line of sight. In what follows, we chose to ignore contamination from GCs associated to other subhalos, as observational studies would purposely remove such complicated systems from their samples.

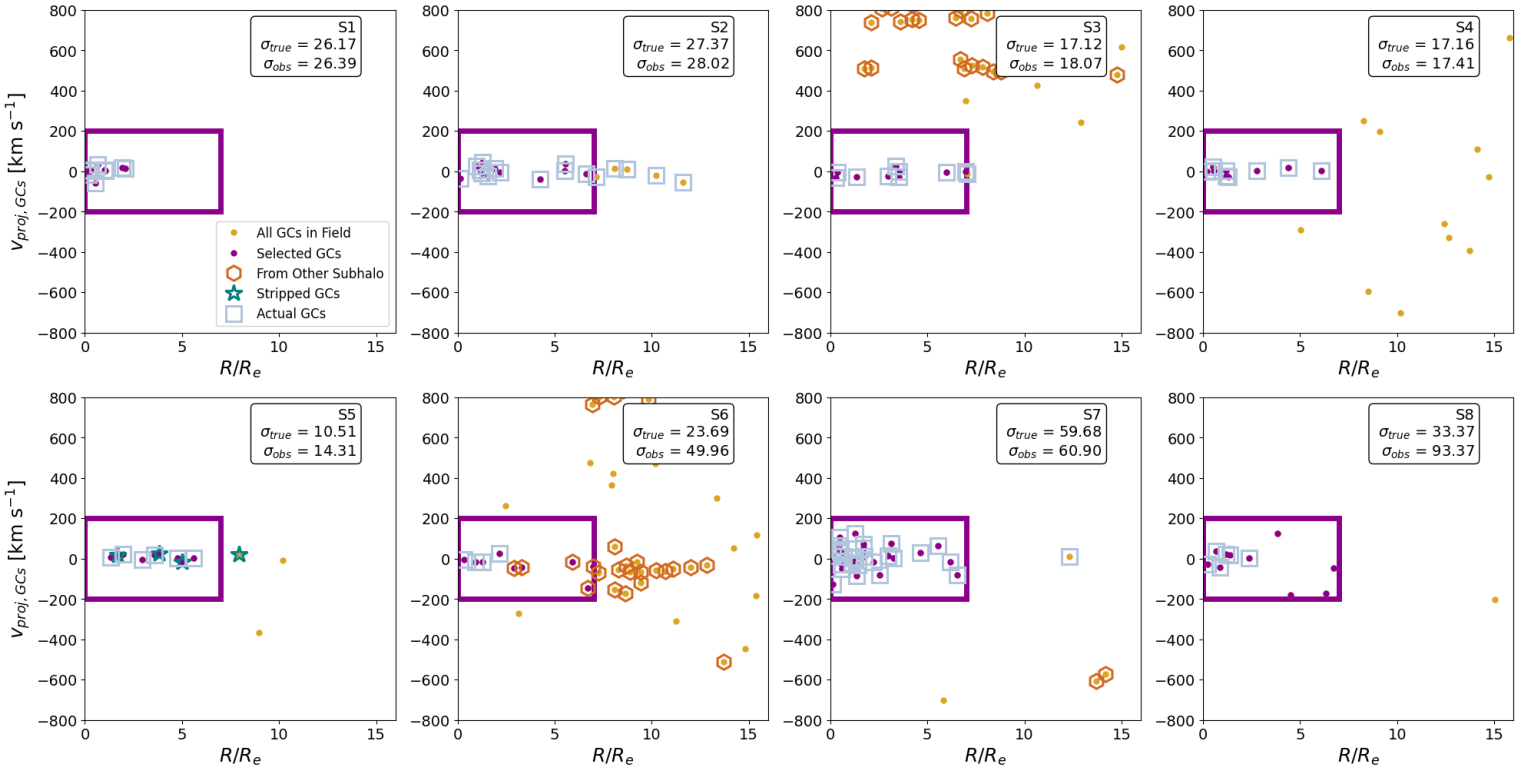
S1
σ_{true} = 26.17
σ_{obs} = 26.39
S2
σ_{true} = 27.37
σ_{obs} = 28.02
S3
σ_{true} = 17.12
σ_{obs} = 18.07
S4
σ_{true} = 17.16
σ_{obs} = 17.41
S5
σ_{true} = 10.51
σ_{obs} = 14.31
S6
σ_{true} = 23.69
σ_{obs} = 49.96
S7
σ_{true} = 59.68
σ_{obs} = 60.90
S8
σ_{true} = 33.37
σ_{obs} = 93.37
All GCs in Field
Selected GCs
From Other Subhalo
Stripped GCs
Actual GCs
$v_{proj,GCs}$ [km s^{-1}]
R/R_e

Figure 4.4 *(previous page)*: A mock observation of the radial velocity of the GCs associated to the eight UDGs in Fig. 4.3. Boundness of GCs is determined to be those that fall within $7R_e$ of a given galaxy whose radial velocities are within $\pm 200 km/s$ of that of their host galaxies. The wide range in acceptable velocities allows for the possibility of detecting UDGs that follow the "failed galaxy" formation scenario. All GCs in the $16R_e$ field of view are represented by light orange circles, with those selected as bound by the radius and velocity cuts shown in burgundy within the burgundy box. GCs that have been tidally stripped from their host UDG are outlined teal stars, with GCs known to belong to the UDGs highlighted by unfilled gray squares, and those that belong to other subhalos in the field of view are outlined by brown hexagons. We can see that even in the presence of additional galaxies in the field of view, such as S3 that the actual GCs can be recovered by the selection method described in section 4.5. For some UDGs (namely S3, S4, and S7 in the set of UDGs presented here), we find the observed radial cut of $7R_e$ to be somewhat conservative. Additionally, we can see that assigning GCs based on kinematics is overall a powerful tool, with a nearly correct set of GCs often being picked out of crowded fields (e.g., S3). Interestingly, GCs that are considered part of the ICGCs that have been tidally stripped from their hosts are often difficult to distinguish kinematically or radially from the set of actual GCs, with S5 suffering from this sort of contamination quite prominently. S6 represents a "worst case scenario" that likely would be thrown out from an observational sample. A different sort of worst case scenario can be found for S8 with a large number of ICGC interlopers that increase the observed velocity dispersion quite substantially. Thus, kinematic information about GCs can help substantially in determining their boundness, though it can still be non-trivial to remove the presence of interloping GCs.

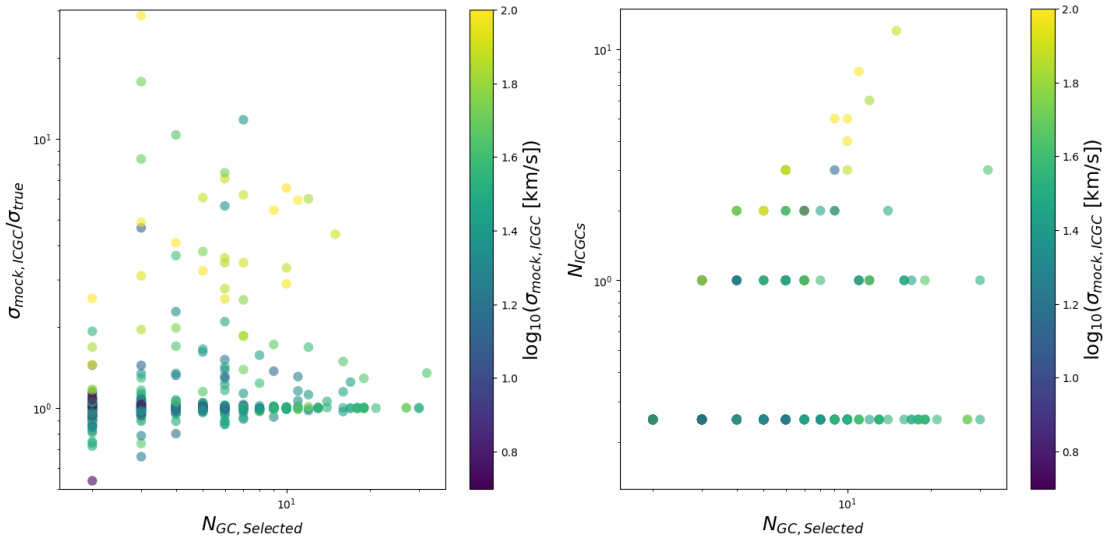

Figure 4.5: *Left:* The ratio of the GC velocity dispersion measured via mock observations, $\sigma_{mock,ICGC}$. to the actual GC velocity dispersion, σ_{true} as a function of total GCs selected, $N_{GC,Selected}$ via the method described in sec. 4.5, with points colored by $\log_{10}(\sigma_{mock,ICGC})$. We can see that for small GC numbers, the $\sigma_{mock,ICGC}$ can be greatly inflated from its true value from ICGC contaminants. *Right:* The number of interloping ICGCs from mock observations, N_{ICGCs} as a function of $N_{GC,Selected}$, colored again by $\log_{10}(\sigma_{mock,ICGC})$. Interestingly, we do see a spike in N_{ICGCs}, particularly around $N_{GC,Selected} = 10$. Points that do not have ICGC contamination are assigned the value 0.25, and we can see that, for most galaxies, the mock observations do not pick up significant ICGC contamination.

However, a more interesting contamination case is that of S8 in our sample. S8 is seemingly isolated, but several intra-cluster GCs fall within the selection box, artificially enhancing the velocity dispersion measured by a factor of ~ 3. This galaxy would be placed in a massive dark matter halo with ~ 100 km/s velocity, while in reality it inhabits a dwarf-mass one with $\sigma_{\rm true} \sim 35$ km/s. This presents a concrete example where an otherwise relatively normal UDG could be kinematically mistaken as a failed galaxy.

Are cases like S8 common in our sample? For that we need to evaluate how often contamination from the intra-cluster component sneaks into the selection box. We quantify this in Fig. 4.5. The left panel shows, as a function of the number of GCs within

the selection box in our UDGs, $N_{\rm GC,Selected}$, the ratio of the measured velocity dispersion (including intra-cluster interlopers) and the true value (computed with only bound GCs according to SubFind). For the vast majority of simulated UDGs the velocity dispersion estimate remains within 20% of its true value, suggesting that it is not likely that interlopers will play a dominant effect in the majority of UDG measurements. However, for systems with less than 10 GCs, the inclusion of intra-cluster contamination may cause overestimation of the velocity by factors 2-10.

Reassuringly, when considering UDGs with 10 GCs or more, as done in the sample of Toloba et al. (2023), only a handful of cases suffer from interloper contamination from the intra-cluster component leading to a velocity overestimation larger than $\sim \times 2$. For such cases, the color scale in Fig. 4.5 indicates an inferred velocity dispersion ~ 100 km/s, consistent with massive failed galaxies. As shown by the right panel of the same figure, selecting UDGs with 10 GCs or more leads typically to galaxies with 0 or 1 GC interloper, and a median $\sigma_{\rm mock,ICGC} \sim 1.001 \sigma_{\rm true}$ Those few UDGs with $N_{\rm GC,Selected} > 10$ and $\sigma \sim 100$ km/s include typically 4+ GCs from the intra-cluster component, but such cases are rare.

Can intra-cluster GCs then explain the high-incidence of large velocity dispersion UDGs found in Virgo? In order to evaluate this more closely, we restrict now our sample to only UDGs with $N_{\rm GC,Selected} \geq 10$, following Toloba et al. (2023). A total of 75 UDGs satisfy these criteria when using 3 different projections along the x-, y- and z- axis of our 39 groups and clusters in TNG50. We derive from these mock projections: the corresponding 1D MCMC velocity dispersion, the half-number radius of the GCs and the dynamical mass at half-number radius following Jeans modeling as in Wolf et al. (2010). The dynamical

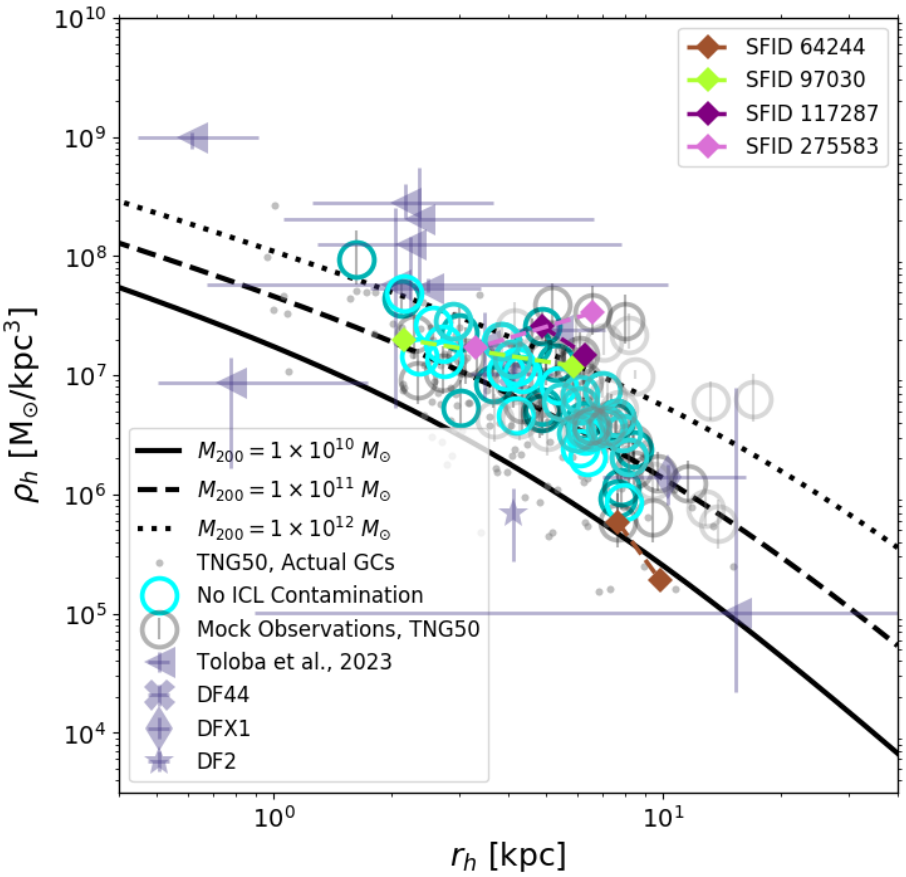

Figure 4.6: Density as a function of radius. Density profiles for NFW halos with halo masses of $M_{200} = 10^{10}, 10^{11}, 10^{12}$ $M_\odot$are shown as the solid, dashed, and dotted lines respectively. The instantaneous density at the half number radius of GCs (r_h) unfilled black circles with errorbars (using the GCs selected via the method in sec. 4.5, where the cyan circles indicate that no interloping ICGCs are present in the mock observations, with the cyan shaded region representing the 25%-75% spread for UDGs with no interloping GCs. Observations from (Toloba et al. 2023) are shown as translucent purple triangles, with those from DF44 and DFX1 (using stellar kinematics), DF2, DGSAT-1, and UDG1137+16 shown by the purple 'x', diamond, star, square, plus sign and hexagon respectively. Instantaneous densities at the GC (or stellar) halfmass radius for each galaxy (simulated or observed) is calculated using its GC velocity dispersion and GC half-number radius via dynamical mass estimation (see Wolf et al. 2010), with the shapes. To increase statistics, we include mock observations using projections in the XY, XZ, and YZ planes for each UDG. We can see that using the cuts described in section 4.5 to assign GCs to their host UDGs generally agrees with ρ_h calculations using the actual GCs, but the presence of ICGC interlopers can artificially inflate both σ_{GC} and ρ_h enough to suggest that some UDGs could reside in overmassive halos. Specific cases from Figures 4.4 and 4.3 are shown as colored diamonds, connecting their density calculated using their actual GCs and those selected via observational methods.

mass may be trivially transformed into mass density by dividing by the spherical volume enclosed within the half-number radii.

Fig. 4.6 shows the inferred mass density for these subsample of simulated UDGs as a function of the half-number radius of their selected GCs (black open circles). For reference, the gray lines represent NFW profiles with virial masses $M_{200} = 10^{10}, 10^{11}$ and $10^{12}\mathrm{M}_{\odot}$ and a concentration $c = 10$. We do find that for most cases, galaxies cluster around the $10^{11}\mathrm{M}_{\odot}$ line, which is in agreement with the prediction in TNG50 that UDGs occupy dwarf-mass halos with $M_{200} \sim 10^{9} - 10^{11}$ $\mathrm{M}_{\odot}$(Benavides et al. 2023).

However, we find several instances in which the mocked galaxies wonder close to (or above) the $M_{200} \sim 10^{12}\mathrm{M}_{\odot}$ line, despite their true halo mass being substantially smaller. This happens mostly due to the effect of contamination from interloper GCs, as can be appreciated by looking at the cyan symbols, which excludes intra-cluster GCs in the calculation of the velocity dispersion and follow quite closely an average distribution for a $M_{200} \sim 10^{11}\mathrm{M}_{\odot}$ halo. When allowing intra-cluster GCs to take part in the velocity estimation, this artificially inflates σ_{obs} driving the density estimation higher for those systems.

Such is the case of S8 introduced before in Figs. 4.3 and 4.4, highlighted in pink, which moves from a true mass-density consistent with the dashed line ($M_{200} \sim 10^{11}\mathrm{M}_{\odot}$), to its inferred density more consistent with a MW-mass halo with $M_{200} > 10^{12}\mathrm{M}_{\odot}$. Worth discussing is also the case of S7, highlighted here in purple. As shown in Fig. 4.4, S7 does not include contamination by GC interlopers, yet its inner density is high and consistent with MW-like halos either when applying the mock selection in projection or when considering all

bound GCs according to Subfind. We have checked that this high density is not the result of an overly-massive halo, but instead corresponds to a dwarf-mass halo with a larger-than-typical concentration. The virial mass before infall for S7 is $M_{200} \sim 8.7 \times 10^{10} \mathrm{M}_{\odot}$. This galaxy is a good reminder that variations in concentration may also drive some of the scatter in the inferred dark matter content of UDGs.

In summary, contamination by intra-cluster GCs could produce some UDGs that appear to be consistent with the halo masses inferred by some of the quite extreme Virgo UDGs (translucent purple triangles) reported recently in Toloba et al. (2023), but it is not enough to reproduce the *frequency* of such objects: half of the sample in Toloba et al. (2023) show such massive halos, while only a handful of our systems are driven close to the dotted $M_{200} \sim 10^{12} \mathrm{M}_{\odot}$ line due to contamination effects. While ICGC contamination can create cases where UDGs appear to reside in the overmassive halos indicative of failed galaxies, the selection effects adopted so far in the literature are effective at preventing contamination and only $\sim 16\%$ of the UDGs with 10 GCs or more show a velocity dispersion overestimation by a factor of 2 or above.

4.6 Conclusions

We have utilized the highest resolution run of the TNG50 simulation, in conjunction with its GC catalog, to study the GC systems and DM content of a set of 183 morphologically defined UDGs within the simulation. A number of conclusions can be made from this investigation.

- We find that the number and specific frequency of the GCs of the TNG50 UDGs paints UDGs as regular dwarf galaxies rather than DM deficient or failed galaxies. In fact, the GC systems of UDGs do not at all distinguish UDGs from regular dwarf galaxies within the simulation.

- While the GC abundances predicted by TNG50 do agree with a wide range of observations of both UDGs and dwarf galaxies, we do not reproduce the most extreme values. We additionally find that there is no environmental dependence on GC abundance. The variety of environments in TNG50, however, does not span galaxy clusters more massive than Virgo. Further work into the GCs of UDGs in Coma-like systems is necessary to understand the cause of this observed increase.

- We find that the GC kinematics predicted by TNG50 additionally does not distinguish UDGs from regular dwarf galaxies. Owing to the relatively small number of GCs for low-mass UDGs in TNG50, there is a wide range of GC velocity dispersions predicted for these systems. It should be noted that this is in part due to small number statistics. While using an MCMC technique with a Jeffrey's prior does, on average, recover the GC velocity dispersion relatively well, for small number of tracers, a large scatter is expected. However, despite this scatter, we do find good agreement with GC velocity dispersions of a variety of UDGs—particularly DGSAT-1, DFX1, UDG7, and several UDGs in the Virgo cluster. We are not however able to reproduce the rather high velocity dispersions of several Virgo UDGs.

- We performed mock observations using the same technique as was used to identify GCs that was used by Toloba et al. (2023) to identify overmassive UDGs in the Virgo

cluster. This method, using both spatial and kinematic cuts, is able to recover known GCs with no contamination for $\sim 60\%$ of UDGs. For a number of objects, we find that contaminating GCs from other galaxies and those in the intracluster medium (including GCs tidally stripped from the target UDG) can contribute to both an increase in inferred GC number, velocity dispersion, and thus DM content of UDGs.

- While the most extreme UDGs in TNG50 are still not as extreme as those in the Virgo Cluster, performing mock observations on their GC systems can, in the instance of contamination from ICGCs, elevate GC velocity dispersion such that the inferred DM content of some UDGs is much higher than expected. Additionally, residing in a more concentrated DM halo, and statistical errors in velocity dispersion or dynamical mass estimation—even in the instance of no contamination—could also artificially place a UDG in an inferred DM more massive than expected.

TNG50 and its GC catalog overwhelmingly do not predict UDGs representative of the extremes of UDGs: GC velocity dispersions consistent with DM-deficient UDGs appear as a result of low number statistics, and those suggestive of UDGs with overmassive DM halos appear most often as a result of interloping ICGCs in mock observations. One potential avenue that is unavailable to explore at the time of writing is a systematic study of GCs in higher mass environments, particularly those on par with the Coma Cluster ($M_{200} \sim 10^{15}$ $M_\odot$) or higher mass estimates of the Virgo Cluster ($M_{200} \sim 5 \times 10^{14}$ $M_\odot$). Similar numerical and theoretical studies exploring the UDGs of Coma and higher-mass Virgo type environments are necessary to disentangle whether UDG, and other galaxies by extension, do indeed simply possess more GCs in these environments, or whether ICGC

contamination plays a role in these increased GC numbers. Additionally, the lack of extreme UDGs in TNG50 may be an issue of sampling: perhaps the DM-deficient UDGs and those that are failed galaxies are extreme outliers in abundance matching or evolutionary situation that a larger sample of simulated UDGs could reveal. This work is left to future theoretical and observational exploration.

Chapter 5

Conclusions

GCs, while still enigmatic in their origins, can tell us quite a bit about both the dark matter content galaxies and the processes that shape the galaxies we see today. Through their relative ubiquity, as well as their brightness compared to the diffuse light of their hosts, GCs can serve as a powerful observational tool, provided we understand the systematics and limitations of their use. The limitations on DM inference using GCs becomes most pronounced for galaxies with low GC numbers (see ch. 2 and ch. 4), namely, for galaxies in the dwarf regime. The characterization of biases and errors in different mass estimation techniques is thus imperative for tests probing the DM content of these galaxies to differentiate between different DM models.

Through our investigations in both the Illustris and TNG50 simulations, we find that GCs serve as excellent tracers of the DM content across a range of galaxies, from low-mass dwarf galaxies to the dense environments of galaxy clusters, but with some caveats. Ch. 2 and Ch. 4 show that low numbers of GCs can introduce a number of uncertainties.

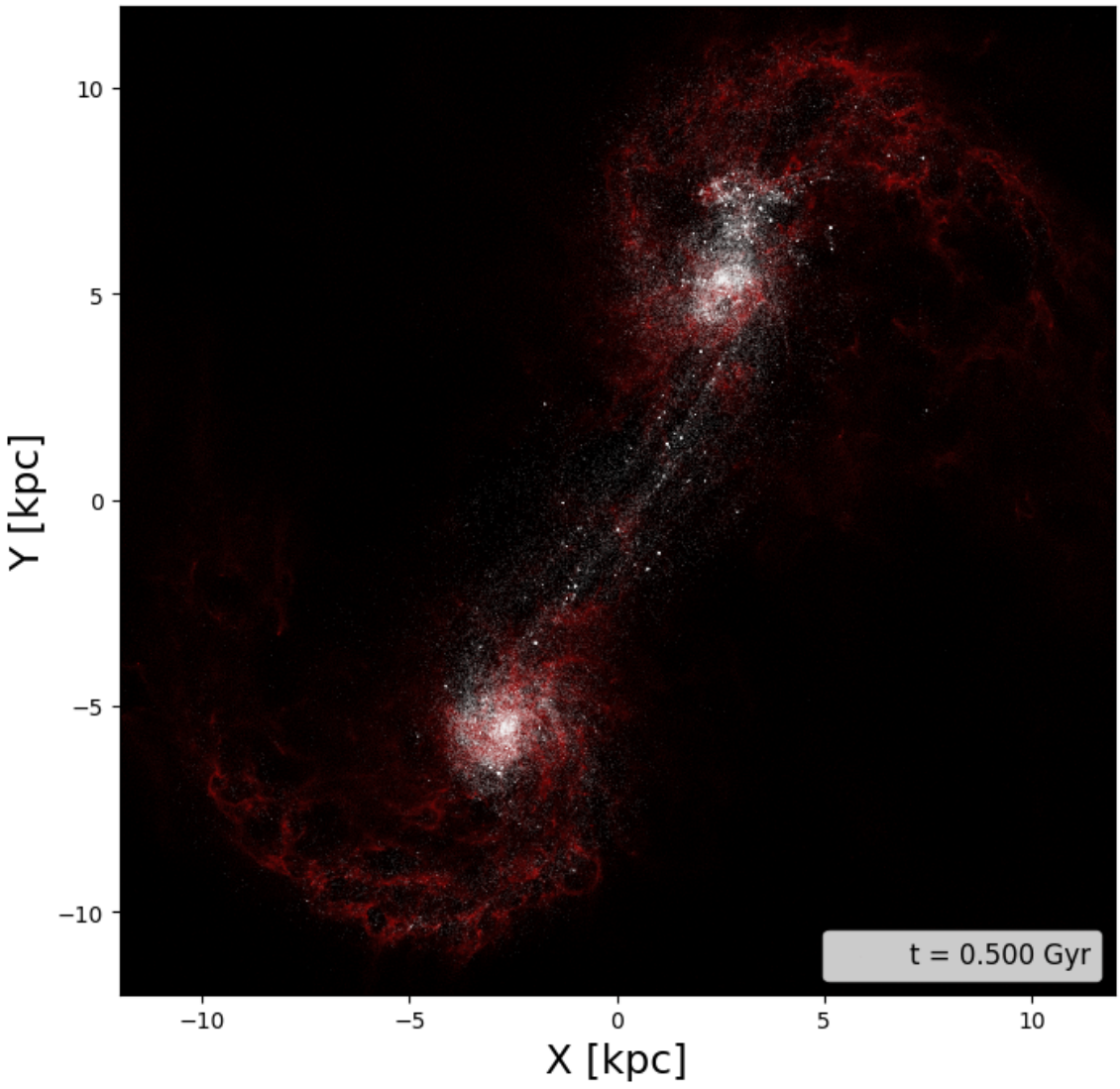

Figure 5.1: A high resolution run using SMUGGLE of a very gas rich, 1:1 dwarf galaxy merger just after their first pass. The presence of stellar clusters is quite prominent both in the stream between the two interacting galaxies as well as associated to the galaxies themselves. This particular simulation has a mass resolution of $\sim 600 M_{\odot}$for baryonic particles, with a gravitational softening of 5pc, meaning that many of the resultant stellar clusters are well resolved.

Even using sophisticated methods to translate GC kinematics and number into DM tracers, mock observations presented in this work show a large scatter in potential inferences about DM halo mass from these measurements. We have characterized the errors and biases present in many methods of estimating GC velocity dispersion and thus inferred DM mass. While we do find large galaxy-to-galaxy scatter in recovering the true DM mass of galaxies with less than 10 GCs, we do find that, for the median case, an MCMC method with a Jeffreys prior will remove the biases seen in other methods, and is thus recommended for galaxies with low N_{GC}.

Interestingly, the large scatter in observations of GC numbers (e.g., Peng et al. 2008; Forbes et al. 2018; Amorisco et al. 2018; Lim et al. 2018; Prole et al. 2019; Somalwar et al. 2020; Lim et al. 2020; Gannon et al. 2022; Toloba et al. 2023) is reproduced by our GC tagging model, particularly when careful consideration of GC masses are included. An even more interesting (and perhaps observationally valuable) suggestion of this result is that the power-law relation between GC mass and halo mass (Peng et al. 2008; Harris et al. 2015) appears to hold down into the dwarf regime. Additionally, this assumption has reproduced other observables, including the observed range of GC velocity dispersion (as discussed in Ch. 4), the dropoff in the GC occupation fraction (in a similar manner to observations from Sánchez-Janssen et al. 2019; Carlsten et al. 2022), and the buildup of in inter-cluster component of GCs that is on par with observational constraints (Lee et al. 2010; Taylor et al. 2017). Connecting GCs in this way to their host halos themselves certainly provides a cheap, first estimate or prior on the potential DM content of both dwarf satellite galaxies in groups and clusters and the groups and clusters themselves.

The intracluster GCs component formed in this model can provide meaningful predictions not only for the DM mass of galaxy groups and clusters (as was explored in Ramos-Almendares et al. (2020)), but also on the shape of the halo itself and its accretion history (see Ahvazi et al, in prep). In the era of telescopes like JWST, Euclid, Roman, and future extremely large telescopes, the constraints on the DM distribution provided from the GCs of dense environments at intermediate redshift can, for example, help build more accurate lensing maps (see e.g., Diego et al. 2023). Such work requires the use of larger cosmological volumes, such as TNG100 and TNG300 (Pillepich et al. 2018b,a; Nelson et al. 2018), across a wider range of times, but the framework set in this dissertation allows for the relatively easy implementation of the GC tagging model in any simulation with a collisionless component.

However, there are improvements to be made to this model as more science pertaining to the formation of GCs is uncovered. Particularly in the context of dwarf galaxies and UDGs, we do not find the expected environmental dependence in GC number (e.g., Carlsten et al. 2022). While this could be a consequence of not exploring dense enough environments (see App. F), or the effect of contamination from ICGCs and other sources in observations of such environments, it cannot yet be excluded that GC number (or mass) could have ties to star formation events in their hosts related to perhaps mergers or starbursts (e.g., Mistani et al. 2016; Carleton et al. 2021). As evidenced by the motivation behind post-processing GC tagging models, resolving the formation of GCs is, at the scales we consider in this work, impossible. However, one attempt to potentially connect GCs to

star formation events in their host galaxies is to utilize very high resolution simulations of isolated galaxies.

Going beyond the scope of this dissertation, and inspired by observations of young, massive star clusters forming in galaxy mergers (Portegies Zwart et al. 2010), is my recent, preliminary work using the SMUGGLE model (Marinacci et al. 2019) to study the formation of stellar clumps that form in mergers of dwarf galaxies. Figure 5.1 shows one such run of an ongoing 1:1 merger of two dwarf galaxies residing in DM halos with $M_{200} \sim 2 \times 10^{10}$ $M_{\odot}$. Using dwarf mergers in particular allows us to push both the mass ($M_{baryon} \sim 600$ $M_{\odot}$and $M_{DM} \sim 6000$ $M_{\odot}$) and spatial (5pc) resolution to a point fine enough to form both bound and unbound stellar clumps and to study their gaseous formation sites. The aim of this future work is to both better characterize the initial properties of these stellar clusters as well as the baryonic conditions necessary to form them. The results of these simulations have the potential to better inform the relevant formation physics and properties assigned to GCs in future work.

Bibliography

Roberto G. Abraham and Pieter G. van Dokkum. Ultra-Low Surface Brightness Imaging with the Dragonfly Telephoto Array. *Astronomical Society of the Pacific*, 126(935):55, January 2014. doi: 10.1086/674875.

Adebusola B. Alabi, Duncan A. Forbes, Aaron J. Romanowsky, Jean P. Brodie, Jay Strader, Joachim Janz, Vincenzo Pota, Nicola Pastorello, Christopher Usher, Lee R. Spitler, Caroline Foster, Zachary G. Jennings, Alexa Villaume, and Sreeja Kartha. The SLUGGS survey: the mass distribution in early-type galaxies within five effective radii and beyond. *MNRAS*, 460(4):3838–3860, August 2016. doi: 10.1093/mnras/stw1213.

Adebusola B. Alabi, Duncan A. Forbes, Aaron J. Romanowsky, Jean P. Brodie, Jay Strader, Joachim Janz, Christopher Usher, Lee R. Spitler, Sabine Bellstedt, and Anna Ferré-Mateu. The SLUGGS survey: dark matter fractions at large radii and assembly epochs of early-type galaxies from globular cluster kinematics. *MNRAS*, 468(4):3949–3964, July 2017. doi: 10.1093/mnras/stx678.

K. A. Alamo-Martínez and J. P. Blakeslee. Specific Frequencies and Luminosity Profiles of Cluster Galaxies and Intracluster Light in Abell 1689. *ApJ*, 849(1):6, November 2017. doi: 10.3847/1538-4357/aa8f44.

N. C. Amorisco and A. Loeb. Ultradiffuse galaxies: the high-spin tail of the abundant dwarf galaxy population. *MNRAS*, 459(1):L51–L55, Jun 2016. doi: 10.1093/mnrasl/slw055.

N. C. Amorisco, A. Monachesi, A. Agnello, and S. D. M. White. The globular cluster systems of 54 Coma ultra-diffuse galaxies: statistical constraints from HST data. *MNRAS*, 475 (3):4235–4251, April 2018. doi: 10.1093/mnras/sty116.

L. P. Bassino, S. A. Cellone, J. C. Forte, and B. Dirsch. Globular cluster candidates within the Fornax Cluster: Intracluster globulars? *A&A*, 399:489–496, February 2003. doi: 10.1051/0004-6361:20021810.

Nate Bastian, Joel Pfeffer, J. M. Diederik Kruijssen, Robert A. Crain, Sebastian Trujillo-Gomez, and Marta Reina-Campos. The globular cluster system mass-halo mass relation in the E-MOSAICS simulations. *MNRAS*, 498(1):1050–1061, October 2020. doi: 10.1093/mnras/staa2453.

Michael A. Beasley and Ignacio Trujillo. Globular Clusters Indicate That Ultra-diffuse Galaxies Are Dwarfs. *ApJ*, 830(1):23, October 2016. doi: 10.3847/0004-637X/830/1/23.

Michael A. Beasley, Aaron J. Romanowsky, Vincenzo Pota, Ignacio Martin Navarro, David Martinez Delgado, Fabian Neyer, and Aaron L. Deich. An Overmassive Dark Halo around an Ultra-diffuse Galaxy in the Virgo Cluster. *ApJL*, 819(2):L20, Mar 2016. doi: 10.3847/2041-8205/819/2/L20.

T. C. Beers, K. Flynn, and K. Gebhardt. Measures of location and scale for velocities in clusters of galaxies - A robust approach. *AJ*, 100:32–46, July 1990. doi: 10.1086/115487.

Kenji Bekki and Masashi Chiba. Formation of Galactic Disk Globular Clusters in Early Dissipative Minor Merging. *ApJ*, 566(1):245–251, February 2002. doi: 10.1086/337984.

José A. Benavides, Laura V. Sales, and Mario G. Abadi. Accretion of galaxy groups into galaxy clusters. *MNRAS*, 498(3):3852–3862, November 2020. doi: 10.1093/mnras/staa2636.

José A. Benavides, Laura V. Sales, Mario G. Abadi, Federico Marinacci, Mark Vogelsberger, and Lars Hernquist. Origin and evolution of ultradiffuse galaxies in different environments. *MNRAS*, 522(1):1033–1048, June 2023. doi: 10.1093/mnras/stad1053.

Alejandro Benitez-Llambay. py-sphviewer: Py-sphviewer v1.0.0, July 2015. URL http://dx.doi.org/10.5281/zenodo.21703.

James Binney and Scott Tremaine. *Galactic Dynamics: Second Edition*. 2008a.

James Binney and Scott Tremaine. *Galactic Dynamics: Second Edition*. 2008b.

John P. Blakeslee, John L. Tonry, and Mark R. Metzger. Globular Clusters in 19 Northern Abell Clusters. *AJ*, 114:482–506, August 1997. doi: 10.1086/118488.

Michael Boylan-Kolchin. The globular cluster-dark matter halo connection. *MNRAS*, 472 (3):3120–3130, December 2017. doi: 10.1093/mnras/stx2164.

Michael Boylan-Kolchin, James S. Bullock, and Manoj Kaplinghat. Too big to fail? The puzzling darkness of massive Milky Way subhaloes. *MNRAS*, 415(1):L40–L44, July 2011. doi: 10.1111/j.1745-3933.2011.01074.x.

A. H. Broeils. The mass distribution of the dwarf spiral NGC 1560. *A&A*, 256:19–32, March 1992.

J. S. Bullock, T. S. Kolatt, Y. Sigad, R. S. Somerville, A. V. Kravtsov, A. A. Klypin, J. R. Primack, and A. Dekel. Profiles of dark haloes: evolution, scatter and environment. *Monthly Notices of the Royal Astronomical Society*, 321(3):559–575, 03 2001. ISSN 0035-8711. doi: 10.1046/j.1365-8711.2001.04068.x. URL https://doi.org/10.1046/j.1365-8711.2001.04068.x.

James S. Bullock and Kathryn V. Johnston. Tracing Galaxy Formation with Stellar Halos. I. Methods. *ApJ*, 635(2):931–949, December 2005. doi: 10.1086/497422.

Claude Carignan and Kenneth C. Freeman. DDO 154: A "Dark" Galaxy? *ApJL*, 332:L33, September 1988. doi: 10.1086/185260.

Timothy Carleton, Raphaël Errani, Michael Cooper, Manoj Kaplinghat, Jorge Peñarrubia, and Yicheng Guo. The formation of ultra-diffuse galaxies in cored dark matter haloes through tidal stripping and heating. *MNRAS*, 485(1):382–395, May 2019. doi: 10.1093/mnras/stz383.

Timothy Carleton, Yicheng Guo, Ferah Munshi, Michael Tremmel, and Anna Wright. An excess of globular clusters in Ultra-Diffuse Galaxies formed through tidal heating. *MNRAS*, 502(1):398–406, March 2021. doi: 10.1093/mnras/stab031.

Scott G. Carlsten, Jenny E. Greene, Rachael L. Beaton, and Johnny P. Greco. ELVES II: Globular Clusters and Nuclear Star Clusters of Dwarf Galaxies: the Importance of Environment. *ApJ*, 927(1):44, March 2022. doi: 10.3847/1538-4357/ac457e.

T. K. Chan, D. Kereš, A. Wetzel, P. F. Hopkins, C. A. Faucher-Giguère, K. El-Badry, S. Garrison-Kimmel, and M. Boylan-Kolchin. The origin of ultra diffuse galaxies: stellar feedback and quenching. *MNRAS*, 478(1):906–925, Jul 2018. doi: 10.1093/mnras/sty1153.

Yingtian Chen and Oleg Y. Gnedin. Modeling the kinematics of globular cluster systems. *arXiv e-prints*, art. arXiv:2203.00599, March 2022.

Igor V. Chilingarian, Anton V. Afanasiev, Kirill A. Grishin, Daniel Fabricant, and Sean Moran. Internal Dynamics and Stellar Content of Nine Ultra-diffuse Galaxies in the Coma Cluster Prove Their Evolutionary Link with Dwarf Early-type Galaxies. *ApJ*, 884 (1):79, October 2019. doi: 10.3847/1538-4357/ab4205.

Nick Choksi and Oleg Y. Gnedin. Origins of scaling relations of globular cluster systems. *MNRAS*, 488(4):5409–5419, October 2019. doi: 10.1093/mnras/stz2097.

A. P. Cooper, S. Cole, C. S. Frenk, S. D. M. White, J. Helly, A. J. Benson, G. De Lucia, A. Helmi, A. Jenkins, J. F. Navarro, V. Springel, and J. Wang. Galactic stellar haloes in the CDM model. *MNRAS*, 406(2):744–766, August 2010. doi: 10.1111/j.1365-2966.2010.16740.x.

Stéphanie Côté, Claude Carignan, and Kenneth C. Freeman. The Various Kinematics of Dwarf Irregular Galaxies in Nearby Groups and Their Dark Matter Distributions. *AJ*, 120(6):3027–3059, December 2000. doi: 10.1086/316883.

Peter Creasey, Omid Sameie, Laura V. Sales, Hai-Bo Yu, Mark Vogelsberger, and Jesús Zavala. Spreading out and staying sharp - creating diverse rotation curves via baryonic and self-interaction effects. *MNRAS*, 468(2):2283–2295, June 2017. doi: 10.1093/mnras/stx522.

Peter Creasey, Laura V. Sales, Eric W. Peng, and Omid Sameie. Globular clusters formed within dark haloes I: present-day abundance, distribution, and kinematics. *MNRAS*, 482 (1):219–230, January 2019. doi: 10.1093/mnras/sty2701.

Shany Danieli, Pieter van Dokkum, Charlie Conroy, Roberto Abraham, and Aaron J. Romanowsky. Still Missing Dark Matter: KCWI High-resolution Stellar Kinematics of NGC1052-DF2. *ApJL*, 874(2):L12, April 2019. doi: 10.3847/2041-8213/ab0e8c.

Shany Danieli, Pieter van Dokkum, Sebastian Trujillo-Gomez, J. M. Diederik Kruijssen, Aaron J. Romanowsky, Scott Carlsten, Zili Shen, Jiaxuan Li, Roberto Abraham, Jean Brodie, Charlie Conroy, Jonah S. Gannon, and Johnny Greco. NGC 5846-UDG1: A Galaxy Formed Mostly by Star Formation in Massive, Extremely Dense Clumps of Gas. *ApJL*, 927(2):L28, March 2022. doi: 10.3847/2041-8213/ac590a.

M. Davis, G. Efstathiou, C. S. Frenk, and S. D. M. White. The evolution of large-scale structure in a universe dominated by cold dark matter. *ApJ*, 292:371–394, May 1985. doi: 10.1086/163168.

Arianna Di Cintio, Chris B. Brook, Aaron A. Dutton, Andrea V. Macciò, Aura Obreja, and Avishai Dekel. NIHAO - XI. Formation of ultra-diffuse galaxies by outflows. *MNRAS*, 466(1):L1–L6, Mar 2017. doi: 10.1093/mnrasl/slw210.

J. M. Diego, M. Pascale, B. Frye, A. Zitrin, T. Broadhurst, G. Mahler, G. B. Caminha, M. Jauzac, Myung Gyoon Lee, Jang Ho Bae, In Sung Jang, and Mireia Montes. On the correlation between dark matter, intracluster light and globular cluster distribution in SMACS0723. *arXiv e-prints*, art. arXiv:2301.03629, January 2023. doi: 10.48550/arXiv.2301.03629.

Jürg Diemand, Piero Madau, and Ben Moore. The distribution and kinematics of early high-σ peaks in present-day haloes: implications for rare objects and old stellar populations. *MNRAS*, 364(2):367–383, December 2005. doi: 10.1111/j.1365-2966.2005.09604.x.

K. Dolag, S. Borgani, G. Murante, and V. Springel. Substructures in hydrodynamical cluster simulations. *MNRAS*, 399(2):497–514, October 2009. doi: 10.1111/j.1365-2966.2009.15034.x.

Martina Donnari, Annalisa Pillepich, Gandhali D. Joshi, Dylan Nelson, Shy Genel, Federico Marinacci, Vicente Rodriguez-Gomez, Rüdiger Pakmor, Paul Torrey, Mark Vogelsberger, and Lars Hernquist. Quenched fractions in the IllustrisTNG simulations: the roles of AGN feedback, environment, and pre-processing. *MNRAS*, 500(3):4004–4024, January 2021a. doi: 10.1093/mnras/staa3006.

Martina Donnari, Annalisa Pillepich, Dylan Nelson, Federico Marinacci, Mark Vogelsberger, and Lars Hernquist. Quenched fractions in the IllustrisTNG simulations: comparison with observations and other theoretical models. *MNRAS*, 506(4):4760–4780, October 2021b. doi: 10.1093/mnras/stab1950.

Jessica E. Doppel, Laura V. Sales, Julio F. Navarro, Mario G. Abadi, Eric W. Peng, Elisa Toloba, and Felipe Ramos-Almendares. Globular clusters as tracers of the dark matter content of dwarfs in galaxy clusters. *MNRAS*, 502(2):1661–1677, April 2021. doi: 10.1093/mnras/staa3915.

Jessica E. Doppel, Laura V. Sales, Dylan Nelson, Annalisa Pillepich, Mario G. Abadi, Eric W. Peng, Federico Marinacci, Jill Naiman, Paul Torrey, Mark Vogelsberger, Rainer Weinberger, and Lars Hernquist. Modelling globular clusters in the TNG50 simulation: predictions from dwarfs to giant galaxies. *MNRAS*, 518(2):2453–2470, January 2023. doi: 10.1093/mnras/stac2818.

Michael J. Drinkwater, Michael D. Gregg, and Matthew Colless. Substructure and Dynamics of the Fornax Cluster. *ApJL*, 548(2):L139–L142, February 2001. doi: 10.1086/319113.

Patrick R. Durrell, Patrick Côté, Eric W. Peng, John P. Blakeslee, Laura Ferrarese, J. Christopher Mihos, Thomas H. Puzia, Ariane Lançon, Chengze Liu, Hongxin Zhang, Jean-Charles Cuillandre, Alan McConnachie, Andrés Jordán, Katharine Accetta, Samuel Boissier, Alessandro Boselli, Stéphane Courteau, Pierre-Alain Duc, Eric Emsellem, Stephen Gwyn, Simona Mei, and James E. Taylor. The Next Generation Virgo Cluster Survey. VIII. The Spatial Distribution of Globular Clusters in the Virgo Cluster. *ApJ*, 794(2):103, October 2014. doi: 10.1088/0004-637X/794/2/103.

Gwendolyn M. Eadie, William E. Harris, and Aaron Springford. Clearing the Hurdle: The Mass of Globular Cluster Systems as a Function of Host Galaxy Mass. *ApJ*, 926(2):162, February 2022. doi: 10.3847/1538-4357/ac33b0.

Kareem El-Badry, Eliot Quataert, Daniel R. Weisz, Nick Choksi, and Michael Boylan-Kolchin. The formation and hierarchical assembly of globular cluster populations. *MNRAS*, 482(4):4528–4552, February 2019. doi: 10.1093/mnras/sty3007.

Lydia M. Elias, Laura V. Sales, Peter Creasey, Michael C. Cooper, James S. Bullock, R. Michael Rich, and Lars Hernquist. Stellar halos in Illustris: probing the histories of Milky Way-mass galaxies. *MNRAS*, 479(3):4004–4016, September 2018. doi: 10.1093/mnras/sty1718.

Bruce G. Elmegreen. Globular cluster formation at high density: A model for elemental enrichment with fast recycling of massive-star debris. *The Astrophysical Journal*, 836 (1):80, feb 2017. doi: 10.3847/1538-4357/836/1/80. URL https://doi.org/10.3847/1538-4357/836/1/80.

Eric Emsellem, Remco F. J. van der Burg, Jérémy Fensch, Tereza Jeřábková, Anita Zanella, Adriano Agnello, Michael Hilker, Oliver Müller, Marina Rejkuba, Pierre-Alain Duc, Patrick Durrell, Rebecca Habas, Federico Lelli, Sungsoon Lim, Francine R. Marleau, Eric Peng, and Rubén Sánchez-Janssen. The ultra-diffuse galaxy NGC 1052-DF2 with MUSE. I. Kinematics of the stellar body. *A&A*, 625:A76, May 2019. doi: 10.1051/0004-6361/201834909.

Christoph Engler, Annalisa Pillepich, Gandhali D. Joshi, Dylan Nelson, Anna Pasquali, Eva K. Grebel, Thorsten Lisker, Elad Zinger, Martina Donnari, Federico Marinacci, Mark Vogelsberger, and Lars Hernquist. The distinct stellar-to-halo mass relations of satellite and central galaxies: insights from the IllustrisTNG simulations. *MNRAS*, 500(3):3957–3975, January 2021a. doi: 10.1093/mnras/staa3505.

Christoph Engler, Annalisa Pillepich, Anna Pasquali, Dylan Nelson, Vicente Rodriguez-Gomez, Kun Ting Eddie Chua, Eva K. Grebel, Volker Springel, Federico Marinacci, Rainer Weinberger, Mark Vogelsberger, and Lars Hernquist. The abundance of satellites around Milky Way- and M31-like galaxies with the TNG50 simulation: a matter of diversity. *MNRAS*, 507(3):4211–4240, November 2021b. doi: 10.1093/mnras/stab2437.

R. Errani, J. Peñarrubia, and M. G. Walker. Systematics in virial mass estimators for pressure-supported systems. *MNRAS*, 481:5073–5090, December 2018. doi: 10.1093/mnras/sty2505.

Raphaël Errani, Julio F. Navarro, Rodrigo Ibata, Nicolas Martin, Zhen Yuan, David S. Aguado, Piercarlo Bonifacio, Elisabetta Caffau, Jonay I. González Hernández, Khyati Malhan, Rubén Sánchez-Janssen, Federico Sestito, Else Starkenburg, Guillaume F. Thomas, and Kim A. Venn. The Pristine survey XVIII: C-19: Tidal debris of a dark matter-dominated globular cluster? *arXiv e-prints*, art. arXiv:2203.02513, March 2022.

C. Firmani, E. D'Onghia, V. Avila-Reese, G. Chincarini, and X. Hernández. Evidence of self-interacting cold dark matter from galactic to galaxy cluster scales. *MNRAS*, 315(3): L29–L32, July 2000. doi: 10.1046/j.1365-8711.2000.03555.x.

Ricardo A. Flores and Joel R. Primack. Observational and Theoretical Constraints on Singular Dark Matter Halos. *ApJL*, 427:L1, May 1994. doi: 10.1086/187350.

Duncan A. Forbes. How large are the globular cluster systems of early-type galaxies and do they scale with galaxy halo properties? *MNRAS*, 472(1):L104–L108, November 2017. doi: 10.1093/mnrasl/slx148.

Duncan A. Forbes, Adebusola Alabi, Jean P. Brodie, Aaron J. Romanowsky, Jay Strader, Caroline Foster, Christopher Usher, Lee Spitler, Sabine Bellstedt, Nicola Pastorello, Alexa Villaume, Asher Wasserman, and Vincenzo Pota. The SLUGGS Survey: A Catalog of Over 4000 Globular Cluster Radial Velocities in 27 Nearby Early-type Galaxies. *AJ*, 153 (3):114, March 2017. doi: 10.3847/1538-3881/153/3/114.

Duncan A. Forbes, Justin I. Read, Mark Gieles, and Michelle L. M. Collins. Extending the globular cluster system-halo mass relation to the lowest galaxy masses. *MNRAS*, 481(4): 5592–5605, December 2018. doi: 10.1093/mnras/sty2584.

Duncan A. Forbes, Adebusola Alabi, Aaron J. Romanowsky, Jean P. Brodie, and Nobuo Arimoto. Globular clusters in Coma cluster ultra-diffuse galaxies (UDGs): evidence for two types of UDG? *MNRAS*, 492(4):4874–4883, March 2020. doi: 10.1093/mnras/staa180.

Duncan A. Forbes, Jonah S. Gannon, Aaron J. Romanowsky, Adebusola Alabi, Jean P. Brodie, Warrick J. Couch, and Anna Ferré-Mateu. Stellar velocity dispersion and dynamical mass of the ultra diffuse galaxy NGC 5846_UDG1 from the keck cosmic web imager. *MNRAS*, 500(1):1279–1284, January 2021. doi: 10.1093/mnras/staa3289.

Jonah S. Gannon, Bililign T. Dullo, Duncan A. Forbes, R. Michael Rich, Javier Román, Warrick J. Couch, Jean P. Brodie, Anna Ferré-Mateu, Adebusola Alabi, and Jeremy Mould. A photometric and kinematic analysis of UDG1137+16 (dw1137+16): Probing ultradiffuse galaxy formation in a group environment. *MNRAS*, 502(3):3144–3157, April 2021. doi: 10.1093/mnras/stab277.

Jonah S. Gannon, Duncan A. Forbes, Aaron J. Romanowsky, Anna Ferré-Mateu, Warrick J. Couch, Jean P. Brodie, Song Huang, Steven R. Janssens, and Nobuhiro Okabe. Ultra-diffuse galaxies in the perseus cluster: comparing galaxy properties with globular cluster system richness. *MNRAS*, 510(1):946–958, February 2022. doi: 10.1093/mnras/stab3297.

Jonah S. Gannon, Duncan A. Forbes, Jean P. Brodie, Aaron J. Romanowsky, Warrick J. Couch, and Anna Ferré-Mateu. Keck spectroscopy of the coma cluster ultra-diffuse galaxy Y358: dynamical mass in a wider context. *MNRAS*, 518(3):3653–3666, January 2023. doi: 10.1093/mnras/stac3264.

S. Genel, M. Vogelsberger, V. Springel, D. Sijacki, D. Nelson, G. Snyder, V. Rodriguez-Gomez, P. Torrey, and L. Hernquist. Introducing the Illustris project: the evolution of galaxy populations across cosmic time. *MNRAS*, 445:175–200, November 2014. doi: 10.1093/mnras/stu1654.

Iskren Y. Georgiev, Thomas H. Puzia, Paul Goudfrooij, and Michael Hilker. Globular cluster systems in nearby dwarf galaxies - III. Formation efficiencies of old globular clusters. *MNRAS*, 406(3):1967–1984, August 2010. doi: 10.1111/j.1365-2966.2010.16802.x.

M. Girardi, R. Barrena, W. Boschin, and E. Ellingson. Cluster Abell 520: a perspective based on member galaxies. A cluster forming at the crossing of three filaments? *A&A*, 491(2):379–395, November 2008. doi: 10.1051/0004-6361:200810549.

Michael Y. Grudić, Dávid Guszejnov, Philip F. Hopkins, Stella S. R. Offner, and Claude-André Faucher-Giguère. STARFORGE: Towards a comprehensive numerical model of star cluster formation and feedback. *MNRAS*, 506(2):2199–2231, September 2021. doi: 10.1093/mnras/stab1347.

Charles R. Harris, K. Jarrod Millman, Stéfan J. van der Walt, Ralf Gommers, Pauli Virtanen, David Cournapeau, Eric Wieser, Julian Taylor, Sebastian Berg, Nathaniel J. Smith, Robert Kern, Matti Picus, Stephan Hoyer, Marten H. van Kerkwijk, Matthew Brett, Allan Haldane, Jaime Fernández del Río, Mark Wiebe, Pearu Peterson, Pierre Gérard-Marchant, Kevin Sheppard, Tyler Reddy, Warren Weckesser, Hameer Abbasi, Christoph Gohlke, and Travis E. Oliphant. Array programming with NumPy. *Nature*, 585(7825):357–362, September 2020. doi: 10.1038/s41586-020-2649-2. URL https://doi.org/10.1038/s41586-020-2649-2.

W. E. Harris and S. van den Bergh. Globular clusters in galaxies beyond the local group. I. New cluster systems in selected northern ellipticals. *AJ*, 86:1627–1642, November 1981. doi: 10.1086/113047.

William E. Harris, Gretchen L. H. Harris, and Matthew Alessi. A CATALOG OF GLOBULAR CLUSTER SYSTEMS: WHAT DETERMINES THE SIZE OF a GALAXY's GLOBULAR CLUSTER POPULATION? *The Astrophysical Journal*, 772(2):82, jul 2013. doi: 10.1088/0004-637x/772/2/82. URL https://doi.org/10.1088/0004-637x/772/2/82.

William E. Harris, Gretchen L. Harris, and Michael J. Hudson. Dark Matter Halos in Galaxies and Globular Cluster Populations. II. Metallicity and Morphology. *ApJ*, 806(1): 36, June 2015. doi: 10.1088/0004-637X/806/1/36.

Eric Hayashi and Julio F. Navarro. Hiding cusps in cores: kinematics of disc galaxies in triaxial dark matter haloes. *MNRAS*, 373(3):1117–1124, December 2006. doi: 10.1111/j.1365-2966.2006.10927.x.

Kohei Hayashi and Shigeki Inoue. Effects of mass models on dynamical mass estimate: the case of ultradiffuse galaxy NGC 1052-DF2. *MNRAS*, 481(1):L59–L63, November 2018. doi: 10.1093/mnrasl/sly162.

Lars Hernquist. An Analytical Model for Spherical Galaxies and Bulges. *ApJ*, 356:359, June 1990. doi: 10.1086/168845.

G. Hinshaw, D. Larson, E. Komatsu, D. N. Spergel, C. L. Bennett, J. Dunkley, M. R. Nolta, M. Halpern, R. S. Hill, and N. Odegard. Nine-year Wilkinson Microwave Anisotropy Probe (WMAP) Observations: Cosmological Parameter Results. *ApJS*, 208(2):19, Oct 2013. doi: 10.1088/0067-0049/208/2/19.

David W. Hogg, Jo Bovy, and Dustin Lang. Data analysis recipes: Fitting a model to data. *arXiv e-prints*, art. arXiv:1008.4686, August 2010.

Michael J. Hudson and Bailey Robison. The correlation between the sizes of globular cluster systems and their host dark matter haloes. *MNRAS*, 477(3):3869–3885, July 2018. doi: 10.1093/mnras/sty844.

Michael J. Hudson, Gretchen L. Harris, and William E. Harris. DARK MATTER HALOS IN GALAXIES AND GLOBULAR CLUSTER POPULATIONS. *The Astrophysical Journal*, 787(1):L5, apr 2014. doi: 10.1088/2041-8205/787/1/l5. URL https://doi.org/10.1088/2041-8205/787/1/l5.

Michael J. Hudson, Bryan R. Gillis, Jean Coupon, Hendrik Hildebrandt, Thomas Erben, Catherine Heymans, Henk Hoekstra, Thomas D. Kitching, Yannick Mellier, Lance Miller, Ludovic Van Waerbeke, Christopher Bonnett, Liping Fu, Konrad Kuijken, Barnaby Rowe, Tim Schrabback, Elisabetta Semboloni, Edo van Uitert, and Malin Velander. CFHTLenS: co-evolution of galaxies and their dark matter haloes. *MNRAS*, 447(1):298–314, February 2015. doi: 10.1093/mnras/stu2367.

J. D. Hunter. Matplotlib: A 2d graphics environment. *Computing in Science & Engineering*, 9(3):90–95, 2007. doi: 10.1109/MCSE.2007.55.

Steven R. Janssens, Aaron J. Romanowsky, Roberto Abraham, Jean P. Brodie, Warrick J. Couch, Duncan A. Forbes, Seppo Laine, David Martínez-Delgado, and Pieter G. van Dokkum. The globular clusters and star formation history of the isolated, quiescent ultra-diffuse galaxy DGSAT I. *MNRAS*, 517(1):858–871, November 2022. doi: 10.1093/mnras/stac2717.

Fangzhou Jiang, Avishai Dekel, Jonathan Freundlich, Aaron J. Romanowsky, Aaron A. Dutton, Andrea V. Macciò, and Arianna Di Cintio. Formation of ultra-diffuse galaxies in the field and in galaxy groups. *MNRAS*, 487(4):5272–5290, August 2019. doi: 10.1093/mnras/stz1499.

Michael G. Jones, Ananthan Karunakaran, Paul Bennet, David J. Sand, Kristine Spekkens, Burçin Mutlu-Pakdil, Denija Crnojević, Steven Janowiecki, Lukas Leisman, and Catherine E. Fielder. Gas-rich, Field Ultra-diffuse Galaxies Host Few Gobular Clusters. *ApJL*, 942(1):L5, January 2023. doi: 10.3847/2041-8213/acaaab.

Andrés Jordán, Dean E. McLaughlin, Patrick Côté, Laura Ferrarese, Eric W. Peng, Simona Mei, Daniela Villegas, David Merritt, John L. Tonry, and Michael J. West. The ACS Virgo Cluster Survey. XII. The Luminosity Function of Globular Clusters in Early-Type Galaxies. *ApJS*, 171(1):101–145, July 2007. doi: 10.1086/516840.

Gandhali D. Joshi, Annalisa Pillepich, Dylan Nelson, Federico Marinacci, Volker Springel, Vicente Rodriguez-Gomez, Mark Vogelsberger, and Lars Hernquist. The fate of disc galaxies in IllustrisTNG clusters. *MNRAS*, 496(3):2673–2703, August 2020. doi: 10.1093/mnras/staa1668.

Gandhali D. Joshi, Annalisa Pillepich, Dylan Nelson, Elad Zinger, Federico Marinacci, Volker Springel, Mark Vogelsberger, and Lars Hernquist. The cumulative star formation histories of dwarf galaxies with TNG50. I: environment-driven diversity and connection to quenching. *MNRAS*, 508(2):1652–1674, December 2021. doi: 10.1093/mnras/stab2573.

Junais, S. Boissier, A. Boselli, M. Boquien, A. Longobardi, Y. Roehlly, P. Amram, M. Fossati, J. C. Cuillandre, S. Gwyn, L. Ferrarese, P. Côté, J. Roediger, S. Lim, E. W. Peng, G. Hensler, G. Trinchieri, J. Koda, and N. Prantzos. A Virgo Environmental Survey Tracing Ionised Gas Emission (VESTIGE). X. Formation of a red ultra-diffuse galaxy and an almost dark galaxy during a ram-pressure stripping event. *A&A*, 650:A99, June 2021. doi: 10.1051/0004-6361/202040185.

I. D. Karachentsev and O. G. Nasonova. The observed infall of galaxies towards the Virgo cluster. *MNRAS*, 405(2):1075–1083, June 2010. doi: 10.1111/j.1365-2966.2010.16501.x.

Igor D. Karachentsev, R. Brent Tully, Andrew Dolphin, Margarita Sharina, Lidia Makarova, Dmitry Makarov, Shoko Sakai, Edward J. Shaya, Olga G. Kashibadze, Valentina Karachentseva, and Luca Rizzi. The Hubble Flow around the Centaurus A/M83 Galaxy Complex. *AJ*, 133(2):504–517, February 2007. doi: 10.1086/510125.

Olga G. Kashibadze, Igor D. Karachentsev, and Valentina E. Karachentseva. Structure and kinematics of the Virgo cluster of galaxies. *A&A*, 635:A135, March 2020. doi: 10.1051/0004-6361/201936172.

Benjamin W. Keller, J. M. Diederik Kruijssen, Joel Pfeffer, Marta Reina-Campos, Nate Bastian, Sebastian Trujillo-Gomez, Meghan E. Hughes, and Robert A. Crain. Where did the globular clusters of the Milky Way form? Insights from the E-MOSAICS simulations. *MNRAS*, 495(4):4248–4267, July 2020. doi: 10.1093/mnras/staa1439.

Ji-hoon Kim, Xiangcheng Ma, Michael Y Grudić, Philip F Hopkins, Christopher C Hayward, Andrew Wetzel, Claude-André Faucher-Giguère, Dušan Kereš, Shea Garrison-Kimmel, and Norman Murray. Formation of globular cluster candidates in merging proto-galaxies at high redshift: a view from the FIRE cosmological simulations. *Monthly Notices of the Royal Astronomical Society*, 474(3):4232–4244, 11 2017. ISSN 0035-8711. doi: 10.1093/mnras/stx2994. URL https://doi.org/10.1093/mnras/stx2994.

Evan N. Kirby, James S. Bullock, Michael Boylan-Kolchin, Manoj Kaplinghat, and Judith G. Cohen. The dynamics of isolated Local Group galaxies. *MNRAS*, 439(1):1015–1027, March 2014. doi: 10.1093/mnras/stu025.

Anatoly Klypin, Andrey V. Kravtsov, Octavio Valenzuela, and Francisco Prada. Where Are the Missing Galactic Satellites? *ApJ*, 522(1):82–92, September 1999. doi: 10.1086/307643.

Youkyung Ko, Ho Seong Hwang, Myung Gyoon Lee, Hong Soo Park, Sungsoon Lim, Jubee Sohn, In Sung Jang, Narae Hwang, and Byeong-Gon Park. To the Edge of M87 and Beyond: Spectroscopy of Intracluster Globular Clusters and Ultracompact Dwarfs in the Virgo Cluster. *ApJ*, 835(2):212, February 2017. doi: 10.3847/1538-4357/835/2/212.

Youkyung Ko, Eric W. Peng, Patrick Côté, Laura Ferrarese, Chengze Liu, Alessia Longobardi, Ariane Lançon, Roberto P. Muñoz, Thomas H. Puzia, Karla A. Alamo-Martínez, Laura V. Sales, Felipe Ramos-Almendares, Mario G. Abadi, Myung Gyoon Lee, Ho Seong Hwang, Nelson Caldwell, John P. Blakeslee, Alessandro Boselli, Jean-Charles Cuillandre, Pierre-Alain Duc, Susana Eyheramendy, Puragra Guhathakurta, Stephen Gwyn, Andrés Jordán, Sungsoon Lim, Rubén Sánchez-Janssen, and Elisa Toloba. The Next Generation Virgo Cluster Survey. XXXIII. Stellar Population Gradients in the Virgo Cluster Core Globular Cluster System. *arXiv e-prints*, art. arXiv:2204.05318, April 2022.

Jin Koda, Masafumi Yagi, Hitomi Yamanoi, and Yutaka Komiyama. Approximately a Thousand Ultra-diffuse Galaxies in the Coma Cluster. *ApJL*, 807(1):L2, July 2015. doi: 10.1088/2041-8205/807/1/L2.

Demao Kong, Manoj Kaplinghat, Hai-Bo Yu, Filippo Fraternali, and Pavel E. Mancera Piña. The Odd Dark Matter Halos of Isolated Gas-rich Ultradiffuse Galaxies. *ApJ*, 936(2):166, September 2022. doi: 10.3847/1538-4357/ac8875.

Andrey V. Kravtsov and Oleg Y. Gnedin. Formation of Globular Clusters in Hierarchical Cosmology. *ApJ*, 623(2):650–665, April 2005. doi: 10.1086/428636.

J. M. Diederik Kruijssen. Globular clusters as the relics of regular star formation in 'normal' high-redshift galaxies. *Monthly Notices of the Royal Astronomical Society*, 454(2):1658–1686, 10 2015. ISSN 0035-8711. doi: 10.1093/mnras/stv2026. URL https://doi.org/10.1093/mnras/stv2026.

J. M. Diederik Kruijssen and Andrew P. Cooper. The initial mass spectrum of old globular clusters in dwarf galaxies. *Monthly Notices of the Royal Astronomical Society*, 420(1): 340–345, 01 2012. ISSN 0035-8711. doi: 10.1111/j.1365-2966.2011.20037.x. URL https://doi.org/10.1111/j.1365-2966.2011.20037.x.

J. M. Diederik Kruijssen, F. Inti Pelupessy, Henny J. G. L. M. Lamers, Simon F. Portegies Zwart, and Vincent Icke. Modelling the formation and evolution of star cluster populations in galaxy simulations. *MNRAS*, 414(2):1339–1364, June 2011. doi: 10.1111/j.1365-2966.2011.18467.x.

J. M. Diederik Kruijssen, F. Inti Pelupessy, Henny J. G. L. M. Lamers, Simon F. Portegies Zwart, Nate Bastian, and Vincent Icke. Formation versus destruction: the evolution of the star cluster population in galaxy mergers. *MNRAS*, 421(3):1927–1941, April 2012. doi: 10.1111/j.1365-2966.2012.20322.x.

Antonio La Marca, Enrichetta Iodice, Michele Cantiello, Duncan A. Forbes, Marina Rejkuba, Michael Hilker, Magda Arnaboldi, Laura Greggio, Chiara Spiniello, Steffen Mieske, Aku Venhola, Marilena Spavone, Giuseppe D'Ago, Maria Angela Raj, Rossella Ragusa, Marco Mirabile, Roberto Rampazzo, Reynier Peletier, Maurizio Paolillo, Nelvy Choque Challapa, and Pietro Schipani. Galaxy populations in the Hydra I cluster from the VEGAS survey II. The ultra-diffuse galaxy population. *arXiv e-prints*, art. arXiv:2206.07385, June 2022.

Natalia Lahén, Thorsten Naab, Peter H. Johansson, Bruce Elmegreen, Chia-Yu Hu, and Stefanie Walch. The formation of low-metallicity globular clusters in dwarf galaxy mergers. *The Astrophysical Journal*, 879(2):L18, jul 2019. doi: 10.3847/2041-8213/ab2a13. URL https://doi.org/10.3847/2041-8213/ab2a13.

Natalia Lahén, Thorsten Naab, Peter H. Johansson, Bruce Elmegreen, Chia-Yu Hu, Stefanie Walch, Ulrich P. Steinwandel, and Benjamin P. Moster. The GRIFFIN Project—Formation of Star Clusters with Individual Massive Stars in a Simulated Dwarf Galaxy Starburst. *ApJ*, 891(1):2, March 2020. doi: 10.3847/1538-4357/ab7190.

Siu Kwan Lam, Antoine Pitrou, and Stanley Seibert. Numba: A llvm-based python jit compiler. In *Proceedings of the Second Workshop on the LLVM Compiler Infrastructure in HPC*, pages 1–6, 2015.

C. F. P. Laporte, M. G. Walker, and J. Penarrubia. Measuring the slopes of mass profiles for dwarf spheroidals in triaxial cold dark matter potentials. *MNRAS*, 433:L54–L58, June 2013a. doi: 10.1093/mnrasl/slt057.

C. F. P. Laporte, A. Agnello, and J. F. Navarro. Reconciling mass estimates of ultradiffuse galaxies. *MNRAS*, 484:245–251, March 2019. doi: 10.1093/mnras/sty2891.

Chervin F. P. Laporte, Simon D. M. White, Thorsten Naab, and Liang Gao. The growth in size and mass of cluster galaxies since z = 2. *MNRAS*, 435(2):901–909, October 2013b. doi: 10.1093/mnras/stt912.

Søren S. Larsen, Aaron J. Romanowsky, Jean P. Brodie, and Asher Wasserman. An extremely metal-deficient globular cluster in the Andromeda Galaxy. *Science*, 370(6519): 970–973, November 2020. doi: 10.1126/science.abb1970.

Jeong Hwan Lee, Jisu Kang, Myung Gyoon Lee, and In Sung Jang. The Nature of Ultra-diffuse Galaxies in Distant Massive Galaxy Clusters: A370 in the Hubble Frontier Fields. *ApJ*, 894(1):75, May 2020. doi: 10.3847/1538-4357/ab8632.

Myung Gyoon Lee, Hong Soo Park, and Ho Seong Hwang. Detection of a Large-Scale Structure of Intracluster Globular Clusters in the Virgo Cluster. *Science*, 328(5976):334, April 2010. doi: 10.1126/science.1186496.

Myung Gyoon Lee, Jisu Kang, Jeong Hwan Lee, and In Sung Jang. Detection of a Large Population of Ultradiffuse Galaxies in Massive Galaxy Clusters: Abell S1063 and Abell 2744. *ApJ*, 844(2):157, August 2017. doi: 10.3847/1538-4357/aa78fb.

Myung Gyoon Lee, Jang Ho Bae, and In Sung Jang. Detection of Intracluster Globular Clusters in the First JWST Images of the Gravitational Lens Cluster SMACS J0723.3-7327 at z = 0.39. *ApJL*, 940(1):L19, November 2022. doi: 10.3847/2041-8213/ac990b.

Nathan W. C. Leigh and Giacomo Fragione. A New Method to Constrain the Origins of Dark-matter-free Galaxies and Their Unusual Globular Clusters. *ApJ*, 892(1):32, March 2020. doi: 10.3847/1538-4357/ab7a8f.

Lukas Leisman, Martha P. Haynes, Steven Janowiecki, Gregory Hallenbeck, Gyula Józsa, Riccardo Giovanelli, Elizabeth A. K. Adams, David Bernal Neira, John M. Cannon, William F. Janesh, Katherine L. Rhode, and John J. Salzer. (Almost) Dark Galaxies in the ALFALFA Survey: Isolated H I-bearing Ultra-diffuse Galaxies. *ApJ*, 842(2):133, June 2017. doi: 10.3847/1538-4357/aa7575.

Geraint F. Lewis, Brendon J. Brewer, and Zhen Wan. The globular cluster population of NGC 1052-DF2: evidence for rotation. *MNRAS*, 491(1):L1–L5, January 2020. doi: 10.1093/mnrasl/slz157.

Chao Li, Ling Zhu, R. J. Long, Shude Mao, Eric W. Peng, Marc Sarzi, Glenn van de Ven, Hongxin Zhang, Rui Guo, Xiangxiang Xue, Alessia Longobardi, Patrick Côté, Laura Ferrarese, Chengze Liu, Stephen Gwyn, Sungsoon Lim, and Youkyung Ko. A discrete chemo-dynamical model of M87's globular clusters: Kinematics extending to ∼400 kpc. *MNRAS*, 492(2):2775–2795, February 2020. doi: 10.1093/mnras/staa027.

Dayi David Li, Gwendolyn M. Eadie, Roberto Abraham, Patrick E. Brown, William E. Harris, Steven R. Janssens, Aaron J. Romanowsky, Pieter van Dokkum, and Shany Danieli. Light from the Darkness: Detecting Ultra-diffuse Galaxies in the Perseus Cluster through Over-densities of Globular Clusters with a Log-Gaussian Cox Process. *ApJ*, 935(1):3, August 2022. doi: 10.3847/1538-4357/ac7b22.

Hui Li and Oleg Y. Gnedin. Modeling the Formation of Globular Cluster Systems in the Virgo Cluster. *ApJ*, 796(1):10, November 2014. doi: 10.1088/0004-637X/796/1/10.

Hui Li, Oleg Y. Gnedin, Nickolay Y. Gnedin, Xi Meng, Vadim A. Semenov, and Andrey V. Kravtsov. Star Cluster Formation in Cosmological Simulations. I. Properties of Young Clusters. *ApJ*, 834(1):69, January 2017. doi: 10.3847/1538-4357/834/1/69.

Hui Li, Mark Vogelsberger, Greg L. Bryan, Federico Marinacci, Laura V. Sales, and Paul Torrey. Formation and evolution of young massive clusters in galaxy mergers: a SMUGGLE view. *arXiv e-prints*, art. arXiv:2109.10356, September 2021.

Sungsoon Lim, Eric W. Peng, Patrick Côté, Laura V. Sales, Mark den Brok, John P. Blakeslee, and Puragra Guhathakurta. The Globular Cluster Systems of Ultra-diffuse Galaxies in the Coma Cluster. *ApJ*, 862(1):82, July 2018. doi: 10.3847/1538-4357/aacb81.

Sungsoon Lim, Patrick Côté, Eric W. Peng, Laura Ferrarese, Joel C. Roediger, Patrick R. Durrell, J. Christopher Mihos, Kaixiang Wang, S. D. J. Gwyn, Jean-Charles Cuillandre, Chengze Liu, Rubén Sánchez-Janssen, Elisa Toloba, Laura V. Sales, Puragra Guhathakurta, Ariane Lançon, and Thomas H. Puzia. The Next Generation Virgo Cluster Survey (NGVS). XXX. Ultra-diffuse Galaxies and Their Globular Cluster Systems. *ApJ*, 899(1):69, August 2020. doi: 10.3847/1538-4357/aba433.

Alessia Longobardi, Eric W. Peng, Patrick Côté, J. Christopher Mihos, Laura Ferrarese, Thomas H. Puzia, Ariane Lançon, Hong-Xin Zhang, Roberto P. Muñoz, John P. Blakeslee, Puragra Guhathakurta, Patrick R. Durrell, Rúben Sánchez-Janssen, Elisa Toloba, Andrés Jordán, Susana Eyheramendy, Jean-Charles Cuilland re, Stephen D. J. Gwyn, Alessandro Boselli, Pierre-Alain Duc, Chengze Liu, Karla Alamo-Martínez, Mathieu Powalka, and Sungsoon Lim. The Next Generation Virgo Cluster Survey (NGVS). XXXI. The Kinematics of Intracluster Globular Clusters in the Core of the Virgo Cluster. *ApJ*, 864 (1):36, September 2018. doi: 10.3847/1538-4357/aad3d2.

Jennifer M. Lotz, Bryan W. Miller, and Henry C. Ferguson. The Colors of Dwarf Elliptical Galaxy Globular Cluster Systems, Nuclei, and Stellar Halos. *ApJ*, 613(1):262–278, September 2004. doi: 10.1086/422871.

Aaron D. Ludlow, Sownak Bose, Raúl E. Angulo, Lan Wang, Wojciech A. Hellwing, Julio F. Navarro, Shaun Cole, and Carlos S. Frenk. The mass-concentration-redshift relation of cold and warm dark matter haloes. *MNRAS*, 460(2):1214–1232, August 2016. doi: 10.1093/mnras/stw1046.

Xiangcheng Ma, Michael Y. Grudić, Eliot Quataert, Philip F. Hopkins, Claude-André Faucher-Giguère, Michael Boylan-Kolchin, Andrew Wetzel, Ji-hoon Kim, Norman Murray, and Dušan Kereš. Self-consistent proto-globular cluster formation in cosmological simulations of high-redshift galaxies. *MNRAS*, 493(3):4315–4332, April 2020. doi: 10.1093/mnras/staa527.

Andrea V. Macciò, Daniel Huterer Prats, Keri L. Dixon, Tobias Buck, Stefan Waterval, Nikhil Arora, Stéphane Courteau, and Xi Kang. Creating a galaxy lacking dark matter in a dark matter dominated universe. *arXiv e-prints*, art. arXiv:2010.02245, October 2020.

Andrea V. Macciò, Daniel Huterer Prats, Keri L. Dixon, Tobias Buck, Stefan Waterval, Nikhil Arora, Stéphane Courteau, and Xi Kang. Creating a galaxy lacking dark matter in a dark matter-dominated universe. *MNRAS*, 501(1):693–700, February 2021. doi: 10.1093/mnras/staa3716.

Juan P. Madrid, Conor R. O'Neill, Alexander T. Gagliano, and Joshua R. Marvil. A Wide-field Map of Intracluster Globular Clusters in Coma. *ApJ*, 867(2):144, November 2018. doi: 10.3847/1538-4357/aae206.

Pavel E. Mancera Piña, Filippo Fraternali, Kyle A. Oman, Elizabeth A. K. Adams, Cecilia Bacchini, Antonino Marasco, Tom Oosterloo, Gabriele Pezzulli, Lorenzo Posti, Lukas Leisman, John M. Cannon, Enrico M. di Teodoro, Lexi Gault, Martha P. Haynes, Kameron Reiter, Katherine L. Rhode, John J. Salzer, and Nicholas J. Smith. Robust H I kinematics of gas-rich ultra-diffuse galaxies: hints of a weak-feedback formation scenario. *MNRAS*, 495(4):3636–3655, May 2020. doi: 10.1093/mnras/staa1256.

Federico Marinacci, Mark Vogelsberger, Rüdiger Pakmor, Paul Torrey, Volker Springel, Lars Hernquist, Dylan Nelson, Rainer Weinberger, Annalisa Pillepich, Jill Naiman, and Shy Genel. First results from the IllustrisTNG simulations: radio haloes and magnetic fields. *MNRAS*, 480(4):5113–5139, November 2018. doi: 10.1093/mnras/sty2206.

Federico Marinacci, Laura V. Sales, Mark Vogelsberger, Paul Torrey, and Volker Springel. Simulating the interstellar medium and stellar feedback on a moving mesh: implementation and isolated galaxies. *MNRAS*, 489(3):4233–4260, November 2019. doi: 10.1093/mnras/stz2391.

Francine R. Marleau, Rebecca Habas, Mélina Poulain, Pierre-Alain Duc, Oliver Müller, Sungsoon Lim, Patrick R. Durrell, Rubén Sánchez-Janssen, Sanjaya Paudel, Syeda Lammim Ahad, Abhishek Chougule, Michal Bílek, and Jérémy Fensch. Ultra diffuse galaxies in the MATLAS low-to-moderate density fields. *A&A*, 654:A105, October 2021. doi: 10.1051/0004-6361/202141432.

David J. E. Marsh and Ana-Roxana Pop. Axion dark matter, solitons and the cusp-core problem. *MNRAS*, 451(3):2479–2492, August 2015. doi: 10.1093/mnras/stv1050.

N. F. Martin, M. L. M. Collins, N. Longeard, and E. Tollerud. Current Velocity Data on Dwarf Galaxy NGC 1052-DF2 do not Constrain it to Lack Dark Matter. *ApJL*, 859:L5, May 2018. doi: 10.3847/2041-8213/aac216.

Nicolas F. Martin, Kim A. Venn, David S. Aguado, Else Starkenburg, Jonay I. González Hernández, Rodrigo A. Ibata, Piercarlo Bonifacio, Elisabetta Caffau, Federico Sestito, Anke Arentsen, Carlos Allende Prieto, Raymond G. Carlberg, Sébastien Fabbro, Morgan Fouesneau, Vanessa Hill, Pascale Jablonka, Georges Kordopatis, Carmela Lardo, Khyati Malhan, Lyudmila I. Mashonkina, Alan W. McConnachie, Julio F. Navarro, Rubén Sánchez-Janssen, Guillaume F. Thomas, Zhen Yuan, and Alessio Mucciarelli. A stellar stream remnant of a globular cluster below the metallicity floor. *Nature*, 601(7891):45–48, January 2022. doi: 10.1038/s41586-021-04162-2.

Ignacio Martín-Navarro, Aaron J. Romanowsky, Jean P. Brodie, Anna Ferré-Mateu, Adebusola Alabi, Duncan A. Forbes, Margarita Sharina, Alexa Villaume, Viraj Pandya, and David Martinez-Delgado. Extreme chemical abundance ratio suggesting an exotic origin for an ultradiffuse galaxy. *MNRAS*, 484(3):3425–3433, April 2019. doi: 10.1093/mnras/stz252.

David Martínez-Delgado, Ronald Läsker, Margarita Sharina, Elisa Toloba, Jürgen Fliri, Rachael Beaton, David Valls-Gabaud, Igor D. Karachentsev, Taylor S. Chonis, Eva K. Grebel, Duncan A. Forbes, Aaron J. Romanowsky, J. Gallego-Laborda, Karel Teuwen, M. A. Gómez-Flechoso, Jie Wang, Puragra Guhathakurta, Serafim Kaisin, and Nhung Ho. Discovery of an Ultra-diffuse Galaxy in the Pisces–Perseus Supercluster. *AJ*, 151(4): 96, April 2016. doi: 10.3847/0004-6256/151/4/96.

J. Christopher Mihos, Patrick R. Durrell, Laura Ferrarese, John J. Feldmeier, Patrick Côté, Eric W. Peng, Paul Harding, Chengze Liu, Stephen Gwyn, and Jean-Charles Cuillandre. Galaxies at the Extremes: Ultra-diffuse Galaxies in the Virgo Cluster. *ApJL*, 809(2):L21, August 2015. doi: 10.1088/2041-8205/809/2/L21.

I. F. Mirabel, H. Dottori, and D. Lutz. Genesis of a dwarf galaxy from the debris of the Antennae. *A&A*, 256:L19–L22, March 1992.

Pouria A. Mistani, Laura V. Sales, Annalisa Pillepich, Rubén Sanchez-Janssen, Mark Vogelsberger, Dylan Nelson, Vicente Rodriguez-Gomez, Paul Torrey, and Lars Hernquist. On the assembly of dwarf galaxies in clusters and their efficient formation of globular clusters. *MNRAS*, 455(3):2323–2336, January 2016. doi: 10.1093/mnras/stv2435.

Matteo Monelli and Ignacio Trujillo. The TRGB Distance to the Second Galaxy "Missing Dark Matter": Evidence for Two Groups of Galaxies at 13.5 and 19 Mpc in the Line of Sight of NGC 1052. *ApJL*, 880(1):L11, July 2019. doi: 10.3847/2041-8213/ab2fd2.

Mireia Montes, Raúl Infante-Sainz, Alberto Madrigal-Aguado, Javier Román, Matteo Monelli, Alejandro S. Borlaff, and Ignacio Trujillo. The galaxy "missing dark matter" NGC1052-DF4 is undergoing tidal disruption. *arXiv e-prints*, art. arXiv:2010.09719, October 2020.

Ben Moore. Evidence against dissipation-less dark matter from observations of galaxy haloes. *Nature*, 370(6491):629–631, August 1994. doi: 10.1038/370629a0.

Jorge Moreno, Shany Danieli, James S. Bullock, Robert Feldmann, Philip F. Hopkins, Onur çatmabacak, Alexander Gurvich, Alexandres Lazar, Courtney Klein, Cameron B. Hummels, Zachary Hafen, Francisco J. Mercado, Sijie Yu, Fangzhou Jiang, Coral Wheeler, Andrew Wetzel, Daniel Anglés-Alcázar, Michael Boylan-Kolchin, Eliot Quataert, Claude-André Faucher-Giguère, and Dušan Kereš. Galaxies lacking dark matter produced by close encounters in a cosmological simulation. *Nature Astronomy*, 6:496–502, April 2022. doi: 10.1038/s41550-021-01598-4.

Lamiya A. Mowla, Kartheik G. Iyer, Guillaume Desprez, Vicente Estrada-Carpenter, Nicholas S. Martis, Gaël Noirot, Ghassan T. Sarrouh, Victoria Strait, Yoshihisa Asada,

Roberto G. Abraham, Gabriel Brammer, Marcin Sawicki, Chris J. Willott, Marusa Bradac, René Doyon, Kate Gould, Adam Muzzin, Camilla Pacifici, Swara Ravindranath, and Johannes Zabl. The Sparkler: Evolved High-Redshift Globular Clusters Captured by JWST. *arXiv e-prints*, art. arXiv:2208.02233, August 2022.

Oliver Müller, Patrick R. Durrell, Francine R. Marleau, Pierre-Alain Duc, Sungsoon Lim, Lorenzo Posti, Adriano Agnello, Rubén Sánchez-Janssen, Mélina Poulain, Rebecca Habas, Eric Emsellem, Sanjaya Paudel, Remco F. J. van der Burg, and Jérémy Fensch. Dwarf Galaxies in the MATLAS Survey: Hubble Space Telescope Observations of the Globular Cluster System in the Ultra-diffuse Galaxy MATLAS-2019. *ApJ*, 923(1):9, December 2021. doi: 10.3847/1538-4357/ac2831.

Jill P. Naiman, Annalisa Pillepich, Volker Springel, Enrico Ramirez-Ruiz, Paul Torrey, Mark Vogelsberger, Rüdiger Pakmor, Dylan Nelson, Federico Marinacci, Lars Hernquist, Rainer Weinberger, and Shy Genel. First results from the IllustrisTNG simulations: a tale of two elements - chemical evolution of magnesium and europium. *MNRAS*, 477(1): 1206–1224, June 2018. doi: 10.1093/mnras/sty618.

Priyamvada Natarajan, Steinn Sigurdsson, and Joseph Silk. Quasar outflows and the formation of dwarf galaxies. *MNRAS*, 298(2):577–582, August 1998. doi: 10.1046/j.1365-8711.1998.01703.x.

Julio F. Navarro, Vincent R. Eke, and Carlos S. Frenk. The cores of dwarf galaxy haloes. *MNRAS*, 283(3):L72–L78, December 1996a. doi: 10.1093/mnras/283.3.L72.

Julio F. Navarro, Carlos S. Frenk, and Simon D. M. White. The Structure of Cold Dark Matter Halos. *ApJ*, 462:563, May 1996b. doi: 10.1086/177173.

D. Nelson, A. Pillepich, S. Genel, M. Vogelsberger, V. Springel, P. Torrey, V. Rodriguez-Gomez, D. Sijacki, G. F. Snyder, B. Griffen, F. Marinacci, L. Blecha, L. Sales, D. Xu, and L. Hernquist. The illustris simulation: Public data release. *Astronomy and Computing*, 13:12–37, November 2015. doi: 10.1016/j.ascom.2015.09.003.

D. Nelson, A. Pillepich, V. Springel, R. Pakmor, R. Weinberger, S. Genel, P. Torrey, M. Vogelsberger, F. Marinacci, and L. Hernquist. First Results from the TNG50 Simulation: Galactic outflows driven by supernovae and black hole feedback. *arXiv e-prints*, February 2019a.

Dylan Nelson, Annalisa Pillepich, Volker Springel, Rainer Weinberger, Lars Hernquist, Rüdiger Pakmor, Shy Genel, Paul Torrey, Mark Vogelsberger, Guinevere Kauffmann, Federico Marinacci, and Jill Naiman. First results from the IllustrisTNG simulations: the galaxy colour bimodality. *MNRAS*, 475(1):624–647, March 2018. doi: 10.1093/mnras/stx3040.

Dylan Nelson, Volker Springel, Annalisa Pillepich, Vicente Rodriguez-Gomez, Paul Torrey, Shy Genel, Mark Vogelsberger, Ruediger Pakmor, Federico Marinacci, Rainer Weinberger, Luke Kelley, Mark Lovell, Benedikt Diemer, and Lars Hernquist. The IllustrisTNG

simulations: public data release. *Computational Astrophysics and Cosmology*, 6(1):2, May 2019b. doi: 10.1186/s40668-019-0028-x.

Kyle A. Oman, Julio F. Navarro, Azadeh Fattahi, Carlos S. Frenk, Till Sawala, Simon D. M. White, Richard Bower, Robert A. Crain, Michelle Furlong, Matthieu Schaller, Joop Schaye, and Tom Theuns. The unexpected diversity of dwarf galaxy rotation curves. *MNRAS*, 452(4):3650–3665, October 2015. doi: 10.1093/mnras/stv1504.

Kyle A. Oman, Antonino Marasco, Julio F. Navarro, Carlos S. Frenk, Joop Schaye, and Alejand ro Benítez-Llambay. Non-circular motions and the diversity of dwarf galaxy rotation curves. *MNRAS*, 482(1):821–847, January 2019. doi: 10.1093/mnras/sty2687.

E. Papastergis, E. A. K. Adams, and A. J. Romanowsky. The HI content of isolated ultra-diffuse galaxies: A sign of multiple formation mechanisms? *A&A*, 601:L10, May 2017. doi: 10.1051/0004-6361/201730795.

Jorge Peñarrubia, Julio F. Navarro, and Alan W. McConnachie. The Tidal Evolution of Local Group Dwarf Spheroidals. *ApJ*, 673(1):226–240, January 2008. doi: 10.1086/523686.

Jorge Peñarrubia, Julio F. Navarro, Alan W. McConnachie, and Nicolas F. Martin. The Signature of Galactic Tides in Local Group Dwarf Spheroidals. *ApJ*, 698(1):222–232, June 2009. doi: 10.1088/0004-637X/698/1/222.

P. J. E. Peebles. Dark matter and the origin of galaxies and globular star clusters. *ApJ*, 277:470–477, February 1984. doi: 10.1086/161714.

E. W. Peng, A. Jordán, P. Côté, J. P. Blakeslee, L. Ferrarese, S. Mei, M. J. West, D. Merritt, M. Milosavljević, and J. L. Tonry. The ACS Virgo Cluster Survey. IX. The Color Distributions of Globular Cluster Systems in Early-Type Galaxies. *ApJ*, 639:95–119, March 2006. doi: 10.1086/498210.

Eric W. Peng and Sungsoon Lim. A Rich Globular Cluster System in Dragonfly 17: Are Ultra-diffuse Galaxies Pure Stellar Halos? *ApJL*, 822(2):L31, May 2016. doi: 10.3847/2041-8205/822/2/L31.

Eric W. Peng, Andrés Jordán, Patrick Côté, Marianne Takamiya, Michael J. West, John P. Blakeslee, Chin-Wei Chen, Laura Ferrarese, Simona Mei, John L. Tonry, and Andrew A. West. The ACS Virgo Cluster Survey. XV. The Formation Efficiencies of Globular Clusters in Early-Type Galaxies: The Effects of Mass and Environment. *ApJ*, 681(1):197–224, July 2008. doi: 10.1086/587951.

Eric W. Peng, Henry C. Ferguson, Paul Goudfrooij, Derek Hammer, John R. Lucey, Ronald O. Marzke, Thomas H. Puzia, David Carter, Marc Balcells, Terry Bridges, Kristin Chiboucas, Carlos del Burgo, Alister W. Graham, Rafael Guzmán, Michael J. Hudson, Ana Matković, David Merritt, Bryan W. Miller, Mustapha Mouhcine, Steven Phillipps, Ray Sharples, Russell J. Smith, Brent Tully, and Gijs Verdoes Kleijn. The HST/ACS

Coma Cluster Survey. IV. Intergalactic Globular Clusters and the Massive Globular Cluster System at the Core of the Coma Galaxy Cluster. *ApJ*, 730(1):23, March 2011. doi: 10.1088/0004-637X/730/1/23.

Joel Pfeffer, J. M. Diederik Kruijssen, Robert A. Crain, and Nate Bastian. The E-MOSAICS project: simulating the formation and co-evolution of galaxies and their star cluster populations. *MNRAS*, 475(4):4309–4346, April 2018. doi: 10.1093/mnras/stx3124.

A. Pillepich, D. Nelson, V. Springel, R. Pakmor, P. Torrey, R. Weinberger, M. Vogelsberger, F. Marinacci, S. Genel, A. van der Wel, and L. Hernquist. First Results from the TNG50 Simulation: The evolution of stellar and gaseous disks across cosmic time. *arXiv e-prints*, February 2019.

Annalisa Pillepich, Dylan Nelson, Lars Hernquist, Volker Springel, Rüdiger Pakmor, Paul Torrey, Rainer Weinberger, Shy Genel, Jill P. Naiman, Federico Marinacci, and Mark Vogelsberger. First results from the IllustrisTNG simulations: the stellar mass content of groups and clusters of galaxies. *MNRAS*, 475(1):648–675, March 2018a. doi: 10.1093/mnras/stx3112.

Annalisa Pillepich, Volker Springel, Dylan Nelson, Shy Genel, Jill Naiman, Rüdiger Pakmor, Lars Hernquist, Paul Torrey, Mark Vogelsberger, Rainer Weinberger, and Federico Marinacci. Simulating galaxy formation with the IllustrisTNG model. *MNRAS*, 473(3):4077–4106, January 2018b. doi: 10.1093/mnras/stx2656.

Juan C. B. Pineda, Christopher C. Hayward, Volker Springel, and Claudia Mendes de Oliveira. Rotation curve fitting and its fatal attraction to cores in realistically simulated galaxy observations. *MNRAS*, 466(1):63–87, April 2017. doi: 10.1093/mnras/stw3004.

Planck Collaboration, Ade, P. A. R., Aghanim, N., Arnaud, M., Ashdown, M., Aumont, J., Baccigalupi, C., Banday, A. J., Barreiro, R. B., Bartlett, J. G., Bartolo, N., Battaner, E., Battye, R., Benabed, K., Benoît, A., Benoit-Lévy, A., Bernard, J.-P., Bersanelli, M., Bielewicz, P., Bock, J. J., Bonaldi, A., Bonavera, L., Bond, J. R., Borrill, J., Bouchet, F. R., Boulanger, F., Bucher, M., Burigana, C., Butler, R. C., Calabrese, E., Cardoso, J.-F., Catalano, A., Challinor, A., Chamballu, A., Chary, R.-R., Chiang, H. C., Chluba, J., Christensen, P. R., Church, S., Clements, D. L., Colombi, S., Colombo, L. P. L., Combet, C., Coulais, A., Crill, B. P., Curto, A., Cuttaia, F., Danese, L., Davies, R. D., Davis, R. J., de Bernardis, P., de Rosa, A., de Zotti, G., Delabrouille, J., Désert, F.-X., Di Valentino, E., Dickinson, C., Diego, J. M., Dolag, K., Dole, H., Donzelli, S., Doré, O., Douspis, M., Ducout, A., Dunkley, J., Dupac, X., Efstathiou, G., Elsner, F., Enßlin, T. A., Eriksen, H. K., Farhang, M., Fergusson, J., Finelli, F., Forni, O., Frailis, M., Fraisse, A. A., Franceschi, E., Frejsel, A., Galeotta, S., Galli, S., Ganga, K., Gauthier, C., Gerbino, M., Ghosh, T., Giard, M., Giraud-Héraud, Y., Giusarma, E., Gjerløw, E., González-Nuevo, J., Górski, K. M., Gratton, S., Gregorio, A., Gruppuso, A., Gudmundsson, J. E., Hamann, J., Hansen, F. K., Hanson, D., Harrison, D. L., Helou, G., Henrot-Versillé, S., Hernández-Monteagudo, C., Herranz, D., Hildebrandt, S. R., Hivon, E., Hobson, M., Holmes, W. A., Hornstrup, A., Hovest, W., Huang, Z., Huffenberger, K. M., Hurier, G., Jaffe, A. H., Jaffe, T. R., Jones, W. C., Juvela, M.,

Keihänen, E., Keskitalo, R., Kisner, T. S., Kneissl, R., Knoche, J., Knox, L., Kunz, M., Kurki-Suonio, H., Lagache, G., Lähteenmäki, A., Lamarre, J.-M., Lasenby, A., Lattanzi, M., Lawrence, C. R., Leahy, J. P., Leonardi, R., Lesgourgues, J., Levrier, F., Lewis, A., Liguori, M., Lilje, P. B., Linden-Vørnle, M., López-Caniego, M., Lubin, P. M., Macías-Pérez, J. F., Maggio, G., Maino, D., Mandolesi, N., Mangilli, A., Marchini, A., Maris, M., Martin, P. G., Martinelli, M., Martínez-González, E., Masi, S., Matarrese, S., McGehee, P., Meinhold, P. R., Melchiorri, A., Melin, J.-B., Mendes, L., Mennella, A., Migliaccio, M., Millea, M., Mitra, S., Miville-Deschênes, M.-A., Moneti, A., Montier, L., Morgante, G., Mortlock, D., Moss, A., Munshi, D., Murphy, J. A., Naselsky, P., Nati, F., Natoli, P., Netterfield, C. B., Nørgaard-Nielsen, H. U., Noviello, F., Novikov, D., Novikov, I., Oxborrow, C. A., Paci, F., Pagano, L., Pajot, F., Paladini, R., Paoletti, D., Partridge, B., Pasian, F., Patanchon, G., Pearson, T. J., Perdereau, O., Perotto, L., Perrotta, F., Pettorino, V., Piacentini, F., Piat, M., Pierpaoli, E., Pietrobon, D., Plaszczynski, S., Pointecouteau, E., Polenta, G., Popa, L., Pratt, G. W., Prézeau, G., Prunet, S., Puget, J.-L., Rachen, J. P., Reach, W. T., Rebolo, R., Reinecke, M., Remazeilles, M., Renault, C., Renzi, A., Ristorcelli, I., Rocha, G., Rosset, C., Rossetti, M., Roudier, G., Rouillé d´Orfeuil, B., Rowan-Robinson, M., Rubiño-Martín, J. A., Rusholme, B., Said, N., Salvatelli, V., Salvati, L., Sandri, M., Santos, D., Savelainen, M., Savini, G., Scott, D., Seiffert, M. D., Serra, P., Shellard, E. P. S., Spencer, L. D., Spinelli, M., Stolyarov, V., Stompor, R., Sudiwala, R., Sunyaev, R., Sutton, D., Suur-Uski, A.-S., Sygnet, J.-F., Tauber, J. A., Terenzi, L., Toffolatti, L., Tomasi, M., Tristram, M., Trombetti, T., Tucci, M., Tuovinen, J., Türler, M., Umana, G., Valenziano, L., Valiviita, J., Van Tent, F., Vielva, P., Villa, F., Wade, L. A., Wandelt, B. D., Wehus, I. K., White, M., White, S. D. M., Wilkinson, A., Yvon, D., Zacchei, A., and Zonca, A. Planck 2015 results - xiii. cosmological parameters. *A&A*, 594:A13, 2016. doi: 10.1051/0004-6361/201525830. URL https://doi.org/10.1051/0004-6361/201525830.

Andrew Pontzen and Fabio Governato. How supernova feedback turns dark matter cusps into cores. *MNRAS*, 421(4):3464–3471, April 2012. doi: 10.1111/j.1365-2966.2012.20571.x.

Simon F. Portegies Zwart, Stephen L. W. McMillan, and Mark Gieles. Young Massive Star Clusters. *ARA&A*, 48:431–493, September 2010. doi: 10.1146/annurev-astro-081309-130834.

Francisco Prada, Mayrita Vitvitska, Anatoly Klypin, Jon A. Holtzman, David J. Schlegel, Eva K. Grebel, H. W. Rix, J. Brinkmann, T. A. McKay, and I. Csabai. Observing the Dark Matter Density Profile of Isolated Galaxies. *ApJ*, 598(1):260–271, November 2003. doi: 10.1086/378669.

José L. Prieto and Oleg Y. Gnedin. Dynamical Evolution of Globular Clusters in Hierarchical Cosmology. *ApJ*, 689(2):919–935, December 2008. doi: 10.1086/591777.

D. J. Prole, M. Hilker, R. F. J. van der Burg, M. Cantiello, A. Venhola, E. Iodice, G. van de Ven, C. Wittmann, R. F. Peletier, S. Mieske, M. Capaccioli, N. R. Napolitano, M. Paolillo, M. Spavone, and E. Valentijn. Halo mass estimates from the globular cluster populations

of 175 low surface brightness galaxies in the Fornax cluster. *MNRAS*, 484(4):4865–4880, April 2019. doi: 10.1093/mnras/stz326.

F. Ramos, V. Coenda, H. Muriel, and M. Abadi. Tidal Stripping of Globular Clusters in a Simulated Galaxy Cluster. *ApJ*, 806(2):242, June 2015. doi: 10.1088/0004-637X/806/2/242.

Felipe Ramos-Almendares, Mario Abadi, Hernán Muriel, and Valeria Coenda. Intra-cluster Globular Clusters in a Simulated Galaxy Cluster. *ApJ*, 853(1):91, January 2018. doi: 10.3847/1538-4357/aaa1ef.

Felipe Ramos-Almendares, Laura V. Sales, Mario G. Abadi, Jessica E. Doppel, Hernan Muriel, and Eric W. Peng. Simulating the spatial distribution and kinematics of globular clusters within galaxy clusters in illustris. *MNRAS*, 493(4):5357–5368, April 2020. doi: 10.1093/mnras/staa551.

J. I. Read, O. Agertz, and M. L. M. Collins. Dark matter cores all the way down. *MNRAS*, 459(3):2573–2590, July 2016a. doi: 10.1093/mnras/stw713.

J. I. Read, G. Iorio, O. Agertz, and F. Fraternali. Understanding the shape and diversity of dwarf galaxy rotation curves in ΛCDM. *MNRAS*, 462(4):3628–3645, November 2016b. doi: 10.1093/mnras/stw1876.

Marta Reina-Campos, Sebastian Trujillo-Gomez, Alis J. Deason, J. M. Diederik Kruijssen, Joel L. Pfeffer, Robert A. Crain, Nate Bastian, and Meghan E. Hughes. Radial distributions of globular clusters trace their host dark matter halo: insights from the E-MOSAICS simulations. *MNRAS*, 513(3):3925–3945, July 2022. doi: 10.1093/mnras/stac1126.

Florent Renaud, Frédéric Bournaud, and Pierre-Alain Duc. A parsec-resolution simulation of the Antennae galaxies: formation of star clusters during the merger. *MNRAS*, 446(2):2038–2054, January 2015. doi: 10.1093/mnras/stu2208.

Stephen D. Riggs, Jon Loveday, Peter A. Thomas, Annalisa Pillepich, Dylan Nelson, and Benne W. Holwerda. Exploring the effect of baryons on the radial distribution of satellite galaxies with GAMA and IllustrisTNG. *MNRAS*, 514(4):4676–4695, August 2022. doi: 10.1093/mnras/stac1591.

Vicente Rodriguez-Gomez, Shy Genel, Mark Vogelsberger, Debora Sijacki, Annalisa Pillepich, Laura V. Sales, Paul Torrey, Greg Snyder, Dylan Nelson, Volker Springel, Chung-Pei Ma, and Lars Hernquist. The merger rate of galaxies in the Illustris simulation: a comparison with observations and semi-empirical models. *MNRAS*, 449(1):49–64, May 2015. doi: 10.1093/mnras/stv264.

Vicente Rodriguez-Gomez, Laura V. Sales, Shy Genel, Annalisa Pillepich, Jolanta Zjupa, Dylan Nelson, Brendan Griffen, Paul Torrey, Gregory F. Snyder, Mark Vogelsberger, Volker Springel, Chung-Pei Ma, and Lars Hernquist. The role of mergers and halo spin in shaping galaxy morphology. *MNRAS*, 467(3):3083–3098, May 2017. doi: 10.1093/mnras/stx305.

Javier Román and Ignacio Trujillo. Ultra-diffuse galaxies outside clusters: clues to their formation and evolution. *MNRAS*, 468(4):4039–4047, July 2017. doi: 10.1093/mnras/stx694.

Javier Román, Michael A. Beasley, Tomás Ruiz-Lara, and David Valls-Gabaud. Discovery of a red ultra-diffuse galaxy in a nearby void based on its globular cluster luminosity function. *MNRAS*, 486(1):823–835, June 2019. doi: 10.1093/mnras/stz835.

Yu Rong, Qi Guo, Liang Gao, Shihong Liao, Lizhi Xie, Thomas H. Puzia, Shuangpeng Sun, and Jun Pan. A Universe of ultradiffuse galaxies: theoretical predictions from ΛCDM simulations. *MNRAS*, 470(4):4231–4240, October 2017. doi: 10.1093/mnras/stx1440.

Yu Rong, Pavel E. Mancera Piña, Elmo Tempel, Thomas H. Puzia, and Sven De Rijcke. Exploring the origin of ultra-diffuse galaxies in clusters from their primordial alignment. *MNRAS*, 498(1):L72–L76, November 2020. doi: 10.1093/mnrasl/slaa129.

V. C. Rubin, Jr. Ford, W. K., and N. Thonnard. Extended rotation curves of high-luminosity spiral galaxies. IV. Systematic dynamical properties, Sa -¿ Sc. *ApJL*, 225:L107–L111, November 1978. doi: 10.1086/182804.

Mohammadtaher Safarzadeh and Evan Scannapieco. The Fate of Gas-rich Satellites in Clusters. *ApJ*, 850(1):99, Nov 2017. doi: 10.3847/1538-4357/aa94c8.

Teymoor Saifollahi, Ignacio Trujillo, Michael A. Beasley, Reynier F. Peletier, and Johan H. Knapen. The number of globular clusters around the iconic UDG DF44 is as expected for dwarf galaxies. *MNRAS*, 502(4):5921–5934, April 2021. doi: 10.1093/mnras/staa3016.

L. V. Sales, M. Vogelsberger, S. Genel, P. Torrey, D. Nelson, V. Rodriguez-Gomez, W. Wang, A. Pillepich, D. Sijacki, V. Springel, and L. Hernquist. The colours of satellite galaxies in the Illustris simulation. *MNRAS*, 447:L6–L10, February 2015. doi: 10.1093/mnrasl/slu173.

Laura V. Sales, Julio F. Navarro, Louis Peñafiel, Eric W. Peng, Sungsoon Lim, and Lars Hernquist. The formation of ultradiffuse galaxies in clusters. *MNRAS*, 494(2):1848–1858, March 2020. doi: 10.1093/mnras/staa854.

Laura V. Sales, Andrew Wetzel, and Azadeh Fattahi. Baryonic solutions and challenges for cosmological models of dwarf galaxies. *Nature Astronomy*, 6:897–910, June 2022. doi: 10.1038/s41550-022-01689-w.

Omid Sameie, Michael Boylan-Kolchin, Philip F. Hopkins, Andrew Wetzel, Xiangcheng Ma, James S. Bullock, Kareem El-Badry, Eliot Quataert, Jenna Samuel, Anna T. P. Schauer, and Daniel R. Weisz. Formation of proto-globular cluster candidates in cosmological simulations of dwarf galaxies at $z > 4$. *arXiv e-prints*, art. arXiv:2204.00638, April 2022.

Rubén Sánchez-Janssen, Patrick Côté, Laura Ferrarese, Eric W. Peng, Joel Roediger, John P. Blakeslee, Eric Emsellem, Thomas H. Puzia, Chelsea Spengler, James Taylor, Karla A. Álamo-Martínez, Alessandro Boselli, Michele Cantiello, Jean-Charles Cuillandre, Pierre-Alain Duc, Patrick Durrell, Stephen Gwyn, Lauren A. MacArthur, Ariane Lançon, Sungsoon Lim, Chengze Liu, Simona Mei, Bryan Miller, Roberto Muñoz,

J. Christopher Mihos, Sanjaya Paudel, Mathieu Powalka, and Elisa Toloba. The Next Generation Virgo Cluster Survey. XXIII. Fundamentals of Nuclear Star Clusters over Seven Decades in Galaxy Mass. *ApJ*, 878(1):18, June 2019. doi: 10.3847/1538-4357/aaf4fd.

Isabel M. E. Santos-Santos, Julio F. Navarro, Andrew Robertson, Alejandro Benítez-Llambay, Kyle A. Oman, Mark R. Lovell, Carlos S. Frenk, Aaron D. Ludlow, Azadeh Fattahi, and Adam Ritz. Baryonic clues to the puzzling diversity of dwarf galaxy rotation curves. *MNRAS*, 495(1):58–77, April 2020. doi: 10.1093/mnras/staa1072.

Y. Schuberth, T. Richtler, L. Bassino, and M. Hilker. Intra-cluster globular clusters around NGC 1399 in Fornax? *A&A*, 477(2):L9–L12, January 2008. doi: 10.1051/0004-6361:20078668.

F. Schweizer. Galaxies with Long Tails. In E. M. Berkhuijsen and R. Wielebinski, editors, *Structure and Properties of Nearby Galaxies*, volume 77 of *IAU Symposium*, page 279, January 1978.

Debora Sijacki, Mark Vogelsberger, Shy Genel, Volker Springel, Paul Torrey, Gregory F. Snyder, Dylan Nelson, and Lars Hernquist. The Illustris simulation: the evolving population of black holes across cosmic time. *MNRAS*, 452(1):575–596, September 2015. doi: 10.1093/mnras/stv1340.

Joshua D. Simon and Marla Geha. The Kinematics of the Ultra-faint Milky Way Satellites: Solving the Missing Satellite Problem. *ApJ*, 670(1):313–331, November 2007. doi: 10.1086/521816.

Joshua D. Simon, Thomas M. Brown, Alex Drlica-Wagner, Ting S. Li, Roberto J. Avila, Keith Bechtol, Gisella Clementini, Denija Crnojević, Alessia Garofalo, Marla Geha, David J. Sand, Jay Strader, and Beth Willman. Eridanus II: A Fossil from Reionization with an Off-center Star Cluster. *ApJ*, 908(1):18, February 2021. doi: 10.3847/1538-4357/abd31b.

R. Smith, R. Sánchez-Janssen, M. Fellhauer, T. H. Puzia, J. A. L. Aguerri, and J. P. Farias. The impact of galaxy harassment on the globular cluster systems of early-type cluster dwarf galaxies. *MNRAS*, 429(2):1066–1079, February 2013. doi: 10.1093/mnras/sts395.

Gregory F. Snyder, Paul Torrey, Jennifer M. Lotz, Shy Genel, Cameron K. McBride, Mark Vogelsberger, Annalisa Pillepich, Dylan Nelson, Laura V. Sales, Debora Sijacki, Lars Hernquist, and Volker Springel. Galaxy morphology and star formation in the Illustris Simulation at z = 0. *MNRAS*, 454(2):1886–1908, December 2015. doi: 10.1093/mnras/stv2078.

Jean J. Somalwar, Jenny E. Greene, Johnny P. Greco, Song Huang, Rachael L. Beaton, Andy D. Goulding, and Lachlan Lancaster. Hyper Suprime-Cam Low Surface Brightness Galaxies. II. A Hubble Space Telescope Study of the Globular Cluster Systems of Ultradiffuse Galaxies in Groups. *ApJ*, 902(1):45, October 2020. doi: 10.3847/1538-4357/abb1b2.

Rachel S. Somerville, Peter Behroozi, Viraj Pandya, Avishai Dekel, S. M. Faber, Adriano Fontana, Anton M. Koekemoer, David C. Koo, P. G. Pérez-González, Joel R. Primack, Paola Santini, Edward N. Taylor, and Arjen van der Wel. The relationship between galaxy and dark matter halo size from z $\sim$ 3 to the present. *MNRAS*, 473(2):2714–2736, January 2018. doi: 10.1093/mnras/stx2040.

David N. Spergel and Paul J. Steinhardt. Observational Evidence for Self-Interacting Cold Dark Matter. , 84(17):3760–3763, April 2000. doi: 10.1103/PhysRevLett.84.3760.

L. R. Spitler and D. A. Forbes. A new method for estimating dark matter halo masses using globular cluster systems. *Monthly Notices of the Royal Astronomical Society: Letters*, 392(1):L1–L5, 01 2009. ISSN 1745-3925. doi: 10.1111/j.1745-3933.2008.00567.x. URL https://doi.org/10.1111/j.1745-3933.2008.00567.x.

V. Springel, J. Wang, M. Vogelsberger, A. Ludlow, A. Jenkins, A. Helmi, J. F. Navarro, C. S. Frenk, and S. D. M. White. The Aquarius Project: the subhaloes of galactic haloes. *MNRAS*, 391(4):1685–1711, December 2008. doi: 10.1111/j.1365-2966.2008.14066.x.

Volker Springel, Simon D. M. White, Giuseppe Tormen, and Guinevere Kauffmann. Populating a cluster of galaxies - I. Results at [formmu2]z=0. *MNRAS*, 328(3):726–750, December 2001. doi: 10.1046/j.1365-8711.2001.04912.x.

Volker Springel, Rüdiger Pakmor, Annalisa Pillepich, Rainer Weinberger, Dylan Nelson, Lars Hernquist, Mark Vogelsberger, Shy Genel, Paul Torrey, Federico Marinacci, and Jill Naiman. First results from the IllustrisTNG simulations: matter and galaxy clustering. *MNRAS*, 475(1):676–698, March 2018. doi: 10.1093/mnras/stx3304.

Louis E. Strigari, James S. Bullock, Manoj Kaplinghat, Joshua D. Simon, Marla Geha, Beth Willman, and Matthew G. Walker. A common mass scale for satellite galaxies of the Milky Way. *Nature*, 454(7208):1096–1097, August 2008. doi: 10.1038/nature07222.

R. A. Swaters, R. Sancisi, T. S. van Albada, and J. M. van der Hulst. The rotation curves shapes of late-type dwarf galaxies. *A&A*, 493(3):871–892, January 2009. doi: 10.1051/0004-6361:200810516.

Takayuki Tamura, Kazuo Makishima, Yasushi Fukazawa, Yasushi Ikebe, and Haiguang Xu. X-Ray Measurements of the Gravitational Potential Profile in the Central Region of the Abell 1060 Cluster of Galaxies. *ApJ*, 535(2):602–614, June 2000. doi: 10.1086/308882.

Matthew A. Taylor, Thomas H. Puzia, Roberto P. Muñoz, Steffen Mieske, Ariane Lançon, Hongxin Zhang, Paul Eigenthaler, and Mia Sauda Bovill. The Survey of Centaurus A's Baryonic Structures (SCABS) – II. The extended globular cluster system of NGC 5128 and its nearby environment. *Monthly Notices of the Royal Astronomical Society*, 469 (3):3444–3467, 04 2017. ISSN 0035-8711. doi: 10.1093/mnras/stx1021. URL https://doi.org/10.1093/mnras/stx1021.

E. Toloba, B. Li, P. Guhathakurta, E. W. Peng, L. Ferrarese, P. Côté, E. Emsellem, S. Gwyn, H. Zhang, A. Boselli, J.-C. Cuillandre, A. Jordan, and C. Liu. The Next Generation Virgo Cluster Survey XVI: The Angular Momentum of Dwarf Early-type Galaxies

from Globular Cluster Satellites. *ApJ*, 822:51, May 2016. doi: 10.3847/0004-637X/822/1/51.

Elisa Toloba, Sungsoon Lim, Eric Peng, Laura V. Sales, Puragra Guhathakurta, J. Christopher Mihos, Patrick Côté, Alessandro Boselli, Jean-Charles Cuillandre, Laura Ferrarese, Stephen Gwyn, Ariane Lançon, Roberto Muñoz, and Thomas Puzia. Dark Matter in Ultra-diffuse Galaxies in the Virgo Cluster from Their Globular Cluster Populations. *ApJL*, 856(2):L31, April 2018. doi: 10.3847/2041-8213/aab603.

Elisa Toloba, Laura V. Sales, Sungsoon Lim, Eric W. Peng, Puragra Guhathakurta, Joel Roediger, Kaixiang Wang, J. Christopher Mihos, Patrick Cote, Patrick R. Durrell, and Laura Ferrarese. The Next Generation Virgo Cluster Survey (NGVS). XXXV. First Kinematical Clues of Overly-Massive Dark Matter Halos in Several Ultra-Diffuse Galaxies in the Virgo Cluster. *arXiv e-prints*, art. arXiv:2305.06369, May 2023. doi: 10.48550/arXiv.2305.06369.

Paul Torrey, Mark Vogelsberger, Shy Genel, Debora Sijacki, Volker Springel, and Lars Hernquist. A model for cosmological simulations of galaxy formation physics: multi-epoch validation. *MNRAS*, 438(3):1985–2004, March 2014. doi: 10.1093/mnras/stt2295.

M. Tremmel, A. C. Wright, A. M. Brooks, F. Munshi, D. Nagai, and T. R. Quinn. The formation of ultradiffuse galaxies in the RomulusC galaxy cluster simulation. *MNRAS*, 497(3):2786–2810, September 2020. doi: 10.1093/mnras/staa2015.

Ignacio Trujillo, Michael A. Beasley, Alejandro Borlaff, Eleazar R. Carrasco, Arianna Di Cintio, Mercedes Filho, Matteo Monelli, Mireia Montes, Javier Román, Tomás Ruiz-Lara, Jorge Sánchez Almeida, David Valls-Gabaud, and Alexandre Vazdekis. A distance of 13 Mpc resolves the claimed anomalies of the galaxy lacking dark matter. *MNRAS*, 486(1):1192–1219, June 2019. doi: 10.1093/mnras/stz771.

Sebastian Trujillo-Gomez, J. M. Diederik Kruijssen, Marta Reina-Campos, Joel L. Pfeffer, Benjamin W. Keller, Robert A. Crain, Nate Bastian, and Meghan E. Hughes. The kinematics of globular cluster populations in the E-MOSAICS simulations and their implications for the assembly history of the Milky Way. *MNRAS*, 503(1):31–58, May 2021. doi: 10.1093/mnras/stab341.

Sebastian Trujillo-Gomez, J. M. Diederik Kruijssen, and Marta Reina-Campos. The emergence of dark matter-deficient ultra-diffuse galaxies driven by scatter in the stellar mass-halo mass relation and feedback from globular clusters. *MNRAS*, 510(3):3356–3378, March 2022. doi: 10.1093/mnras/stab3401.

Sidney van den Bergh. The Mass of the Centaurus A Group of Galaxies. *AJ*, 119(2):609–611, February 2000. doi: 10.1086/301214.

Remco F. J. van der Burg, Henk Hoekstra, Adam Muzzin, Cristóbal Sifón, Massimo Viola, Malcolm N. Bremer, Sarah Brough, Simon P. Driver, Thomas Erben, Catherine Heymans, Hendrik Hildebrandt, Benne W. Holwerda, Dominik Klaes, Konrad Kuijken, Sean

McGee, Reiko Nakajima, Nicola Napolitano, Peder Norberg, Edward N. Taylor, and Edwin Valentijn. The abundance of ultra-diffuse galaxies from groups to clusters. UDGs are relatively more common in more massive haloes. *A&A*, 607:A79, November 2017. doi: 10.1051/0004-6361/201731335.

P. van Dokkum, R. Abraham, J. Brodie, C. Conroy, S. Danieli, A. Merritt, L. Mowla, A. Romanowsky, and J. Zhang. A High Stellar Velocity Dispersion and 100 Globular Clusters for the Ultra-diffuse Galaxy Dragonfly 44. *ApJL*, 828:L6, September 2016. doi: 10.3847/2041-8205/828/1/L6.

P. van Dokkum, S. Danieli, Y. Cohen, A. Merritt, A. J. Romanowsky, R. Abraham, J. Brodie, C. Conroy, D. Lokhorst, L. Mowla, E. O'Sullivan, and J. Zhang. A galaxy lacking dark matter. *Nature*, 555:629–632, March 2018a. doi: 10.1038/nature25767.

P. van Dokkum, S. Danieli, R. Abraham, C. Conroy, and A. J. Romanowsky. A Second Galaxy Missing Dark Matter in the NGC 1052 Group. *ApJL*, 874:L5, March 2019a. doi: 10.3847/2041-8213/ab0d92.

Pieter van Dokkum, Roberto Abraham, Aaron J. Romanowsky, Jean Brodie, Charlie Conroy, Shany Danieli, Deborah Lokhorst, Allison Merritt, Lamiya Mowla, and Jielai Zhang. Extensive Globular Cluster Systems Associated with Ultra Diffuse Galaxies in the Coma Cluster. *ApJL*, 844(1):L11, July 2017. doi: 10.3847/2041-8213/aa7ca2.

Pieter van Dokkum, Yotam Cohen, Shany Danieli, J. M. Diederik Kruijssen, Aaron J. Romanowsky, Allison Merritt, Roberto Abraham, Jean Brodie, Charlie Conroy, Deborah Lokhorst, Lamiya Mowla, Ewan O'Sullivan, and Jielai Zhang. An Enigmatic Population of Luminous Globular Clusters in a Galaxy Lacking Dark Matter. *ApJL*, 856(2):L30, April 2018b. doi: 10.3847/2041-8213/aab60b.

Pieter van Dokkum, Yotam Cohen, Shany Danieli, Aaron Romanowsky, Roberto Abraham, Jean Brodie, Charlie Conroy, J. M. Diederik Kruijssen, Deborah Lokhorst, Allison Merritt, Lamiya Mowla, and Jielai Zhang. A Revised Velocity for the Globular Cluster GC-98 in the Ultra Diffuse Galaxy NGC 1052-DF2. *Research Notes of the American Astronomical Society*, 2(2):54, June 2018c. doi: 10.3847/2515-5172/aacc6f.

Pieter van Dokkum, Asher Wasserman, Shany Danieli, Roberto Abraham, Jean Brodie, Charlie Conroy, Duncan A. Forbes, Christopher Martin, Matt Matuszewski, Aaron J. Romanowsky, and Alexa Villaume. Spatially Resolved Stellar Kinematics of the Ultra-diffuse Galaxy Dragonfly 44. I. Observations, Kinematics, and Cold Dark Matter Halo Fits. *ApJ*, 880(2):91, August 2019b. doi: 10.3847/1538-4357/ab2914.

Pieter van Dokkum, Zili Shen, Aaron J. Romanowsky, Roberto Abraham, Charlie Conroy, Shany Danieli, Dhruba Dutta Chowdhury, Michael A. Keim, J. M. Diederik Kruijssen, Joel Leja, and Sebastian Trujillo-Gomez. Monochromatic globular clusters as a critical test of formation models for the dark matter deficient galaxies NGC1052-DF2 and NGC1052-DF4. *arXiv e-prints*, art. arXiv:2207.07129, July 2022.

Pieter G. van Dokkum, Roberto Abraham, Allison Merritt, Jielai Zhang, Marla Geha, and Charlie Conroy. Forty-seven Milky Way-sized, Extremely Diffuse Galaxies in the Coma Cluster. *ApJL*, 798(2):L45, January 2015a. doi: 10.1088/2041-8205/798/2/L45.

Pieter G. van Dokkum, Aaron J. Romanowsky, Roberto Abraham, Jean P. Brodie, Charlie Conroy, Marla Geha, Allison Merritt, Alexa Villaume, and Jielai Zhang. Spectroscopic Confirmation of the Existence of Large, Diffuse Galaxies in the Coma Cluster. *ApJL*, 804 (1):L26, May 2015b. doi: 10.1088/2041-8205/804/1/L26.

J. Veljanoski, A. D. Mackey, A. M. N. Ferguson, A. P. Huxor, P. Côté, M. J. Irwin, N. R. Tanvir, J. Peñarrubia, E. J. Bernard, M. Fardal, N. F. Martin, A. McConnachie, G. F. Lewis, S. C. Chapman, R. A. Ibata, and A. Babul. The outer halo globular cluster system of M31 - II. Kinematics. *MNRAS*, 442(4):2929–2950, August 2014. doi: 10.1093/mnras/stu1055.

Aku Venhola, Reynier F. Peletier, Heikki Salo, Eija Laurikainen, Joachim Janz, Caroline Haigh, Michael H. F. Wilkinson, Enrichetta Iodice, Michael Hilker, Steffen Mieske, Michele Cantiello, and Marilena Spavone. The Fornax Deep Survey with the VST. XII. Low surface brightness dwarf galaxies in the Fornax cluster. *A&A*, 662:A43, June 2022. doi: 10.1051/0004-6361/202141756.

Alexa Villaume, Daniel Foreman-Mackey, Aaron J. Romanowsky, Jean Brodie, and Jay Strader. The Assembly History of M87 through Radial Variations in Chemical Abundances of Its Field Star and Globular Cluster Populations. *ApJ*, 900(2):95, September 2020. doi: 10.3847/1538-4357/aba616.

Pauli Virtanen, Ralf Gommers, Travis E. Oliphant, Matt Haberland, Tyler Reddy, David Cournapeau, Evgeni Burovski, Pearu Peterson, Warren Weckesser, Jonathan Bright, Stéfan J. van der Walt, Matthew Brett, Joshua Wilson, K. Jarrod Millman, Nikolay Mayorov, Andrew R. J. Nelson, Eric Jones, Robert Kern, Eric Larson, C J Carey, İlhan Polat, Yu Feng, Eric W. Moore, Jake VanderPlas, Denis Laxalde, Josef Perktold, Robert Cimrman, Ian Henriksen, E. A. Quintero, Charles R. Harris, Anne M. Archibald, Antônio H. Ribeiro, Fabian Pedregosa, Paul van Mulbregt, and SciPy 1.0 Contributors. SciPy 1.0: Fundamental Algorithms for Scientific Computing in Python. *Nature Methods*, 17:261–272, 2020. doi: 10.1038/s41592-019-0686-2.

M. Vogelsberger, S. Genel, D. Sijacki, P. Torrey, V. Springel, and L. Hernquist. A model for cosmological simulations of galaxy formation physics. *MNRAS*, 436:3031–3067, December 2013. doi: 10.1093/mnras/stt1789.

M. Vogelsberger, S. Genel, V. Springel, P. Torrey, D. Sijacki, D. Xu, G. Snyder, S. Bird, D. Nelson, and L. Hernquist. Properties of galaxies reproduced by a hydrodynamic simulation. *Nature*, 509(7499):177–182, May 2014a. doi: 10.1038/nature13316.

M. Vogelsberger, S. Genel, V. Springel, P. Torrey, D. Sijacki, D. Xu, G. Snyder, D. Nelson, and L. Hernquist. Introducing the Illustris Project: simulating the coevolution of dark and visible matter in the Universe. *MNRAS*, 444:1518–1547, October 2014b. doi: 10.1093/mnras/stu1536.

Mark Vogelsberger, Jesus Zavala, Christine Simpson, and Adrian Jenkins. Dwarf galaxies in CDM and SIDM with baryons: observational probes of the nature of dark matter. *MNRAS*, 444(4):3684–3698, November 2014c. doi: 10.1093/mnras/stu1713.

Mark Vogelsberger, Federico Marinacci, Paul Torrey, and Ewald Puchwein. Cosmological simulations of galaxy formation. *Nature Reviews Physics*, 2(1):42–66, January 2020. doi: 10.1038/s42254-019-0127-2.

M. G. Walker and J. Peñarrubia. A Method for Measuring (Slopes of) the Mass Profiles of Dwarf Spheroidal Galaxies. *ApJ*, 742:20, November 2011. doi: 10.1088/0004-637X/742/1/20.

Matthew G. Walker, Mario Mateo, Edward W. Olszewski, Oleg Y. Gnedin, Xiao Wang, Bodhisattva Sen, and Michael Woodroofe. Velocity Dispersion Profiles of Seven Dwarf Spheroidal Galaxies. *ApJL*, 667(1):L53–L56, September 2007. doi: 10.1086/521998.

Asher Wasserman, Aaron J. Romanowsky, Jean Brodie, Pieter van Dokkum, Charlie Conroy, Roberto Abraham, Yotam Cohen, and Shany Danieli. A Deficit of Dark Matter from Jeans Modeling of the Ultra-diffuse Galaxy NGC 1052-DF2. *ApJL*, 863(2):L15, August 2018. doi: 10.3847/2041-8213/aad779.

Rainer Weinberger, Volker Springel, Lars Hernquist, Annalisa Pillepich, Federico Marinacci, Rüdiger Pakmor, Dylan Nelson, Shy Genel, Mark Vogelsberger, Jill Naiman, and Paul Torrey. Simulating galaxy formation with black hole driven thermal and kinetic feedback. *MNRAS*, 465(3):3291–3308, March 2017. doi: 10.1093/mnras/stw2944.

Simone M. Weinmann, Thorsten Lisker, Qi Guo, Hagen T. Meyer, and Joachim Janz. Dwarf galaxy populations in present-day galaxy clusters - I. Abundances and red fractions. *MNRAS*, 416(2):1197–1214, September 2011. doi: 10.1111/j.1365-2966.2011.19118.x.

S. D. M. White and M. J. Rees. Core condensation in heavy halos: a two-stage theory for galaxy formation and clustering. *MNRAS*, 183:341–358, May 1978. doi: 10.1093/mnras/183.3.341.

Simon D. M. White and Carlos S. Frenk. Galaxy Formation through Hierarchical Clustering. *ApJ*, 379:52, September 1991. doi: 10.1086/170483.

Lawrence M. Widrow, Brent Pym, and John Dubinski. Dynamical Blueprints for Galaxies. *ApJ*, 679(2):1239–1259, June 2008. doi: 10.1086/587636.

J. Wolf, G. D. Martinez, J. S. Bullock, M. Kaplinghat, M. Geha, R. R. Muñoz, J. D. Simon, and F. F. Avedo. Accurate masses for dispersion-supported galaxies. *MNRAS*, 406:1220–1237, August 2010. doi: 10.1111/j.1365-2966.2010.16753.x.

Masafumi Yagi, Jin Koda, Yutaka Komiyama, and Hitomo Yamanoi. Catalog of Ultra-diffuse Galaxies in the Coma Clusters from Subaru Imaging Data. *ApJS*, 225(1):11, July 2016. doi: 10.3847/0067-0049/225/1/11.

Hideki Yahagi and Kenji Bekki. Formation of intracluster globular clusters. *Monthly Notices of the Royal Astronomical Society: Letters*, 364(1):L86–L90, 11 2005. ISSN 1745-3925. doi: 10.1111/j.1745-3933.2005.00111.x. URL https://doi.org/10.1111/j.1745-3933.2005.00111.x.

Kiyun Yun, Annalisa Pillepich, Elad Zinger, Dylan Nelson, Martina Donnari, Gandhali Joshi, Vicente Rodriguez-Gomez, Shy Genel, Rainer Weinberger, Mark Vogelsberger, and Lars Hernquist. Jellyfish galaxies with the IllustrisTNG simulations - I. Gas-stripping phenomena in the full cosmological context. *MNRAS*, 483(1):1042–1066, February 2019. doi: 10.1093/mnras/sty3156.

Ling Zhu, R. J. Long, Shude Mao, Eric W. Peng, Chengze Liu, Nelson Caldwell, Biao Li, John P. Blakeslee, Patrick Côté, Jean-Charles Cuilland re, Patrick Durrell, Eric Emsellem, Laura Ferrarese, Stephen Gwyn, Andrés Jordán, Ariane Lançon, Simona Mei, Roberto Muñoz, and Thomas Puzia. The Next Generation Virgo Cluster Survey. V. Modeling the Dynamics of M87 with the Made-to-measure Method. *ApJ*, 792(1):59, September 2014. doi: 10.1088/0004-637X/792/1/59.

F. Zwicky. Multiple Galaxies. *Ergebnisse der exakten Naturwissenschaften*, 29:344–385, January 1956.

Ewa L. Łokas and Gary A. Mamon. Properties of spherical galaxies and clusters with an NFW density profile. *Monthly Notices of the Royal Astronomical Society*, 321(1):155–166, 02 2001. ISSN 0035-8711. doi: 10.1046/j.1365-8711.2001.04007.x. URL https://doi.org/10.1046/j.1365-8711.2001.04007.x.

Appendix A

Velocity Dispersion Measurements

Here is a more detailed discussion of the calculations of each of the methods used to calculate velocity dispersion in this work.

- **The r.m.s dispersion,** $\sigma_{\rm rms}$

  This methods assumes that the underlying velocity distribution is Gaussian, and it is calculated using:

  $$\sigma_{\rm rms} = \sqrt{\frac{\sum_{\rm i}^{\rm N} ({\rm v_i} - \bar{\rm v})^2}{N}} \tag{A.1}$$

  where N is the number of GC tracers, $\rm v_i$ are the individual velocities of the GCs, and $\bar{\rm v}$ is the center of mass velocity of the galaxy the GCs are associated with.

  We first use this calculation to perform 3-σ clipping of the GC candidate particles from which we later draw our realistic sample of GCs. This removes most of the GC particles within the cutoff radius that belong to the intracluster population and thus would contaminate our sample.

- **The biweight velocity dispersion** $\sigma_{\rm biweight}$

  This method does not assume an underlying Gaussian velocity distribution and instead assigns different set of weights to each velocity measurement, where larger weight values are given to velocities closer to the median of the distribution. This method is advantageous for highly contaminated samples of tracers, where the biweight estimation downweights possible outliers or contaminants making them less influential in the final σ estimate compared to the simpler r.m.s calculation.

  As introduced in (Beers et al. 1990), to calculate the biweight estimation of scale, we first need to calculate the mean absolute deviation (MAD):

$$\mathrm{MAD} = \mathrm{median}(|\mathrm{v_i} - \mathrm{M}|) \tag{A.2}$$

  where $\mathrm{v_i}$ are the individual velocities and M is the median of those velocities. Next, we calculate u_i, the weight associated with each velocity following:

$$\mathrm{u_i} = \frac{\mathrm{v_i} - \mathrm{M}}{\mathrm{cMAD}} \tag{A.3}$$

  where c is the "tuning" parameter, which is to be set to 9 according to Beers et al. (1990). The biweight estimation of scale is then given by:

$$\sigma_{\rm biweight} = \frac{\mathrm{N}^{1/2}[\sum_{|\mathrm{u_i}|<1}(\mathrm{v_i} - \mathrm{M})(1 - \mathrm{u_i})^4]^{1/2}}{|\sum_{|\mathrm{u_i}|<1}(1 - \mathrm{u_i^2})(1 - 5\mathrm{u_i^2})|} \tag{A.4}$$

  where N again is the number of tracers. A minimum of 5 tracers is required for this method to work (see Beers et al. (1990) for a brief discussion).

- **MCMC velocity dispersion,** $\sigma_{\rm MCMC}$

  This method takes the line of sight velocity distribution and stochastically finds the best σ and $\bar{\rm v}$ to fit a Gaussian to the distribution. The likelihood used in this estimation is given by

$$\mathcal{L} = \prod_{\rm i}^{\rm N_{GC}} \frac{1}{\sigma\sqrt{2\pi}} \exp\left(-0.5 \left(\frac{\rm v_i - < v >}{\sigma} \right)^2 \right) \tag{A.5}$$

  where $\rm v_i$ are the line of sight velocities of the tracers and $\bar{\rm v}$ and σ are allowed to vary. MCMC methods tend to be quite computationally expensive and the results can depend on the shape of the prior assumed (see Martin et al. (2018) for a specific example using DF2). Here we explore two different assumptions for the priors: a uniform distribution (flat prior) and Jeffreys prior, which in the case of a Gaussian function like assumed here, corresponds to a prior distribution $\propto 1/\sigma$.

  In practice, Jeffreys prior amounts to multiplying equation A.5 by $(1/\sigma)$ and has the net effect of shortening the long tails in the posterior PDF for the velocity dispersion in figures alike A.1 (see right panel in Fig. 2.4). The Jeffreys prior is, however, improper, which means the distribution of posterior probabilities might not necessarily integrate to 1 unless a lower limit in σ is specified. We have used $\sigma = 0.5$ km s^{-1} in our calculations, but we have explicitly checked that changing that to 0.5 or 1 km s^{-1} does not qualitatively change our results. We have confirmed that the use of the Jeffreys prior is particularly powerful for systems with small $\rm N_{GC}$, where the differences with a flat prior are most significant (see Fig. 2.6).

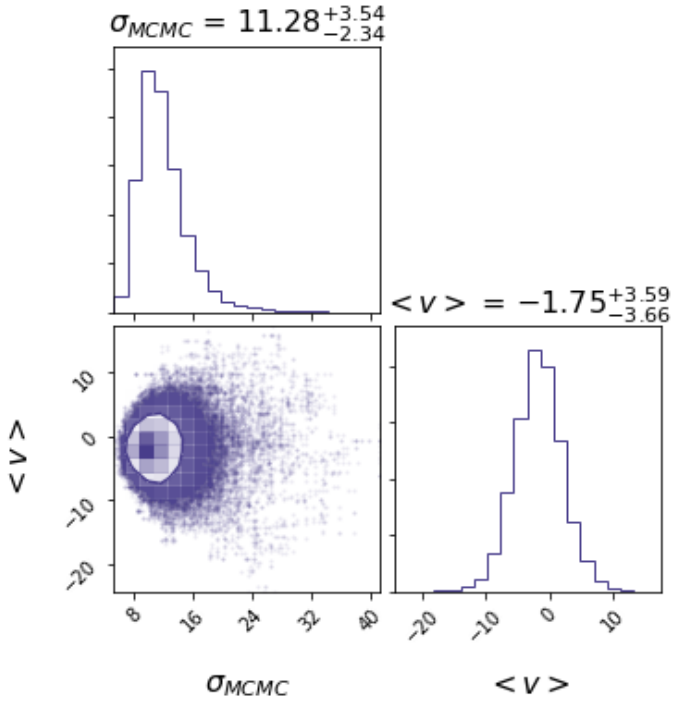

Figure A.1: An illustration of the MCMC method for a randomly selected galaxy with GCs in Illustris. This pdf estimates both the velocity dispersion σ and the expectation value $< v >$ using stochastic sampling of parameter space using 10 globular clusters. This method assumes an intrinsic error on the order of 5km/s in the velocity measurements.

We employ the Metropolis-Hastings technique to find the posterior PDF of $\sigma_{\rm los}$, the result of which is illustrated in Figure A.1 In short, this technique involves the following:

1. set initial estimates for the parameters in question.
2. randomly select one of those variables. Calculate the likelihood.
3. select a random point from a Gaussian jumping distribution centered on the current value of the parameter with a dispersion set in the case of this study to 5 km s^{-1}. This becomes the new value of the selected parameter.
4. calculate the likelihood with this new parameter value. Then,

- if the likelihood at the new value is greater than the likelihood of the old value, we keep the new value of the parameter.
- if the likelihood at the new value if less than the likelihood at the new value, the if the ratio of the new likelihood to the old likelihood is greater than some random number between 0 and 1, we keep the new value of the parameter. Else, we keep the old value.

5. repeat until the parameter space of all variables has been sufficiently explored.

We have illustrated this process in Figure A.1. The corner panel shows the 2D pdf of the line of sight velocity dispersion $\sigma_{\rm MCMC}$ and the expectation value of the line of sight velocity distribution $< \rm v >$. The top panel shows the resulting posterior for $\sigma_{\rm MCMC}$ and the bottom right panel the posterior for $< \rm v >$.

Appendix B

Errors in individual velocity measurements

We explore in Fig. B.1 the effect of adding measurement errors to the individual velocity of GCs in each galaxy. We compare the MCMC (flat prior) velocity dispersion calculated with and without errors, where errors have been modeled assuming a Gaussian distribution of 5 and 10 km s^{-1} dispersion (red and blue, respectively). These values have been chosen to coincide with typical velocity errors in recent observations of dwarf galaxies (Toloba et al. 2016, 2018; van Dokkum et al. 2018a).

One can expect that these added uncertainty will only be relevant in objects where the intrinsic velocity dispersion of the GC system is of the order of the added errors to each individual GC velocity. We therefore show in Fig. B.1 a subsample of our galaxies with intrinsic $\sigma_{\rm MCMC,f} \leq 30$ km s^{-1}. As expected, we find that the addition of errors will tend

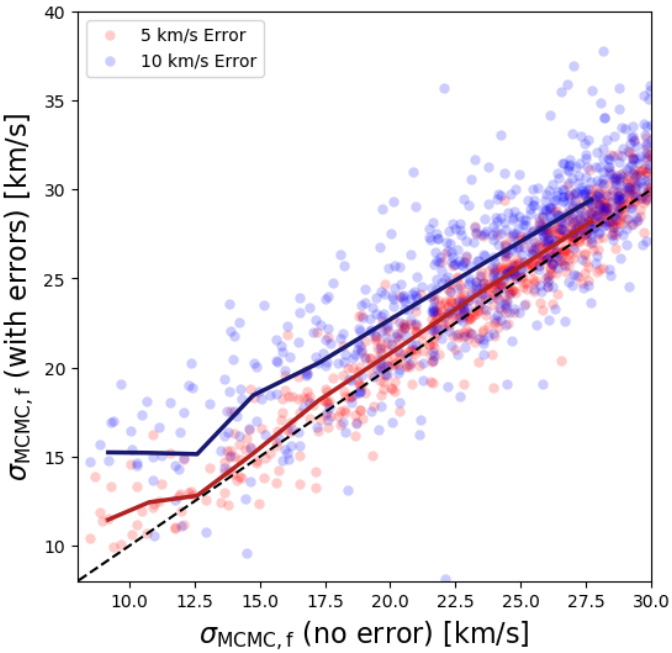

Figure B.1: Impact of adding errors to individual GC's velocity measures on the recovered velocity dispersion of the system using the MCMC method with a flat prior. The horizontal axis shows $\sigma_{\mathrm{MCMC,f}}$ (assuming no errors) and the y-axis shows for the same GC systems the $\sigma_{\mathrm{MCMC,f}}$ calculated assigning to each GC velocity an error drawn from a Gaussian distribution with dispersion 5 (red) and 10 (blue) km s^{-1}. Solid lines with the same color indicate the median at fixed $\sigma_{\mathrm{MCMC,f}}$.

(on the median) to increase the velocity dispersion estimates, with an impact that naturally depends on the level of errors included.

The maximum effect is found for our lowest velocity dispersion objects, where the overestimation on the median may reach 20% in the case of 10 km s^{-1} errors. Note that this quickly decreases to 5% if the errors are instead 5 km s^{-1}. The solid red and blue lines indicating the median MCMC determination including errors show that the systematic overestimation decreases as the intrinsic velocity dispersion increases, being negligible for objects with $\sigma_{\mathrm{MCMC,f}} \sim 25$ km s^{-1} and above. This study indicates that the inclusion

of observational errors in our calculations does not qualitatively change the results and conclusions presented in our paper.

Appendix C

Impact of non-Gaussian distributions on Confidence Intervals

Confidence intervals represent the probability (or fraction of times) that the true variance s^2 of a sample with $N_{\rm tot}$ events falls within the variance d^2 plus/minus the confidence interval of a given subsample with N objects (where $N < N_{\rm tot}$). This confidence intervals have a well-known functional form in the case of an underlying Gaussian distribution, an assumption commonly made to estimate the accuracy of velocity measurements in observations. In this Appendix we test how well the Gaussian confidence intervals perform for 5 individual objects in our sample when using each of the three methods to measure velocity dispersion explored in this paper: r.m.s, biweight and MCMC.

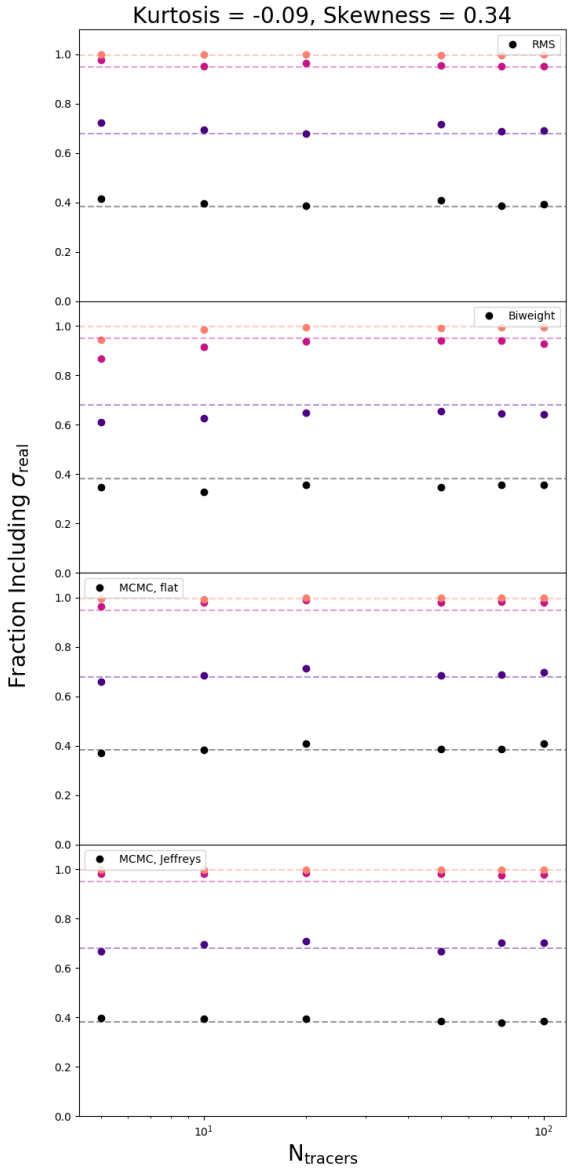

Figure C.1: For 1000 realizations of 5, 10, 20, 50, 75, and 100 GCs, the fraction of times that $\sigma_{\rm real}$ of the underlying distribution of GC candidates falls within the specified confidence interval (38.3% (black), 68% (purple), 95% (magenta) and 99.7% (orange)) of the specified σ estimate for the realization. Trials from top to bottom are for $\sigma_{\rm rms}$, $\sigma_{\rm biweight}$, $\sigma_{\rm MCMC,f}$ and $\sigma_{\rm MCMC,j}$. This particular subhalo, from the top panel of Fig. 2.1, has a relatively Gaussian distribution of GC candidates. The Gaussian confidence seem to hold quite well across all $N_{\rm GC}$ with the exception for $\sigma_{\rm biweight}$ for which the confidence intervals are underestimated.

We start by using the galaxy introduced in the upper row of Fig. 2.1, which shows a nearly Gaussian line-of-sight velocity distribution (see upper right panel in the same figure). The kurtosis and skewness for the GCs candidates in this object are -0.09 and 0.34, respectively. We sample 1000 times $N = 5$, 10, 20, 50, 75 and 100 GCs out of the ~ 400 GC candidates that remain bound to this galaxy at $z = 0$. For each set of samplings, we count the fraction of times than the true variance of all *candidate* GCs is contained within the variance of each random sampling with N tracer GCs plus the confidence interval computed assuming a Gaussian distribution.

The upper panel in Fig. C.1 shows the result of such exercise as a function of the number of tracers N selected. We show with circles the results for confidence interval levels: 38.3% black, 68% (purple), 95% (magenta) and 99.7% (orange). Dashed horizontal lines highlight the position of each level in the plot. For a perfectly Gaussian distribution and a reliable method to estimate velocity dispersion, one would expect the symbols to follow these horizontal lines.

We find that this is the case of the r.m.s velocity dispersion estimate in this galaxy roughly independent of the number of tracers (upper panel in Fig. C.1). Similarly, computing the velocity dispersion using MCMC (either with flat or Jeffreys prior, bottom 2 panels in Fig. C.1) yields a similar result. In this case, the confidence interval is not computed from the Gaussian form, but extracted directly from the PDFs of the MCMC method.

In the case of $\sigma_{\rm biweight}$ (top second panel in Fig. C.1), assuming Gaussian confidence intervals seems to slightly overestimate the accuracy (dashed lines are above the calculated symbols), specially for a number of tracers 10 and below. However, the effect is only mild.

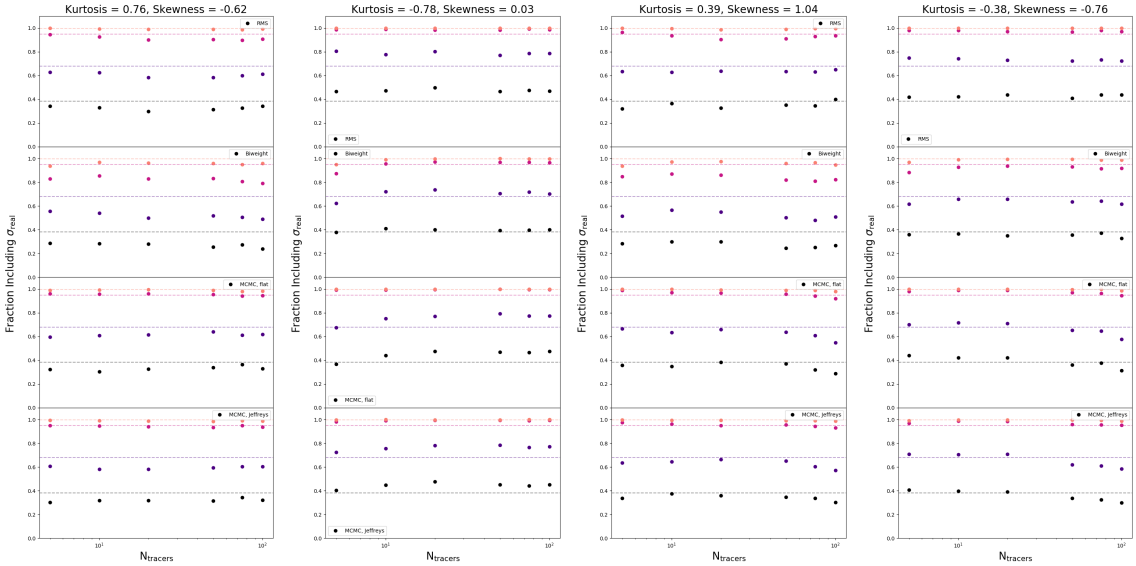

Figure C.2: For 1000 realizations of $N_{\rm tracers}$ = 5, 10, 20, 50, 75, and 100 GCs, the fraction of times that $\sigma_{\rm real}$ of the underlying distribution of GC candidates falls within the corresponding confidence interval (38.3% (black), 68% (purple), 95% (magenta) and 99.7% (orange)) for the different σ estimates. Trials from top to bottom in each panel are for $\sigma_{\rm rms}$, $\sigma_{\rm biweight}$, $\sigma_{\rm MCMC,f}$ and $\sigma_{\rm MCMC,j}$. From left to right, each panel shows the effect of large positive kurtosis, large negative kurtosis, large positive skewness, and large negative skewness on the correctness of Gaussian confidence intervals. All methods seem to suggest that confidence intervals are underestimated in the case of negative kurtosis (points above horizontal lines) while the opposite is true for positive kurtosis. The trend with number of tracers is rather weak.

We repeat this calculation using 4 galaxies that deviate more substantially in either kurtosis or skewness from a Gaussian distribution (those highlighted in Fig. 2.7). We show this in Fig. C.2. We find that all methods show in general similar trends: high positive kurtosis results on underestimated confidence intervals (symbols below the dashed lines) while high negative kurtosis means that measurements are more accurate than expected from a perfectly Gaussian distribution (symbols above corresponding dashed lines). Similar trends might be found for deviations in skewness (rightmost two panels in Fig. C.2), although the impact seems smaller than in the case of kurtosis. The dependence with the number of tracers is rather weak.

Such exercise (and the ratio between the symbols and the horizontal levels) can now be applied to the whole sample to derive, for each galaxy, a correction to the confidence intervals calculated assuming a Gaussian distribution. This is shown in Fig. 2.9 of the main text.

Appendix D

Mass-to-light calibrations

Simulated galaxies in TNG50 have stellar masses and corresponding luminosities calculated in several bands, including information on the V-band magnitudes necessary, for example, for computing the specific frequency S_N in Fig. 3.6. However, the simulated luminosities include only evolution due to stellar population models and might neglect important effects, such as dust attenuation. We therefore compute the V-band luminosities of our sample by using a mass-to-light ratio calibration fit to the Virgo cluster data (using stellar masses and V-band absolute magnitudes from Peng et al. (2008)).

This is shown in Fig. D.1, where gray symbols indicate the results directly from the simulations and green stars are data from Virgo. Thin colored lines indicate constant mass-to-light ratios, as labeled, while the thick black solid line highlights the conversion used in this paper. As expected, the calibrated relation differs from the simulated values mostly at the high-mass end, where dust effects might be playing a more important role. While this correction does not significantly impact any of the results in this paper, considering a

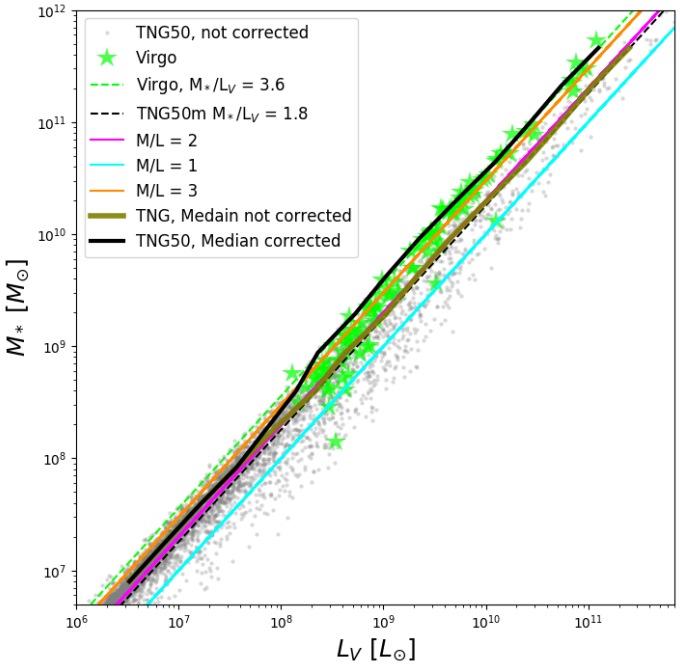

Figure D.1: Mass to light ratio for TNG50 (gray points that show individual galaxies, with the gray-green line showing the median bins of stellar mass and the black dotted line showing the best fit) compared to that of Virgo galaxies overplotted as lime green stars (with the best fit shown as the dotted lime green line). At fixed stellar mass, Virgo galaxies tend to be less luminous at higher-masses than simulated objects. This discrepancy at face value in mass-to-light ratio between TNG50 and Virgo for high-mass galaxies causes a discrepancy in both M_V and S_N for those masses. We therefore adopt a "corrected" mass-to-light ratio (shown in black line) to compute S_N in our results.

mass-to-light ratio equal to 3.6 for more massive galaxies (instead of ~ 2 as suggested by the simulation) improves the agreement with S_N data reported in Sec. 3.5.1.

The evolution in mass-to-light ratio and changes in star formation rate once a galaxy becomes a satellite make necessary an additional calibration in our model. This calibration is related to the dispersion in the luminosity (or mass) function of individual GC masses, σ_z, described in Sec. 3.3.4 in our main article and shown in Fig. 3.1 as a function of stellar mass M_*. This z-band luminosity dispersion σ_z is observationally constrained at $z = 0$ as a function of the *present-day* B-band magnitude (Jordán et al. 2007). However,

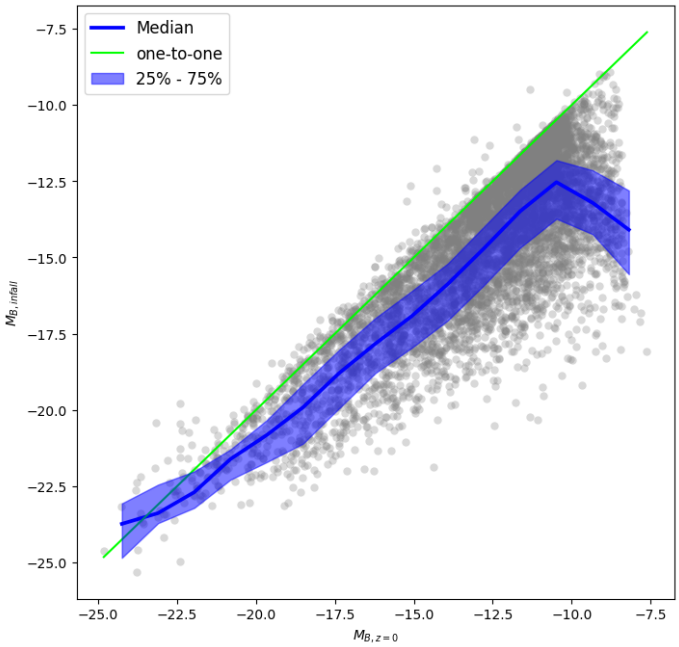

Figure D.2: Comparison between galaxy M_B at infall and at $z = 0$. Since observational results ara available at $z = 0$ but our tagging occurs at infall, we require a calibration that seeks to take the brighter B-luminosities at infall into account when calculating GC luminosity function.

the GC tagging and mass assignment in our model is done at infall (and not present day), requiring of an adjustment at the moment to perform the GC tagging to reproduce the desired results at $z = 0$.

For illustration, we show in Fig. D.2 the B-band luminosity evolution in all our galaxies from infall to $z = 0$. To compensate for this evolution, we first calculate the "target" relation between σ_z and stellar mass M_* (shown in orange in the bottom panel of Fig. 3.3), where M_* is calculated as the median M_* in our simulated galaxies with a given B-band luminosity, all at $z = 0$. Next, we correct the initial σ_z (e.g., at infall time) by calculating the σ_z that would correspond to each galaxy assuming their infall stellar mass and then multiply that by a constant factor: $\sigma_{z,\mathrm{inf}} = \alpha * \sigma_z(M_*)$, where $\sigma_z(M_*)$ is our target

relation at $z = 0$ as described before. After experimenting with different values, we find $\alpha = 0.75$ a reasonable choice, in particular to reproduce the median σ_z at $z = 0$ observed in low-mass galaxies, which is the main focus of this work.

Appendix E

Potential Effects of Dynamical Friction

Massive objects such as GCs can experience dynamical friction as they move within the gravitational potential of the smoothly distributed mass in the host galaxy. Our tagging method does not self-consistently follow this effect since we tag them onto the dark matter particles and all components (dark matter, baryons and GCs) have similar particle mass in our simulations. By default, our GC catalog ignores dynamical friction effects since the method is tailored to tag only the "surviving" population of GCs and not the initial one. However, it is important to double-check that after tagging our GCs they would not be substantially affected by dynamical friction and expected to coalesce to the center of the galaxies and be dissolved.

To gain some intuition, we estimate analytically the typical timescales for dynamical friction in our systems following Eq. 8.17 in Binney and Tremaine (2008a):

$$t_{\rm fric} = \frac{2.7 Gyr}{\ln\Lambda} \frac{r_i}{30\ {\rm kpc}} \left(\frac{\sigma_H}{200\ {\rm km/s}}\right)^2 \left(\frac{100{\rm km/s}}{\sigma_{GC}}\right)^3,$$

where σ_H is the typical velocity dispersion in the host, $\sigma_{\rm GC}$ is the velocity dispersion of the GC, both as proxies for mass, r_i is the initial radius of the GC orbit and $\ln\Lambda = 5.8$ is assumed as a typical Coulomb logarithm. We vary the velocity dispersion of the host assuming $\sigma_H = 800, 200, 50, 20$ and 10 km/s corresponding roughly to the scales of a cluster, a MW like galaxy and dwarfs with $M_* \sim 10^9, 10^8$ and $10^{6.5}$ $M_\odot$, respectively. For the GCs, we compare the effects on two scales: a 2×10^5 $M_\odot$ (typical GC mass) and 1×10^4 $M_\odot$ (our lower limit and common value in low-mass galaxies). We assume a half-mass radius $r_h = 3$ pc to translate GC mass into velocity dispersion σ_{GC}. Finally, we consider the radius r_i as the distance of the GC to the center of the host at infall (the moment of the tagging).

We show the results in Fig. E.1, where the dynamical friction timescales are shown as a function of the distance of the GC. For reference, we indicate the age of the Universe with a thick dashed horizontal line, areas where $t_{\rm fric}$ is above the Hubble time t_H indicates that dynamical friction effects are unimportant. As expected, the dynamical friction timescales increase with radius, meaning that only GCs in the very inner regions are potentially affected. Fig. E.1 also shows that $t_{\rm fric}$ is shorter for more massive GCs, as expected, but even in this case only GCs within $\sim$ 1 kpc have the potential to decay and coalesce due to dynamical friction forces. In the case of a lighter GC, as the one shown on the right panel, the relevant distance where dynamical friction effects might be important shrinks to $\sim$ 0.5 kpc.

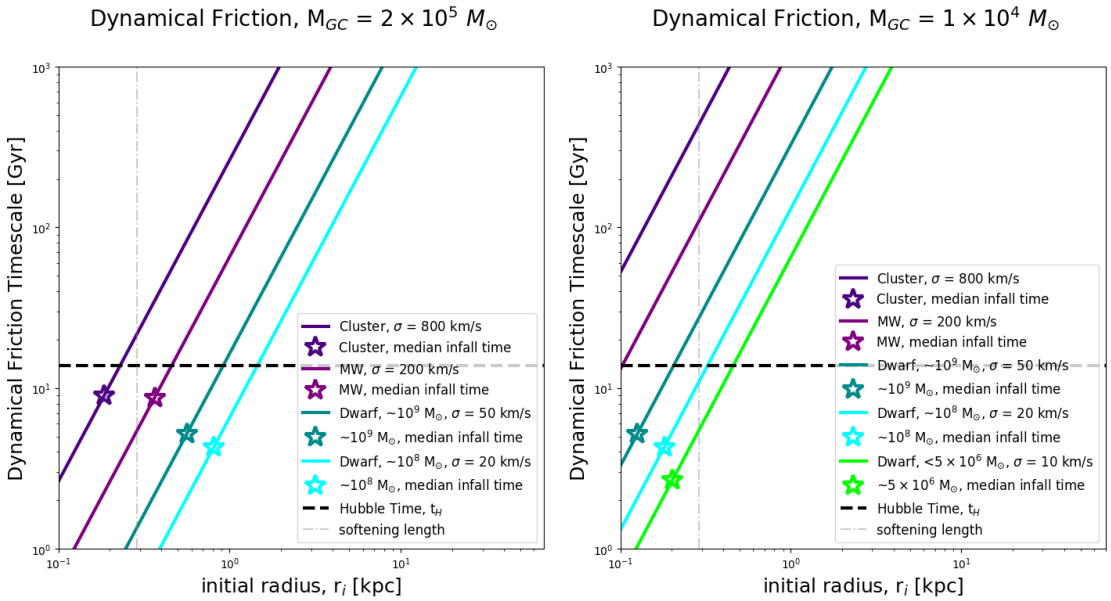

Figure E.1: Dynamical friction timescales for different types of GC host systems, assuming the median GC mass of 2×10^5 $M_\odot$ (left) and 10^4 $M_\odot$ (right). The typical timescales associated to dynamical friction are longer than the age of the Universe for most initial radii and in particular for high-mass hosts. We also indicate the median infall time for galaxies in each mass range with a starry symbol. For dwarf galaxies, dynamical friction timescales might be lower than a Hubble time only for GCs at very small radii $r < 0.5$-1.0 kpc, depending on GC mass, but comparable to the time since their infall time, when GCs are tagged. We therefore expect not a significant change in any of the results when including dynamical friction. Notice that our least massive dwarfs do not have GCs as massive as 2×10^5 $M_\odot$ and therefore are not included on the left panel.

Reassuringly, the distances where dynamical friction migth be a factor of concern are quite small compared to the typical GCs radial extension (see Fig. 3.7) and suggest that dynamical friction effects are not important in our sample. Moreover, the time of relevance is not the age of the Universe but the time since infall, when the GC is tagged. Those are highlighted with a starry symbol in Fig. E.1 and correspond to the median infall times of galaxies of a given stellar mass in our sample. On average, dynamical friction effects are negligible and if present, may impact only the lowest mass galaxies in the sample.

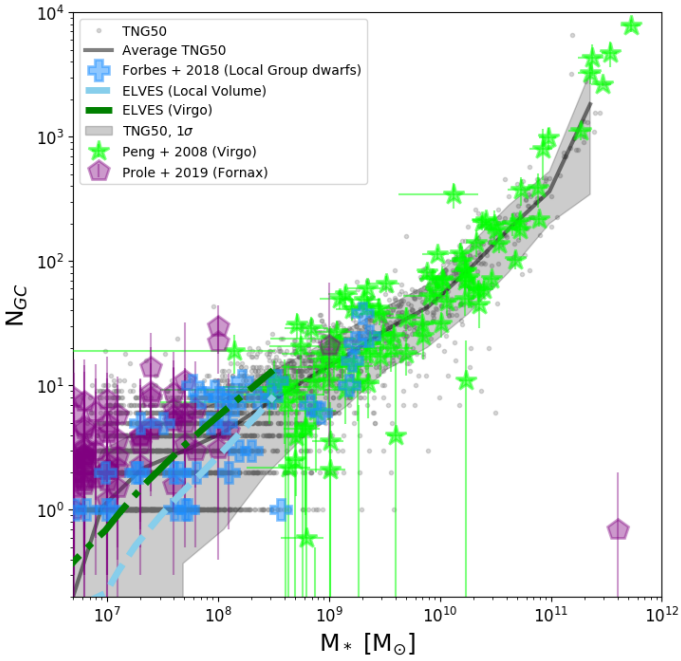

Figure E.2: The same as the left panel of Fig 3.6, but including an estimation of the removal of GCs by dynamical friction. We see very little change in the overall behavior of the GC abundances with stellar mass when including dynamical friction.

Next, using the same equation above, we compute a dynamical friction time individually for each tagged GC and comparing $t_{\rm fric}$ to the particular infall time of that host galaxy we can individually assess whether GCs are expected to decay or not. We flag all GCs where $t_{\rm fric} < (t_H - t_{\rm inf})$ as "merged", and remove them from our sample at $z = 0$. Fig. E.2 and Fig. E.3 show that this would have no significant consequences for our main results, including the number of GCs per galaxy or the occupation fraction, respectively. We therefore conclude that while dynamical friction might impact a few of our GC on an individual basis none of the statistical results presented here changes appreciably. In our released catalog, we provide a dynamical friction flag to allow the user to decide whether to include these objects or not in their calculations.

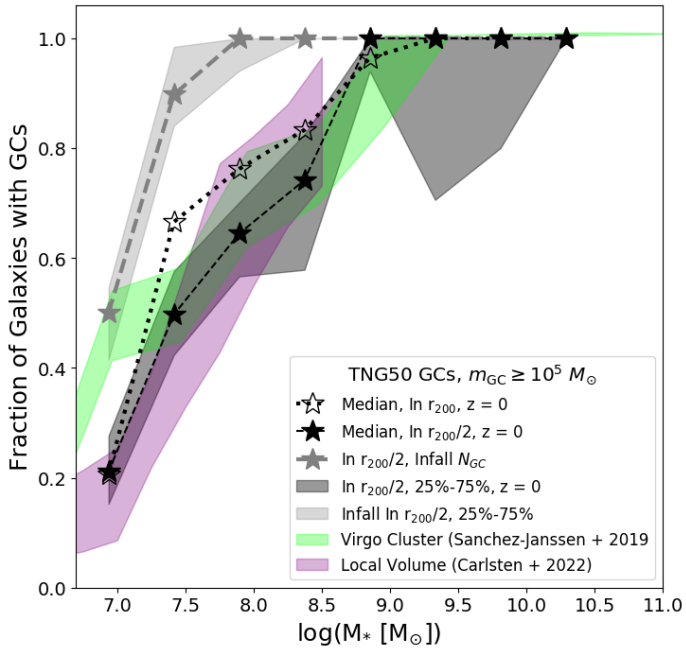

Figure E.3: The same as figure 3.8, but including an estimation for removal of GCs by dynamical friction. We see that the dwarf galaxy stellar mass bins that previously sat above observed values fall nicely within the range of observations when including this effect.

Appendix F

Environmental Effects

Inspired by observations of galaxies in higher density environments showing a higher GC abundance (e.g. Peng et al. 2008; Carlsten et al. 2022), we have checked if this phenomenon was present in our tagged GCs catalog in TNG50. We split the environments in bins of virial mass, and within those bins, we computed the median and $25\% - 75\%$ range of GC abundance in bins of host galaxy stellar mass. Fig. F.1 shows the result of this test. There is little if any variation in both the median and the scatter between the different virial mass bins. Running the same check on S_N shows the same lack of dependence with the host.

The GC tagging model employed in this work relies on the infall virial mass of a galaxy; thus we checked to see how infall virial mass varies across the tagged environments in Fig. F.2. Binning again in host environment virial mass, we calculated the median infall virial mass in bins of *present-day* host galaxy stellar mass, $M_{*,\mathrm{z=0}}$. We find a weak environmental dependence on the infall halo masses at fixed $z = 0$ stellar mass that goes

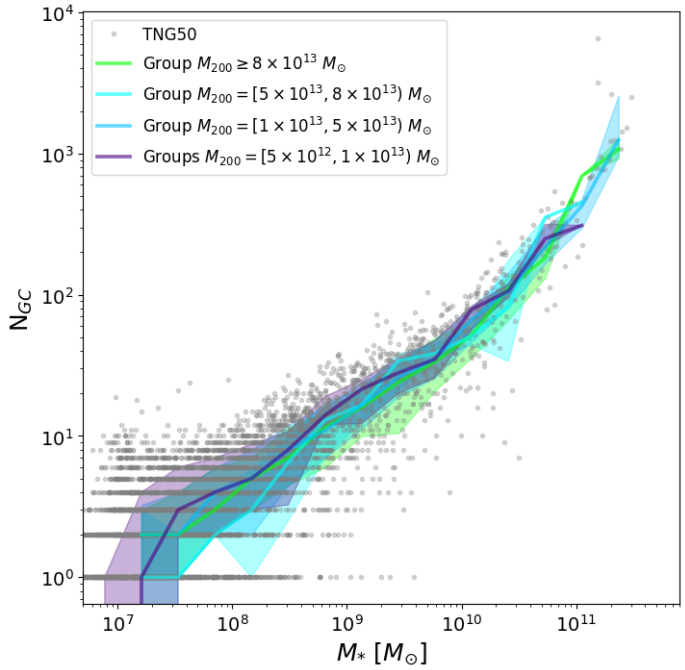

Figure F.1: Number of GCs, $N_{\rm GC}$ as a function of host galaxy stellar mass M_* binned in host cluster virial mass. The solid lines show the median in bins of host galaxy stellar mass with the shaded region showing the $25\% - 75\%$ scatter in each bin. We find no pronounced dependence on GC abundance with host group or cluster environment.

in the direction expected: galaxies of a given stellar mass today had a larger infall virial mass for high density environments (see e.g., Mistani et al. 2016). However, we had had to include low-mass host halos with present-day $M_{200} \geq 10^{11}$ M$\odot$ (which are not included in our catalog) in order to observe the effect. Limiting the host halo mass to the ones included in this study ($M_{200} > 5 \times 10^{12}$ M$_\odot$) shrinks the effect appreciably, explaining why our GC catalog shows no significant dependence with environment. Thus, it may be necessary to study a much wider range of host halo masses in order to see the observed environmental dependence on GC abundance.

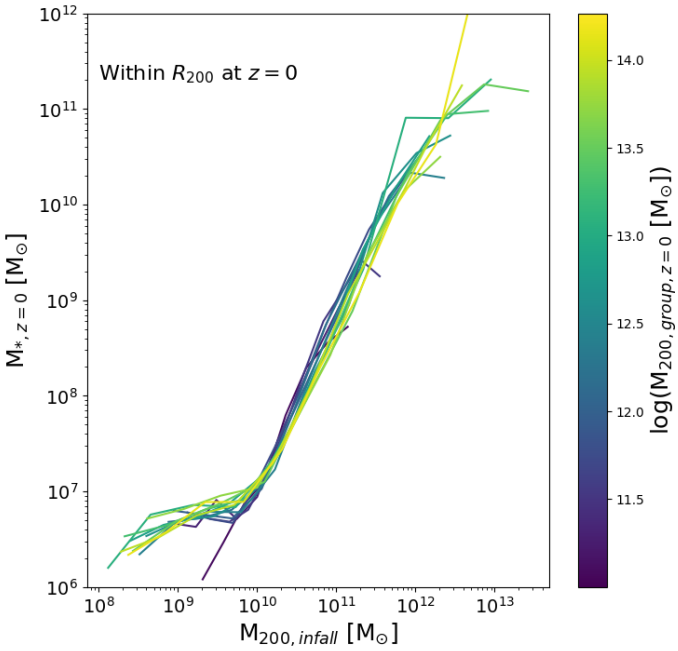

Figure F.2: M_* at $z = 0$ as a function of infall virial mass $M_{200,\mathrm{infall}}$ for galaxies within R_{200} of their $z = 0$ host environment in TNG50. Medians are colored by $z = 0$ host virial mass (color bar on the right). There is a weak but systematic trend for satellites with fixed stellar mass today to have a larger infall virial mass in more massive hosts, in particular for $M_* > 10^7$ $M_\odot$. Note that we extend the calculation to host virial masses $M_{200} = 10^{11}$ $M_\odot$, which is well below our minimum host halo mass tagged, in order to clearly see the effect. For hosts with $M_{200} > 5 \times 10^{12}$ $M_\odot$, as studied here, there is not enough difference in satellite infall masses to lead to any environmental trend on GC content.

Appendix G

Halo Masses of Ultradiffuse Galaxies

In Figure G.1, we show the stellar mass at $z = 0$ ($M_{*,z=0}$ as a function of infall virial mass ($M_{vir,infall}$) for dwarf galaxies in the TNG50 simulation. All dwarf galaxies are represented by points colored by their infall time (the last time they were their own central within the simulation), with UDGs highlighted by orange circles. A subset of UDGs, those in the top 15% of specific frequency S_N at fixed M_V are represented by red hexagons. We can see that in this relation, UDGs with higher S_N tend to reside at the edge of this abundance matching relation, with higher halo masses and preferentially earlier infall times that less extreme UDGs, consistent with results from Ramos-Almendares et al. (2020). Interestingly, even UDGs that are extreme in this relation reside in DM halos that are consistent with those of typical dwarf galaxies.

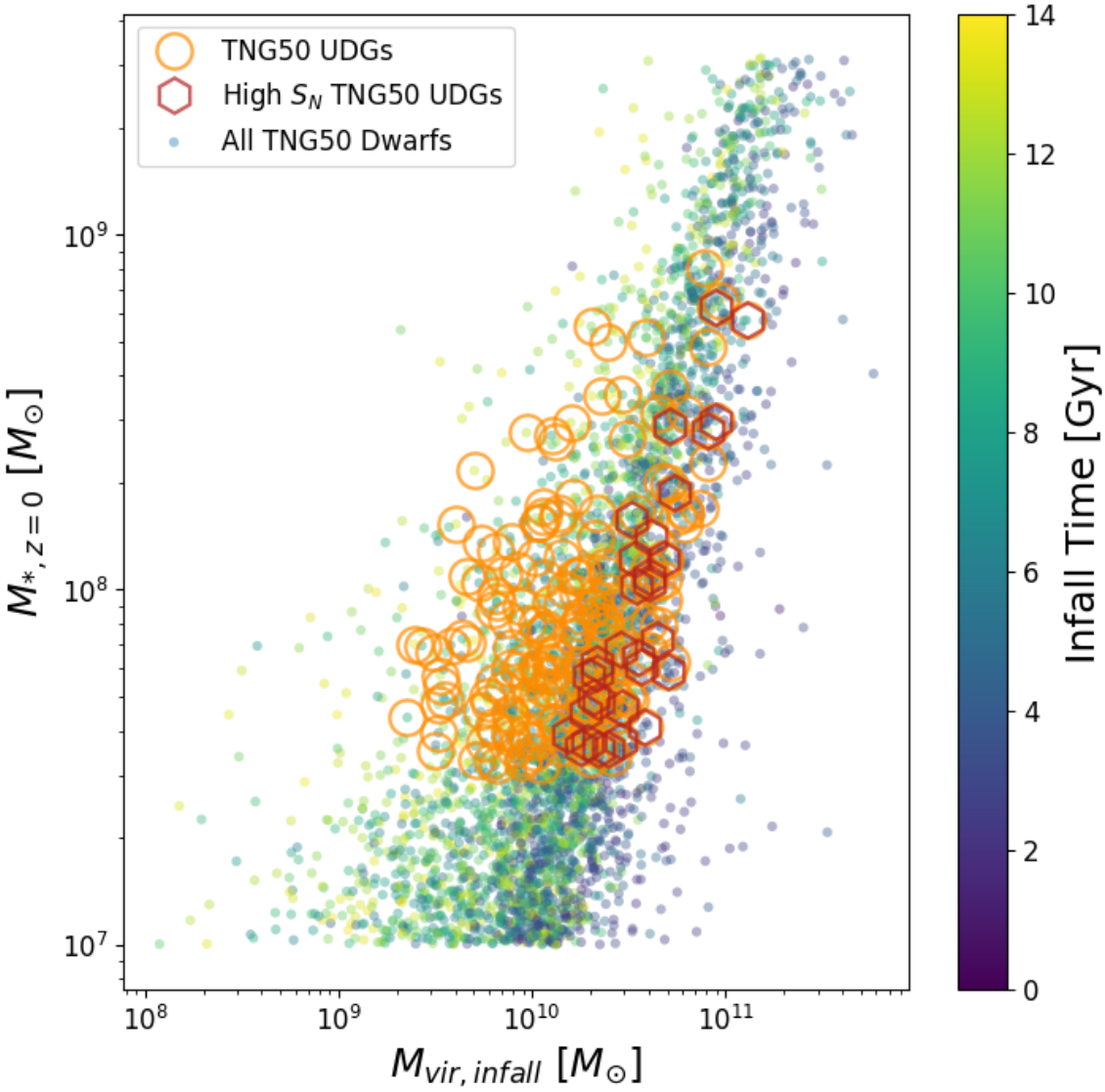

Figure G.1: $z = 0$ stellar mass, M_*, vs infall halo mass, $M_{vir,infall}$. All dwarfs in this mass range are points colored by their infall time, with UDGs highlighted by orange circles. Red hexagons represent UDGs that are in the top 15% of S_N at fixed M_V, meaning that they are particularly extreme within the simulation. We find that these extreme UDGs tend to have earlier infall times and more massive halos than their less extreme counterparts, but that all UDGs appear to reside within the range of normal dwarf galaxies.